THE ZEBRAFISH AS A MODEL FOR STUDIES OF
CARDIAC MECHANO-ELECTRIC FUNCTION

by

Jonathan S. Baillie

Submitted in partial fulfilment of the requirements
for the degree of Doctor of Philosophy

at

Dalhousie University
Halifax, Nova Scotia
November 2022

Dalhousie University is located in Mi'kma'ki,
the ancestral and unceded territory of the Mi'kmaq.
We are all Treaty people.

DEDICATION PAGE

TBoyd,

I remember how excited you were when I told you I was embarking on this journey.

Thanks for helping me follow through.

I've been telling everybody that you're the man, à la Aloe Blacc.

TABLE OF CONTENTS

LIST OF TABLES

LIST OF FIGURES

ABSTRACT

Factors affecting cardiac function include those external to the heart (*e.g.*, the autonomic nervous system, ANS) and intrinsic processes that allow rapid beat-by-beat adaptation to change in physiological demands. The overall objective of my PhD research was to develop and utilise methods to investigate the integrated control of cardiac electrical and mechanical activity by intrinsic and extrinsic mechanisms in the zebrafish. This involved: i) creation of a micro-cannulation technique to acutely manipulate the heart's hemodynamic load *in vivo* in intact zebrafish larvae and ii) intracellular microelectrode measurements of cellular electrical activity *in situ* in isolated zebrafish hearts combined with its optogenetic manipulation.

In the developing heart, effects of acute changes in hemodynamic load on cardiac function are not well established but may be critical for the pre-neuronal control of cardiac excitation and contraction. The specific aims of the primary portion of my thesis were to determine the influence of acute changes in hemodynamic load on cardiac function *in vivo* in intact zebrafish larvae during: i) different stages of cardiac development, to define its evolution in the developing heart and ii) pharmacological interrogation of the ANS and stretch-activated channels, to determine intrinsic and extrinsic mechanisms driving observed functional changes, along with measurement of membrane potential and intracellular calcium-dynamics using genetically-expressed fluorescent reporters. It was found that an acute increase in hemodynamic load at 2 days post fertilisation (dpf) causes a small decrease in heart rate, which becomes an increase by 6 dpf and is further increased at 14 dpf, while stroke volume was increased at all developmental stages. Interventions indicated that effects on cardiac rhythm are mediated by both intrinsic (stretch) and extrinsic (ANS) mechanisms, while the effects on stroke volume are purely intrinsic. Metrics of intracellular calcium handling (time to peak transient, transient duration) were altered with acute hemodynamic loading, while voltage dynamics remained unchanged.

Activation of cation-conducting channelrhodopsins leads to membrane depolarisation, allowing the effective triggering of action potentials (AP) in cardiomyocytes. In contrast, the quest for optogenetic tools for hyperpolarisation-induced inhibition of AP generation has remained challenging. The green-light activated channelrhodopsin GtACR1 mediates chloride-driven photocurrents that have been shown to silence AP generation in neurons. It has been suggested, therefore, to be a suitable tool for inhibition of cardiomyocytes activity. The aim of this project was to determine the effects of GtACR1 with pulsed and sustained light stimulation in intact zebrafish hearts. It was found that both modes of light stimulation resulted in cell depolarisation, such that pulsed light paced the heart, and sustained light caused silencing. While this does not address the need for optogenetic silencing by hyperpolarization, GtACR1 is a potentially attractive tool for activating cardiomyocytes by transient light-induced depolarisation.

Overall, my research has revealed factors involved in the regulation of cardiac function in response to acute changes in hemodynamic load during development and has shed light on the potential use of optogenetics for cardiac control. My novel findings may help us toward a better understanding of disturbances that arise in congenital heart disease during cardiac development and maturation and how they may ultimately be treated.

LIST OF ABBREIVATIONS

ACh   Acetylcholine

ANOVA   Analysis of Variance

ANS   Autonomic Nervous System

AP   Action Potential

APD   Action Potential Duration

ATR   Atropine

AV   Atrioventricular

β-AR   Beta Adrenergic Receptors

BP   Blood Pressure

BR   Beating Rate

Ca^{2+} Calcium

CaTD   Calcium Transient Duration

CHD   Congenital Heart Disease

ChR2   Channelrhodopsin-2

Cl^- Chloride

CM   Cardiomyocyte

CNS   Central Nervous System

CO   Cardiac Output

CO_A Cardiac Output Area Index

CT   Crista Terminalis

CVD   Cardiovascular Disease

cAMP   Cyclic Adenosine Monophosphate

DD	Diastolic Depolarisation
DPF	Days Post Fertilisation
ECC	Excitation-Contraction Coupling
EDA	End Diastolic Area
EDV	End Diastolic Volume
ESA	End Systolic Area
ESPVR	End-Systolic Pressure Volume Relation
ESV	End Systolic Volume
EF	Ejection Fraction
FSL	Frank-Starling Law
HCN4	Hyperpolarization-Activated Cyclic Nucleotide-Gated Channel 4
HR	Heart Rate
HPF	Hours Post Fertilisation
$I_{Ca,L}$	L-type Ca^{2+} current
$I_{CaL1.2}$	L-type Ca^{2+} channel isoform CaV1.2 current
$I_{CaL1.3}$	L-type Ca^{2+} channel isoform CaV1.3 current
$I_{Ca,T}$	T-type Ca^{2+} channel isoform CaV3.1 current
I_f	Funny Current
I_{Kr}	Delayed rectifier potassium current, rapid
I_{Ks}	Delayed rectifier potassium current, slow
I_{NCX}	Sodium Calcium Exchange current
ICNS	Intra Cardiac Nervous System
LV	Left Ventricle

MEC	Mechano-Electric Coupling
MHC	Myosin Heavy Chain
NCX	Sodium Calcium Exchanger
NE	Norepinephrine
P1	Protocol One
P2	Protocol Two
P3	Protocol Three
PNS	Parasympathetic Nervous System
PKA	Protein Kinase A
M_2	Muscarinic Receptor
RV	Right Ventricle
SA	Stroke Volume Area Index
SAC	Stretch Activated Channel
SAC_{NS}	Stretch Activated Channel (non-ion-specific)
SAN	Sinoatrial Node
SM	Streptomycin
SNS	Sympathetic Nervous System
SR	Sarcoplasmic Reticulum
SV	Stroke Volume
SVC	Systemic Venous Capacitance
TIM	Timolol

ACKNOWLEDGEMENTS

Where does one begin to thank everyone involved in such a process. So many people that have contributed to get me to this point. Most of whom, likely have no idea the motivation and inspiration they have provided.

I would like to start off by thanking my external examiner, Dr. Ian Scott. We met briefly at the IZFS conference in Montreal this year. Afterwards, when your name came up in discussion of potential external examiners, I immediately had a great feeling about your knowledge and expertise. Thank you for agreeing to take on this task.

To my incredibly patient and helpful committee. Thank you for your continued support, encouragement, and wise words. Drs. Ketul Chaudary, Yassine El Hiani, Petra Kienesberger, and Frank Smith. Ketul, your addition to my committee as a chair has provided great insight and your support and enthusiasm for my work has not gone unnoticed. Thank you. Yassine your belief in me and the conversations that we have shared have meant a lot to me and I am truly thankful for the inspiration. Petra, although much of our communication has been virtual, your input and encouragement in our meetings has made my presentations and overall progress reach new heights. Frank, a walking encyclopedia, your leadership and guidance have allowed me to develop as a scientist and question everything. Thank you for your patience (especially in the earlier days!).

I would like to thank all the members of the Department of Physiology and Biophysics. The faculty, staff, administration, as well as fellow students. Although I might be the worst at responding to emails and participation, your motivation and support

to the progression of the department does not go unnoticed. It has been a pleasure working and learning with all of you.

Thank you to Drs. David Bark Jr. and Deborah Garrity and all the lab members at Colorado State University departments of Biology and Biomechanical Engineering. Thank you for welcoming me into your labs and allowing me to learn under your expertise to help develop as a scientist. Especially, Alex Gendernalik, some of those times I will never forget. It has been such a privilege to get to know you all.

To my friends and family. Thank you so much for your understanding and support. It has been a long road and I would not be the person I am today if it were not for you. I owe so much of any success that I achieve because of you. Mom (and Dad), thank you for your undying support and unconditional love. Mom, you truly are a saint and your dedication to everyone around you is inspirational. Melanie and Heather, you have both been monumental in the support you have provided (whether you know it, or not). There have been many days where this journey was a lot to bare, thank you for your help in getting me to the other side. To all my brothers, you continue to inspire me and make me want to be better on every level. To all my friends, especially the Cole Harbour boys for the constant laughter and great times. It's a special bond that we share that is quite rare and has lasted the test of time. Thank you for your patience in all the missed events and late arrivals. Nick and Dave, you two have been there for me since day one and I am so grateful and honoured to call you two my friends. Special shout out to the Brown Hound Public House, apparently, they have a fantastic late afternoon brunch ;).

To all members of the Quinn Lab new and old, Bre and Eilidh – you have both been so inspiring and set a high bar in your pursuit to conduct great science. It was truly a

pleasure to get to witness you both become absolute rock stars and I look forward to what the future brings for both of you. Matt, thank you for all the time and dedication you have provided (especially in the early days). You are so willing to help everyone in the lab, and anyone would agree the lab would not be as great without you in it.

To the newer members, I have to say, I was a little reluctant to welcome this new age TAQ lab after Bre and Eilidh parted. However, this second phase has provided some exceptional laughs and a perhaps a few too many whiskies. Ahmed, Katherine, Jessi, Michael, and Zach. You are all great individuals, scientists, and soon to be medical doctors! I will keep my sunglasses close because the future is bright for all of you! Zach, thank you for the daily discussions about baseball, politics, news, literally anything other than writing – these distractions were necessary and extremely welcomed.

Finally, I have to my supervisor, Alex. I have often said that I have put more thought into this acknowledgements section than the actual document, because words are not enough to express my gratitude. You have continued to challenge me and help me grow as a scientist, and as a person. When I first joined the lab, I was (over)confident, and I quickly came tumbling back to earth after being humbled the first few years of this program upon realising how little I knew. There is a quote by Ken Poirot that comes to mind that says, "Greatness is inspiring others to be their best" and for that, Alex, you are truly great. Your inspiration as a scientist, leader, and how you carry yourself in general, made me want to keep going and be at my best. I have found my confidence again and I am very much looking forward to the future, mostly because of you. Creating the environment at the lab, the opportunities to travel and showcase our research, the

resources, and perhaps most importantly, the general conversations about nothing at all,

thank you.

CHAPTER 1: INTRODUCTION

Heart disease does not respect national boundaries. It is most appropriate then, that the pursuit of advancement in medical knowledge must also follow this trend. Medical advancement, treatment options, research findings, must be internationally oriented and collaboration focused, for mankind is strongest when we work together toward a common goal.

1.1. Cardiovascular physiology

Cardiovascular physiology investigates the intricate framework of the heart, blood, and circulatory system, as well as the associated dynamics and function [1]. The initiation of a normal heartbeat is achieved through the spontaneous firing of an electrical impulse from a centralised network of pacemaker cells in the sinoatrial node (SAN). The electrical impulse produces the corresponding mechanical action necessary to deliver blood to the network of vessels containing the necessary nutrients and oxygen to the body [2]. Function of the heart is affected by extrinsic and intrinsic mechanisms that allow adaptation on a beat-by-beat basis [3,4]. Stretch of cardiac tissue is a critical intrinsic modulator of cardiac function, as demonstrated by the increase in heart rate (HR, number of beats per minute) and stroke volume (SV, blood ejected during a single beat) in response to increased venous return to the heart [5,6]. In the developing heart, effects of acute changes in hemodynamic load on cardiac function are not well established but may be critical to the pre-neuronal control of cardiac excitation and contraction - prior to intrinsic neuronal and autonomic nervous system (ANS) contribution. This chapter will discuss opportunities for the investigation of cardiac electrophysiology relating to two

modalities of measurement of cardiac function i) increased hemodynamic load and ii) optogenetic measurement and manipulation. Additionally, this chapter will briefly discuss studies that have been conducted in small mammalian and zebrafish models – highlighting advantages and limitations of each model.

1.1.1. Cardiac excitation

The cardiac action potential (AP) consists of a brief change in voltage across the membrane of CM, facilitated by movement of ions inside and outside of the cell, through ion channels [7]. When a channel is opened, the electrical conductance of specific ions through that ion channel is increased. Closure of ion channels causes ion conductance to decrease. As ions flow through open channels, they generate electrical currents that change membrane potential (V_m).

The initiation of each AP occurs in pacemaker cells of the SAN , characterised as having no true resting potential, instead displaying a cyclic, spontaneous diastolic depolarisation (DD) [8]. This process involves a positive inward current ('funny' current, I_f) that occurs through the slow activation of hyperpolarisation activated cyclic nucleotide-gated (HCN) channels during the early phase of diastole, acting against outward potassium (I_{Ko}) currents [9]. As diastole progresses and V_m becomes more depolarised, trans-sarcolemmal calcium (Ca^{2+}) influx through CaV3.1 transient Ca^{2+} channels (I_{CaT}) and CaV1.3 long-lasting (L-type) Ca^{2+} channels ($I_{Ca,L}$) becomes dominant [10]. Once V_m depolarises to reach the threshold for activation of CaV1.2-$I_{Ca,L}$, an AP is fired [11].

In a typical mammalian heart, the SAN generates an electrical stimulus that first activates the atria, and then travels along the conduction pathways, pausing briefly (100

ms) at the atrioventricular (AV) node, continuing down the conduction pathway of the Purkinje fibres and throughout the ventricles via the bundle of His. The bundle of His divides into right and left pathways, called bundle branches, to stimulate the right and left ventricles[12]. The AP of the working myocardium is different from that of pacemaker cells, consisting of five phases, as opposed to three in pacemaker cells of the SAN. The initial phase (phase 4) consists of a resting membrane potential near -90mV. Phase 0 is defined by a rapid depolarisation initiated by the opening of voltage-gated Na^+ channels, resulting in a rapid influx of Na^+ ions, causing a steep upstroke in the AP, as V_m changes from -90mV to +50mV. As the AP transitions into phase 1, I_{Na} becomes inactivated coinciding with the activation of transient outward K^+ current (I_{to}) causing a small repolarisation in the V_m producing a characteristic 'notch' in the morphology of the AP. Phase 2 represents the plateau phase where a Ca^{2+} influx occurs through an opening of voltage-gated $I_{Ca,L}$ in the transverse-tubules of the sarcolemma. The Ca^{2+} influx balances the K^+ efflux, creating a plateau at an electrochemical potential of +50mV, during which the influx of Ca^{2+} also stimulates Ca^{2+} release from the sarcoplasmic reticulum (SR), initiating muscle contraction. The last step of the AP is phase 3 and consists of cellular repolarisation, during which there is a K^+ efflux through the opening of delayed rectifier K^+ channels (I_{Kr}, I_{Ks}, I_{K1}) and closing of the voltage-gated $I_{Ca,L}$, returning V_m back to the resting potential of -90mV (phase 0), allowing the sequence to repeat.

1.2. Excitation-contraction coupling

Excitation–contraction coupling (ECC) describes the relationship between the electrical excitation of the cardiomyocytes (CM) preluding the active contraction causing a mechanical transformation of the heart [13]. During this process, second messenger Ca^{2+}

is an essential component in the electrical activity and the principle activator of myofilaments, responsible for contraction [14].

During the cardiac AP, as Ca^{2+} enters the cell, this entry triggers Ca^{2+} release from the SR *via* ryanodine receptors located in the membrane of the SR. The combination of Ca^{2+} influx and release, raises the free intracellular Ca^{2+} concentration ($[Ca^{2+}]_i$), which diffuses to the myofilaments and binds with the myofilament protein troponin C (TnC), enabling the contractile machinery to become activated. In order for the contraction to relax, $[Ca^{2+}]_i$ must decrease to allow Ca^{2+} dissociation from TnC, which requires Ca^{2+} removal from the cytosol by three pathways involving SR Ca^{2+}-ATPase (*i.e.*, SR reuptake), sarcolemmal Na^+/Ca^{2+} exchange (NCX), and sarcolemmal Ca^{2+}-ATPase (*i.e.,* cell extrusion) [13].

1.2.1. Cardiac contraction

A sarcomere is the basic contractile unit of muscle fiber, which is comprised of the two main protein filaments: actin and myosin [15,16]. The most popular model that describes a muscle contraction, is the sliding filament theory [17]. In this theory, active force is generated as actin filaments slide past the myosin filaments, resulting in contraction of an individual sarcomere. This is powered using adenosine triphosphate (ATP), but first Ca^{2+} ions must bind the protein complex TnC, exposing the active-binding sites on actin [18]. Once the actin-binding sites are uncovered, the high-energy myosin head bridges the gap between itself and actin, forming a cross-bridge with the actin filament. A phosphate is then removed from the ATP bound to myosin, resulting in a change in confirmation of the protein becoming adenosine diphosphate, and what is known as the "power stroke". At the end of the power stroke, the myosin is in a low-

energy position.Adenosine diphosphate is released, but the cross-bridge formed is still in place and requires ATP to unbind [19]. ATP binds to myosin again, moving to a high-energy state and allowing the myosin head to release from the active actin site.

There are two main ways the strength of cardiac contraction is altered: by changing the amplitude or duration of the Ca^{2+} transient, and by altering the sensitivity of the myofilaments to Ca^{2+} [13].

1.3. Mechano-mechanical coupling

Acute myocardial stretch from acute changes in hemodynamic load can be observed in various physiological and pathophysiological conditions (e.g., postural changes, exercise, myocardial ischemia, hypertensive crises, valvular diseases, and heart failure) [20,21]. On a beat-to-beat basis, cardiac contractile function is driven by a multifaceted and dynamic process that is regulated by both intrinsic (*e.g.*, mechanical loading) and extrinsic (*e.g.*, neuro-hormonal) factors [22]. Specifically, the level of contractile activation of adult mammalian CM is modulated by the magnitude of the Ca^{2+} transient, the dynamic activation–relaxation kinetic response of the sarcomere to activator Ca^{2+}, and the responsiveness of the myofilament to Ca^{2+}, the last of which is dependent on sarcomere length and is a primary mediator of the Frank–Starling mechanism (FSM)[23].

The basis of the FSM is the intrinsic ability of the myocardium to produce a greater active force, during contraction in response to stretch, known as length-dependent activation. A feedback mechanism transmitted from cross-bridge formation to TnC to enhance Ca^{2+} binding has long been proposed to account for length-dependent activation [24]. Advances in muscle physiology research have identified a third filament system

5

composed of the elastic protein titin, showing significant coupling of active and passive forces in cardiac muscle. Titan-based passive force promotes cross-bridge recruitment, resulting in greater active force production in response to stretch [24].

1.4. Mechano-electric coupling

The primary purpose of the heart is to pump blood to the body, matching the metabolic needs of the body, accomplished through the delicate balance between electrical excitation and mechanical contraction [4]. During basal conditions, ECC is generally sufficient to sustain the demands of the body [13]. However, during instances of increased metabolic demand, ranging from small postural or hormonal alterations to larger demands related to exercise or heightened stress, the cardiovascular system must adapt to supply the body during these dynamic scenarios [25]. This is accomplished in part through a feedback system driven by mechanical input preceding the electrical contribution, or more eloquently termed mechano-electric coupling (MEC) [4,25–28]. Both processes of ECC and MEC are critical in the modulation and sustainability of normal cardiac function, and together comprise a "mechano-electric regulatory loop" (Figure 1.1) [4].

Early experimental evidence of MEC was reported by Francis Bainbridge who demonstrated that a rapid increase in HR coincides with right atrial distension by intravenous fluid injection in anaesthetised canines [29]. This indicates that the heart responds to increases in hemodynamic load on an acute, time-sensitive, beat-by-beat basis. This effect is now appropriately termed the Bainbridge reflex. More recently, this reflex has been recognised as an effect that is intrinsic to the heart (*i.e.*, does not act through extracardiac reflex loops), as it has been shown in the denervated [30] and

transplanted heart [31], *ex situ* animal hearts [6], isolated tissue [32], and in isolated pacemaker cells [33]. It is also insensitive to ablation of intracardiac neurons [34], block of neuronal Na^+ channels [34,35], as well as adrenergic and cholinergic blockers [34–37], further indicating that this effect is associated with an intracardiac mechanism. This effect does not appear to be species dependent, as it has also been observed in a variety of vertebrates [38], including human [39].

MEC is essential for the heart's adaptation to constantly changing physiological conditions and is important for normal heart function (Quinn, 2015). In some instances relating to pathophysiological mechanical perturbations, or specific disease states, MEC can instead create an environment that promotes the development of atrial and ventricular arrythmias, as well as the overall destabilisation of cardiac rhythm [40–48].

In terms of the increase in HR that occurs with an increase in atrial load, intracellular microelectrode recordings in SAN tissue under stretch have shown increased maximum diastolic V_m, decreased maximum systolic V_m, and increased DD rate [49]. Patch-clamp recordings in axially stretched isolated SAN cells combined with computational modelling have provided an explanation for these changes by demonstrating that stretch responses occur through a mechano-sensitive whole-cell current, with a reversal potential of ~-11mV [33], likely being carried by the cation non-selective stretch-activated channels (SAC_{NS}). Evidence supporting this rapidly activating effect which involves a current with a reversal potential between 0 to -20 mV [50,51]. This effect has been demonstrated from studies in which SAC_{NS} has been blocked, causing a reduction of the stretch-induced effect on HR [52]. This effect may also be driven by SAC_{NS} in fibroblasts [53], which appear to be electrically coupled to SAN cells [54], so could

support stretch-induced depolarisation [55,56]. A similar effect has also been demonstrated in stretched Purkinje fibers during ventricular diastole [57], which display a mechanically-induced increase in automaticity [58,59] and conduction velocity [49,60,61].

An interaction between intrinsic mechanical control and autonomic modulation has been shown in intact animals [62,63] as well as isolated atria [64–66]. It was demonstrated that with an increase in atrial pressure, a corresponding increase in HR was paired with a decrease in response to vagal stimulation. This effect was also present when HR was reduced through vagal stimulation as the stretch-induced HR response was increased. This interaction may be mediated by muscarinic K^+ channels, as has been more recently demonstrated with atrial distension [67]. This suggests that parasympathetic nervous system (PNS) control of HR may be continuously modified by atrial load, further implicating stretch-induced adjustments of HR to changes in hemodynamic demand as critical for maintaining cardiac output (CO) [68].

In physiological conditions, the magnitude of end-diastolic volume (filling) of the right atrium is directly related to the degree to which the SAN is exposed to stretch. The amount of venous return is increased during activities that are above basal conditions. Through the Bainbridge reflex, HR is increased in response to an increase in right atrial volume. In coordination with this effect are the cell length-dependent changes in SV that occur though the Frank-Starling mechanism. These two stretch-induced responses act to mitigate the imbalance in supply by increasing CO, which is the product of HR x SV.

1.4.1. Mechano-sensitive channels

Over the last three decades, molecular drivers of cardiac mechano-sensitivity have gained increased recognition in the scientific and clinical communities. Stretch-activated

channels (SAC) have been identified as one contributor to mechano-sensitive autoregulation of the heartbeat. SAC appear to play important roles in the development of cardiac pathologies, most notably stretch-induced arrhythmias [69]. Specifically, mechano-sensitive ion channels sense changes in mechanical stimuli, such as when atrial or ventricular tissue is stretched and/or pressure is applied, causing depolarisation of the CM V_m, which results in changes in action potential duration (APD) and QT interval [70].

Increases in cell volume (volume activated channels; VAC), whether by swelling [71] or pipette-based cell inflation [72] has been shown to increase Cl^- [71] or K^+ conductance [73]. Increased cell volume induces a morphological deformation, however, from an acute cardiac electrophysiological perspective, the delay in response time from VAC is on the order of tens of seconds to minutes after the onset of cell volume changes [74]. This has created more doubt as opposed to solid confirmations regarding the role of mechanical stimuli as the primary driver of VAC gating. as it has been suggested that swelling-induced changes in cytoskeletal structures must take place before mechanosensitive electrophysiological responses are seen [75].

The first whole-cell K^+ selective stretch-activated channel (SAC$_{K)}$ currents ($I_{SAC,K}$) were identified in cardiac cells [73]. SAC$_K$ pass an outward rectifying current, allowing easy efflux of K^+ ions out of the cell. These currents are ion-specific, have large single-channel conductance, and become inactive in a time-dependent manner [76]. Activation of SAC$_K$ currents induces a repolarisation or hyperpolarisation effect [77], and have been identified in adult mammalian atrial [73] and ventricular [78–80] CM.

The identification of cation-specific SAC is a relatively new sub genre of cardiovascular research, first identified in embryonic chick skeletal muscle less than 40

years ago [51], while SAC whole-cell currents in mammalian heart muscle were identified a few years after [50]. In comparison to SAC_K, SAC_{NS} currents have a smaller conductance, and a reversal potential closer to 0 mV. As the reversal potential is positive relative to the resting V_m of a CM, activation of these channels will act to depolarise resting CM. This action can trigger unwanted firing in the form of premature or ectopic excitation [77]. In contrast to SAC_K, single channel recordings have not been identified in SAC_{NS}. This may be due to restricted access to channel expression in membrane regions such as transverse-tubules or intercalated discs. The main molecular candidates for SAC_{NS} are Piezo1 and TRP channels [69,76]. See Figure 1.2 for a more comprehensive list of potential cardiac candidates.

1.4.2. Mechano-sensitive calcium handling

The FSM is an intrinsic property of all vertebrate cardiac tissue, and has been demonstrated in adult and embryonic myocardium [81]. This mechanism of increased force of contraction is vital for linking changes in SV to changes in venous return [82]. An increase in venous return dilates the working myocardium, stretching the tissue and resulting in an increase in SV to accommodate the increase in venous return. In this way, the FSM is a central component to the regulation of CO [83]. Myofilament Ca^{2+} sensitivity is enhanced dynamically by stretching the myofilaments (as the heart fills with blood), resulting in a stronger contraction. This is due, in part, to the transverse filament lattice compression that occurs with stretch, enhancing actin–myosin interactions [13]. The stretch-induced increases in myofilament Ca^{2+} sensitivity involve a contribution from cross-bridge formation. In the absence of Ca^{2+}, the thin filament TnC prevents binding of actin and myosin [83]. Tropomyosin is bound to the troponin complex, which contains troponin T

(TnT; tropomyosin binding), TnC (Ca^{2+} binding), and troponin I (TnI; inhibitory). When Ca^{2+} binds to TnC, an increased interaction with TnI allows tropomyosin to partially move into a groove along the actin thin filament, allowing myosin heads to form weak and strong cross-bridges with actin [84]. When a strong cross-bridge forms, this generates increased tension, further shifting tropomyosin into the actin groove, promoting neighbouring myosin head cross-bridge formation [85,86]. Strong binding cross-bridges also induce cooperative activation of actin by increasing the affinity of TnC for Ca^{2+} [87], indicating coupling between the Ca^{2+} regulatory sites on TnC and cross-bridge interactions in the thin filament [88]. This mechanism of propagated activation may be particularly important as small changes in the proportion of strong cross-bridge formations have drastic effects on the Ca^{2+} sensitivity of force [85].

The cell membrane controls the balance between intracellular and extracellular Ca^{2+} *via* various proteins, and thus helps maintain Ca^{2+} homeostasis. Plasma membrane Ca^{2+} ATPase, voltage-gated Ca^{2+} channel, and NCX have been identified as the main Ca^{2+} regulatory proteins on the cell membrane [89–92]. The SR as an important Ca^{2+} reservoir in the cell also contains Ca^{2+} regulatory proteins. Such proteins in the SR include stromal interaction molecules, inositol 1,4,5-trisphosphate receptor (IP$_3$R), and Sarcoendoplasmic Reticulum Calcium ATPase (SERCA). All these proteins are critical in controlling cell functions, such as growth, migration, apoptosis, and metabolism [93–95]. As a general feedback mechanism, these key Ca^{2+} regulatory proteins are also regulated by intracellular Ca^{2+} levels [96].

Mechanical forces are essential for cardiovascular function and therefore the discoveries of mechano-sensitive ion channels represent a major breakthrough in

understanding cardiovascular mechanobiology. In particular, the endothelium in the cardiovascular system is subjected to regular mechanical stimuli from transmural blood pressure (BP) and shear stress from blood flow. The recently discovered mechano-sensitive ion channels including Piezo1 and TRP channels are nonselective and permeable to Na^+, K^+, and Ca^{2+}; their activation in response to pressure stimulation or shear stress induces cell depolarization and Ca^{2+} influx [97–101]. Dysfunction of Piezo1 and TRP channels are closely linked to the development of cardiovascular disease. In some cardiovascular diseases, such as hypertension, atherosclerosis, or aneurysmal plaques, altered mechanical stress directly activating mechano-sensitive ion channels has been reported [96,102]. Ca^{2+} regulatory proteins sensitise any subtle change of intracellular Ca^{2+}. It has emerged that these proteins can cross-talk to mechanosensitive ion channels and such cross-talk can take place with direct and physical interactions between them, such as Piezo1 and SERCA [96,103].

Piezo1 and Piezo2, which assemble as transmembrane triskelions to combine exquisite force sensing with regulated calcium influx. There is emerging evidence for their importance in endothelial shear stress sensing and secretion, nitric oxide generation, vascular tone, angiogenesis, atherosclerosis, vascular permeability and remodeling, blood pressure regulation, insulin sensitivity, exercise performance, and baroreceptor reflex [104], Additionally, there are early suggestions of relevance to cardiac fibroblasts and myocytes [100]. Human genetic analysis points to significance in lymphatic disease, anemia, varicose veins, and potentially heart failure, hypertension, aneurysms, and stroke [102]. These channels appear to be versatile force sensors, used creatively to inform various force-sensing situations.

1.5. Autonomic control of cardiac contraction

The ANS is predominantly an efferent system which transmits impulses from the central nervous system (CNS) to peripheral organs. The actions of autonomic nerves are mediated by the release of neurotransmitters that bind to specific cardiac and vascular receptors [105,106]. The classic understanding of autonomic control of the cardiac function consists of regulatory processes by extrinsic cardiac nerves acting to either facilitate (sympathetic nervous system; SNS) or inhibit (PNS) cardiac activity [105,107,108]. Post-ganglionic SNS neurons originating in the intrathoracic or cervical sympathetic ganglia directly innervate cardiac cells, while pre-ganglionic PNS neurons originating in the medulla of the brainstem innervate the cardiac plexuses in the heart *via* the right and left vagus nerves [109]. Postganglionic axons originating in those ganglia running parallel with the coronary vessels innervate the SAN, AV node, cardiac conduction system, myocardial cells, and coronary vessels [110]. Together, the ANS is responsible for influencing HR, force of contraction, and thus CO of the cardiac chambers [106,111].

What is less appreciated is that the cardiac neurons that constitute an intrinsic plexus may in fact act independently from extracardiac inputs. This is supported by responses observed in hearts that have been surgically severed from extracardiac inputs [112]. The intrinsic neurons are organized in multiple aggregates and neural interconnections, localized to discrete atrial, and ventricular regions. These distinct ganglionated plexuses constitute the intracardiac nervous system (ICNS) [105].

1.5.1. Neuronal responses

Determinants of hemodynamic load are systemic vascular resistance and CO. The modulation of CO is a fundamental component to the balance within the cardiovascular system which is maintained through alterations in HR and SV. The product of SV can be determined by subtracting end-systolic volume (ESV; the volume of blood in the heart chamber at the end of systole) from the end-diastolic volume (EDV; the volume of blood in the heart chamber at the end of the diastole).

The primary control centre of HR modulation is through the sympathetic and parasympathetic nervous systems. An increase in SNS activity leads to an increase in CO through an increase in HR and myocardial contractility. This is achieved through the actions of neurotransmitters epinephrine and norepinephrine on beta-adrenergic receptors (β_1 and β_2) via stimulatory G proteins. This effect induces an increase in adenylyl cyclase activity, intracellular cyclic adenosine monophosphate (cAMP) concentrations, and protein kinase A (PKA) activity. The effect of cAMP increases SAN activity through the direct effect on I_f, while PKA increases SAN firing rate through increasing $I_{Ca,L}$ and SR Ca^{2+} handling. Conversely, the PNS neurotransmitter, ACh is released from the vagus nerve and acts to reduce HR by binding to muscarinic (M_2) receptors on the SAN, coupled to inhibitory G proteins that mediate reductions in adenylyl cyclase activity, cAMP levels, and PKA activity, all of which contribute to the inhibition of I_f, $I_{Ca,L}$, and SR Ca^{2+} handling at the SAN. Additionally, the $\beta\gamma$-subunits of the inhibitory G protein directly bind to and stimulate the acetylcholine-activated K^+ current (I_{KACh}), hyperpolarising the SAN and further inhibiting its activity [113].

The pressure-volume relationship is influenced by the position of the end-systolic pressure volume relation (ESPVR), an increase in contractility is indicated by a leftward or upward shift in the curve [114]. ESV, a function of changes in chamber contractility, affects the ESPVR, where a shift to the left represents an increase in contractility. When EDV and afterload remain constant, increasing contractility decreases ESV [115].

The carotid sinuses, aortic arch, and right subclavian artery all contain nerve endings which sense changes in arterial BP which relay these signals to the brainstem [116,117]. The baroreceptor reflex is initiated by vascular distention, such as when there is an increase in BP, causing mechanically-induced depolarization of the receptor terminals of baroreceptor neurons, which then depolarize and transmit the signal via neuronal APs to the medulla oblongata [118–120]. This results in an increase in baroreceptor activity, which increases the input to the vasomotor centre. The resulting effect is a decrease in SNS activity and an increase in PNS activity. The effect of the dual-action acts to decrease HR, thereby decreasing CO. The decrease in SNS activity elicits three other effects: (i) an increase in systemic venous capacitance (SVC), which results in a decrease in EDV; (ii) a decrease in left ventricle (LV) contractility, which results in an increase in ESV, and along with the increase in SVC contributes to a decrease in SV; and (iii) arterial dilation. The primary aim of the above actions is to restore BP toward baseline levels [113]. In contrast, a decrease in BP results in the opposite effects, via a decrease in baroreceptor and PNS activity, and an increase in SNS activity [121,122].

Baroreceptors are adaptive, and sustained changes in arterial pressure will lead to resetting of the pressure threshold. Over extended periods of increased pressure, baroreceptor activity will decline [123,124], leading to an increase in the pressure threshold

for baroreceptor reflex activation [125]. Decreased sensitivity may contribute to multiple pathological conditions and is symptomatic of diseases that are characterised by increased sympathetic cardiac excitation [126,127]. In contrast to other cardiovascular feedback systems, the baroreceptors are continuously modulating changes in BP and HR, and the constantly active feedback circuits allow them to be dynamically sensitive [128–130].

1.6. Models of cardiac electrophysiology

The use of animal models for research advancement , along with the development of human induced pluripotent stem cells (iPSC)have contributed to numerous important cardiac medical breakthroughs. Developments such as the artificial cardiac pacemaker, the cardioverter defibrillator, the heart-and-lung machine, as well as numerous drug and gene therapies were all made possible due to the knowledge gained from animal research [131]. The field of cardiac electrophysiology has particularly benefited from experimental and naturally occurring heart diseases in animal models [132].

1.6.1. Human induced pluripotent stem cells

The recent advent of the human iPSC technology and an increasingly refined capacity to differentiate iPSC into disease-relevant cell types such as CM (iPSC-CMs) [133], provide an unprecedented opportunity for the generation of human patient-specific cells for use in disease modeling, personalized drug screening, and regenerative approaches toward precision medicine [134,135]. Implementation of this unique and clinically relevant model system presents a significant advantage in cardiovascular research as it can circumvent complications in translating data from models across different species and biological characteristics.

1.6.1.1. Calcium dynamics in human induced pluripotent stem cells

HiPSC-CMs display functional and loaded ryanodine receptor-regulated intracellular Ca^{2+} stores. These stores can release Ca^{2+} via ryanodine receptors and can reload their content through SR Ca^{2+} uptake utilizing functional SERCA pumps. Evidence showing the expression and functionality of inositol-1,4,5-trisphosphate receptors (IP3Rs) demonstrating that the observed whole-cell $[Ca^{2+}]_i$ transients in hiPSC-CMs depend on both sarcolemmal Ca^{2+} entry via L-type Ca^{2+} channels and on intracellular store Ca^{2+} release. Taken together hiPSC-CMs recapitulate functional key Ca^{2+} handling proteins that have been shown to be expressed and functional in mouse embryonic stem cells-CMs [136–138], human embryonic stem cells-CMs [139–141], and adult cardiac tissue [13].

1.6.1.2. SAN, atrium, ventricle

Although functional cardiomyocytes have been obtained from human embryonic stem cells and iPSC, significant challenges remain in optimizing these cell preparations for experimental and potential clinical applications. The heterogeneity of cells produced in differentiation protocols can be great even if one succeeds in isolating cardiomyocytes [142]. For example, using a mixed population of cardiomyocytes including nodal, atrial, and ventricular cells in attempts at left ventricular repair raises concerns for proarrhythmic effects. Likewise, a preparation including undifferentiated cells could lead to tumorigenesis. Thus, approaches to produce homogenous or well-characterized mixed cell preparations remain a great need. Techniques to isolate cardiovascular progenitor cell

populations from human ES cells have recently been described which help address this concern [143].

1.6.1.3. Advantages

Human iPSC-derived CM provide an unlimited source of CM and, therefore, a valuable human-based tool for basic research and drug development [144]. The main advantage of iPSC-derived CM is that they retain the same genetic information as the donor thus enable the patient- or disease-specific phenotype and drug response studies [145](Karakikes et al., 2015). Human iPSC-derived CM exhibit the major cardiac structural proteins (Kujala et al., 2012, Ojala et al., 2016), ion channels (Zhao et al., 2018), calcium (Ca2+) cycling components (Itzhaki et al., 2011), and adrenergic receptors (Foldes et al., 2014). In addition, they have been shown to faithfully recapitulate many genetic cardiac diseases such as long QT -syndrome, catecholaminergic polymorphic ventricular tachycardia, and hypertrophic cardiomyopathy (Jung et al., 2012, Kiviaho et al., 2015, Kujala et al., 2012, Ojala et al., 2016, Spencer et al., 2014).

1.6.1.4. Limitations

The main issue is the use of retroviruses to generate iPSCs as they are associated with cancer. More specifically, retroviruses can insert their DNA anywhere in the genome and subsequently trigger cancer-causing gene expression. Also, as mentioned before, the c-Myc (one of the genes used in reprogramming) is a known oncogene, and its overexpression can cause cancer [134,146].

Also, in certain non-dividing cell types (such as PBMCs or elderly skin fibroblasts) the reprogramming rate of somatic cells to iPSCs is very low (less than 0.02

%). There is also a need to assess the quality and variability of the reprogramming process. For example, iPSCs often have a tendency not to fully differentiate. Hence, there is a need to pursue a quantitative assessment of the final quality of cells and screen for any genetic or epigenetic alterations during the reprogramming process [147].

1.6.2. Rabbit

The rabbit heart shares many similarities with the human heart, including morphology, AP characteristics, ion channel expression, as well as biophysical and biochemical properties [148]. The utility of the rabbit has made it the most studied model for human heart physiology and pathophysiology [149], and one of the more optimal models for studies of MEC [6], myocardial repolarization [150], regional patterns of myocardial deformation [151], cardiac cell electrophysiology [152–154], heart size to excitation wavelength ratio [155], coronary architecture [156], response to ischaemia, and pharmacological interventions [157].

The working myocyte AP morphology of the rabbit consists of a prominent plateau phase, comparable with the human AP [158–163]. Rabbit hearts express similar K^+ channel function and gating kinetics, containing a major contribution from I_{Kr} and a minor contribution from I_{Ks} [159,161,163]. Regarding the biophysical properties, the similarities in cardiac ion currents of I_{Kr} show utility in the comparison of pharmacological interrogations [158,162].

1.6.2.1. Calcium dynamics in rabbit

Cardiac Ca^{2+} dynamics have been studied in the rabbit model extensively. Ca^{2+} fluxes can be mediated by a range of factors, including I_{CaL}, SR Ca^{2+}-ATPase,

sarcolemmal NCX, mitochondrial Ca^{2+}, and sarcolemmal Ca^{2+}-ATPase. In comparison of these factors, the Ca^{2+} flux characteristics in rabbit and human are very comparable [164]. Furthermore, in the rabbit ventricle, SERCA and NCX systems have been shown to remove 70 – 74 percent and 23 – 28 percent of Ca^{2+} [165,166]. Comparatively, the removal of SERCA and NCX in the human ventricles has been reported at 76 and 24 percent, respectively [167]. However, when acting in isolation, such as when NCX activity is blocked in isolated rabbit CM, it was shown that SERCA resequesters Ca^{2+} faster than human SERCA by itself as the time constant of SERCA dependent Ca^{2+} is 50 percent slower in humans compared to rabbits [168]. Thus, highlighting that although many similarities exist, there are slight differences in Ca^{2+} handling between rabbit and human CM.

In some instances, a species-dependent effect on post-rest potentiation seems to be present in isolated CM. During periods of continuous electrical pacing with a designated pause period, first twitch tension is measured once stimulation is resumed. Upon re-starting pacing, rabbits exhibit a post-rest decay where the first twitch tension is decreased. Humans show post-rest potentiation of increased tension, and demonstrate a further increase correlated with prolonged rest period duration [169,170]. Although, as previously discussed, the SR resequestration of the SR is similar between species, the decrease in rabbit and increase in human have largely been attributed to changes in SR Ca^{2+} content during rest periods [170,171].

1.6.2.2. SAN, atrium, ventricle

Studies involving SAN structure, composition, and the response to stretch have been well established in the rabbit [6,172]. The composition of the SAN is divided into

roughly fifty percent extracellular matrix and fibroblasts and the other fifty percent consists of pacemaker cells [173,174]. Pacemaker cells have been characterised with heterogeneous cell volumes, morphologies, and ion current densities [175,176]. The architecture of the SAN contains a dense area of smaller, spindle-shaped pacemaker cells, interwoven and embedded within a collagen network. In the outer areas, the cell design is more ordered, in a parallel orientation in line with the crista terminalis [173].

Experimentation involving the use of rabbit atria dates back over 60 years, involving intracellular microelectrode recordings to investigate the site of origin and direction of activation [177]. Additional studies involve the measurement of the wavelength of the cardiac impulse during periods of re-entrant tachycardia induction [178] and pharmacological interrogation for re-entrant circuits [179], whole cell patch-clamp technique to define the mechanism of cardiac I_{to} with comparison to human atrial myocytes [180,181]. Beyond the SAN, the rabbit has also been used to detail the network of the specialised conduction system (the bundle of His, the bundle branches, and the Purkinje fibre network) into ventricular electrophysiology models, and its role in modulating ventricular activation sequence [182].

1.6.2.3. Advantages

Rabbits have several advantages that make them a highly attractive model for studies of cardiac research. They are highly amenable to assessment of myocardial function in intact animals, as various *in vivo* quantitative and imaging techniques such as echocardiography [183], hemodynamic cardiac catheterisation [184,185], electrocardiography [183], and cardiac magnetic resonance imaging [151].

Another advantage of the rabbit is the *in vivo* HR range, reported between 150 – 360 bpm [186,187], and although significantly higher than humans [188,189], it is much closer than that of mice.

1.6.2.4. Limitations

One of the disadvantages of using the rabbit model is the associated cost of acquiring and housing, compared to their rodent counterparts, particularly for longitudinal studies and genetic models [190]. However, on a cost-basis, rabbits are less expensive than larger animal models such as canine, ovine, or porcine options. Differences between species that could interrupt the translation of therapeutic interventions are the atrial I_{to} [181,191], ventricular expression levels of some K^+ ion channel subunits [192], relative expression levels of cardiac titin isoforms (*i.e.,* N_2B and N_2BA) [193–196], and LV wall motion [151]. Additionally, rabbits demonstrate faster kinetics of cardiac contractile parameters studied in both *in vivo* and *ex vivo* settings [190].

1.6.3. Rats

Rat models have dominated research into heart damage because, while rats share many of the benefits of mice (low cost, ease of handling, etc.), their larger size greatly facilitates surgical and postsurgical procedures. Myocardial damage in rat hearts is induced by three procedures: surgical, pharmacological, or electrical [197]. Some of the most prominent heart disease models used for this model are myocardial infarction [198,199], hypertrophy and heart failure [200–202], and AF [203–205]. Indeed, most of the work done on ventricular fibrillation in rat hearts indicates that VF in this species occurs at a time

corresponding to the IB arrhythmias, and no clear separation of IA from IB arrhythmias has been described in small animal species.

1.6.3.1. Calcium dynamics in rats

Besides the macroscopic dimension of the ventricles, intrinsic differences in normoxic metabolism may also exist among species. In rats such differences have been shown with respect to the duration and shape of the transmembrane action potential and the homeostasis of cellular Na^+ and Ca^{2+}. Thus, the relatively high normal intracellular Na^+ activity in the normal rat affects the working mode of the NCX and may lead to earlier Ca^{2+} overload in depolarized cells. Interestingly in rats, this difference can be reversed by inhibition of thyroid hormone production [206].

1.6.3.2. SAN, atrium, ventricle

Electrophysiological evidence for a bio-electrical interaction of mechanosensitive fibroblasts with surrounding CM has been studied in isolated spontaneously beating atrium of rat hearts, cell cultures of the neonatal rat heart. It was demonstrated that cardiac fibroblasts and surrounding CM can be either electrically well isolated from each other or coupled both capacitively and electrotonically [55]. Electrotonic interaction of these cells showed that stretch of the fibroblast during atrial diastole, simulating increased atrial wall tension during atrial filling, can raise the spontaneous depolarization rate of the pacemaker cell in a stretch-dependent manner by up to 24% [55]. These results show that cardiac mechanosensitive fibroblasts could form a cellular basis for the positive chronotropic response of the heart to stretch of the right atrium.

In isolated atrial rat tissue, using a selective blocker of the α1-adrenergic receptor (Prazosin; preganglionic location), ANP may interfere with norepinephrine activation of this receptor. It was shown that ANP did not attenuate HR increases owing to norepinephrine, arguing against a postsynaptic mechanism. Comparison of rat and human ventricular myocytes isolated from failing and non-failing hearts looking at specific I_{to} was conducted. The current density of I_{to} was similar in cells from failing and non-failing hearts, but smaller in human than in normal rat myocytes, respectively. Half maximum activation was found at more positive potentials in human than in rat cells [207]. The characteristics of Ito in human cells were similar though not identical to Ito in rat heart cells. This current may be a potential target for antiarrhythmic drug action.

1.6.3.3. Advantages

The advantages of using these models are that the housing, feeding, and hygiene management are highly standardised. They have a short gestation period (20-23 days), with sexual maturity occurring at 7 weeks [190]. They present significantly lower cost than larger animals, and the ability to investigate roles of various proteins and signaling pathways in progression of heart disease by combining intervention models. Right-sided hypertrophy [208,209] and heart failure [209–211] can be induced in rats with relative ease with use of monocrotaline, a plant alkaloid which causes pulmonary hypertension without affecting systemic BP [210]. This model is particularly attractive as it can be established via a single injection without the need of surgical procedures.

1.6.3.4. Limitations

In rodents, the AP shape is markedly different than in human and other bigger species: the plateau phase of the action potential is missing, resulting in a more triangular AP shape with a very short APD. In contrast to humans, repolarization in mice and rats is mainly driven by the rapidly activating, slowly inactivating delayed rectifier potassium currents $I_{K,slow1}$ and $I_{K,slow2}$ and the fast and slow components of the transient outward potassium current $I_{to,f}$ and $I_{to,s}$ [154]. The rapid and slow delayed rectifier K^+ currents (I_{Kr} and I_{Ks}) are functionally irrelevant. In addition, other repolarizing ion currents such as the atrial I_{Kur} are differentially expressed in rodents [212].

In contrast to all other species (aside from mice) it may be appreciated that in the rat there is no shortening of refractory periods at the shorter cycle lengths. When examining the diastolic interval along the ordinate versus the cycle length, it is clear that the rat ventricle should not be the first choice if one aims at 'filling up' the diastolic interval by means of a class I, class III, or experimental anti-arrhythmic agent [213].

Additionally, one of the factors that make the mouse so appealing is the abundance of genetically modified variants available, which at this point are only marginally available in the rat model.

1.6.4. Mouse

The AP shape in the mouse model is vastly different from humans and most animal models, such that the plateau phase is not present, resulting in a triangular AP shape with a significantly shortened APD [172,214,215]. In contrast to humans, rabbits, and zebrafish, repolarisation in mice is mainly driven by the rapidly activating, slowly

inactivating, delayed rectifier K$^+$ currents ($I_{k,slow1}$, $I_{k,slow2}$) and the fast and slow

components of I_{to} (fast and slow) [154]. Meanwhile, the main characteristic of repolarising

fast and slow delayed rectifier K$^+$ currents (I_{Kr}, I_{Ks}) in human CM are functionally

irrelevant in this model [212]. Therefore, studies on repolarisation mice have limited value

[161].

Technological advances have allowed *in vivo* measurement of parameters of

cardiac function and structure in the mouse, to complement *in vitro* molecular and

functional studies. These include a range of techniques such as echocardiography [216,217],

cardiovascular magnetic resonance imaging [218,219], electrocardiography [217,220], pressure-

volume loops [221–223] and BP measurement [217,220].

Perhaps the most attractive aspect of utilising mice is the ability to genetically

produce specific models. Of course, this is not a characteristic exclusive to the mouse

model, however, the time frame associated with their gestational age of ~18-21 days is a

key attribute, in addition to substantially lower production costs [224]. Genetic editing has

been used to affect a host of cardiovascular processes ranging from excitation to

metabolism. These models of dysfunction provide valuable insights into areas of protein

function related to the onset and development of cardiovascular disease (CVD). Cardiac

excitation, contraction, and relaxation of mice and humans share a lot of the same

dynamics and expression of proteins with similar functions [190]. Genetically modified

mouse models have demonstrated their utility in understanding the function of genes

relating to states of cardiac physiology and pathophysiology allowing for rapid proof-of-

principle interactions that can be extended to larger animal models.

1.6.4.1. SAN, atrium, ventricle

The structure of the mouse SAN has similarities to the rabbit, such as a centralised dense area of tightly packed pacemaker cells. However, there are differences in the alignment and orientation. In the mouse, pacemaker cells are in a perpendicular orientation to the crista terminalis, as opposed to a parallel orientation in rabbit [172,225]. The outer area is similar to the rabbit as the pacemaker cells become less compact and aligned in a parallel fashion relative to the crista terminalis [225]. Additionally, the composition of the mouse SAN is substantially different comprising 25 percent of extracellular matrix and fibroblasts, while 75 percent consists of pacemaker cells [226,227], proportionately much more compared to the rabbit SAN.

Human genes share 99 percent of direct murine orthologs, a factor which has been utilised with success in knock out models to investigate mechanisms involved in atherogenesis [228], dilated cardiomyopathy [229,230], hypertrophic cardiomyopathy [231,232], autoimmune cardiomyopathy [233], Duchenne muscular dystrophy [234–239], AF [240], and arrhythmogenesis as well as critical substrates necessary for sustaining micro re-entrant circuits. Despite the small mass of the normal mouse atria, sustained atrial tachycardia and fibrillation can be reproducibly induced with endocardial pacing after cholinergic agonist administration [241], which makes this a beneficial method for understanding the role of I_{KACh} in AF [242].

1.6.4.2. Calcium dynamics in mice

As discussed, Ca^{2+} is necessary for the activation of myofilaments during contraction, and the removal of Ca^{2+} is essential in relaxation to allow normal diastolic

filling. SERCA is predominantly responsible for the resequestration of 90-92 percent of available Ca^{2+} in mice [165,243], whereas this accounts for only 76 percent in humans [167], while NCX accounts for the remaining uptake in both groups. This variance of the distribution of sarcolemmal and $[Ca^{2+}]_i$ fluxes compared to humans does not make them a good model for the interaction between Ca^{2+}-sensitive transporters (particularly NCX and $I_{Ca,L}$) and Ca^{2+}-insensitive modulators of the AP [244].

1.6.4.3. Advantages

Small rodents are easier to handle and house, have a shorter gestation time, and have lower maintenance cost than larger animal models. These characteristics make small rodent models logistically and economically the most used model for cardiac physiology and disease, genetics, pharmacology, and long-term survival studies [190].

Overexpression of genes using cardiac-specific promotors is a benefit of this nature, deletion through knock-out strategies or CRISPR-Cas technology, tamoxifen-induced conditional targeting, or AAV-based gene transfer to cardiac regions of interest [245]. Mice are generally bred by inbreeding which causes an identical background that is highly effective for intraspecies repeatability, while a outbreeding enables identification of potential genetic modifiers [246]. Additionally, randomly mutagenized mice can be bred to identify novel genes modulating cardiac traits including electrical function [247–249].

1.6.4.4. Limitations

The mouse heart has adapted to function at a very high HR possessing rapid systolic contraction as well as diastolic filling – both of which are necessary for maintaining CO. The ventricular APD as discussed is much shorter in mice [250,251]

compared to humans [252,253], as they have a rapid repolarisation, lacking a prominent plateau phase found in humans [250]. Differences between small animal models and human CM exist in myofilaments. The mouse ventricular CM express almost entirely (94-100 percent) fast α-MHC [254–258], resulting in faster kinetics [259], tension cost, and lower economy [260,261] compared to the slow β-MHC typically found in human ventricles [262,263].

Perhaps the most important limitation of the mouse model is the intrinsic differences that are present including ion current characteristics, sympathetic tone [249], and HR response to stretch – as the mouse heart, when mechanically stimulated has a decreased HR response compared to all other animal models, including human, which experience an increase in HR under the same circumstances [52]. This effect complicates the ability to translate any experimental effects relating to the intrinsic mechanical stretch response from mouse to human.

1.6.5. Zebrafish

The zebrafish has become an increasingly popular model for studies of cardiac physiology and pathophysiology [264–266]. The zebrafish has a fully sequenced genome, which may be altered using standard genetic techniques [267,268], and almost every cardiac gene has a human ortholog with analogous function [269]. Functionally, the zebrafish heart has HR, AP morphologies, ion channels [270,271], and Ca^{2+}-handling proteins [272,273] that are generally more similar to human than are rodent characteristics.

1.6.5.1. SAN, atrium, ventricle

The function and genetic composition of the zebrafish SAN is similar to the human. The zebrafish SAN is designed in a ring-like fashion, located at the border

between the venous sinus and the atrium, embedded within the leaflets of the sinoatrial valve [274–278]. SAN development in the zebrafish and human both share *isl1-, tbx-, bmp4-, and hcn4*-expressing cells under control of *shox2*, all facilitated by the suppression of *nkx2.5* through Wnt signalling [279–281]. Initial studies reporting on the currents involved in zebrafish SAN automaticity were found in the discovery of a *slow mo* mutation that caused a reduction in HR by affecting a hyperpolarisation-activated inward current, representative of the I_f [282,283].

1.6.5.2. Calcium dynamics in zebrafish

Involvement of the membrane and Ca^{2+} "clocks" in SAN automaticity were investigated using pharmacological interventions, which confirmed the role of I_f (block of HCN channels reduced HR by ~65%) and demonstrated a role for $[Ca^{2+}]_i$ cycling (block of SR Ca^{2+} release with ryanodine, combined with block of SR Ca^{2+} reuptake with thapsigargin reduced HR by ~40%) [284].

In contrast to mammalian systems, Ca^{2+} release from the SR plays a relatively small role in activating the contractile apparatus in teleosts, which may contribute to differences in restitution. The contractile function of the zebrafish heart is closely tied to extracellular Ca^{2+} which enters CM through L-type Ca^{2+} channel, T-type Ca^{2+} channel, and the NCX [272].

1.6.5.3. Advantages

Unlike mammals, zebrafish can fully regenerate cardiac tissue after heart injury [285]. Following amputation of up to 20% of the ventricle, new CM form and replace the lost myocardium within 30 days without scar formation. This characteristic, which is not

present in the mammalian system, provides the ability to investigate an *ex vivo* tool for studying cardiac regeneration mechanisms [286–288]. Since zebrafish CM retain their proliferative potential throughout their lifetime, regenerative events can be monitored live and reprogramming pathways can be dissected [287].

During embryogenesis, the zebrafish heart lends itself to high throughput testing of drug effects on HR because the embryo is transparent and allows for direct observation of rate and rhythm [289]. In addition, forward genetic screens, reverse genetic methods, and transgenic technology have been successfully used to identify factors regulating cardiogenesis and function of the embryonic zebrafish heart [289]

1.6.5.4. Limitations

As with any experimental model, there are also limitations to the zebrafish's use (Table 1.1). The zebrafish heart is small, has only two chambers (one atrium and one ventricle, rather than the four chambers in human), and generates relatively low chamber pressure [290]. While over 70% of human genes have at least one zebrafish ortholog, 24% of genes have more than one ortholog (due to the zebrafish's diploid genome), which can confer redundancy in gene function and confound results of genetic manipulations [269]. Functionally, while cardiac electrophysiology appears strikingly similar to humans [270,271], there are important differences in cellular Ca^{2+} cycling [273,291]. Zebrafish CM have a lack of transverse tubules [292], and even though SR Ca^{2+} levels are much higher in the zebrafish compared to human, release of Ca^{2+} from the SR following excitation (Ca^{2+}-induced Ca^{2+} release) appears to be limited (due in part to a low sensitivity of ryanodine receptors to Ca^{2+}) [293]. As a result, sarcolemmal Ca^{2+} influx is responsible for ~80% of the Ca^{2+} transient in zebrafish CM (compared to 25% in human) [293], although this remains

31

somewhat controversial, as others have shown a strong dependence of contractile force

on SR Ca^{2+} release [294] and the existence of Ca^{2+} sparks with characteristics similar to

mammals [295]. Zebrafish also have a higher NCX current than in mammals, such that its

reverse-mode has been shown to trigger SR Ca^{2+} release [296].

1.7. Application of zebrafish for studies of cardiac electrophysiology

The zebrafish atrial and ventricular AP have been characterised from intracellular

microelectrode recordings in intact adult hearts showing an overall AP morphology

similar to that of humans [289]. Like most mammals, the zebrafish display functional ACh-

activated K^+ channels in the atrium, but not in the ventricle. The AP upstroke is

dominated by fast Na^+ channels, and $I_{Ca,L}$ contributing to the plateau phase, while I_{Kr} are

involved in repolarization [271,289]. In the zebrafish heart ventricular contraction is

abolished by mutation in the α-1C subunit (CaV1.2) strongly suggesting that $I_{Ca,L}$ is

produced by orthologous genes in humans and zebrafish. In the heart of adult zebrafish

transcripts of the α-1D (CaV1.3) are also expressed [297].

$I_{Ca,T}$ is an important component of pacemaker and conductive tissue, usually

absent in atrial and ventricular muscle of adult mammals. In this respect zebrafish vary

from humans and other mammals. Two α subunits of T-type Ca^{2+} channels (CaV3.1 and

CaV3.2) are expressed in mammalian hearts [298,299]. T-type channel composition of the

zebrafish has not been studied, but T-type Ca^{2+} channel blocker with Ni^{2+} suggests that it

might be an ortholog to the mammalian CaV3.1, [289] while immunofluorescence findings

suggest the presence of CaV3.2 [300].

1.7.1. Heart development

During development, the embryonic heart undergoes a series of complex morphogenetic and differentiation processes to form the mature cardiac structures [301–304]. These processes are mediated by mechanosensitive proteins that convert mechanical stimuli into biochemical or electrical signals which alter gene expression necessary for differentiation and morphogenesis [305]. Hemodynamic forces due to the continuous flow of blood through the heart induce mechanosensitive signaling within endocardial cells that trigger their differentiation and a remodeling [306].

The hemodynamic forces that are driven by blood flow include shear, pressure, and stretch which have associated mechanical mechanisms, which can be sensed at the cellular level [307,308] impacting gene and protein expression [309], cell morphology [310], and tissue organisation [311]. Hemodynamic forces have greater implications in the earlier stages of development as the architectural foundation has not yet developed and has greater cardiac plasticity [306,312,313]. Initiation of the heartbeat has been studied in the chick and zebrafish embryo [310,314–318], both of which allow easy accessibility during stages of development, enabling manipulations and observation of the embryo, such as dissection, grafting, micro-injection, and labeling.

The ability to observe cardiac development has provided insight into the study of contractility and flow influences on heart development, indicating a critical role for cardiac contraction and the resulting fluid forces in shaping the heart [319]. Studies have uncovered the essential role for cardiac contraction-responsive transcriptional changes in endocardial cells in regulation of cardiac chamber maturation [320,321] and endocardial *Notch1* signaling to modulate trabeculation [322]. Several types of cell behaviors are likely

33

to contribute to the process of chamber emergence. Both CM proliferation and cell size increase can help to facilitate chamber expansion [323–325].

Cultured CM robustly display hypertrophic growth when stretched [326,327], suggesting that hypertrophic growth taking place in the embryonic heart could be triggered by biomechanical forces. Embryonic circulation is initiated as soon as the heart tube forms [328], and so chamber emergence takes place while CM are contracting and while blood is flowing. When blood flow is reduced, CM fail to expand normally at the outer curvature of the embryonic zebrafish ventricle [325]. This impact of blood flow on CM cell size suggests that hemodynamics could have a major influence on hypertrophic growth during chamber emergence. Even minor perturbations of cardiac specification or morphogenesis can have catastrophic consequences for cardiac function [329]. Because of the exquisite coordination of these events, the slightest cardiac developmental perturbation (genetic or environmental) can easily lead to catastrophic heart defects and subsequent embryonic/fetal demise. Thus, congenital heart diseases (CHD), including both structural and functional cardiovascular defects, are amongst the most common and most devastating birth defects in humans, occurring in about 5% of live births, and resulting in significant mortality and morbidity [330]. A large proportion of CHD are due to defects in specific structures of the heart, which can lead to hemodynamic compromise and catastrophic clinical outcomes. In order to illuminate the etiologies of these defects, better understanding of the cellular and molecular events of cardiac development is required.

1.7.2. Transgenic models

Forward and reverse genetic approaches have been successfully applied in zebrafish to identify novel signaling pathways, study gene function, and develop a range of disease models. Reverse genetics refers to assessment of the role of a previously identified, and sequenced gene. Temporary knockdown of expression of a known gene during zebrafish development can be achieved by injection of morpholino antisense oligonucleotides into the fertilized egg [331]. Forward genetics refers to identifying novel genes responsible for a particular phenotype of an organism. Two large-scale forward genetic screens have identified hundreds of mutant phenotypes relevant to various aspects of development and embryogenesis [332].

Specific to studies of cardiac research, the activity of the cell cycle in CM can now be directly visualized *in vivo* using lines carrying the ubiquitin-based cell cycle indicator (fluorescent ubiquitination-based cell cycle indicator) system [333]. This system labels cells with red and green fluorescent proteins depending on whether they are in G0/G1 or S/ G2/M, respectively [334]. Because no staining is required, the analysis of these animals is based on imaging the fluorescence directly. These transgenics have been used to screen over 1200 compounds for factors controlling CM proliferation [333,335].

1.7.3. Intracardiac nervous system

The ICNS is sometimes referred as the "little brain" of the heart [336,337]. In the mammalian heart, it makes continuous adjustments of the mechanical and electrical activity, and it consists of a network of neurons that communicate with each other and with neurons located in the extracardiac thoracic ganglia, all under the control of the

central nervous system [112]. The ICNS comprises afferent (sensory), interconnecting (local circuit), and cardio-motor (efferent sympathetic and parasympathetic) neurons [336,338]. The intrinsic cardiac neurons are mainly concentrated in intracardiac ganglia residing in specific regions of the heart, mostly in the atria, and each ganglion has a preferential region of action [338]. The activation of efferent neurons results in the modulation of the HR, atrio-ventricular node conduction as well as inotropism of atria and ventricles. Local circuit neurons work as inter- and intra-ganglionic connections, whilst afferent neurons transduce information of the cardiovascular milieu [336,339].

Although the relatively small size of the zebrafish heart presents its own technical challenges, it permits visualisation of, and accessibility to, the entire ICNS and its external inputs in the whole, intact organ. Thus, the zebrafish model has been paramount to expand our understanding of the ICNS [277] and its role in modulating chronotropy [276]. The basic structure of the ICNS has been described previously [276] and identified as sharing the same foundation with that of humans and other mammalian models [340–344].

1.7.4. Effects of stretch

The zebrafish appears to retain all critical components of intrinsic SAN regulation seen in mammals, making it a potentially powerful experimental model for studies of underlying mechanisms [32]. In regards to the utility of zebrafish for the study of SAN function, it has been shown that pacemaker activity is clearly present, functions similarly to mammals, and is found in a ring-like structure at the location of the sinoatrial valve (the border between the sinus venosus and the atrium) [274–277].

The effect of mechanical stretch in isolated zebrafish SAN was found to share a similar response to human (and most other mammals) [32], with an immediate magnitude-

dependent increase in HR. This is an important mechanism for intrinsic regulation of SAN function, which allows the heart to adapt to changes in hemodynamic load on a beat-by-beat basis.

1.7.5. Optogenetic studies

Optogenetics, involving the optical measurement and manipulation of cellular activity with genetically encoded light-sensitive microbial proteins ('reporters' and 'actuators'), is a powerful experimental technique for probing (patho-)physiological function. Originally developed as a tool for neuroscience, it has now been utilised in cardiac research for over a decade, providing novel insight into the electrophysiology of the healthy and diseased heart. Among the pioneering cardiac applications of optogenetic actuators were studies in zebrafish, which first demonstrated their use for precise spatiotemporal control of cardiac activity [274].

Zebrafish have been used as an experimental model for the use of optogenetic reporters, including genetically encoded voltage- and Ca^{2+}-sensitive indicators (GEVI, GECI). For optogenetic studies, zebrafish provide additional advantages, as the whole zebrafish heart can be visualised and interrogated *in vivo* in the transparent, externally developing embryo [345], and the relatively small adult heart allows for *in situ* cell-specific observation and control [346] not possible in mammals. With the advent of increasingly sophisticated fluorescence imaging approaches and methods for spatially-resolved light stimulation in the heart, the zebrafish represents an experimental model with unrealised potential for cardiac optogenetic studies.

1.8. Goals and hypotheses

Project 1: During embryogenesis, mechanical load is thought to be a critical factor in the development and control of the heart's mechanical and electrical activity. The control of cardiac activity includes acute adaptation to changes in mechanical load, driven by feedback of the heart's mechanical state to its electrical and mechanical function ('mechano-electric' and 'mechano-mechanical coupling'). Studying electrical and mechanical function of the early embryonic heart, however, is difficult in mammalian models, as development occurs *in utero* and the heart is not easily accessible in the whole embryo. As a result, experiments are generally performed in explanted hearts. The zebrafish offers multiple advantages for studies of cardiac development, as their larvae develop externally, and are nearly transparent, allowing for measurement and manipulation of structure and function *in vivo*. **The aim of this project** was to develop a novel method allowing the control of acute changes in hemodynamic load *in vivo*, to study the presence of MEC- and MMC-mediated control of CO during early development in the larval zebrafish heart.

Project 2: CHD are the most common type of human birth defect and feature structural abnormalities that arise during cardiac development and maturation [314]. Understanding the mechanisms driving the adaptations to changing hemodynamic load in an acute setting, may provide insight into the dysfunction that occurs in the chronic setting. Although the existence and importance of these acute stretch responses are well established in the adult heart, their presence and role in the developing heart are ill-defined. **The aim of this project** was to utilise the method developed in project one and adapt it to zebrafish embryo during different stages of cardiac development to investigate

mechanisms driving the effect of acute increased hemodynamic load on the heart. **The hypothesis of this project is that** in earlier stages of development, control of the HR is driven primarily by intrinsic mechanisms (intrinsic; internal to the heart) which respond to changes in mechanical load. As development progresses, the response to changes in mechanical load is shifted from purely intrinsic, to an integrated intrinsic-extrinsic (extrinsic; external to the heart) controlled system.

Project 3: Acute changes in preload or afterload require rapid alterations in the electrical and mechanical activity of the heart. These rapid changes in cardiac function are driven by autoregulatory mechanisms intrinsic to the heart (MEC, MMC) as opposed to slower adaptations via the CNS or hormonal alterations (Quinn and Kohl, 2016; Quinn and Kohl, 2021). Based on the results from project two, **the aims of this project were to:** i) determine the role of neurons in driving changes in cardiac function, through pharmacological block of SNS and PNS effector cell and ii) determine the role of SACs in driving changes in cardiac function with pharmacological block of a SAC_{NS}. **The hypotheses were**: the cardiac response to increased hemodynamic load will i) be blunted by SNS inhibition, as the SNS is cardioexcitatory, inhibition will interfere with proper cardiac function and cause the system to overload or become completely dysfunctional to the point of cessation of contraction; ii) be increased by PNS inhibition, as the PNS is cardioinhibitory, inhibition will result in an increased response in cardiac function; iii) be blunted by SAC_{NS} inhibition, as SAC_{NS} drive V_m depolarization, inhibition will result in a decrease in the HR response to the point of acute cardiac dysfunction, through cessation of contraction.

Project 4: This chapter will provide a review of the utility of the zebrafish model for studies of cardiac optogenetics, highlighting their advantages and limitations. Additionally, this chapter will provide a project demonstrating the effectiveness of this application in the adult zebrafish. Activation of cation-conducting ChR leads to membrane depolarization, allowing one to effectively trigger APs in CM. In contrast, the quest for optogenetic tools for hyperpolarization-induced inhibition of AP generation has remained challenging. The green-light activated ChR from GtACR1 mediates chloride (Cl^-)-driven photocurrents that have been shown to silence AP generation in different types of neurons [347]. It has been suggested, therefore, to be a suitable tool for inhibition of CM activity. **The aim of this project was to**: determine the effects of GtACR1 with pulsed and sustained light stimulation in intact zebrafish hearts. **The hypotheses of this project were:** i) pulsed light stimulation of GtACR1 can cause controlled depolarisation of ventricular cells in isolated zebrafish hearts, and ii) sustained light stimulation of GtACR1 can cause depolarisation inhibition by shifting the V_m toward the reversal potential for Cl^-.

1.9. Tables

Table 1.1 | Advantages and limitations of the zebrafish for cardiac optogenetic studies.

Advantages	Limitations
- Relatively low cost (time, effort, money)	- Diploid genome (24% of genes have more than one ortholog)
- Fully sequenced genome	- Small, two-chambered heart
- Relatively easy genetic manipulation	- Relatively low-pressure system
- Large number of available transgenic lines	- Lack transverse tubules
- Majority of cardiac genes have human ortholog	- Limited release of calcium from sarcoplasmic reticulum following excitation
- Externally developing, transparent embryo	- Low sensitivity of ryanodine receptors to calcium
- Amenable to high throughput studies	- Dependence of calcium transient on sarcolemmal influx
- Comparable heart rate, action potential morphologies, ion channels, and calcium-handling proteins to human	
- Intrinsic and extrinsic cardiac regulatory pathways and mechanisms similar to human	
- Human cardiac diseases can be recapitulated	

Figure 1.1 | The cardiac mechano-electric regulatory loop. The feedforward and feedback links between cardiac electrophysiology and mechanics, forming the intracardiac mechano-electric regulatory loop. The feedforward between electrical excitation and mechanical contraction, involving intracellular calcium handling and actin-myosin cross-bridge cycling, is a process known as "excitation-contraction coupling." Feedback from myocardial deformation to cell electrophysiology and intracellular calcium dynamics occurs via multiple interdependent mechano-sensitive mechanisms, which in turn affect the origin and spread of excitation, a phenomenon known as "mechano-electric feedback" or more broadly "mechano-electric coupling" (From Quinn & Kohl, 2021 with permission through the Copyright Clearance Center).
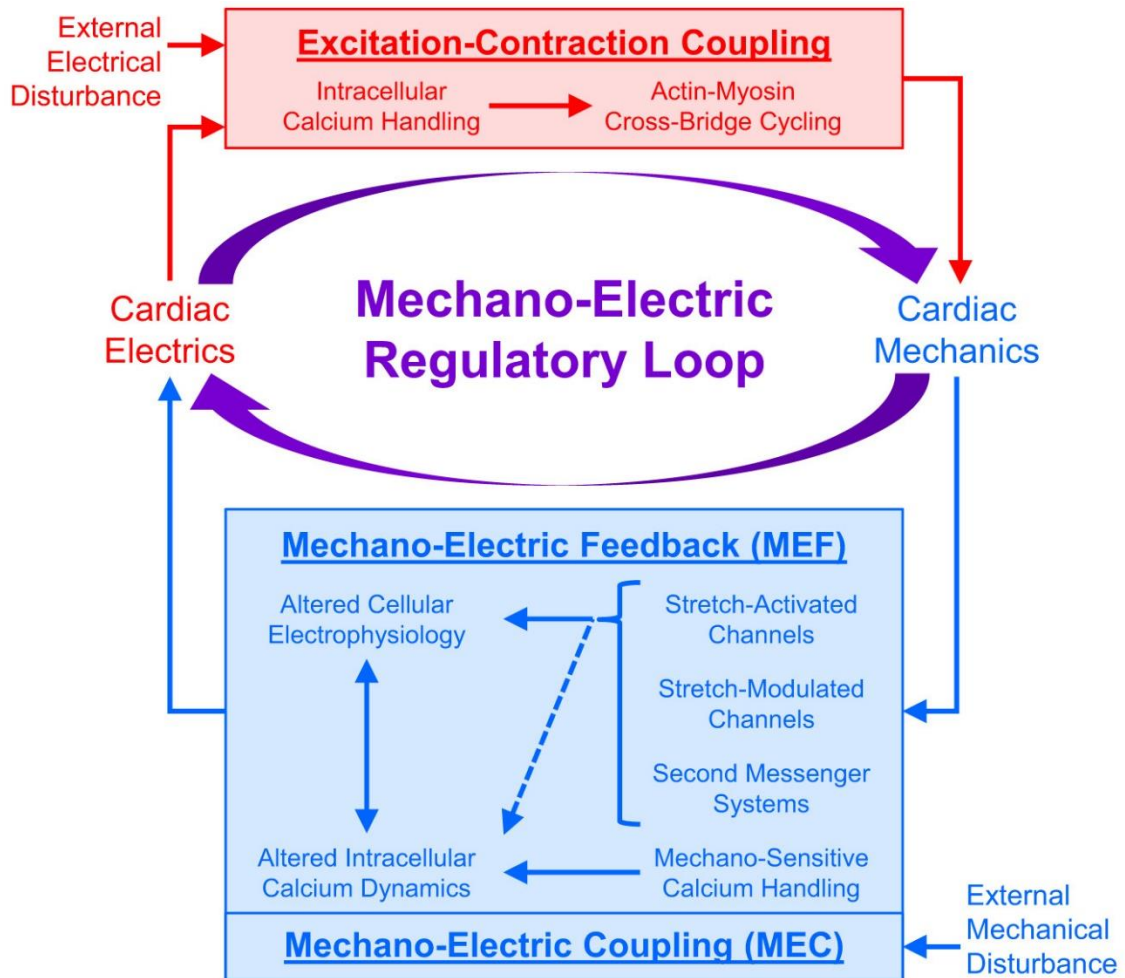
Figure 1.2 | Mechanically gated channel and mechanically modulated channel candidates are present throughout living organisms. Several mammalian channels have homologues in other organisms: e.g. NOMPC, OSM9, TRP4, TRPY1 and LOV-1 are TRP homologues; MEC channels are members of the DEG/ENaC superfamily whose mammalian representatives are ASIC channels; TPK is a homologue of K2P channels; Mid1 is homologous to voltage-gated calcium channels. In red: channels expressed in the heart; underlined: channels clearly identified as MGC; channels with no known mammalian homologues are marked by *. "SAC$_{NS}$": stretch-activated channels, cation non selective; "SAC$_K$": stretch-activated channels, potassium selective; "Mito": mitochondria; "SR": sarcoplasmic reticulum. Only a selection of the more well-known channels and receptors is presented (From Peyronnet et al, 2016 with permission through the Copyright Clearance Center).
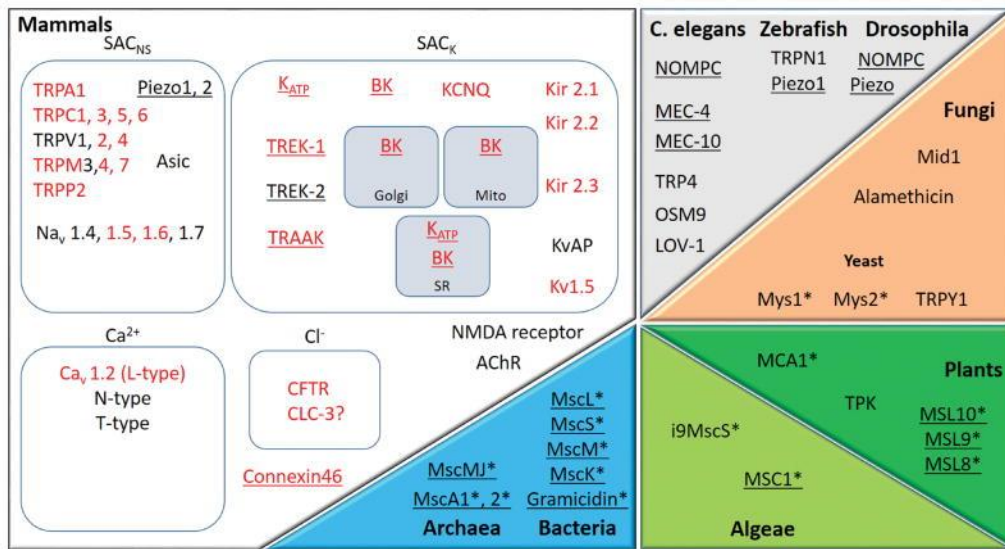
**CHAPTER 2: A NOVEL METHOD FOR THE ACUTE *IN VIVO*
MANIPULATION OF HEMODYNAMIC LOAD IN EMBRYONIC ZEBRAFISH**

2.1.Introduction

The heart is an electrically driven pump that provides the body with a constant

supply of blood during normal physiological conditions. The beating action of the heart

occurs because of cells in the myocardium that contract when electrically excited. These

CM experience a dynamic transformation in size due to varying mechanical forces during

each cardiac cycle. During relaxation (diastole), the cells undergo a physical

transformation as they lengthen and stretch due to the volume of blood filling the heart

chambers (preload). During contraction (systole), force generated by the cells works

against the existing mechanical load and resistance to blood ejection (afterload) to cause

shortening. Preload or afterload are constantly changing (for instance with every breath,

or change in posture, physical activity, *etc*.), with acute changes causing rapid alterations

in the electrical and mechanical activity of the heart. These rapid changes in cardiac

function (rather than slower, central nervous system- or hormonally-mediated alterations)

are driven by autoregulatory mechanisms that are intrinsic to the heart, involving

feedback from the mechanical environment to electrical (mechano-electric coupling,

MEC) and mechanical (mechano-mechanical coupling, MMC) activity [4,6]. This feedback

allows for two distinct means of rapidly adjusting CO, which is the product of HR and

SV on a beat-to-beat basis to acute alterations in venous return (*i.e.*, preload). With

increased preload, there is stretch of the myocardium, which will increase CO by

increasing HR (the 'Bainbridge effect' [348], which occurs due to stretch of the heart's

natural pacemaker, the SAN [349] and contractile force (the 'Frank-Starling mechanism')

[350], an intrinsic property of CM, resulting from changes in myofilament spacing and Ca^{2+} sensitivity [22]. The subsequent increase in CO is critical for matching blood ejection to inflow for each heartbeat, to keep the system in balance. Yet, while the existence and importance of these acute stretch responses are well established in the adult heart, their presence and role in the developing heart are ill-defined.

2.1.1. Importance of mechanical load for cardiac development

In the embryo, the heart is one of the first functional organs to develop and is critical for the further development of the whole animal by supplying nutrients to the body and removing waste products. As embryonic growth progresses, the heart transforms from a linear tube into a multi-chambered structure separated by valves for unidirectional blood flow. This transformation in cardiac morphology is dependent on hemodynamic changes, manifested as an increase in intracardiac pressure, myocardial strain, and wall shear stress, resulting in molecular and cell signalling responses that help coordinate cell differentiation and tissue growth. The structural changes that occur during cardiac morphogenesis are critical for the heart's mechanical function and the effective ejection of blood with each heartbeat. For further details on the influence of the heart's mechanical environment on the development of its structure and mechanical function, we refer the reader to excellent reviews on the subject [306,313,319,351–354]

The heart's electrical activity develops along with its structure and mechanical function and is similarly dependent on mechanical factors. This includes establishment of distinct regional differences in electrophysiology, including the atrial and ventricular myocardium [317,355], the cardiac conduction system [356], and the SAN [357], which is

spontaneously active and thus responsible for the initiation of cardiac excitation and in determining HR [358,359].

Importantly, available evidence suggests that the electrical and mechanical function of the developing heart also respond to acute changes in mechanical load (as in the adult heart). This appears to be important for the pre-neuronal effects of BP on HR (increased BP increases HR in intact chick embryos, prior to cardiac innervation) [360], the coordination of contraction across the heart (when electrical conduction in embryonic chick hearts is prevented by block of gap junctions, the heart continues to beat in a coordinated fashion) [307], and possibly the initiation of the very first heartbeat (as it occurs after fluid pressure build-up in the quiescent heart tube) [361]. However, whether rapid functional responses to acutely altered hemodynamics (*via* MEC and MMC) are an important control mechanism in the developing heart is unknown.

2.1.2. Zebrafish as an experimental model for the study of cardiac development

One reason for our lack of knowledge regarding the importance of MEC and MMC during development are limitations for its study in mammalian models. Acute, controlled *in vivo* alterations in hemodynamics, with simultaneous real-time visualisation of their effects, is difficult in the opaque, *in utero*, mammalian embryo. While recent advances in *in vivo* imaging and experimental techniques have provided critical new data regarding the role of mechanics in heart development [362], information on acute effects of altered load is still lacking.

The zebrafish has become a popular alternative model for studies of development [312,363,364], including the role of mechanics in cardiac morphogenesis [365,366]. The most striking advantage of the zebrafish for developmental studies is the ability to easily

visualise the developing organs *in vivo* in the transparent, externally growing embryo [265].

Basic vertebrate organ patterning is conserved in the zebrafish, and zebrafish embryos

develop a complete body plan with major organ systems, including a beating heart and

major vessels with circulating blood within 48 hours post-fertilisation (hpf) [312].

Importantly, though, while the cardiovascular system is one of the first to form during

development, the zebrafish embryo obtains oxygen by passive diffusion from water for

upwards of seven dpf, and nutrients from their yolks, so that experimental manipulations

and mutant phenotypes that severely perturb cardiac function and would be lethal in

humans and other mammals can be studied [367]. The *in vivo* assessment of heart

development in zebrafish embryos is further enhanced by optogenetic tools that allow for

the optical measurement and manipulation of cardiac activity in the intact embryo with

genetically encoded light-sensitive proteins [368].

There are other important factors that make the zebrafish a powerful model for

studies of cardiac physiology [266]. Genetically, the zebrafish has a fully sequenced

genome, which is easily altered using standard genetic techniques at relatively low cost

(in terms of time, effort, and money) [267,337], and most cardiac genes have a human

ortholog with analogous function [269]. Even though the zebrafish heart is in some ways

structurally different than the human heart [290], functionally the zebrafish heart shares

more similarities to human than rodents, specifically it has a more comparable HR, AP

morphologies, and ion channel dynamics[270,271], additionally, the Ca^{2+}-handling

mechanisms are generally well conserved [272,273]. Furthermore, it has been shown that

mechanisms of both intracardiac [32] and extracardiac [277] control of cardiac function are

similar to human. This is particularly true for the SAN [369] – which is important in the

context of HR control – and importantly includes responses to stretch [32,370], which like the heart's electrophysiology are more similar to that found in human than in rodents.

2.1.3. Studying the importance of mechanical factors for the development of cardiac structure and function in the zebrafish

Recent innovative studies in zebrafish have provided important novel insights into the role of mechanics in cardiac morphogenesis. For instance, it has been shown that spatiotemporal variations in wall shear stress coordinate endothelial and valvular growth [371–373] and trabecular organisation [322], and that its genetic [322], pharmacological [374,375], or mechanical [372] disruption results in morphological defects, dependent on mechanosensitive channel-mediated Hippo-YAP-Notch signaling pathways [322,373,375,376]. Studying acute effects of mechanics on cardiac function in development, however, is much more difficult [377].

2.2. A novel approach for the acute *in vivo* application of cardiac hemodynamic load in zebrafish larvae

Our new approach builds off recent work using a hydrostatic pressurisation technique designed to mechanically load the atrium of zebrafish larvae *in vivo*, for the quantification of passive mechanical properties of the myocardium during development [378]. Similar experiments were performed previously with chick hearts [379], however that work was limited to *ex vivo* studies, using explanted hearts. The newer *in vivo* approach focuses on mechanical loading of the atrium, as at early stages of zebrafish development the atrium provides much of the work required for circulation [380]. Also important for our purposes, the atrium contains the SAN, which is responsible for the HR response to

stretch [32,349]. Here we describe the evolution of our approach from the previous

hydrostatic pressurisation technique to the current electronic flow control system and

demonstrate its use to investigate MEC and MMC responses in 48 hpf zebrafish larvae.

2.2.1. Hydrostatic pressurisation technique

In previous *in vivo* studies examining the passive mechanical properties of the

developing zebrafish atrium, changes in mechanical load were applied by a hydrostatic

pressurisation technique [378]. This consisted of a fluid column, filled with 0.3X Danieau's

solution (which has similar salt concentrations and osmotic pressure to that of zebrafish

larvae) and connected to a syringe pump, which allowed for control of the fluid level in

the column to produce specified pressures. The column was also connected *via* a small

tube to a microcannula, which was made from a borosilicate glass capillary pulled and

broken to an outer diameter of 10-15 μm. A zebrafish larva was embedded ventral side

up in low-melt agarose (for physical immobilisation) containing 2,3-butanedione

monoxime (BDM, an inhibitor of myosin ATPase, to stop contraction of the heart). The

cannula was attached to a micromanipulator and the fluid level in the column was zeroed

at the level of the heart (such that fluid did not enter or exit the cannula). Under an

upright fluorescence microscope, the cannula was advanced to puncture the confluence of

the cardinal veins, posterior to the atrial inlet. Cannulation did not affect the size or

morphology of the heart or initiate a visual response. After the cannula was inserted,

pressure was increased in a stepwise fashion by incremental increases of the fluid level in

the column, with brightfield images of the heart collected through the upright

microscope. The tissue was allowed to stabilize between pressurisation steps and there

was negligible flow out of the cannula once pressure equilibrium was reached (visualised

by the inclusion of fluorescent Rhodamine dye in the column fluid). For further details and specifics about this system, please see the report by [378].

This technique allows for the application of low levels of sustained static pressure to the larval zebrafish atrium and visualisation of the resulting deformation, which has been used to obtain pressure-stretch relationships for constitutive models of the myocardium and estimate tissue stiffness during development. While the system is elegant in its simplicity and ease of use, the resolution of changes in applied pressure is limited and it does not allow for the rapid application of mechanical loading needed for the assessment of acute MEC and MMC responses in beating hearts.

2.2.2. Electronic pressure control system

To allow for rapid injection of small volumes to dilate the heart and assess acute MEC and MMC responses, we modified the previous pressurisation approach to one using a high-resolution electronic pressure control system. For this, the hydrostatic column was replaced by a microfluidic pneumatic device that controls outlet pressure between 0-2000 mbar with a resolution of 600 μbar, step size of 0.03% of the maximum pressure, stability of 0.1%, and a validated 30 ms response time (LU-FEZ-2000, Fluigent, Paris, France), to generate controlled flows that are dependent primarily on system resistance and fluid viscosity. In our configuration, the system outlet pressurised a 15 mL conical tube containing HEPES-buffered saline solution (in mM: NaCl 142, KCl 4.7, $MgCl_2$ 1, $CaCl_2$ 1.8, Glucose 10, HEPES 10). The outlet of the conical tube was connected to the cannula, so that the pressure resulted in outflow of solution. Pressurisation was controlled by computer (connected *via* a LINK module, Fluigent), using commercial software designed for the pressure control device (OxyGEN, Fluigent),

which allowed for custom time-based pressurisation protocols and the recording of outlet pressure.

While this updated approach allowed for more rapid and precise changes in cannula outlet pressure, the rate of outflow from the cannula varied between each preparation, as outflow is a function of system resistance, which varies due to differences in cannula tip diameter, the nature of the cannula puncture, and subject-specific anatomy. As a result, the injected volume and resulting atrial dilation from a given pressure were difficult to predict and varied greatly from heart to heart.

2.2.3. Electronic flow control system

To rectify the variability in injected volume and atrial dilation, we moved to a controlled flow system. In this configuration, the addition of a bidirectional flow rate sensor inline with the cannula outlet allows for the control and monitoring of flow rate between 0-80 µL/min with an accuracy of 5% (FLU-M-D, Fluigent), by automatic pressure adjustment (Figure 2.1). Like the pressure control system, flow is controlled by computer, allowing for custom protocols and the recording of pressure and flow (Figure 2.2). During volume injection, fluorescence videos of the heart tagged with a cardiac-specific fluorescent marker are taken through an upright microscope, which allows for relatively easy measurement of atrial dimensions and HR (Figure 2.3). Hearts tagged with cardiac-specific functional fluorescent probes, such as genetically expressed voltage (GEVI) or Ca^{2+} (GECI) indicators [368], may also be used with this system to measure effects of acute changes in mechanical load on membrane potential or intracellular Ca^{2+} handling.

Here we demonstrate the use of this novel system for the investigation of MEC and MMC responses in 48 hpf zebrafish larvae, a critical stage of early development after the morphological transformation known as 'looping' (during which the linear heart tube gradually bends at the boundary between the ventricle and the atrium to create an S-shaped loop, so that the ventricle comes to lie beside the atrium [381]. We also present GECI-based measurements of intracellular Ca^{2+} dynamics from the earliest cardiac contractions in 24 hpf zebrafish, which demonstrates the potential for measurements of subcellular effects using functional fluorescent imaging.

2.3. Assessing the adaptive response of larval zebrafish heart function to an acute increase in hemodynamic load

All experimental procedures were approved by the Dalhousie University Committee for Laboratory Animals and followed the guidelines of the Canadian Council on Animal Care. Details of experimental protocols have been reported following the Minimum Information about a Cardiac Electrophysiology Experiment (MICEE) reporting standard [382].

2.3.1. Zebrafish larvae preparation

Zebrafish were bred and raised by the Faculty of Medicine Zebrafish Core Facility at Dalhousie University. 48 hpf zebrafish with a point mutation in the *mitfa* and *roy* genes, resulting in a lack of melanocytes and iridophores that makes them mostly transparent (a common background strain known as *casper* [383]), genetically expressing a fluorescent marker (eGFP) specifically in CM (driven by the heart-specific myosin light

chain 7 [*myl7*] promoter, to make the heart easier to visualise) were used for this study

(*Tg*(*myl7*:*eGFP*) on a *casper* background). Animals were anesthetised in 3% Tris-

buffered tricaine solution (0.45 mM, pH 7.4; Tris: BP152, Fisher Scientific, Waltham,

MA; tricaine: MS-222, Sigma-Aldrich, St. Louis, MO) for five minutes, transferred to a

glass depression slide (CSTK01, United Scientific Supplies, Libertyville, IL), and

embedded ventral side up in 1.5% low-melting agarose (IB70051, IBI Scientific,

Dubuque, IA) in HEPES-buffered saline solution (in mM: NaCl 142, KCl 4.7, $MgCl_2$ 1,

$CaCl_2$ 1.8, Glucose 10, HEPES 10) with 3% Tris-buffered tricaine. All experiments were

performed at a controlled room temperature of 21° Celsius. The desired physiological

temperature would be to conduct experiments at 28° Celsius, which would increase the

basal HR in zebrafish at all developmental stages. The response to increased

hemodynamic load on HR at varying temperatures is not known, thus, investigation on

the effect on temperature of SAC is needed.

2.3.2. Cannulation of the larval zebrafish vasculature

Borosilicate glass capillaries (100 mm, 1 mm outer / 0.58 mm inner diameter;

1B100-4, World Precision Instruments, Sarasota, FL) were shaped using a micropipette

puller (P-97, Sutter Instruments, Novato, CA) into cannulas with a tip diameter of ~4 μm.

Cannulas were coupled to the high-resolution electronic flow control system described

above and secured to a three-axis micromanipulator (MM-3, Narishige, Amityville, NY)

on the stage of an upright fluorescence microscope (Eclipse 80i, Nikon, Tokyo, Japan)

with a 10×, 0.30 NA objective (Plan Fluor, Nikon). The cannula was inserted through the

agarose and skin of the larval zebrafish and into the venous circulatory system slightly

upstream of the inlet to the atrium (*sinus venosus*) (Figure 2.1).

2.3.3. Application of controlled volume to the larval zebrafish heart

Volume loading protocols were developed in the flow control software (OxyGEN,

Fluigent), by defining the duration and rate of flow. The combination of flow duration

and rate were optimised for 48 hpf larval zebrafish by co-varying the parameters in

preliminary experiments to find a combination that resulted on average in ~25% (and no

more than 50%) dilation of the atrium at end-diastole (which is the percentage stretch that

gives the most robust HR response in adult zebrafish isolated SAN [32]. The optimal

loading protocol involved a cannula flow of 3 µL/min for 30 s, applied three times, with a

90 s rest period between each (Figure. 2.2A; the amount of time found in preliminary

experiments to allow end-diastolic area [EDA] to return to baseline). Pressure and flow

during the loading protocol were monitored and recorded using the OxyGEN (Fluigent)

software (Figure 2.2B).

2.3.4. Measuring functional effects of acute volume loading

Fluorescent videos of the beating heart were acquired with a colour industrial

CMOS camera (DFK 33UP-1300, The Imaging Source, Charlotte, NC) at 60 frames per

second on the upright microscope by exciting the eGFP with a super high pressure

mercury lamp (HB-10101AF, Nikon) passed through a 480/40 nm filter and a 506 nm

dichroic mirror, with emission collected through a 535/50 nm filter (Chroma, Bellows

Falls, VT). Videos were analysed using custom routines in MATLAB (MathWorks,

Natick, USA) to calculate function parameters immediately before and at the end of each

application of load. Atrial EDA and end-systolic area (ESA) were measured by tracing the area of the atrium at the end of filling and the end of ejection, respectively. Stroke area (SA) was calculated as EDA-ESA, and an area-index of CO (CO_A) was calculated as HR × SA (Figure 2.3A) HR was measured from the time between peaks of filtered image intensity signals, acquired by averaging intensity within a region of interest placed over the atrial wall (Figure 2.3B).

2.3.5. Measurement of intracellular Ca^{2+} dynamics

For fluorescent imaging of intracellular Ca^{2+}, 24 hpf *casper* zebrafish (in which the developing heart is still a linear tube) with CM-specific expression the GECI GCaMP3 were used (*Tg*(*myl7*:*GCaMP3*)). Before embedding in agar, zebrafish were exposed to 100 µM (S)-3'-amino blebbistatin (24170, Cayman Chemical, Ann Arbor, MI; a blebbistatin derivative with increased water solubility and photostability during blue light exposure [384] for 90 min to eliminate contraction-induced artifacts in optical recordings [345]. Fluorescent videos were acquired by exciting the GCaMP3 using the same configuration as the eGFP, with fluorescence emission captured at 250 frames per second by a 128 × 128 pixel, 16-bit electron-multiplying charge-coupled device camera (i-Xon3, Andor, Belfast, United Kingdom). Videos were analysed using custom routines in MATLAB to calculate Ca^{2+} duration at 80% recovery to baseline ($CaTD_{80}$) from fluorescence averaged at 6 evenly spaced 6 × 6 regions-of-interest along the length of the heart tube. All experiments were performed at 28°C (physiological zebrafish temperature).

2.3.6. Statistical analysis

Values are reported as mean±SEM. Statistical analysis was performed in Prism (GraphPad, San Diego, CA). Group means were compared either by paired two-tailed Student's T-tests or paired or unpaired one-way ANOVA, with Tukey or Dunnet *post hoc* tests, as appropriate. Significance was indicated by $p<0.05$.

2.4. Results

2.4.1. Effect of an acute increase in hemodynamic load on atrial EDA in 48 hpf zebrafish larvae

Hemodynamic load of the atrium was acutely increased three times by the injection of a controlled flow (3 μL/min) of saline into the confluence of the cardinal veins over 30 s. Figure 2.4A shows the measured EDA immediately before (B1-B3) and at the end (S1-S3) of each loading period. With each injection of saline there was a significant increase in atrial EDA (Figure 2.4A). Importantly, during the rest period between each saline injection, EDA returned to baseline, as there was no difference between EDA at B1, B2, or B3 (Figure 2.4A). There was also no difference in the amount of atrial dilation with each application of load (Figure 2.5A), indicating a consistent hemodynamic effect. When averaged across all volume injections, the application of load resulted in a 20.5±2.0% increase in atrial EDA (Figure 2.6).

2.4.2. Effect of atrial dilation on electrical and mechanical function in 48 hpf zebrafish larvae

The effect of the increase in atrial EDA on its electrical and mechanical function was assessed by comparing HR and atrial SA before and during saline injection. Figures 2.4B and C show the measured HR and SA before and at the end of each loading period. The first two periods of acute loading had no effect on HR, while the third caused a slight decrease in HR (Figure 2.4B) of $-3.4 \pm 1.1\%$ (Figure 2.5B). For SA, there was a significant increase with each loading period (Figure 2.4C). In both cases there was no difference between values immediately before the application of load, indicating a return to baseline (Figures 2.4B, C). As for EDA, there was no difference in the change in SA with each load application (Figure 2.5C), and the decrease in HR with the third loading period was not significantly different than the first two periods, which showed no change (Figure 2.5B). When averaged across all volume injections, the application of load resulted in a $60.1 \pm 8.5\%$ increase in SA (Figure 2.6).

2.4.3. Effect of altered atrial function on CO

With an increase in venous return to the heart there must be a concomitant increase in CO – to match outflow to inflow and maintain hemodynamic balance – which can occur through an increase in HR, SA, or both. CO_A was calculated as the product of HR and SA, with the effect of the increase in atrial EDA shown in Figure 2.4D. With each dilation of the atrium, there was a significant increase in CO_A, which during each rest period returned to the baseline value (Figure 2.4D). There was no difference in the change of CO_A with each application of load (Figure 2.5D), which when averaged across

all volume injections was $58.1\pm8.8\%$ (Figure 2.6). This increase in CO_A was driven

solely by an increase in SA, supported by a lack of difference in the percentage change of

CO_A compared to SA, and a difference in the change of both compared to the absence of

an effect on HR (Figure 2.6).

2.4.4. *In vivo* GECI-based measurement of Ca^{2+} dynamics in 24 hpf zebrafish larvae

The above results show the *in vivo* effect of an acute increase in hemodynamic

load on atrial function. To better understand mechanisms involved, there is the potential

to combine the above method with the use of genetically-expressed fluorescent reporters

for *in vivo* measurement of subcellular effects. Here we demonstrate the use of the GECI

GCaMP3 to measure Ca^{2+} dynamics in the heart at the very beginning of its contractile

activity in 24 hpf larval zebrafish (Figure 2.7). Changes in fluorescence allowed for the

visualisation of Ca^{2+} transient propagation as it progressed form the *sinus venosus* to the

outflow tract along the heart tube (Figure 2.7A). When $CaTD_{80}$ was measured at 6 evenly

spaced regions of interest along the length of the tube, an increase in $CaTD_{80}$ was seen

halfway along (Figure 2.7B), revealing the early development of regional differentiation

in cellular Ca^{2+} handling.

2.5. Discussion

Here we have presented a novel method for consistent and repeatable rapid *in vivo*

application of mechanical load to the larval zebrafish heart, and measurement of its acute

effect on electrical (HR) and mechanical (SV) cardiac function, as a means to study the

emergence of MEC and MMC responses in development. It was shown that in 48 hpf

zebrafish larvae, an acute increase in hemodynamic load has little effect on HR, but

causes a large increase in SA, such that the concomitant increase in CO_A is driven by MMC mechanisms. We also show the potential for the use of genetically-expressed fluorescent reporters for *in vivo* measurement of subcellular effects, which in 24 hpf larvae revealed the emergence of spatially varying Ca^{2+} handling along the heart tube. Overall, our results demonstrate the potential of our new methodology for future studies exploring the mechanical control of cardiac function during development.

2.5.1. The response of the 48 hpf zebrafish larvae heart to an acute increase in hemodynamic load

With an average acute increase in atrial EDA of ~20% in 48 hpf zebrafish larvae, we found close to a 60% increase in CO_A, with a similar increase in SA and little change in HR. This suggests that acute adaptation to changes in hemodynamic load at early developmental stages in the zebrafish heart are driven solely by MMC mechanisms. This is in contrast to the heart of adult zebrafish [32] and other vertebrates [349], in which there is also a robust rapid increase in HR with stretch of the SAN, such that a combination of both MEC and MMC responses are responsible for the associated increase in CO that ensures the matching of output to venous return [6]. Previous studies in mammalian models, however, have shown evidence for responses of both the heart's mechanical and electrical function to acute changes in mechanical load. For mechanical function it has been demonstrated in embryonic chick hearts that mechanical factors may coordinate contraction across the heart, even without electrical excitation [307], which may also explain initiation of the very first heartbeat in the quiescent heart tube [361]. Electrically, prior to cardiac innervation in chick embryos, it has been shown that an acute increase in BP results in an increase in HR [360]. While the mechanisms responsible for these responses to

changes in the mechanical environment are unknown, they could be driven by MMC or MEC effects. Our data would suggest that MEC mechanisms are not yet present at early developmental stages, so MMC is the primary driver as in the responses seen our experiments, warranting further studies regarding the timing of the emergence of cardiac MEC in the developing heart, made possible by our novel methodology.

What is well established is the critical role in early development that mechanical load, including intracardiac pressure, myocardial strain, and wall shear stress, plays in cardiac morphogenesis and the establishment of normal mechanical and electrical function by driving molecular signalling that helps coordinate cell differentiation and tissue growth [306,313,319,351–354]. In fact, some of the critical insights regarding the dependence of cardiac development on mechanics has come from *in vivo* studies in zebrafish larvae, which have shown the importance of spatiotemporal variations in wall shear stress for coordinating endothelial and valvular growth and trabecular organisation [322,371–375]. Our new methodology for studies in zebrafish is also well suited to allow for experiments aimed at gaining further insights into the critical role of mechanics in the development of cardiac structure and function.

2.5.2. Ca^{2+} dynamics in the heart tube of 24 hpf zebrafish larvae

Here we also showed the potential for *in vivo* fluorescent measurement of the subcellular activity responsible for myocardial contraction. Using the GECI GCaMP, intracellular Ca^{2+} dynamics were measured in 24 hpf zebrafish larvae, showing the release and re-uptake of Ca^{2+} as a wave of excitation proceeded from the *sinus venosus* to the outflow tract in the heart tube. Interestingly, when $CaTD_{80}$ was measured from the recorded signals, an increase was seen halfway along the tube. This spatial difference in

60

CaTD$_{80}$ reveals the beginning of regional cell differentiation, as portions of the heart tube begins to take on atrial and ventricular cellular phenotypes. This is inline with previous work from others using a similar imaging technique in zebrafish, which mapped Ca^{2+} waves across the heart tube in 24 hpf larvae, and showed unidirectional waves of Ca^{2+} release in a relatively slow, linear pattern from the *sinus venosus* to the outflow tract (although in that study they did not measure properties of the Ca^{2+} transient) [385]. In a later study using a combined GEVI-GECI construct for *in vivo* dual voltage-Ca^{2+} imaging to probe the development of regional differentiation of cardiac cellular properties, it was shown that at 36 hpf the cardiac action potential in zebrafish is initiated by Ca^{2+}, but by 96 hpf it becomes sodium driven, while the atrial action potential remains Ca^{2+} dependent [386]. Our work suggests that spatial differences in cardiac cellular function in fact develop earlier, at least by 24 hpf, warranting further studies of the specific timing of the various aspects of functional cellular differentiation.

2.6. Conclusion

As the heart is constantly experiencing acute variations in hemodynamic load, for which it must adapt its activity to compensate, MEC and MMC are critical physiological responses. Little is known about the presence and important of these responses *in vivo* in the developing heart, in part due to experimental limitations. The novel technique presented here allows for rapid variation in the mechanical load of the larval zebrafish heart, while simultaneously imaging its effects, which may be used in future studies to better understand the role of MEC and MMC for acute adaptation during cardiac development.

2.7. Figures

Figure 2.1 | Electronic flow control system for acute *in vivo* application of cardiac hemodynamic load in zebrafish larvae. Outlet pressure of pressurised gas cylinder is controlled by a computer-controlled high-resolution electronic pressure control system, which pressurises a conical tube filled with saline solution. Flow rate from the tube is measured by a bidirectional flow rate sensor and maintained at a set value by adjusting pressure. A micro-cannula is connected to the flow, advanced with a micromanipulator under an upright fluorescence microscope to puncture the confluence of the cardinal veins (posterior to the atrial inlet) and used to inject volume into the heart. Effects of volume loading are visualised through the microscope with an industrial camera.
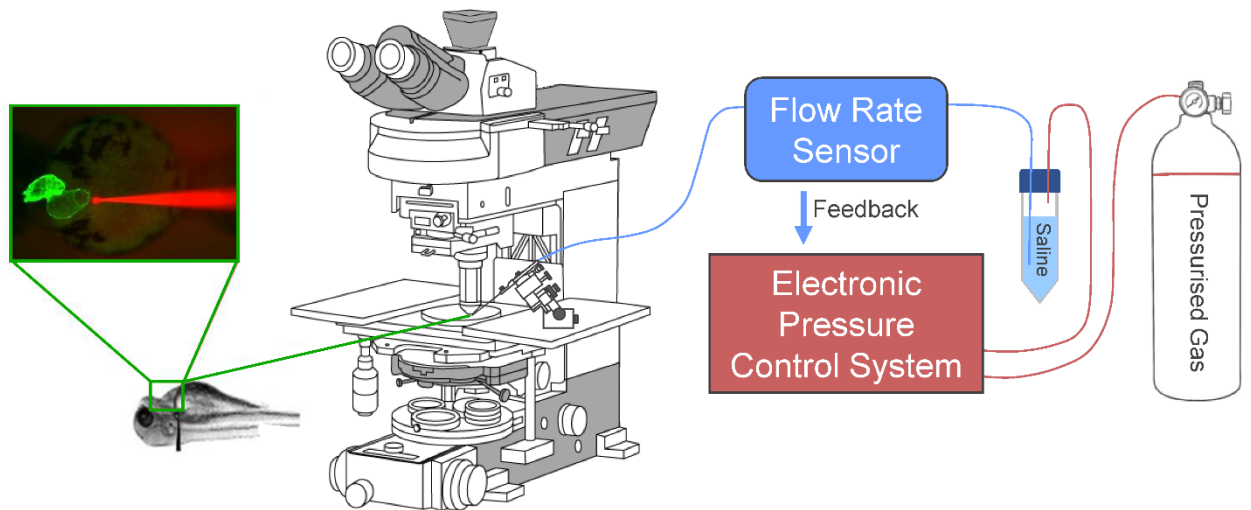
Figure 2.2 | Acute volume loading protocol. (**A**) Acute volume loading involved three 30 s periods of 3 µL/min saline injection through the cannula, with a 90 s rest period between each, and measurements taken immediately before (B1-B3) and at the end of load application (S1-S3). (**B**) The pressure and flow during loading were monitored and recorded by the pressure-flow control software.
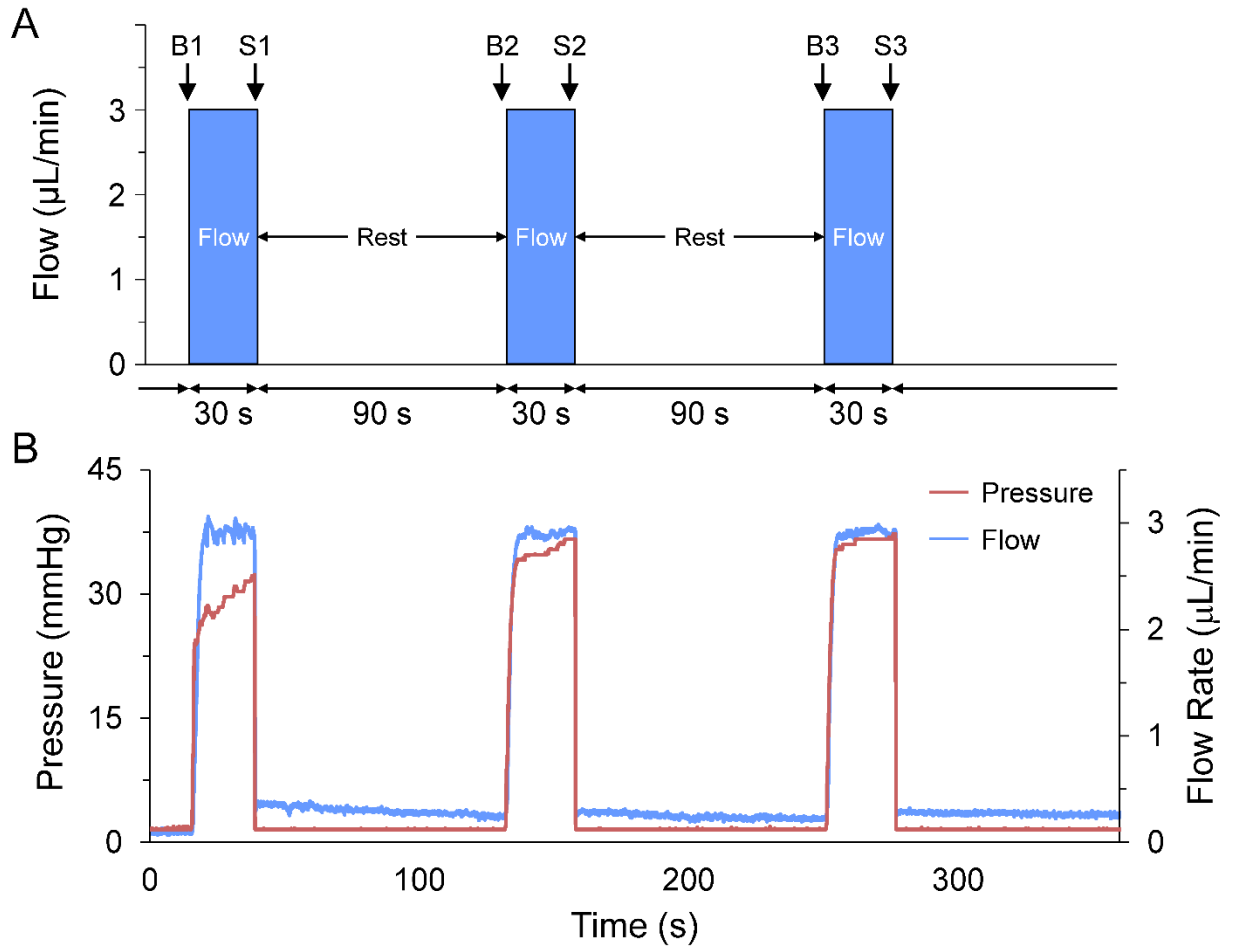
Figure 2.3 | Measurement of atrial dilation and functional effects. (**A**) Videos of 48 hpf zebrafish larvae hearts expressing eGFP (*Tg(myl7:eGFP)*) on a *casper* background were analysed in Matlab to calculate function parameters at baseline immediately before (B1-B3) and at the end of load application (S1-S3). Atrial end-diastolic (EDA) and end-systolic (ESA) area were measured by tracing the area of the atria at the end of filling and the end of ejection, respectively, from which stroke area (SA) was calculated as EDA-ESA. (**B**) HR was measured from the time between peaks of filtered image intensity signals, acquired by averaging intensity within a region of interest placed over the atrial wall (red boxes in **A**).
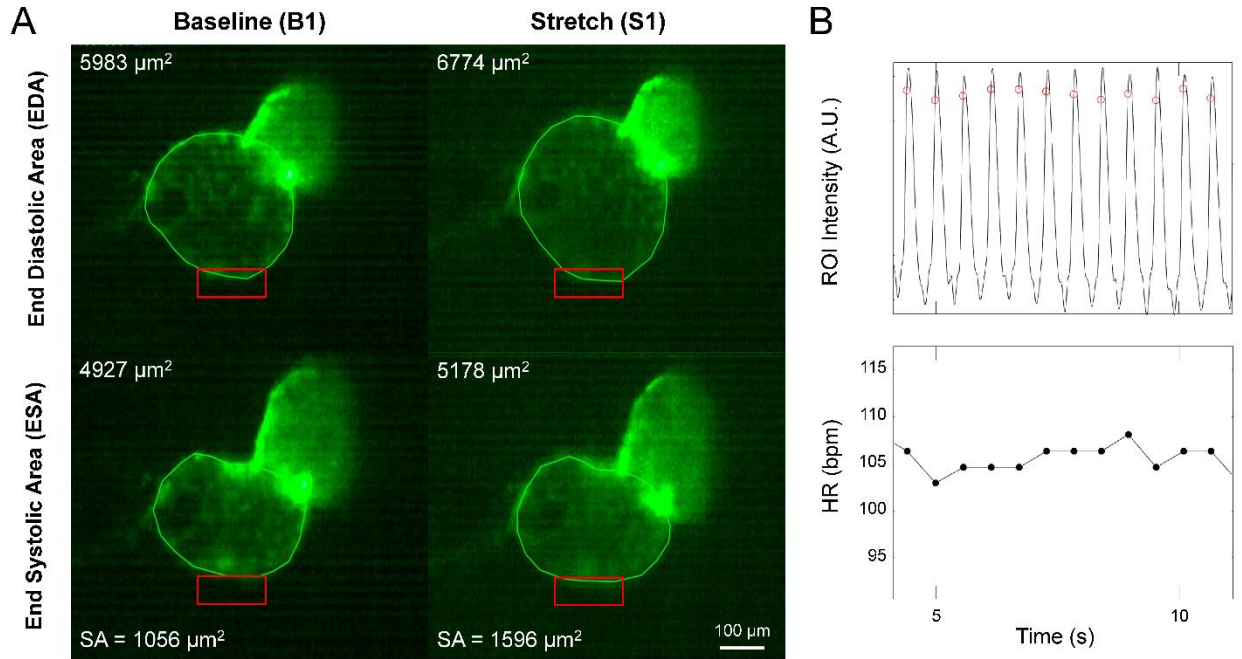
Figure 2.4 | Effects of atrial dilation on functional parameters in 48 hpf zebrafish larvae. (**A**) End-diastolic area (EDA), (**B**) heart rate (HR), (**C**) stroke area (SA), and (**D**) area cardiac output ($CO_A = HR \times SA$) immediately before (B1-B3) and at the end of load application (S1-S3). Mean values before and during each stretch were compared by paired two-tailed Student's T-tests. Significance was indicated by $p<0.05$. *n*=11 larvae.
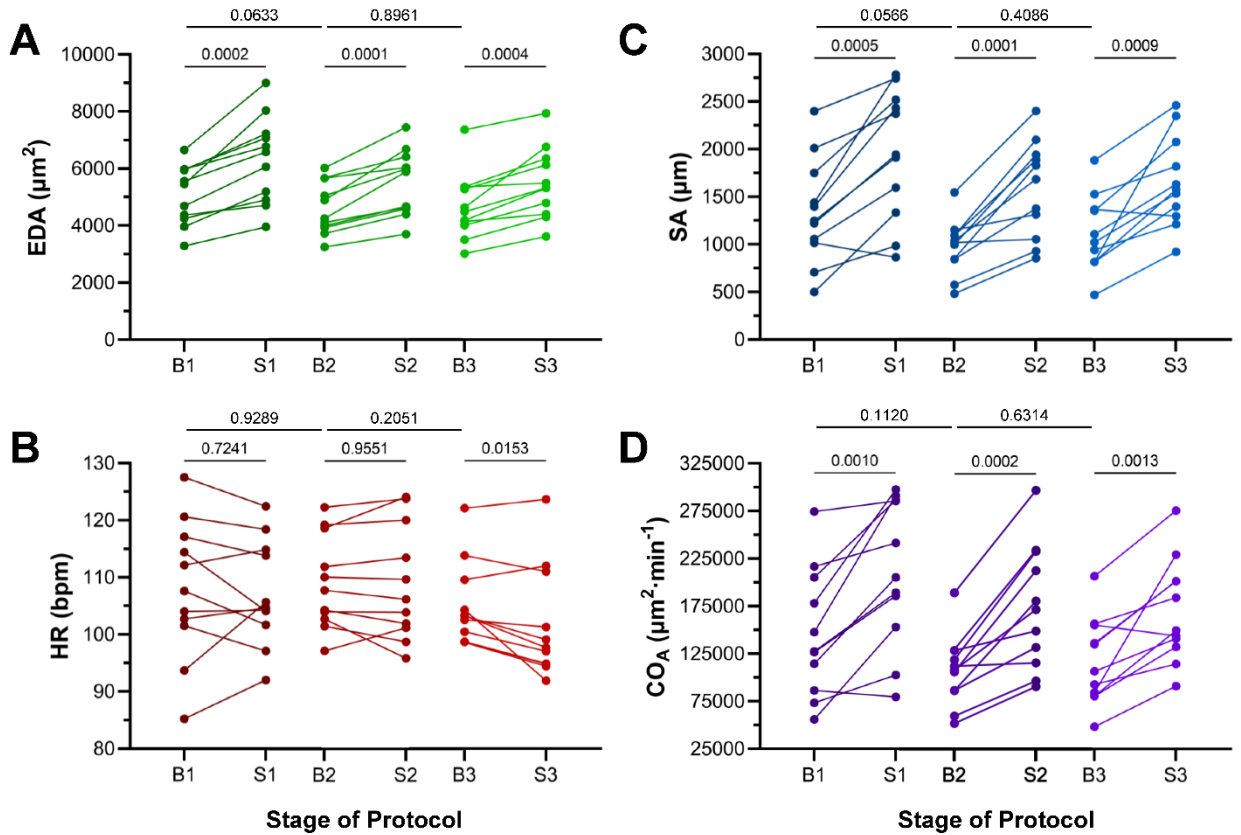
Figure 2.5 | Effect of repeated load application on functional parameters in 48hpf zebrafish larvae. Percentage change (%Δ) of (**A**) end-diastolic area (EDA), (**B**) heart rate (HR), (**C**) stroke area (SA), and (**D**) area cardiac output (CO$_A$) for each period of load application (S1, S2, S3). Average values presented as mean±SEM. Means for each loading period were compared by paired one-way ANOVA, with Tukey *post hoc* tests for individual comparisons. *n*=11 larvae.
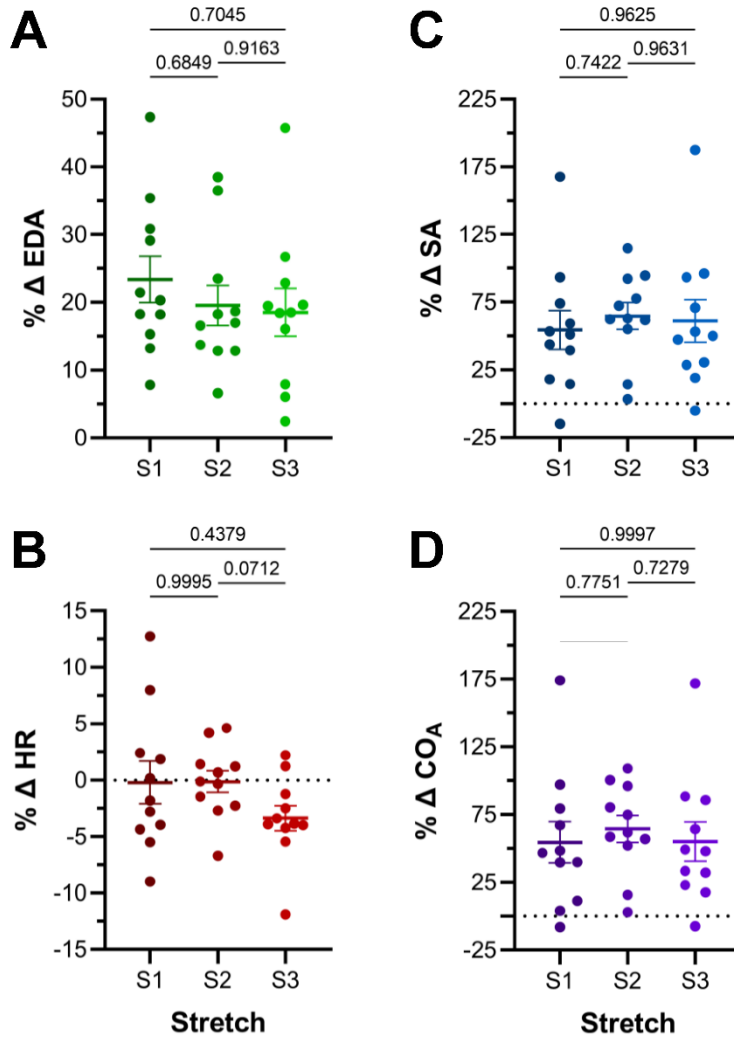
Figure 2.6 | Comparison of effects of load application on functional parameters in 48 hpf zebrafish larvae. Percentage change (%Δ) of end-diastolic area (EDA), heart rate (HR), stroke area (SA), and area cardiac output (CO_A) averaged over all periods of load application. Average values presented as mean±SEM. Means for each measured parameter were compared by unpaired one-way ANOVA, with Tukey *post hoc* tests for individual comparisons. *n*=11 larvae.
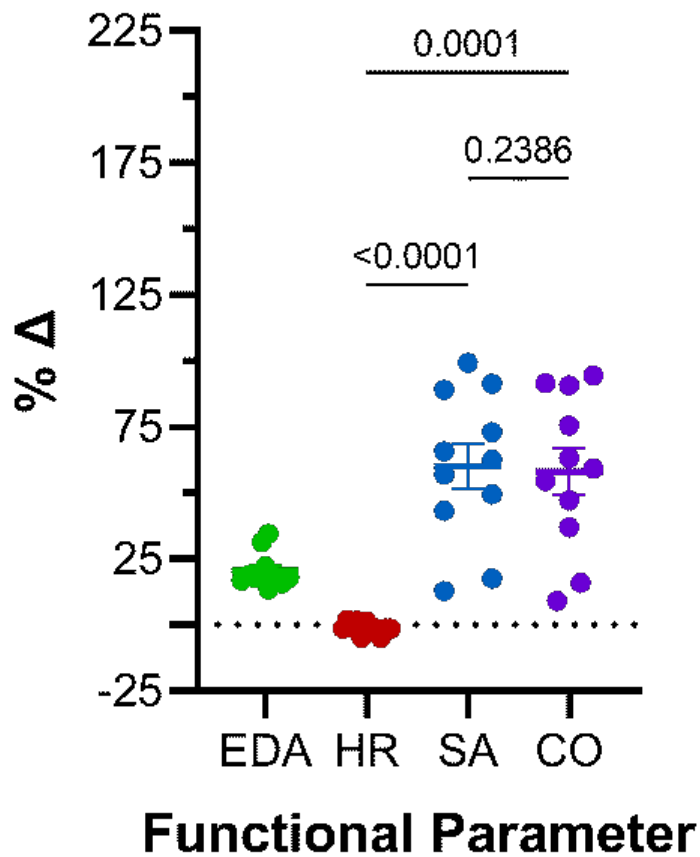
Figure 2.7 | *In vivo* imaging of Ca^{2+} dynamics in the hearts of 24 hpf zebrafish larvae. (**A**) Dynamic changes in intracellular Ca^{2+} (Ca^{2+} transients and wave propagation) measured in the heart tube of 24 hpf zebrafish larvae expressing the GECI GCaMP3. (**B**) Calcium transient duration at 80% recovery (CaTD$_{80}$) measured at 6 even spaced regions of interest along the length of the heart tube. Average values presented as mean±SEM. Means for each ROI were compared by paired one-way ANOVA, with Dunnet *post hoc* tests to compare regions 2-6 with ROI 1. *$p < 0.05$. n=15 larvae.
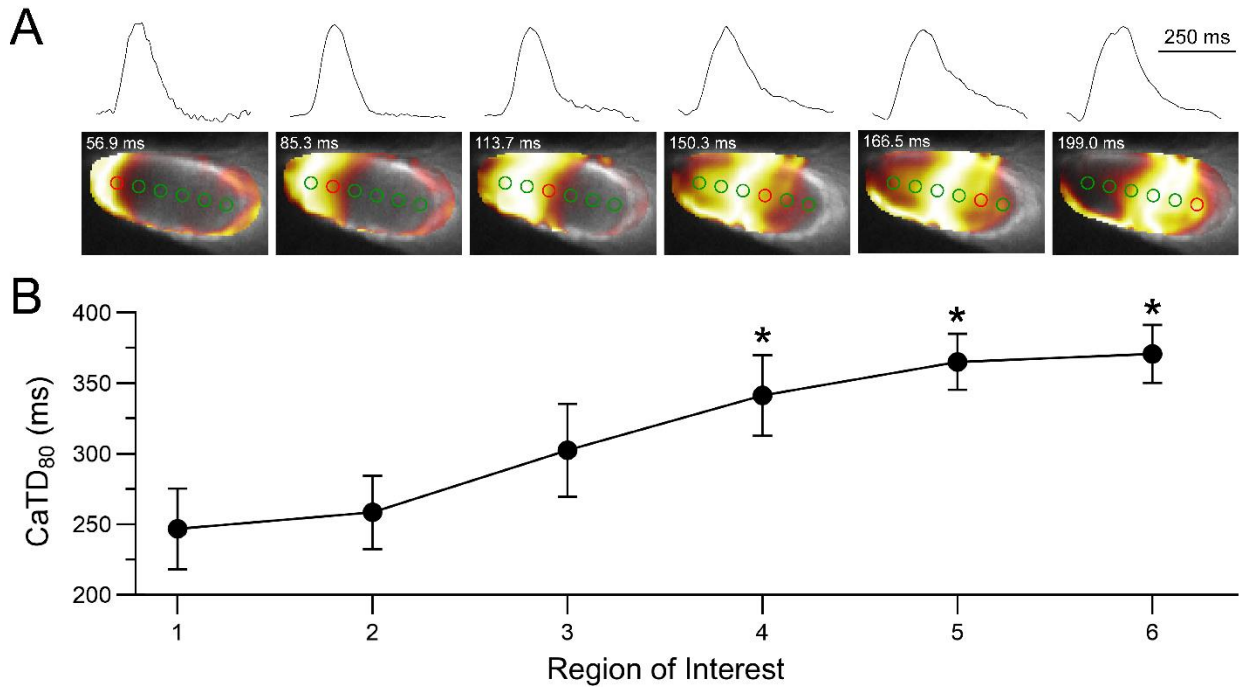
CHAPTER 3: EFFECTS OF AN ACUTE INCREASE IN HEMODYNAMIC LOAD ON CARDIAC FUNCTION IN THE DEVELOPING EMBRYONIC ZEBRAFISH

3.1. Introduction

Cardiac diseases remain a leading cause of morbidity and mortality [387], and many of these diseases arise at least in part from genetic defects that affect the development and maturation of the heart [388,389]. The formation of the heart's architecture involves a precise spatiotemporal series of events that includes genetic, molecular, and cellular mechanisms enabling stages of formation and differentiation in cardiac development [390]. Much of the progression in cardiac development is enabled by mechanical forces acting on the heart's chambers to promote their transformation [313].

Briefly, heart development can be broken down into five general stages: (i) the formation of the primitive heart tube; (ii) cardiac looping; (iii) trabeculation and compaction; (iv) septation; and (v) valve formation [311,391,392]. The primitive heart tube begins with two epithelial tubes, an outer myocardial tube, and an inner endocardial tube, which form on opposite sides of the early embryo [393], separated by an extracellular matrix layer called the cardiac jelly [394]. These tubes merge and fuse along the midline of the embryo to form a single cardiac tube [391]. Once the cardiac tube forms, spontaneous contractions begin [311], which propels the feedforward relationship that controls blood flow, which in turn upregulates the subsequent morphogenetic process of cardiac looping, causing the heart to twist and bend into a curved tube [377].

As the heart progresses from a linear valveless tube into a multi-chambered structure, the influence of hemodynamic forces exerted by the flow of blood acting on surrounding tissue becomes more prominent [311]. Hemodynamic forces are particularly

important in the earlier stages of heart development, as the architectural design that provides the foundation has not yet developed [351], allowing for more radical and rapid changes as it progresses toward the mature heart form [352]. These forces include pressure (the normal force associated with BP), shear stress (the frictional forces exerted by the flow of blood along the side of the wall [395]), and tissue stretch (due to outward force acting directly on the tissue wall). These hemodynamic forces each have associated mechanical effects, which are sensed at the cellular level [307,308] and impact gene and protein expression [309], cell morphology [310], and tissue organisation [311,396–398]. Consequently, this process is also essential for organogenesis and the normal overall development of the embryo through the supply of nutrients and oxygen [399].

The importance of these mechanical forces acting on the developing heart cannot be overstated as even minor disruptions during this vulnerable stage in development can have devastating repercussions in the form of CHD [390]. CHD occurs when cardiac morphogenetic processes are disrupted, which affects 1-2% of newborn children, represents the largest classification of birth defects, accounts for approximately 25% of all congenital abnormalities, and is the leading cause of death in infants under one year of age [387,400]. Despite this prevalence, the etiology of many forms of CHD remains unknown. Clinical and experimental research has identified multiple genetic mutations that result in CHD, but they do not account for the specific disease phenotype. Causes of CHD are often partitioned into genetic and nongenetic categories. Well-recognized nongenetic causes of CHD include environmental teratogens (dioxins, polychlorinated biphenyls, pesticides), [401] maternal exposures (alcohol, isotretinoin, thalidomide, antiseizure medications), [402] and infectious agents (eg, rubella).[403] Despite decades of

international efforts to combat these factors, the compendium of nongenetic causes of CHD continues to increase and to diversify. Antiretroviral medications [404] that are taken by 8 million people worldwide, and the epidemic of obesity [405] with associated phenotypes of diabetes mellitus [406] and hypercholesterolemia [407] are recognized as emerging risk factors for CHD. Deciphering the contributions of genetic and nongenetic causes of CHD has benefited from extensive model organism studies that have provided a wealth of insights into cardiac developmental biology. Molecular pathways have been identified that orchestrate formation of primordial cardiogenic fields that shape the cardiac crescent and linear heart tube, and which drive atrial, ventricular, inflow, and outflow tract morphogenesis.[302,408–410] Within these pathways, details have emerged about molecules that promote lineage specification, differentiation, cell growth, and migration, and that orchestrate temporal and spatial patterns of gene expression.[411–415] Experimental animal studies have provided spectacular insight to the understanding of mechanobiology of heart development [305,313,416], while the integration and advancement of high-resolution imaging modalities has continued to expand our understanding of the importance of hemodynamic flow in the developing heart [417,418]. These advances will prove to be critical for relevant clinically translatable interventions with the aim of identifying and adjusting the trajectory of malforming hearts related to CHD, as well as for providing insight into pressure and volume overload related heart conditions that may increase the risk of CVD. Thus, understanding of the missteps that occur during this formative phase in development is critical for providing insight into disease, and importantly, the associated treatment strategies to repair or regenerate damaged cardiac tissue [388,419].

In vitro studies have demonstrated that vascular endothelial cells can sense and transduce physical energy related to biomechanical stimuli, such as frictional stresses, wall shear stress, and transmural pressure, which can all be related to pulsatile blood flow [420]. However, the applicability of research conducted *in vitro* will remain speculative without an in-depth, quantitative examination of blood flow conditions *in vivo* [421]. The ability to visualise and quantify fluid flow within a living organism would greatly benefit the depth of understanding of the role of fluid forces in development and disease [422].

Over the past few decades, the zebrafish model has continued to provide insight into a multitude of human diseases, particularly relating to cardiovascular and neuronal conditions. One of the more prominent advantages of the zebrafish is the ability to image the progression of nerve innervation and chamber morphology during development [423]. Regarding cardiovascular development, cardiac function and blood flow hemodynamics need to be assessed to study the development of mechanisms that play an essential role in the systems ability to adapt to changes in hemodynamic load. Important parameters to consider include HR, SV, CO, EF, fractional area change, and fractional shortening [423]. Thus, the zebrafish is an important tool to study the analysis of hemodynamics in our understanding of mechanobiological mechanisms of induced defects, which involve determination of flow patterns, measuring flow velocities, calculating heart function parameters, and calculating hemodynamic stress levels [397].

The development of various genetic and cell biology tools, such as forward and reverse genetic approaches that provide the ability to induce a variety of clinically relevant cardiac defects, and transgenesis, lineage tracing, and cell transplantation techniques, provides the zebrafish model distinct advantages for the study of cardiac

development. For example, the development of the zebrafish embryo – especially in the transgenic *casper* line, allows for direct non-invasive real time imaging of heart maturation at a cellular resolution [424,425]. Additionally, due to their small size, zebrafish embryos rely primarily on oxygen diffusion to meet metabolic demands, instead of the cardiovascular system until at least 7 dpf. Therefore, this enables detailed analysis and detailed information relating to phenotype and maturation [388]. Finally, despite the zebrafish heart being more simplistic in structure with two chambers, as opposed to four chambers in the mammalian heart, the genetic expression responsible for the development of the heart are conserved in vertebrates. Thus, studies of cardiac development utilizing the zebrafish as a model organism will only continue to address questions related to cardiac development in the future [388].

The ability to provide sufficient CO is a dynamic process and is constantly varied and modulated in response to changes in hemodynamic load (preload, afterload), contractility, and HR [426–429]. Acute changes in LV hemodynamics and HR can alter LV mechanics [430–435]. Understanding the mechanisms responsible during acute changes in hemodynamic load will allow us to determine the intrinsic contribution of modulation, and perhaps provide insight into the long-term implications of when these mechanisms are altered or compromised. The aim of this project was to expand the method developed in project 1a and adapt it to zebrafish embryo during different stages of development to investigate mechanisms driving the effect of acute increased hemodynamic load on the heart. The hypothesis of this project is that in earlier stages of development, control of the HR is driven primarily by intrinsic mechanisms which respond to changes in mechanical load.

As development progresses, the response to changes in mechanical load is shifted from purely intrinsic, to a balanced intrinsic-extrinsic controlled system.

3.2. Methods

3.2.1. Ethics statement

All experimental procedures were approved by the Dalhousie University Committee for Laboratory Animals and followed the guidelines of the Canadian Council on Animal Care. Details of experimental protocols have been reported following the Minimum Information about a Cardiac Electrophysiology Experiment (MICEE) [382]. .

3.2.2. Zebrafish embryo and larvae preparation

Zebrafish were bred and raised by the Faculty of Medicine Zebrafish Core Facility at Dalhousie University. 48 hpf zebrafish with a point mutation in the mitfa and roy genes, resulting in a lack of melanocytes and iridophores that makes them mostly transparent (a common background strain known as casper [326]), genetically expressing a fluorescent marker (eGFP) specifically in CM (driven by the heart-specific myosin light chain 7 [myl7] promoter, to make the heart easier to visualise) were used for this study (*Tg*(myl7:eGFP) on a casper background). Animals were anesthetised in 3% Tris-buffered tricaine solution (0.45 mM, pH 7.4; Tris: BP152, Fisher Scientific, Waltham, MA; tricaine: MS-222, Sigma-Aldrich, St. Louis, MO) for five minutes, transferred to a glass depression slide (CSTK01, United Scientific Supplies, Libertyville, IL), and embedded ventral side up in 1.5% low-melting agarose (IB70051, IBI Scientific, Dubuque, IA) in HEPES-buffered saline solution (in mM: NaCl 142, KCl 4.7, MgCl2 1,

CaCl2 1.8, Glucose 10, HEPES 10) with 3% Tris-buffered tricaine. All experiments were performed at a controlled room temperature of 21° Celsius.

3.2.3. Electronic flow control system

Depending on the age of the zebrafish, we explored numerous protocols adjusting the magnitude of flow, duration of the flow, and rest between bouts of increased flow, with the desire to apply a repeated increased load that would result in a 25 percent increase in atrial EDA separated by an interval that would allow the atrial EDA to return to near-baseline levels. This initial increase in EDA was derived from previous studies involving isolated zebrafish SAN tissue and the manual manipulation of a mechanically induced stretch response [32].

3.2.4. Inflation and rest protocol development

The duration of increased hemodynamic load previously described [378] provided an entry to understand increasing hemodynamic load in the zebrafish heart. Although the intention of the previous method was to investigate fluid dynamics and the relationship of tissue stiffness over a longer duration (3+ minutes), we were interested in applying a shorter duration to investigate the acute cardiac functional responses to increased hemodynamic load on a beat-by-beat basis (30s). This required an instantaneous ability to control heart volume, instead of a gradual progression in applied load through the water column method.

The introduction of the electronic pressure-controlled system allowed near-instantaneous changes to the applied pressure acting on the reservoir which forced saline solution through the tubular network, through the canular and finally altering the flow

into the intracardiac area of the zebrafish larvae. However, the initial electronic pressure-controlled system that we implemented, had a maximum pressure limit of 25 mbar. Despite efforts to optimize this through manipulation of the cannula tip, the effect on the atria volume was delayed, and not as rapid as desired. To measure the effect of stretch on a beat-by-beat basis we required a more robust, immediate effect. We then implemented the electronic pressure-controlled system that had a maximum pressure limit of 2000 mbar. This system allowed the same near-instantaneous applied pressure, at a greater magnitude and manipulation of the hemodynamic load being injected into the cardiovascular system and directly effecting the chambers of the heart on a beat-by-beat basis.

As we were navigating into now unfounded territory, this required a lot of trial and error to optimize the desired timing of the applied load as well as the magnitude to allow increased atrial stretch to occur without compromising cardiac function. We did see the effect we were seeking; however, it was proving to be difficult to replicate our findings as the main factor that needed to be constant was the diameter of the cannula as this was the primary source of resistance. Using the P-95 Browning Glass Pipette Puller was effective in pulling precise short, blunted cannulae. However, to allow uninterrupted flow of solution into the intracardiac space, the tip needed to be further altered manually, which on the order of μm, has the potential to vary the resistance considerably between individual pipettes.

Through trial and effort, we developed a protocol for 2 dpf zebrafish embryo consisting of three repeated bouts (Stretch 1; S1, Stretch 2; S2, Stretch 3; S3) of a sustained increase in hemodynamic load of 3μL per minute (μL/min) for 30 seconds (s)

to induce stretch of the atrial chamber separated by a two-minute rest period consisting of

0µL/min (Protocol 1); this duration before each phase of increased hemodynamic load is

the adapted baseline phase (Baseline 1; B1, Baseline 2; B2, Baseline 3; B3). The 6

dpf_P2 and 14 dpf, the parameters for duration of flow and rest were the same for

Protocol 2 and 3, the magnitude of flow was adjusted for anatomical size and

functionality, to 4 µL/min and 5 µL/min, respectively.

To summarise for clarity, the protocols used are described below:

Protocol 1 (P1): 30-second flow interval (flow rate: 3 µL/min) followed by a 90-second

rest interval (flow rate: 0 µL/min). Repeated a total of three times.

Protocol 2 (P2): 30-second flow interval (flow rate: 4 µL/min) followed by a 90-second

rest interval (flow rate: 0 µL/min). Repeated a total of three times.

Protocol 3 (P3): 30-second flow interval (flow rate: 5 µL/min) followed by a 90-second

rest interval (flow rate: 0 µL/min). Repeated a total of three times.

P1 was used in 2 dpf zebrafish. P2 was used in 6 dpf and 14 dpf zebrafish that were

incubated with blebbistatin. P3 was used in 14 dpf control and 14 dpf groups exposed to

pharmacological interrogation. Additionally, there was a second 14 dpf group for P2.

This was to ensure that HR response was not simply load-dependent based on the

protocol increases in flow, thus allowing comparison of 6 dpf and 14 dpf with the same

exposure to hemodynamic load (P2), as well as comparison of two 14 dpf groups with

varying hemodynamic load (P2, P3).

3.2.5. Measurements

Measurements of EDA, ESA, HR, SA, and CO_A were collected and calculated as

described in Chapter 2.

3.2.6. Statistical analysis

Data was analysed with GraphPad Prism (version 9.4.1). Differences between baseline measurements (B1 and B2, B2 and B3) were compared using a Repeated Measures One-Way ANOVA (paired). Equal variability of differences (sphericity) was not assumed, instead the Greenhouse-Geisser correction was applied. The Greenhouse-Geisser is used to assess the change in a continuous outcome with three or more observations across time or within-subjects. Tukey's multiple comparisons test was used for post hoc analysis. To analyse changes between baseline and stretch (B1 and S1, B2 and S2, B3 and S3) individual paired t-tests were used. To assess changes between the stretch phases (S1 and S2, S2 and S3), a Repeated Measures One-Way ANOVA was performed. Comparison of average change between groups was assessed using an Ordinary One-Way ANOVA (unpaired). Tukey's multiple comparisons test was used for *post hoc* analysis.

3.3. Results

3.3.1. Effect of increasing hemodynamic load on end diastolic area

Experiments in each age group resulted in a significant increase in EDA during each stretch phase, compared to the corresponding rest phase (B1 and S1, B2 and S2, B3 and S3) ($p < 0.001$). Additionally, in each phase, among each group, the 90-second resting phase allowed EDA to return to baseline or near-baseline, evidenced by no observed significant difference between B1 and B2 and between B2 and B3 ($p > 0.05$). (Figures 3.1 – 3.4).

Examining the EDA percentage change between stretch and baseline within each group showed no significant difference (S1 and S2, S2 and S3) (Figure 3.5). Thus, the three repeated stretches were combined as one averaged stretch to simplify the direct comparison between groups. Among these results, there were no significant differences in the average percentage change of EDA between the 2 dpf_P1 group and both P2 groups (6 dpf_P2 ($p = 0.095$), 14 dpf_P2 ($p = 0.648$)). There was also no significant difference between 6 dpf_P2 and both 14 dpf groups (14 dpf_P2 ($p = 0.622$), 14 dpf_P3 ($p = 0.129$)). The increased hemodynamic load in between the two protocol P3 and P2 in the same age group resulted in a significant difference between 14 dpf_P2 and 14 dpf_P3 ($p = 0.007$). (Figure 3.6).

The plots displaying the absolute change between baseline and stretch phases for HR, SA, and CO_A for each group is included in the appendix, supplemental material. This section will primarily focus on the comparison between groups.

3.3.2. Effect of increased hemodynamic load on heart rate

In 2 dpf_P1, the average percent change in HR between baseline and stretch was -1.7±0.4 percent. In the absolute changes between baseline and stretch there were no significant differences ($p < 0.067$) (Supplemental Figure 3.1). In 6 dpf_P2, the average percent change in HR was 5.1±1.2 percent. There were no differences between the absolute change in the first and second stretch phases (B1 and S1 or B2 and S2 ($p < 0.147$)), however, this group did see a significant increase between B3 and S3 ($p = 0.044$) (Supplemental Figure 3.2). The average percent change in HR in the 14dpf_P2 group was 10.7±2.2 percent and there was a significant increase between each baseline and stretch phase ($p < 0.002$) (Supplemental Figure 3.3), while the average percent change in HR in

the 14 dpf_P3 group was 14.9±3.4 percent and there was a significant increase between

each baseline and stretch phase (p < 0.002) (Supplemental Figure 3.4). Comparison of

average absolute HR change between groups resulted in significant differences between 2

dpf_P1 and 6 dpf_P2, 14 dpf_P2, and 14 dpf_P3 (p < 0.046). There were no significant

differences between groups comparing P2 (6 dpf_P2 and 14 dpf_P2) (p = 0.093), but

there was a significant difference between 6 dpf_P2 and 14 dpf_P3 (p < 0.001). There

were no significant differences between 14 dpf aged zebrafish (14 dpf_P2 and 14 dpf_P3)

(p = 0.322) (Figure 3.7). Within each group there were no significant differences between

absolute HR measurements between baseline phases (B1 and B2; B2 and B3) (p < 0.099)

(Supplemental Figures 3.1 - 3.4), and no significant difference within each group,

comparing the absolute change in HR between stretches (p = 0.112) (Supplemental

Figure 3.5).

3.3.3. Effect of increased hemodynamic load on stroke area

Within each group (2 dpf_P1, 6 dpf_P2, 14 dpf_P2, 14 dpf_P3), there was a

significant increase in SA between each baseline and stretch phase (p < 0.046), with the

single exception of B3 and S3 in the 6 dpf_P2 aged zebrafish (p = 0.059). Additionally,

there were no significant differences between absolute SA measurements between

baseline phases within each group. (B1 and B2; B2 and B3) (p < 0.095) (Supplemental

Figures 3.6 - 3.9). There was no significant difference in the absolute change in SA

across each stretch phase, within each group (Supplemental Figure 3.10). Comparison of

the average absolute SA change between groups showed a significant increase between 6

dpf_P2 and both 14 dpf aged zebrafish (14 dpf_P2; 14 dpf_P3; p < 0.005). There were no

significant differences between 14 dpf aged zebrafish (14 dpf_P2 and 14 dpf_P3) (p = 0.999) (Figure 3.8).

3.3.4. Effect of increased hemodynamic load on cardiac output

Regarding CO_A, there was a significant difference within each group comparing each baseline and stretch phase (p < 0.039), and no significant change between absolute baseline measurements within each group (p < 0.150) (Supplemental Figures 3.11 – 3.14). For absolute change in CO_A across each stretch phase within each group there was no significant differences (Supplemental Figure 3.15). Comparison of average absolute CO_A change between groups found significant differences between 6 dpf_P2 and both 14 dpf aged zebrafish (14 dpf_P2; 14 dpf_P3; p < 0.001). There were no significant differences between 14 dpf aged zebrafish (14 dpf_P2 and 14 dpf_P3) (p = 0.812) (Figure 3.9).

3.4. Discussion

In the 2 dpf zebrafish embryos, after demonstration of the ability to increase atrial EDA with a return to baseline, confirmed by no significant differences between baseline measurements, measurement of functional cardiac parameters (HR, SA, CO_A) were assessed to determine the effect of repeated bouts of applied increased hemodynamic load acting on the atrium. In the 2 dpf zebrafish group, the HR response to repeated bouts of increased hemodynamic load demonstrated no response between baseline and stretch phases. In fact, this response was mathematically, slightly negative (average -1.7±0.3 percent change). This is contrary to what might be expected based on the heart's response to increased hemodynamic load, such as during exercise [436], CO increases as a result of

contributions from increases in HR and force of contraction, and overall ventricular work [437]. However, when consideration is given to the stage of cardiac development in 2 dpf zebrafish embryo this may become less surprising. The zebrafish heart at 2 dpf has just undergone transformation from a linear heart tube at 24 hpf and undergoes a leftward looping into an S-shape at 33 hpf [397], and ventricular displacement causing the initiation of a pronounced two chambered structure. At 36 hpf, the pumping mechanisms begin to transition from slow peristaltic waves into sequential chamber contractions, suggestive of an onset of the cardiac contraction system [397]. By 48 hpf the ventricular chamber is just beginning to develop the outer and inner curvatures, while CM start delaminating from the ventricle to begin trabeculation [438]. Taken together, although the heart has begun to develop into a functional contractile organ, there is still significant maturation of the conduction system, remodeling, as well as nerve innervation that must occur before the heart is capable to sustain the physiological demands [314,395].

By 6 dpf, the progression of the cardiac chambers and valves have developed more completely and have become operational in the propulsion of blood flow, and the prevention of back flow [310,417]. In this group, there was an observed five percent increase in HR, however, as there is no statistical significance, this may be attributed to immature SAC development and could be further evidenced by the fact that a zebrafish embryo can survive for 7 dpf without blood flow [439], and primarily rely on oxygen diffusion due to their small size [265,440].

In the 14 dpf zebrafish, the HR response is much more robust and at this stage in development, the transportation of nutrients is fully dependent on blood flow from the heart which could be driven by the presence of SACs. Some SACs have a permeability

for Ca^{2+}, the activation of SACs has been proposed to mediate a stretch-induced rise in the resting $[Ca^{2+}]i$ and Ca^{2+} transients [73,441], where the the activation of SAC was also suggested to induce Na^+ accumulation with its non-selectivity over cations [442]. The changes in $[Na^+]i$ was thought to increase $[Ca^{2+}]i$ via the activation of Na^+-Ca^{2+} exchangers operating in a reverse-mode [21,441,443].

Comparing the percent change in EDA in 6 dpf_P2 group with the 14 dpf_P3 group, there was no significant difference, nor was there between the 6 dpf_P2 and 14 dpf_P2 groups. There was a significant difference in 14 dpf_P2 and 14 dpf_P3 which is likely attributed to the increase in mass and HR response in the 14 dpf aged fish, as there is a significant difference in HR response between 6 dpf_P2 and 14 dpf_P3 and no significant difference between the 14 dpf groups (14 dpf_P2, 14 dpf_P3), as the HR response was increased in this group, thus moving more flow and preventing EDA to reach the levels of the 14 dpf_P3 group.

The presence of significant differences in SA with atrial dilation across each age group demonstrates the presence of the FSL and that it is not age dependent. This describes the relationship between increased length of myocardial fibres and its mechanical performance and the importance for cardiac function [444,445]. This mechanism plays an important role in the increased venous return of blood to the heart and increases in SV. As the increase in venous return dilates the heart chamber, this causes a stretch in the myocardium, which increases the contractile force generated by the muscle, resulting in an increased SV. The FSL is central to the alteration of CO, particularly important in younger aged groups (2 dpf_P1, 6 dpf_P2) as the responses to increased HR do not

appear to be present in these groups. The stretch of the myocardium thereby increases the contractile force of the muscle and increases SV.

Regarding CO (the product of HR multiplied by SV), this must be altered to meet the changing physiological demands on the system, which can occur either through increased activity [446] or temperature [447]. The increase in CO occurs through an increase in HR or SV, but in most cases the delicate balance of frequency versus volume as a modulatory strategy for adjusting CO occurs from contributions of both factors [83]. In the case of this project, as temperature was a controlled variable, the increase in hemodynamic load is more similar to increased venous return resulting from demands due to strenuous exercise [83].

Ideally, this project would involve samples from each dpf age group in ascending order from 2 dpf_P1 to 14 dpf with incremental responses to HR, specifically identifying when the integrative HR response is initiated at each developmental stage. The zebrafish ventricle chamber begins to develop distinguishable trabeculae at 72 hpf [438,448]. As this is an indicator of cardiac development, this prompted the selection of the next age group to include 4 dpf samples. However, as there were no observed changes in preliminary experiments compared to 2 dpf_P1, the decision was made to pursue an older age group. Trabeculation begins to line the outer curvature of the ventricle at ~5 dpf [438,448], which prompted exploration of the 6 dpf age group. After successfully adapting the hemodynamic flow protocol to this group and identifying a change in the HR response, this prompted further motivation to apply this method in an older age group to determine if a more robust response to increased hemodynamic load would occur. After two weeks, as cardiac development continues and the trabeculae continue to expand and mature up to

this point, the compact myocardium still remains one cell layer thick [438], which is consistent with the relatively thin compact myocardium observed in adult zebrafish ventricles [363]. We explored the potential of expanding this technique into the 14 dpf group. Providing an interval at 10 dpf between these aged sample groups was explored however, given the duration in timing needed to optimize this technique we opted to focus attention on exploring the effects of pharmacological intervention, as described in the next chapter.

Despite the casper zebrafish line providing an excellent tool that allows clear visualisation and *in vivo* imaging of the cardiac chambers, at 14 dpf, the interference of the ventricle overlapping the atrium and thus blocking the potential usage of this as a successful experimental stage became complicated. Thus, further interrogation of this method to measure the effects on the atrium in older aged zebrafish (15+ dpf) could become problematic.

3.5. Conclusion

In conclusion, we have successfully demonstrated the use of a novel method to manipulate the acute hemodynamic load and implement this approach in multiple age groups in the zebrafish model, further validating this model system for the study of mammalian cardiovascular physiology and functional relationships. The zebrafish continues to offer a promising and advantageous model that will contribute significantly to knowledge about the molecular mechanisms of mammalian cardiac modulation of HR and contractile regulation, offering insight into the functional consequences of genetic manipulation and therapeutic strategies in human health and disease.

Figure 3.1 | Absolute EDA Change in 2 dpf zebrafish embryo. Baseline measurements are represented as B1 B2 B3. Stretch phases measurements are represented as S1 S2 S3. In each stretch phase there was a significant increase in EDA, returning to baseline levels after the rest period indicated by no significant differences between baseline phases (ns = p > 0.05, * = p ≤ 0.05. ** p = ≤ 0.01, *** = p ≤ 0.001).

Figure 3.2 | Absolute EDA Change in 6 dpf zebrafish embryo. Baseline measurements are represented as B1 B2 B3. Stretch phases measurements are represented as S1 S2 S3. In each stretch phase there was a significant increase in EDA, returning to baseline levels after the rest period indicated by no significant differences between baseline phases (ns = $p > 0.05$, * = $p \le 0.05$. ** $p = \le 0.01$, *** = $p \le 0.001$).
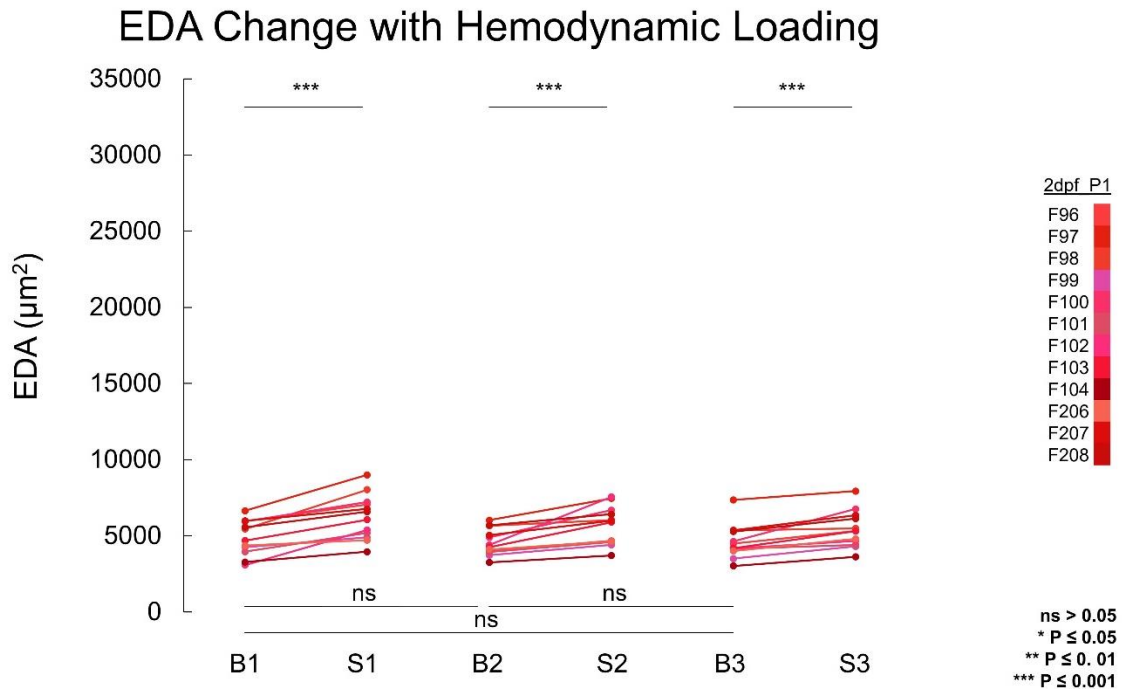

EDA Change with Hemodynamic Loading

Figure 3.3 | Absolute EDA change in 14 dpf zebrafish larvae (protocol 2). Baseline measurements are represented as B1 B2 B3. Stretch phases measurements are represented as S1 S2 S3. In each stretch phase there was a significant increase in EDA, returning to baseline levels after the rest period indicated by no significant differences between baseline phases (ns; non significant = p > 0.05, * = p ≤ 0.05. ** p = ≤ 0.01, *** = p ≤ 0.001).
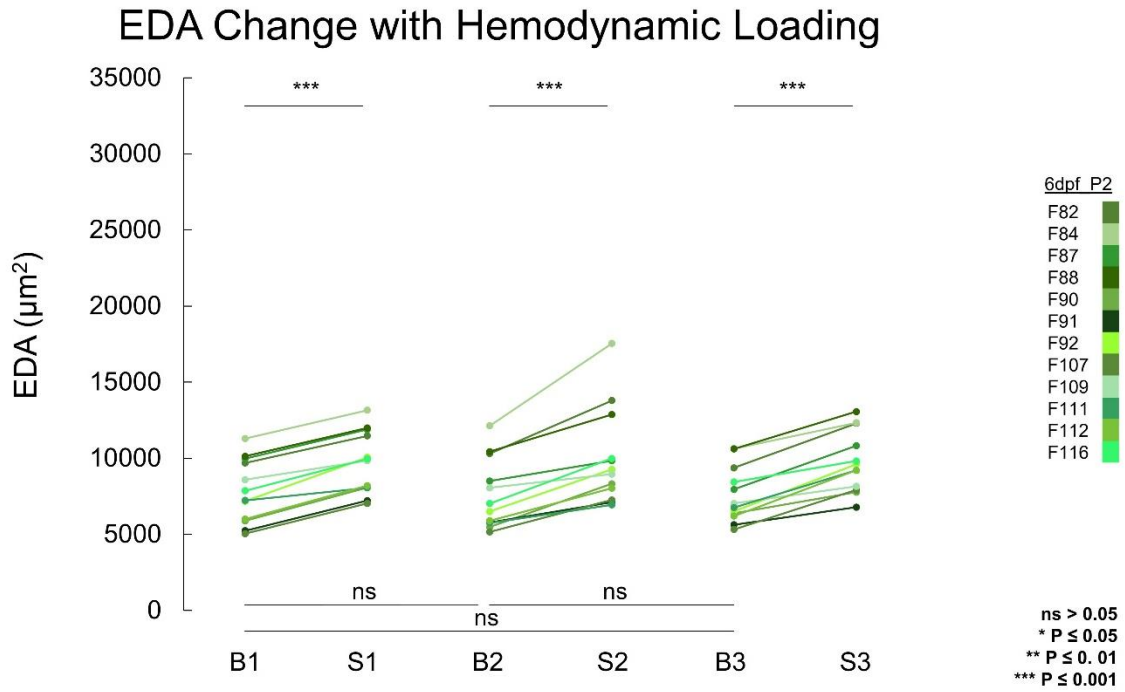

EDA Change with Hemodynamic Loading
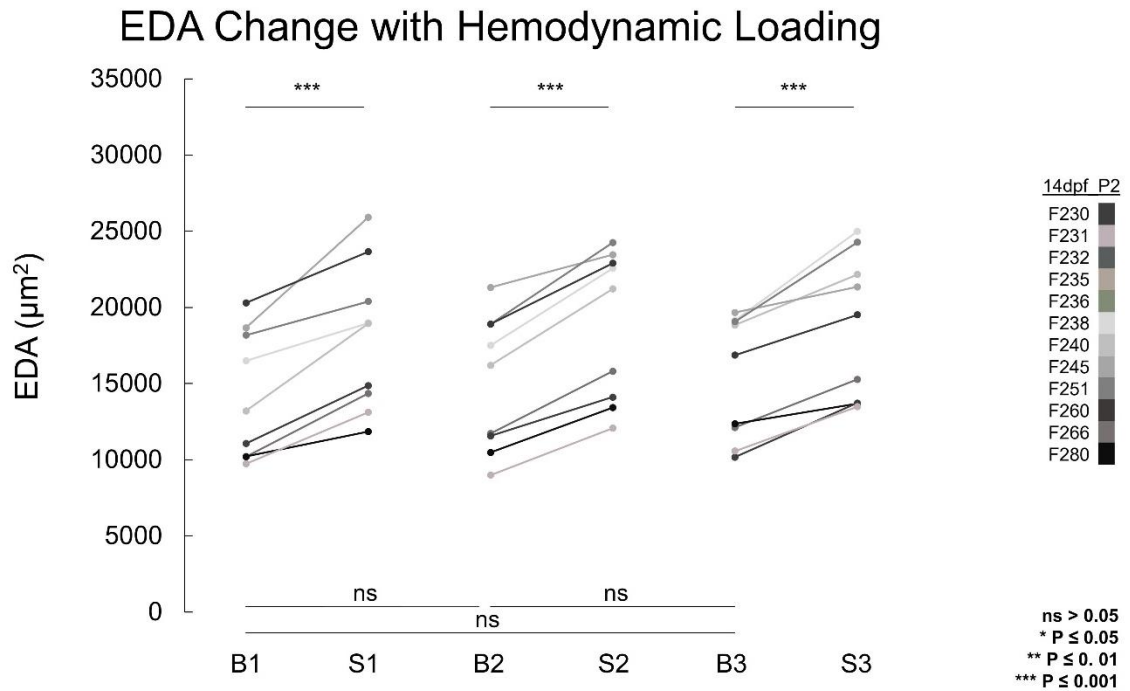
Figure 3.4 | Absolute EDA change in 14 dpf zebrafish larvae. Baseline measurements are represented as B1 B2 B3. Stretch phases measurements are represented as S1 S2 S3. In each stretch phase there was a significant increase in EDA, returning to baseline levels after the rest period indicated by no significant differences between baseline phases (ns = p > 0.05, * = p ≤ 0.05. ** p = ≤ 0.01, *** = p ≤ 0.001).
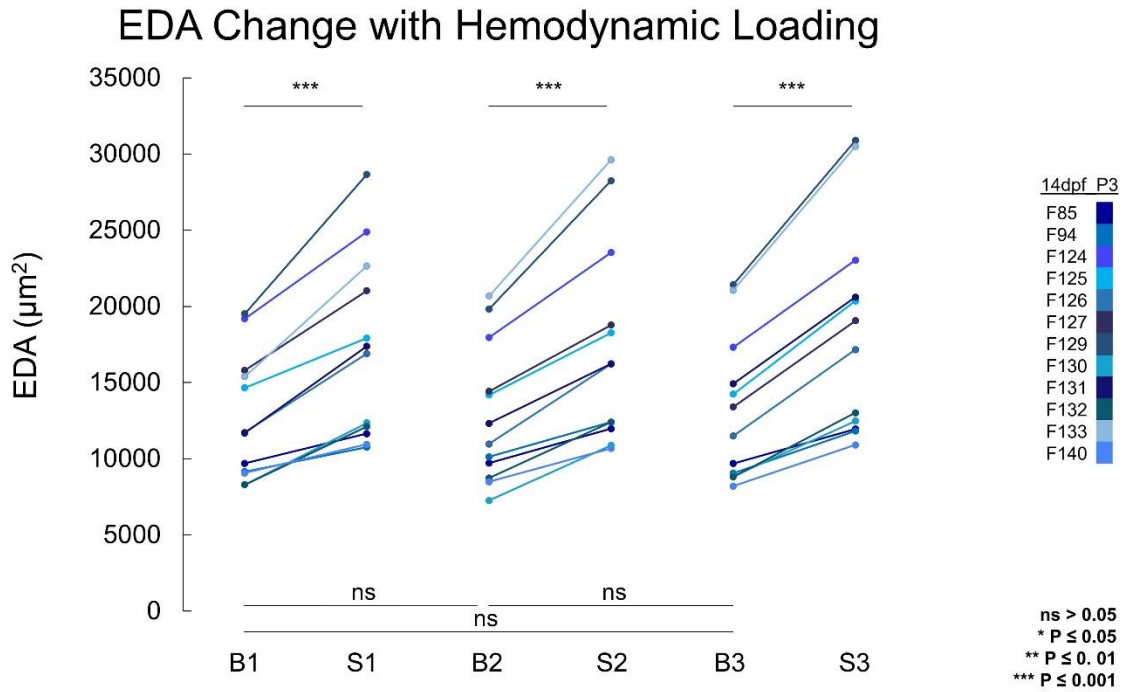
Figure 3.5 | Percent EDA change between each stretch in each age group.
Comparison of percentage EDA change within each group. S1, S2, S3 represents each stretch across each group. 2 dpf; red, 6 dpf; green, 14 dpf_P3; blue, 14 dpf_P2; grey. In each group there were no significant differences within each group (p < 0.05).
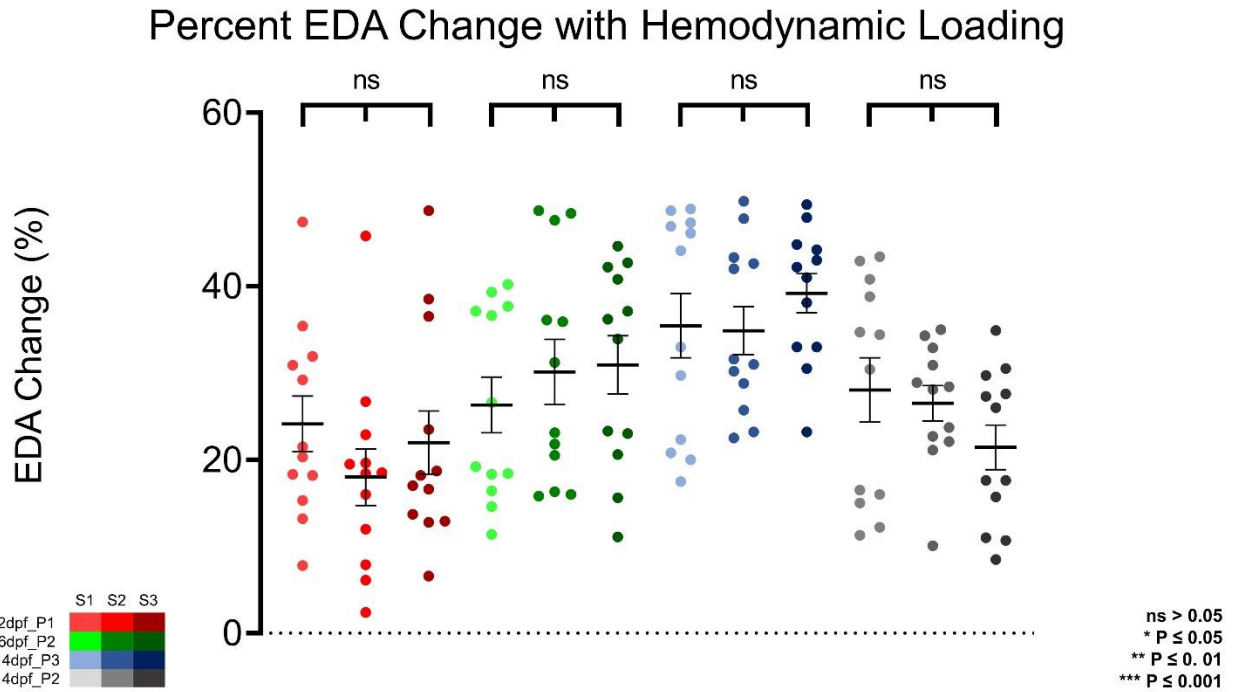
Figure 3.6 | Average percent EDA change in each age group. Percent change in EDA from each stretch, within each group was averaged to allow direct comparison between each age group. 2 dpf; red, 6 dpf; green, 14 dpf_P3; blue, 14 dpf_P2; grey. There was a signifcant difference between 14 dpf groups in protocol 2 and protocol 3. (ns = not significant; p > 0.05, * = p ≤ 0.05, ** = p ≤ 0.01, *** = p ≤ 0.001).

Average EDA Change with Increased Hemodynamic Load
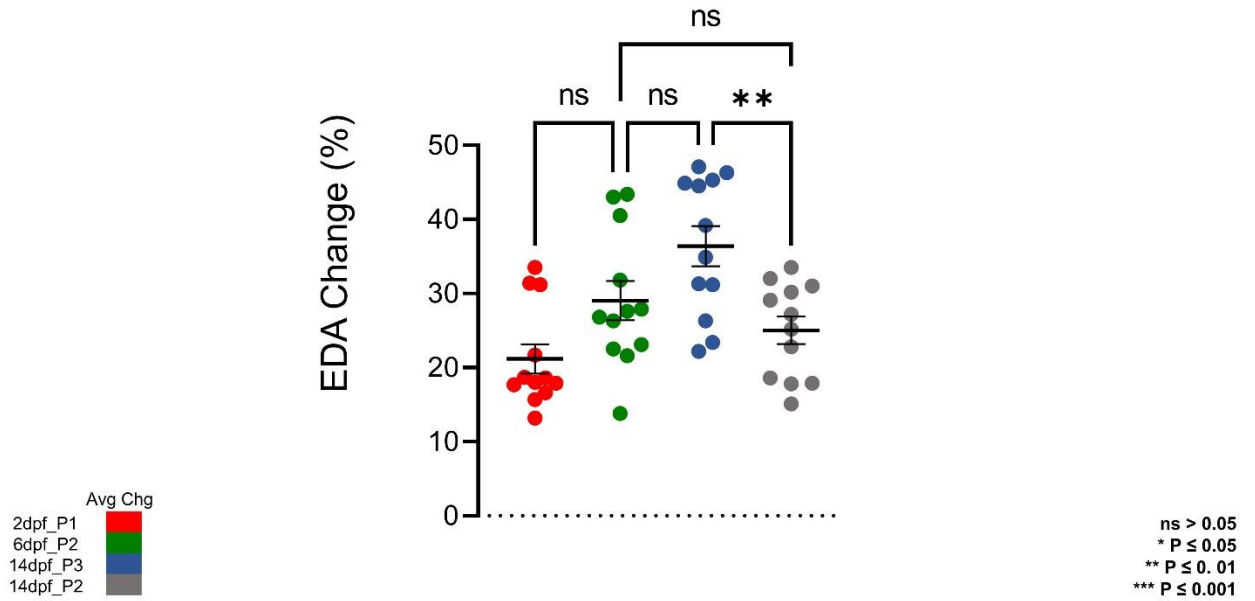
Figure 3.7 | Average percent HR change in each age group. 2 dpf; red, 6 dpf; green, 14 dpf_P3; blue, 14 dpf_P2; grey. There was a signifcant difference between 6 dpf and 14 dpf_P3 and no significant difference between 6 dpf in 14 dpf_P2 (ns = non significance; p > 0.05, * = p ≤ 0.05, ** = p ≤ 0.01, *** = p ≤ 0.001).

Average HR Change with Increased Hemodynamic Load
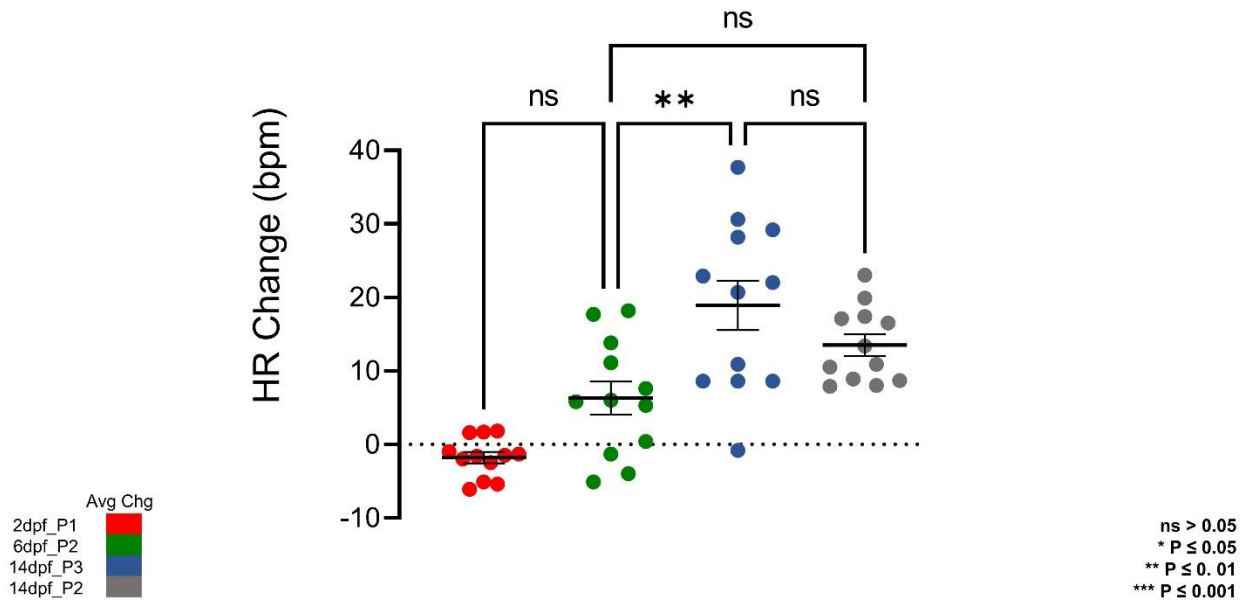
Figure 3.8 | Average percent SA change in each age group. 2 dpf; red, 6 dpf; green, 14 dpf_P3; blue, 14 dpf_P2; grey. SA change was siginificantly increased in both 14 dpf groups compared to 6 dpf. There were no significant change between SA between 14 dpf groups. (ns = non significance; p > 0.05, * = p ≤ 0.05, ** = p ≤ 0.01, *** = p ≤ 0.001).

Average SA Change with Increased Hemodynamic Load

Figure 3.9 | Average percent CO$_A$ change in each age group. 2 dpf; red, 6 dpf; green, 14 dpf_P3; blue, 14 dpf_P2; grey. COA change was siginificantly increased in both 14 dpf groups compared to 6 dpf. There were no significant change between COA between 14 dpf groups. (ns = non significance; p > 0.05, * = p ≤ 0.05, ** = p ≤ 0.01, *** = p ≤ 0.001).
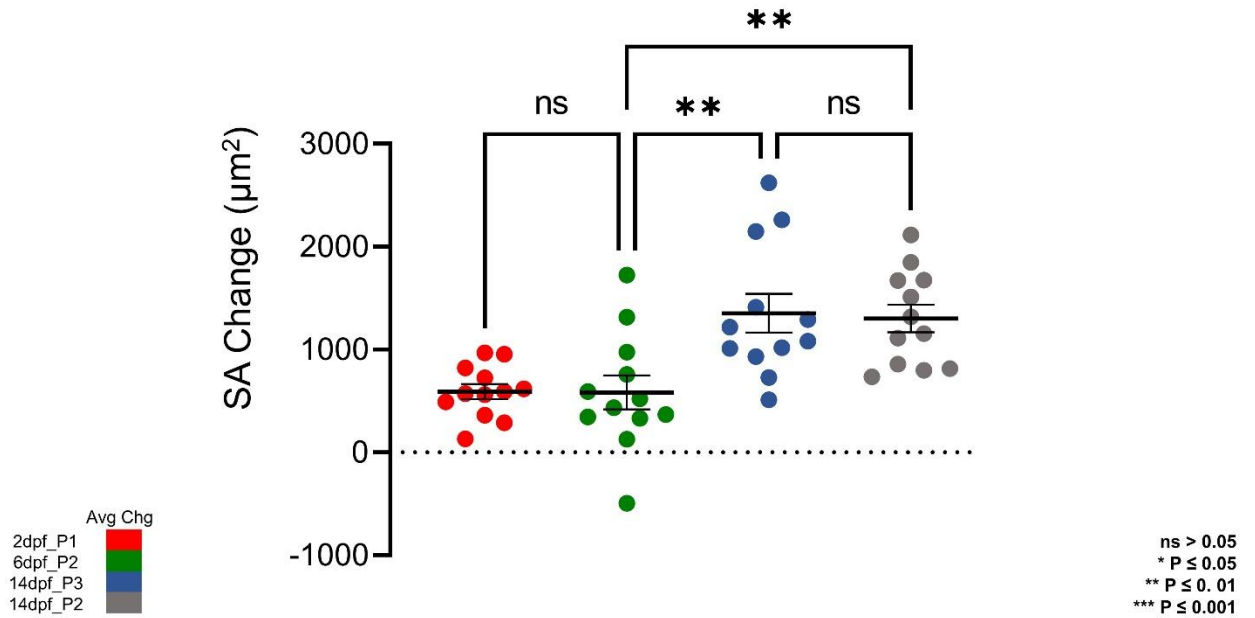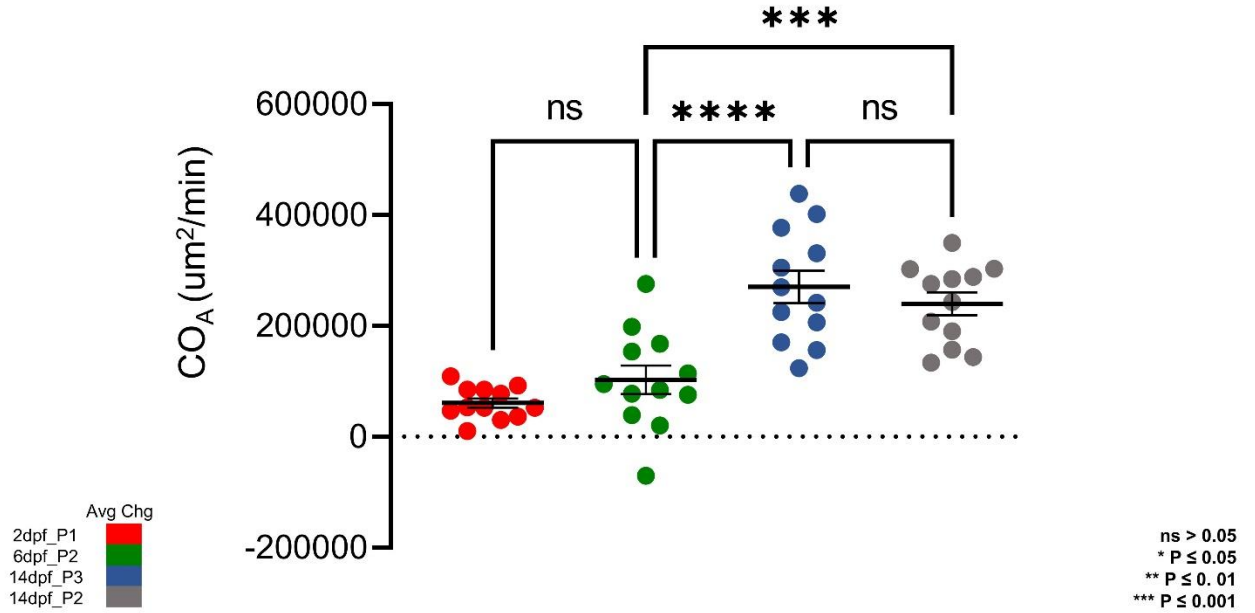

Average CO$_A$ Change with Increased Hemodynamic Load

CHAPTER 4: MECHANISMS DRIVING CARDIAC EFFECTS OF ACUTE INCREASED HEMODYNAMIC LOAD IN EMBRYONIC ZEBRAFISH

4.1. Introduction

This chapter discusses the general organization and physiology of the heart's response to changes in hemodynamic load and will investigate the ANS and the heart's intrinsic ability to self regulate through MEC. The ANS is functionally divided into the SNS (adrenergic) and the PNS (cholinergic) and plays a key role in the regulation and modulation of cardiac activity, including arterial BP, HR, and consequently CO, with its dysregulation being involved in various heart diseases, such as cardiac arrhythmias [112]. The ANS comprises both extrinsic and intrinsic innervation of the heart. The ICNS includes the network of the intracardiac ganglia and interconnecting neurons within the heart tissue. The cardiac ganglia contribute to the tight modulation of cardiac electrophysiology, working as a local hub integrating the inputs of the extrinsic innervation and the ICNS [337].

The β-AR is a component of the SNS and plays an important role in the regulation of cardiac function [449]. When stimulated, CM β-ARs primarily bind to the G stimulatory protein, and subunit, Gα protein responsible for activating adenylyl cyclase, which generates the second messenger cAMP [273,449]. Increased cAMP levels activate cAMP-dependent PKA which subsequently phosphorylates downstream Ca^{2+} regulatory proteins, in order to enhance cardiac contractility [450,451]. Enhanced activation and open probability of L-Type Ca^{2+} channels facilitates an increased contractility of CM, due to a higher availability of cytosolic Ca^{2+} while also elevated release and reuptake into the SR are regulated by PKA [273,451].

Conversely, the PNS acts through the vagus nerve, innervating primarily the atria, with some innervation into the ventricle [452], playing a critical role in reduction of HR, force of contraction, and conduction velocity of the SAN and AV node through cholinergic signaling [453] being mediated by the binding of ACh to M_2 muscarinic receptors in atrial myocytes [454,455]. M_2 receptors are coupled to G inhibitory proteins, which mediate the decrease in inotropic and chronotropic responses through various downstream mechanisms. One mechanism involves direct inhibition of adenylyl cyclase, which leads to decreased production of adenosine 3′,5′-cAMP and inhibition of PKA [456,457]. The negative inotropic and chonotropic effects from activation of muscarinic receptors in the SAN, leads to negative chronotropic responses due to decreased cAMP levels, which results in downstream inhibition of the HCN channel-mediated I_f, resulting in a decrease in pacemaker rate [458,459].

Furthermore, activation of SAC leads to an ion influx that alters $[Ca^{2+}]_i$ and Na^+ concentrations [460], while the elevation of Na^+ favors additional cellular Ca^{2+} accumulation via the NCX. In essence, Ca^{2+} acts as a signaling molecule to switch on Ca^{2+}-dependent signaling cascades including protein kinase C, pyruvate kinase, calmodulin, CaM kinases, and phospholipases that modulate cardiac function by protein phosphorylation [461], ultimately by stimulating transcription factors and protein synthesis [462,463]. Pharmacological inhibition of the stimulatory pathways of the ANS and SAC in response to increases in hemodynamic load may provide insight into the mechanisms responsible for parameters of cardiac function, including HR, SV, and CO. The ability to study these mechanisms in an *in vivo* setting, while manipulating hemodynamic load has not yet been possible in mammalian animal models.

The zebrafish heart has several advantages over traditional mammalian models for investigating the organization and function of the cardiovascular system. The spontaneous electrical activity that occurs in the SAN, as well as propagation of this signal through the atrium, AV canal, and into the ventricle are strikingly similar from the two-chambered hearts of zebrafish to the four-chambered hearts of adult mammals [266,277,346]. Recent reports [289,385,464–466] have established the zebrafish heart as a powerful tool for studying cardiac electrophysiology, with the potential to provide broad insights into cardiovascular function. Because of this striking resemblance to humans, zebrafish have recently been adopted as a model for studies of heart physiology, as well as pharmacological interrogation [289], with the potential to provide broad insights into cardiovascular function. The specific aims of this project were to determine the role of neurons and SACs in driving changes in driving changes in cardiac function with the use of pharmacological block of SNS, PNS, and SAC_{NS}. The hypotheses were the cardiac response to increased hemodynamic load will i) be blunted by SNS inhibition, as the SNS is cardioexcitatory, inhibition will interfere with proper cardiac function and cause the system to overload or become completely dysfunctional to the point of cessation of contraction; ii) be increased by PNS inhibition, as the PNS is cardioinhibitory, inhibition will result in an increased response in cardiac function; iii) be blunted by SAC_{NS} inhibition, as SAC_{NS} drive V_m depolarization, inhibition will result in a decrease in the HR response to the point of acute cardiac dysfunction, through cessation of contraction.

4.2.Methods

4.2.1. Ethics statement

All experimental procedures were approved by the Dalhousie University Committee for Laboratory Animals and followed the guidelines of the Canadian Council on Animal Care. Details of experimental protocols have been reported following the Minimum Information about a Cardiac Electrophysiology Experiment (MICEE) reporting standard [382].

4.2.2. Zebrafish embryo preparation

Each group in this project consisted of 14 dpf zebrafish larvae, as the ICNS should be active at this developmental stage [363]. The experimental setup is described in the methods sections of Chapters 2 and 3. Pharmacological interrogation included independent use of streptomycin (SAC_{NS} inhibitor; 500 µM; Sigma Aldrich), atropine (postjunctional M_2R blocker; 10 µM; Sigma Aldrich), timolol (postjunctional β1 and β2-AR blocker; 100 µM; Sigma Aldrich), a combination of atropine and timolol (10 µM + 100 µM). Drug dose concentrations were determined based on previous literature using isolated adult zebrafish hearts as a starting point, followed by an experimental protocol using a range of concentrations (Figure 4.1).The incubation protocol for each of the pharmacological interventions included the addition of the respective drug to the E3 embryo solution for a 15-minute duration. After this incubation period, zebrafish larvae were placed in MS-222 for a five-minute period before the protocol was initiated. In the promotion of negative results, hexamethonium, a nondepolarizing nicotinic receptor blocker of nicotinic acetylcholine receptors on parasympathetic and sympathetic

preganglionic neurons was initially also tested, but not used after results were inconclusive. The transgenic zebrafish *tg(myl7:eGFP GCamp3 casper),* and *tg(myl7:Chimeric VSFP-butterfly)* were used to study Ca^{2+} and voltage dynamics in the heart in a spatiotemporal manner. GCaMP is a GECI. GECIs are designed to show the Ca^{2+} ion status of a tissue or medium and are either transfected into cell lines or via transgenic crosses. GCaMP is created from the M13 fragment of the chicken Mylk gene, containing the target sequence for calmodulin binding, fused to the N terminus of a circularly permutated form of EGFP. The C terminus of cpEGFP is fused to the rat calmodulin gene. When Ca^{2+} binds to calmodulin, the interaction between Ca^{2+}CaMM13 induces a conformational change in cpEGFP which causes a subsequent change in fluorescence intensity [345,467]. Chimeric VSFP-butterfly CY is a GEVI. The sensor consists of a voltage sensitive domain with transmembrane segments S1-S4, sandwiched between a fluorescence resonance energy transfer pair of the fluorescent proteins mCitrine and mCerulean. Movement of S4 upon membrane depolarization translates into a change of FRET efficiency [345].

The protocol for the GCaMP and butterfly zebrafish included a 45-minute incubation with s-amino blebbistatin (100 µM), and then placed in MS-222 for a 5-minute period before the flow-rest protocol was completed. Blebbistatin is used in optical mapping of cardiac preparations to minimize motion artifacts caused by heart contraction, by blocking the myosin heads from binding to actin [468].

4.1.1. Electronic flow control system

As discussed, protocol 3 (P3) was used for 14 dpf zebrafish under control
conditions and for each group in each pharmacological intervention group. In the
zebrafish expressing fluorescent reporters to collect Ca^{2+} and voltage dynamics protocol
two (P2) was used as the use of blebbistatin uncouples the actin-myosin contraction,
reducing the movement artifact and in the process partially compromising contraction
and thus SV is substantially reduced.

4.2.3. Measurements

Measurements of EDA, ESA, HR, SA, and CO_A were collected and calculated as
described in Chapter 2. Voltage and Ca^{2+} dynamics, including maximum upstroke
velocity, time to peak, as well as APD and CaTD at intervals of 30, 50 and 80 (APD_{80},
APD_{50}, APD_{30} and $CaTD_{80}$, $CaTD_{50}$, $CaTD_{30}$) were collected from the transgenic casper
butterfly and GCaMP3 zebrafish lines.

4.2.4. Statistical analysis

Data was analysed with GraphPad Prism (version 9.4.1). Differences between
baseline measurements (B1 and B2, B2 and B3) were compared using a Repeated
Measures One-Way ANOVA (paired). Equal variability of differences (sphericity) was
not assumed, instead the Geisser-Greenhouse correction was applied. Tukey's multiple
comparisons test was used for *post hoc* analysis. Paired t-tests were conducted to analyse
changes between baseline and stretch (B1 and S1, B2 and S2, B3 and S3) within groups.
To assess changes between the stretch phases (S1 and S2, S2 and S3) and to simplify the

comparison across groups, a Repeated Measures One-Way ANOVA was performed. Equal variability of differences (sphericity) was not assumed, instead the Geisser-Greenhouse correction was applied. Comparison of average change between groups was assessed using an Ordinary One-way ANOVA (unpaired). Tukey's multiple comparisons test was used for *post hoc* analysis.

4.3. Results

4.3.1. Effect of ANS blockers on cardiac function during increased hemodynamic load

Among each ANS drug interaction group, experiments resulted in a significant increase in EDA during each stretch phase compared with each corresponding baseline phase (B1 and S1, B2 and S2, B3 and S3) ($p < 0.001$) (Supplemental Figures 4.1 – 4.3). Additionally, in each experimental drug intervention group, the 90-second rest phase resulted in EDA returning to baseline or near-baseline, evidenced by no observed significant changes between B1 and B2 and between B2 and B3 ($p > 0.063$) (Supplemental Figures 4.1 - 4.3). Examining the EDA percentage change between each stretch and baseline (S1 and S2, S2 and S3) within each group, there was no significant change among any group ($p > 0.068$) (Figure 4.2). Thus, the three repeated stretches were combined as one average stretch to allow direct comparison between groups. There were no significant differences in the average EDA percent change between 14 dpf_P3 and each of the ANS block intervention groups ($p < 0.079$) (Figure 4.3).

Each group saw a significant increase in HR during each stretch phase compared with the corresponding baseline phase (B1 and S1, B2 and S2, B3 and S3) ($p < 0.001$). In

each group, HR response returned to baseline during the resting phase, evidenced by no observed significant difference between B1 and B2, and between B2 and B3 ($p > 0.075$). (Supplemental Figures 4.7 – 4.9). Comparison of the absolute change between each stretch phase showed no significant differences within each group (S1 and S2, S2 and S3) ($p < 0.293$) (Figure 4.8). Comparison of the average HR change showed no significant differences comparing the 14 dpf_P3 group with the atropine group, or atropine+timolol group ($p > 0.964$) (Figure 4.9). The use of atropine (postjunctional M_2R blocker) induced an average increase in baseline HR to 162 bpm from 134 bpm in 14 dpf_P3 zebrafish, which increased to 178 bpm and 153 bpm during stretch phases (Supplemental Figures 3.4, 4.7). Whereas the timolol group had a significantly larger increase in HR response compared to the 14 dpf_P3 group ($p < 0.001$) (Supplemental Figures 3.4, 4.9). This is due to the reduction in resting HR in the timolol group, that still saw a drastic increase in beats per minute, as the average increase in HR in the 14 dpf_P3 group 18.9 bpm, the timolol group saw an average increase of over 55 bpm in response to the increased hemodynamic load. The effect of timolol (postjunctional β-AR blocker) caused the baseline HR response to drop to an average rate of 68 bpm from 134 bpm in 14 dpf_P3, which increased to 123 bpm (153 bpm in 14 dpf_P3) during the stretch phases (Supplemental Figures 3.4, 4.8). Which demonstrates that the heart's ability to respond to the increase in hemodynamic load was able to override the effect of timolol acting on the suppression of the SNS and significantly increase HR.

Within each ANS pharmacological intervention group, there was a significant difference in SA comparing each baseline phase to each corresponding stretch phase (B1 and S1, B2 and S2, B3 and S3) ($p < 0.003$). In each of these groups, there were no

significant differences between baseline SA measurements, evidenced by no observed significant changes between baseline measurements (B1 and B2, B2 and B3) ($p > 0.151$). (Supplemental Figures 4.13 - 4.15). Comparison of the absolute change between each stretch phase resulted in no significant differences within each group (S1 and S2, S2 and S3) ($p < 0.277$) (Figure 4.14). The absolute change from each repeated stretch phase was combined as one average for direct comparison between groups. Among these results, there were no significant differences comparing 14 dpf_P3 with the ANS blocker group ($p > 0.074$) (Figure 4.15).

Regarding analysis of CO_A, there was a significant difference comparing each baseline phase to each corresponding stretch phase (B1 and S1, B2 and S2, B3 and S3) in each ANS pharmacological interrogation group ($p < 0.005$). In each of these groups, there were no significant differences between baseline CO_A measurements, evidenced by no observed significant changes between baseline measurements (B1 and B2, B2 and B3) ($p > 0.151$). (Supplemental Figures 4.17 - 4.19). Comparison of the absolute change between each stretch phase showed no significant differences within each group (S1 and S2, S2 and S3) ($p < 0.345$) (Figure 4.18). The absolute change from each repeated stretch phase was combined as one average for the direct comparison between groups. Among these results, there were no significant differences comparing 14 dpf_P3 with the atropine, or atropine+timolol groups ($p > 0.149$). There was a significant increase in the timolol group compared to the 14 dpf_P3 group ($p < 0.005$), which can be attributed to the substantial increase in HR response in this group (Figures 4.19).

4.3.2. Effect of SAC$_{NS}$ inhibitor on cardiac function during increased hemodynamic load

The streptomycin group showed a significant increase in EDA during each stretch phase compared with each corresponding baseline phase (B1 and S1, B2 and S2, B3 and S3) ($p < 0.001$). The 90-second rest phase resulted in EDA returning to baseline, evidenced by no observed significant changes between B1 and B2 and between B2 and B3 ($p > 0.063$) (Supplemental Figure 4.4). The EDA percentage change in each stretch phase (S1 and S2, S2 and S3) was not significantly different. ($p > 0.068$) (Figure 4.4). There were no significant differences between average percent change in EDA between 14 dpf_P3 and the streptomycin group, indicating that EDA was unaffected ($p < 0.079$) (Figure 4.5).

The effect of streptomycin eliminated the HR response in this group, as there were no significant differences between each stretch phase compared with each corresponding baseline phase (B1 and S1, B2 and S2, B3 and S3) ($p < 0.597$). In this group, there were no significant differences between baseline measurements (i.e., no delayed response) evidenced by no observed significant changes between B1 and B2 and between B2 and B3 ($p > 0.075$). (Supplemental Figure 4.10). Comparison of the absolute change between each stretch phase showed no significant differences within the streptomycin group (S1 and S2, S2 and S3) ($p < 0.293$) (Figure 4.10). Comparison of the streptomycin group to the 14 dpf_P3 group showed a significantly decreased HR response ($p < 0.002$) (Figure 4.11).

Looking into SA response in the streptomycin group, comparison of each baseline phase to each corresponding stretch phase resulted in a significant increase (B1 and S1,

B2 and S2, B3 and S3) (p < 0.003), and no significant differences between baseline SA measurements, evidenced by no observed significant changes between baseline measurements (B1 and B2, B2 and B3) (p > 0.151). (Supplemental Figure 4.16). Again, no significant differences within this group across stretches (S1 and S2, S2 and S3) (p < 0.277) (Figure 4.16). There was a significant increase in the streptomycin group compared to the 14 dpf_P3 group (p < 0.001) (Figure 4.17), mirroring the opposite decreased effect in HR response. These responses cancelled out when examining CO_A, resulting in no significant difference between the 14 dpf_P3 group and the streptomycin group. The significant elimination in HR response combined with the compensatory increase in SA acted to cancel out, resulting in a non-significant change in CO_A compared to 14 dpf_P3 (p > 0.149) (Figure 4.21). Notably, there was a significant difference comparing each baseline phase to each corresponding stretch phase (B1 and S1, B2 and S2, B3 and S3) in the streptomycin group (p < 0.005) and no observed significant changes between baseline measurements (B1 and B2, B2 and B3) (p > 0.151). (Supplemental Figure 4.20) or comparison of absolute change between stretches (p > 0.221) (Figure 4.20).

4.3.3. Effect of increased hemodynamic load on calcium and voltage dynamics

The ability to study Ca^{2+} and voltage dynamics is possible through the fluorescent functional reporters in the *tg (myl7:eGFP GCamp3 casper)*, and *tg (myl7:Chimeric VSFP-butterfly)* zebrafish lines.

Examining the EDA percentage change, there were no significant changes within each group (S1 and S2, S2 and S3) (p > 0.068) (Figure 4.6), however, there was a significant change between baseline measurements, as both the GCaMP and butterfly

groups did not return to baseline after each stretch, as EDA remained elevated ($p < 0.044$) (Supplemental Figures 4.5, 4.6). This is an effect of the compromised SV due to blebbistatin incubation as the atrial size remained in a stretched state, the percent change in EDA decreases during corresponding stretch phases as a result. Regarding HR response, there were no significant differences in absolute change within each group (Figure 4.12) or in either GCaMP or butterfly groups at baseline measurements compared to 14 dpf_P3, indicating that blebbistatin did not interfere with HR response ($p < 0.05$) (Figure 4.13).

The effect of hemodynamic load on voltage and Ca^{2+} dynamics resulted in no significant differences between baseline phases within either group (B1 and B2, B2 and B3) ($p > 0.135$) (Supplemental Figures 4.21 – 4.30). Examining the change from baseline to stretch, both groups displayed significant differences in time to peak ($p < 0.048$) (Supplemental Figures 4.23, 4.24). Hemodynamic load resulted in significant decreases in $CaTD_{80}$ ($p < 0.017$) (Supplemental Figure 4.25), $CaTD_{50}$ (in 2 of 3 stretches) ($p < 0.05$) (Supplemental Figure 4.27), and $CaTD_{30}$ in only one stretch ($p = 0.046$) (Supplemental Figure 4.29). There were no significant differences in maximum upstroke in either group ($p > 0.057$) (Supplemental Figures 4.22, 4.23), nor any significant changes in any APD interval measurements in the *butterfly* group (Supplemental Figures 4.26, 4.28, 4.30). Additionally, there were no significant differences in the absolute change between stretch phases among any of the Ca^{2+} and voltage dynamics in either group (S1 and S2, S2 and S3) ($p > 0.065$) (Figures 4.22 – 4.26).

4.4. Discussion

The primary aim of this chapter was to investigate the role of the ANS and the heart's intrinsic response to increased hemodynamic load on the system. An essential aspect of cardiac function and an overlying focus throughout this thesis is the heart's ability to adapt to meet varying hemodynamic demands. In a typical system, these adaptations to acute stretch of the SAN results in more rapid diastolic depolarisations, increasing HR [4], as well as increased myocardial contractility via reflexes acting through the heart's intrinsic nervous system [4,276]. The sympathetic and parasympathetic pathways of the ANS dually innervate the vertebrate heart [469]. Reflex output from autonomic centers in the CNS are carried by cardiac rami of the vagosympathetic nerve trunks to the ICNS, which represents a common pathway for neuronal control of cardiac function.

4.4.1. Intrinsic factors

Intrinsic factors that are discussed below highlight the balance of controlling CO, particularly when exposed to increases in hemodynamic load, between mechano-sensitive responses, changes in actin myosin interactions, and potentially neuronal activation of the ICNS.

4.4.1.1. Mechano-sensitive processes

The mechanically sensitive functionality of the heart allows an intrinsic level of modulation to occur on a beat-by-beat basis through direct feedback from the myocardium's mechanical state to its electrical activity, through MEC mechanisms [4–6]. The immediate responsiveness to increasing hemodynamic load is a necessary component

for the system to stay in balance for normal heart function [5,25]. Exposure to mechanical stimuli allows SAC to open and become activated rapidly (within tens of milliseconds) and lead to increased ion transients, which result in rapid alterations of cardiac electrical activity and more rapid membrane depolarisation [76,470].

Most of the known SAC-modulators are non-specific inhibitors, including streptomycin [69]. However, there is a minimal number of observed experiments in whole hearts and tissue and the results are contradictory. Cooper and Kohl (2005) reported that streptomycin was not effective in inhibition of positive chronotropy in pacemaker activity induced by stretch of whole SAN tissue, and have questioned its suitability for *in situ* experimentation involving acute block of mechanosensitive channels. Others have shown successful inhibition of SAC in single cells, tissue, and isolated hearts, for instance, decreasing the occurrence of arrhythmias induced by changes in ventricular wall-stress in isolated rat hearts [471] and inhibiting the shortening of repolarisation that is typically induced by stretch in Langendorff-perfused rabbit hearts [472]. More recently, streptomycin treatment in isolated rabbit hearts decreased VF induced by stretching [473] while also aiding in the prevention of stretch related AF incidence [474]. Finally, in hearts from hypertensive rats, streptomycin was successful in reducing stretch-induced ectopic beats by expanding the threshold for stretch-induced arrhythmias [475].

4.4.1.1.1. Bainbridge response

The Bainbridge response is a compensatory effect resulting in an increase in HR following an increase in cardiac preload, which is usually paired with a more rapid DD. This is thought to occur intrinsically, as the response time can be tracked to beat-to-beat adaptation. Primarily a normal physiological response, however, changes in the

myocardial mechanics with age and disease can have resounding negative consequences and may contribute to SAN dysfunction and cardiac rhythm disturbances.

This response was on full display in this study as the 14 dpf_P3 group as well as each ANS pharmacological group expressed a robust increase in HR in response to increasing hemodynamic load. Of note, the robust response from the timolol group helps to shed light on the fact despite the block of the SNS input the HR response was able to 'override' this effect and increase HR intrinsically. The use of streptomycin was used to study the effect of intrinsic activation in the heart during bouts of increased hemodynamic load. This effect appeared evident as both HR and SA were significantly altered in the streptomycin group compared to the 14 dpf_P3 group. Exposure to the same increase in hemodynamic load protocol induced a nonresponse in HR, while the SA was significantly increased, perhaps a compensatory or protective mechanism in an effort to keep the system in balance to account for the blunted HR response.

4.4.1.1.2. Membrane potential

Mechanical stretch has been shown to induce changes in the membrane potential, specifically the depolarization of the resting membrane potential. This has been shown across multiple species and experimental mediums, including isolated rabbit hearts [476], canine hearts [477,478], ventricles of artificially ventilated rats [479], single frog ventricular cells [480] and in situ canine hearts [481]. The diastolic depolarizations by uniaxial stretch of the single CM were also reported in isolated ventricular myocytes from mice [482], humans, and rats [442,483] and in isolated atrial myocytes from rats [443]. In almost all cases, the magnitude of the change in membrane potential was dependent on the magnitude of stretch.

With the use of the *tg(myl7:Chimeric VSFP-butterfly casper)* zebrafish the effect of hemodynamic load on voltage dynamics was investigated. However, in these incidences, there was no effect on any of the parameters investigated, apart from a significant increase in the time to peak from baseline to the stretch phase.

Van Opbergen and colleagues (2018) conducted a study using the VSFP-Butterfly zebrafish line exploring effects of isoproterenol to induce a slight increase in HR, and separate groups of propranolol and I_{kr} block E-4031 to decrease HR. They also showed increased APD, as well as disrupted atria-ventricular electrical conduction with the use of an $I_{Ca,L}$ blocker (nifedipine) in juvenile zebrafish. This helps to verify that the potential to impact the electrical activity is present in this zebrafish line, in this age group (14 dpf) with pharmaceutical interrogation, as well as with altered hemodynamic load as shown in the present study.

4.4.1.1.3. Calcium handling

Axial stretch of ventricular myocytes results in a rapid increase in frequency of Ca^{2+} spark activity through increased ryanodine receptor channel opening [484–488]. The increase in Ca^{2+} spark activity involves an associated mitochondrial Ca^{2+} release through the Na^+-Ca^{2+} exchanger [489], which has previously been shown to alter BR in isolated SAN cells by altering Ca^{2+} spark frequency [490]. In the van Opbergen et al., study (2018), discussed in the membrane potential section above, they also utilised a GCaMP zebrafish line (GCaMP6f) to study the effects of pharmacological intervention on Ca^{2+} dynamics. They found that isoproterenol increased diastolic Ca^{2+} levels and Ca^{2+} transient amplitudes, whereas propranolol caused a profound decrease in Ca^{2+} transient parameters

in embryonic fish and observed differences in atrial and ventricular Ca^{2+} recovery dynamics between 3 dpf and 14 dpf casper fish, but not in Ca^{2+} upstroke dynamics.

We found difference in Ca^{2+} dynamics in the 14 dpf_GC group with atrial dilation, demonstrating a decrease in CaTD and time to peak, further supporting the utility of this model to study *in vivo* cardiac studies with the aim of exploring how Ca^{2+} dynamics are affected in physiological and pathophysiological conditions.

4.4.1.2. Actin myosin interactions

The interaction of actin and myosin plays an important role in the generation of contractile force and the heart's mechanical activity. At the molecular level, the mechanism involves anatomically structural transition between actin and myosin's catalytic domain, and within myosin's light chain domain [491].

4.4.1.2.1. Frank-Starling law

The length-dependent increase in contractility of cardiac muscle is a direct result of a length-dependent increase in myofibrillar Ca^{2+} sensitivity, however; the specific molecular mechanisms have yet to be fully explained [83]. There is evidence demonstrating that the stretch-induced increases in myofilament Ca^{2+} sensitivity is regulated by cross-bridge interaction and can be explained by thin filament activation [83].

The heart's ability to eject a greater SV at greater EDA volumes is an essential property of the myocardium and has been show in the intact zebrafish heart as well as individual myocytes [291]. The force-pCa relationship in myofibrillar bundles are comparable in mice and zebrafish [492]. In regards to the experimental transference into other mammalian models, the zebrafish myofibrils and ventricular cells display a length-

dependent force generation that is similar in magnitude to the mammalian sarcomere [465,493].

In enzymatically isolated zebrafish ventricular myocytes, Dvornikov et al. (2014) used a novel approach that included two modes of contraction to characterise cardiac contractile mechanics, investigating input from extrinsic and intrinsic factors that regulate force production. The modes of contraction included (i) electrically stimulated twitches in mechanically loaded myocytes, and (ii) Ca^{2+}-activated contractions in chemically permeabilized cells.

It was found that, when there is no change in $[Ca^{2+}]_i$, twitch force increased in response to sarcomere stretch, with maximal Ca^{2+}-saturated force increasing with sarcomere length. Furthermore, contractility was shown to respond to increases in extracellular Ca^{2+} concentrations in a dose-dependent manner [465]. These findings provide support for the claims that the FSL and myofilament length-dependent activation are an intrinsic property and important modulator of contractile function of both mammalian and zebrafish CM.

In this current study, across each age group as well as each group involved in the pharmacological interrogation displayed significant increases in SA. Age, nor SNS and PNS block did not appear to have a detrimental effect on the FSL, as the SA remained elevated in response to increased hemodynamic load, demonstrated by no significant differences in baseline and stretch phase measurement between groups. In the incidence of the SAC_{NS} blocker, SM, there was a significantly greater increase in SA with atrial dilation, which is likely due to compensation for the blunted HR response.

4.4.2. Effect of blebbistatin on electrophysiology of the zebrafish heart

The incorporation of blebbistatin is essential for removing the movement artifact and disruption of the signal using genetically-expressed functional fluorescent proteins. In these instances, the heart maintained a partial mechanical contraction, however, this was primarily on the outer perimeter of the atrium, thus allowing for the capture of both Ca^{2+} and voltage signals in the interior aspect of the chamber.

For a study by Stoyek et al., [369], I measured AP characteristics by microelectrode from cells within the isolated adult zebrafish SAN, atrium, and ventricle with and without blebbistatin (Figure 4.22, Supplemental Figure 4.18). SAN cells had a less negative minimum Vm than atrial and ventricular cells, a lower dV/dt_{max}, lower AP amplitude and max Vm, and a shorter APD_{50} and APD_{80} (Figures 4.22 F–K). Atrial cells had a shorter APD_{50} and APD_{80} than ventricular cells (Figures 4.22 J,K). In the SAN, blebbistatin resulted in a reduction of the slope of DD (-39%, $p = 0.028$; Figure 4E), however the effect was not large enough to cause a reduction in HR ($p = 0.463$; although HR did become more variable, Figure 4D). In the atrium, blebbistatin resulted in an increase of APD_{50} and APD_{80} ($+13\%$ and $+9\%$, $p = 0.006$ and $p = 0.012$; Figures 4.22 J,K) and in the ventricle a decrease of APD_{80} (-9%, $p = 0.003$; Figure 4.22 K). No other AP parameters were affected by blebbistatin (Figures 4.22F–K).

Thus, the application of blebbistatin to the isolated zebrafish heart resulted in some changes in its electrophysiology. While HR and most measured AP characteristics were unaffected, blebbistatin caused a decrease in the slope of DD in the SAN, an increase in APD in the atrium, and a decrease of APD in the ventricle. Reports of the effects of blebbistatin on cardiac electrophysiology in mammals have been variable. In

isolated rabbit hearts, right ventricular and atrial tissue, and in rat ventricular myocytes, it was first shown that blebbistatin has no effect on SAN activity or on CM APD [494]. Since that time, studies using rabbit hearts have confirmed a lack of an effect of blebbistatin on APD, while later studies using rabbit and pig hearts have demonstrated an increase [495]. The increase in APD that we observed in the zebrafish atrium agrees with these later findings. It is unclear whether this increase in APD is due to non-specific interactions of blebbistatin with cardiac ion channels and/or transporters or is instead a secondary effect of the loss of contraction caused by excitation-contraction uncoupling, for instance due to a loss of mechano-electric coupling effects or to a decrease in sarcolemmal ATP-sensitive K^+ channel current caused by a decrease in metabolic demand [495]. The other electrophysiological findings in our study (decreased DD slope in the SAN and increased APD in the ventricle) suggest there may be direct effects of blebbistatin on ion channels and/or transporters, warranting further investigations to determine the specific mechanism(s) involved. It is worth noting that blebbistatin may also affect other aspects of cardiac electrophysiology (e.g., conduction, refractoriness, APD restitution, arrhythmia threshold), as well as Ca^{2+} handling (e.g., cytosolic Ca^{2+} levels, Ca^{2+} transient amplitude and duration), important for the function of the SAN and working myocardium [495], which deserve consideration in future studies using zebrafish.

4.4.3. Intracardiac nervous system

In the mammalian system, intracardiac neurons are dispersed in ganglia throughout both atria [496–500], yet the projection patterns of subpopulations of intracardiac neurons to specific targets remain unknown. This highlights yet another unique advantage of zebrafish heart, in that the majority of the neurons within the ICNS are located in the

basal regions of the sinoatrial valves and can be visualised using standard microscope techniques and are accessible for electrophysiological analyses [276,277].

In addition to intracardiac neurons, the presence of schwann cells, small intensely fluorescent cells, and endoneurial fibroblasts have also been identified to play a critical role in ICNS structure and functional capability to exert reflex control of cardiac function, even when isolated from central intrathoracic levels of the extracardiac ganglia and ICNS [277,337,501–503]. As this intricate level of research continues to develop, further exploration in this area will be critical in the advancement of our knowledge in this fascinating field and its importance in identifying target specific treatments for heart disease.

4.4.4. Extrinsic factors

Extrinsic factors that are highlighted below include neuronal responses and humoral responses. Although these responses are vast and intricate the focus will be on the balance of controlling CO, particularly when exposed to increases in hemodynamic load.

4.4.4.1. Neural response in zebrafish

The ANS of the zebrafish heart consists of axons entering the heart from the cardiac rami of the vagosympathetic nerve trunks which form terminals close to the putative pacemaker cells that express HCN4 in the SAN. As previously discussed in Chapter 1, HCN4 channel is the primary supplier in the DD phase in cardiac pacemaker cells [341–344,504]. Immunohistochemistry has shown juxta-pacemaker cell terminals containing both ACh and NE providing evidence for both cardio-inhibitory and

excitatory autonomic control of pacemaker rate through the PNS and SNS [276].

Furthermore, evidence supporting the functional presence of a HCN4 subpopulation has

been identified in the AV canal [274,276] indicating the zebrafish heart may contain a

secondary pacemaker region in this region not unlike that found in the mammalian heart,

which contains multiple levels of a cardiac conduction system [274,505–507].

In the present study, the incubation of pharmacological agents, atropine and/or

timolol, were used to promote selective or combined blockade of the autonomic cardiac

receptors during periods of baseline and increased hemodynamic load

The concentrations of atropine and timolol were combined in a group to

determine if the contribution was stronger from the SNS or PNS. The effect on HR

suggests that the PNS block played a more prominent role, as the average baseline HR in

this group was 139 bpm and increased to 155 bpm with increased hemodynamic load.

These levels of HR are very similar to the levels demonstrated in the 14 dpf_P3 group.

4.4.4.1.1. Baroreceptor Reflex

One of the factors regulating the short-term beat-to-beat stabilization of BP is the

baroreceptor reflex in which pressure sensors located primarily in the arterial walls of the

carotid artery sinus and aortic arch rapidly respond to fluctuations in BP [117,121,508].

Baroreceptor activity has been identified in both adult and larval zebrafish [509–512].

Additionally, in all teleosts studied to date, CO has been found to be modulated by

autonomic reflexes activated by changes to internal variables, such as arterial BP [513] and

alterations in environmental factors - including changes in oxygen and CO_2 levels [514,515].

The level of contribution from the baroreceptors in the present study is difficult to

assess in this experimental setting. Increasing BP causes an increase in baroreceptor

reflex signaling, acting to decrease sympathetic cardiac input and increase parasympathetic input. However, as there are other factors that are acting in opposition that were acting to restore balance, the overall increase in HR, SA, and CO_A was consistent across each 6 dpf and 14 dpf. In 2 dpf zebrafish embryo, as there was no response in HR, this may indicate that early development of the zebrafish does not include maturation of SACs.

4.5. Conclusion

Pharmacological interventions have indicated that effects on cardiac rhythm are mediated by both intrinsic (stretch) and extrinsic (ANS) mechanisms, while the effects on SA appear to be purely intrinsic. Studies looking at the effects of acute hemodynamic loading on membrane potential and intracellular Ca^{2+} dynamics using genetically-expressed functional fluorescent proteins have revealed effects on Ca^{2+} dynamics only. Furthermore, these findings have revealed factors involved in the regulation of cardiac function in response to acute changes in hemodynamic load during development, which include i) showing that the FSM is present during development, even at early stages, and is perhaps a compensatory protective mechanism during acute conditions of overload that otherwise may lead to complications related to CHD, or other long term morphological or electrical disturbances, ii) SAC_{NS} are not present in the initial stages of development and are necessary in the acute intrinsic response to increases in hemodynamic load. Further research in this area is essential for understanding control of cardiac activity in the developing heart and may help us better understand and manage disturbances that occur with CHD.

4.6. Figures

Figure 4.1 | A drug dose table to determine the required concentration. A range of drug concentrations (not all included) were used to determine the appropriate drug dosage for 14 dpf zebrafish larvae. Black = control, green/dark green = atropine (10µM/100µM), rose/red = timolol (10µM/100µM), cerulean = atropine + timolol combination (10µM/100µM), violet/purper = streptomycin (500µM/1000µM).
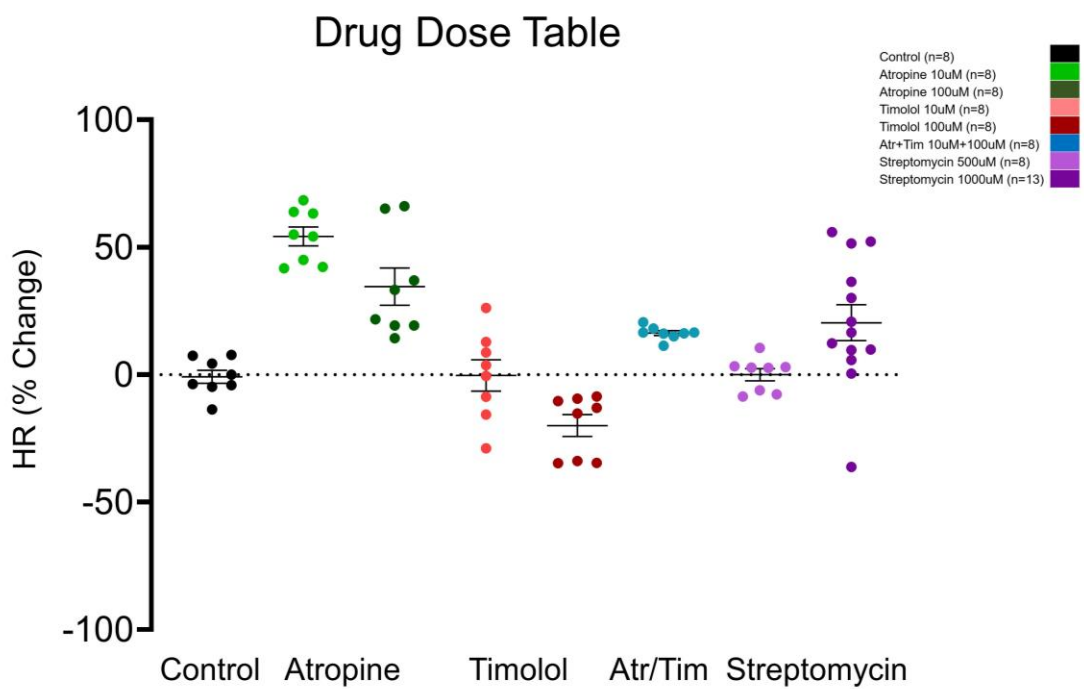
Figure 4.2 | Percent EDA change in 14 dpf zebrafish with and without ANS pharmacological interrogation. S1, S2, S3 represents each stretch across each group. 14 dpf_P3; blue, atropine; green, timolol; cerulean, atropine+timolol; violet. In each group there were no significant differences within each group, across each stretch phase (p < 0.05).
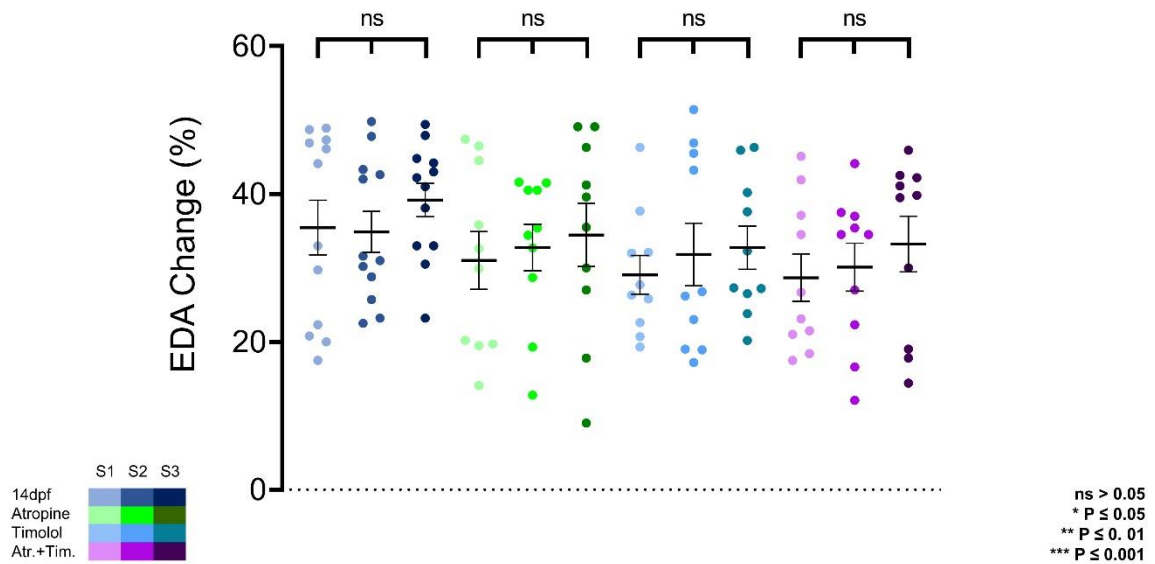
Figure 4.3 | Average percent EDA change in 14 dpf zebrafish with and without ANS pharmacological interrogation. There were no significant differences in EDA between 14 dpf groups. 14 dpf_P3; blue, atropine; green, timolol; cerulean, atropine+timolol; violet. In each group there were no significant differences within each group, across each stretch phase (p < 0.05).
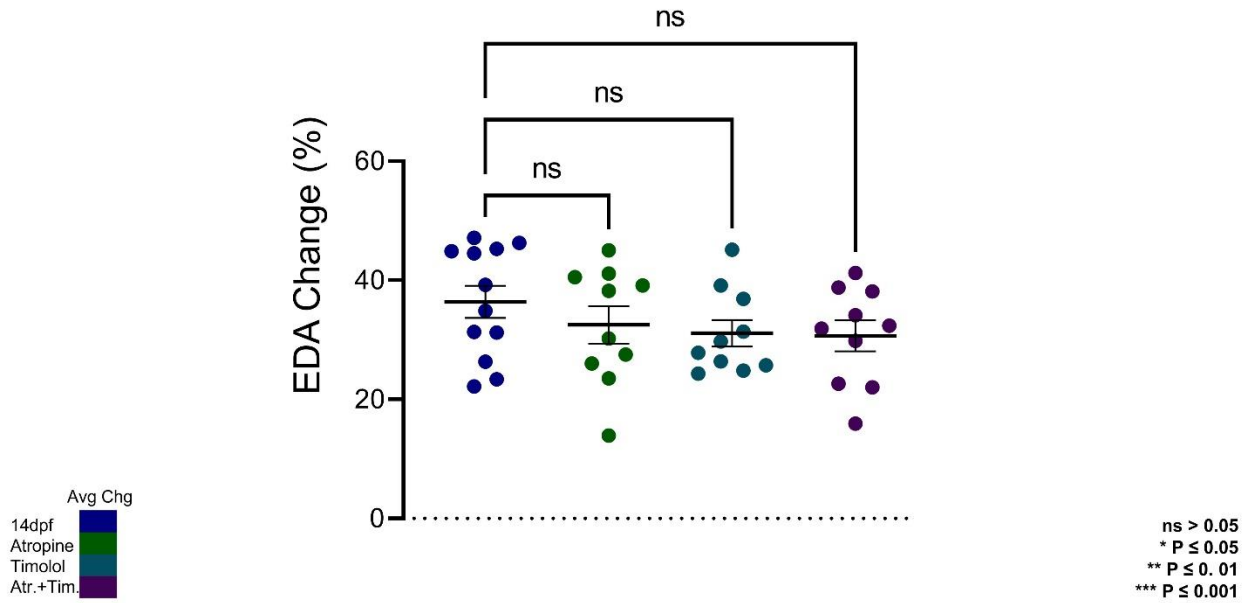

Average EDA Change with Increased Hemodynamic Load

Figure 4.4 | Percent EDA change in 14 dpf zebrafish with and without SAC_{NS} inhibition. S1, S2, S3 represents each stretch across each group. 14 dpf_P3; blue, 14 dpf_Streptomycin; teal. In each group there were no significant differences within each group, across each stretch phase (p < 0.05).
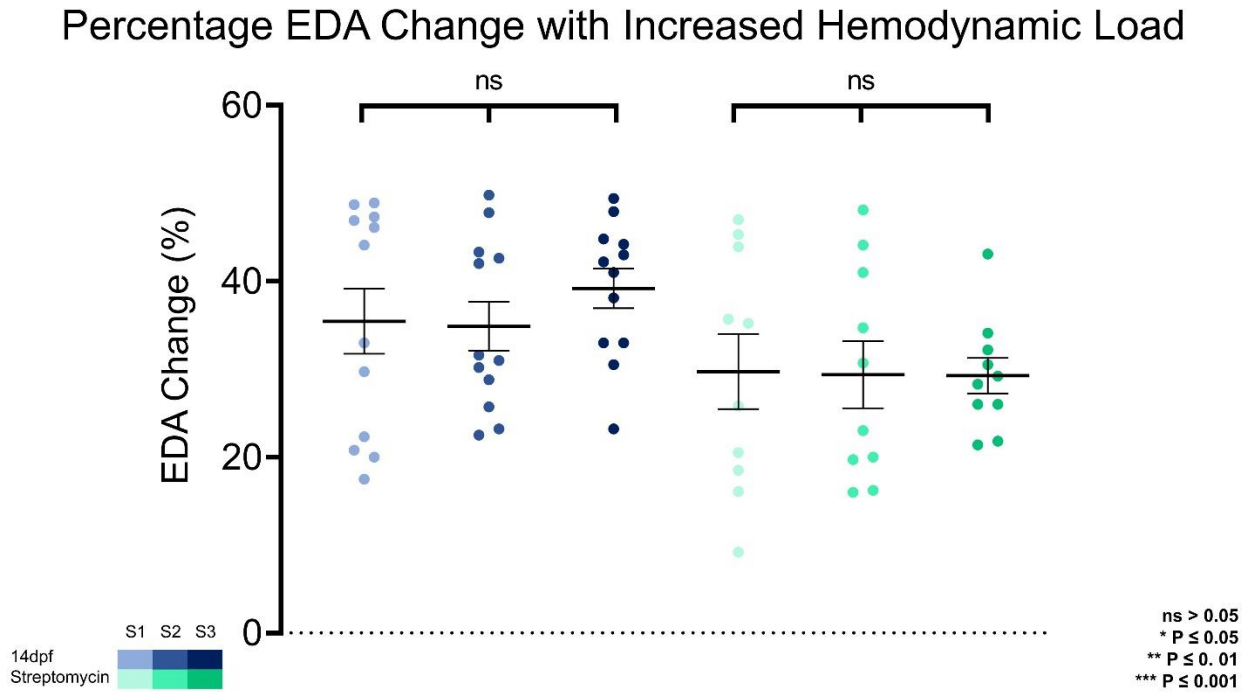

Percentage EDA Change with Increased Hemodynamic Load

Figure 4.5 | Average percent EDA change in 14 dpf zebrafish with and without SAC_{NS} inhibition. There were no significant differences between 14 dpf group exposed to P3. 14 dpf_P3; blue, 14 dpf_Streptomycin; teal. In each group there were no significant differences within each group, across each stretch phase (p < 0.05).
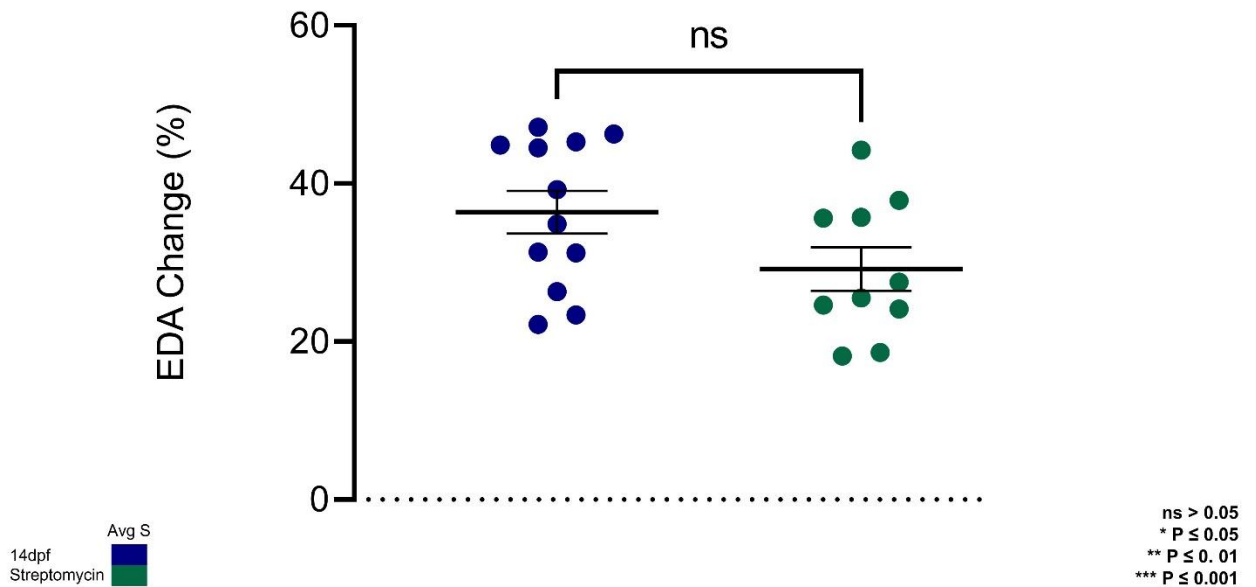

Average EDA Change with Increased Hemodynamic Load

Figure 4.6 | Percent EDA change in 14 dpf zebrafish in 14 dpf, GCaMP and butterfly zebrafish. S1, S2, S3 represents each stretch across each group. 14 dpf_P3; blue, 14 dpf_GCaMP; green, 14 dpf_butterfly; purple. In each group there were no significant differences within each group, across each stretch phase (p < 0.05).
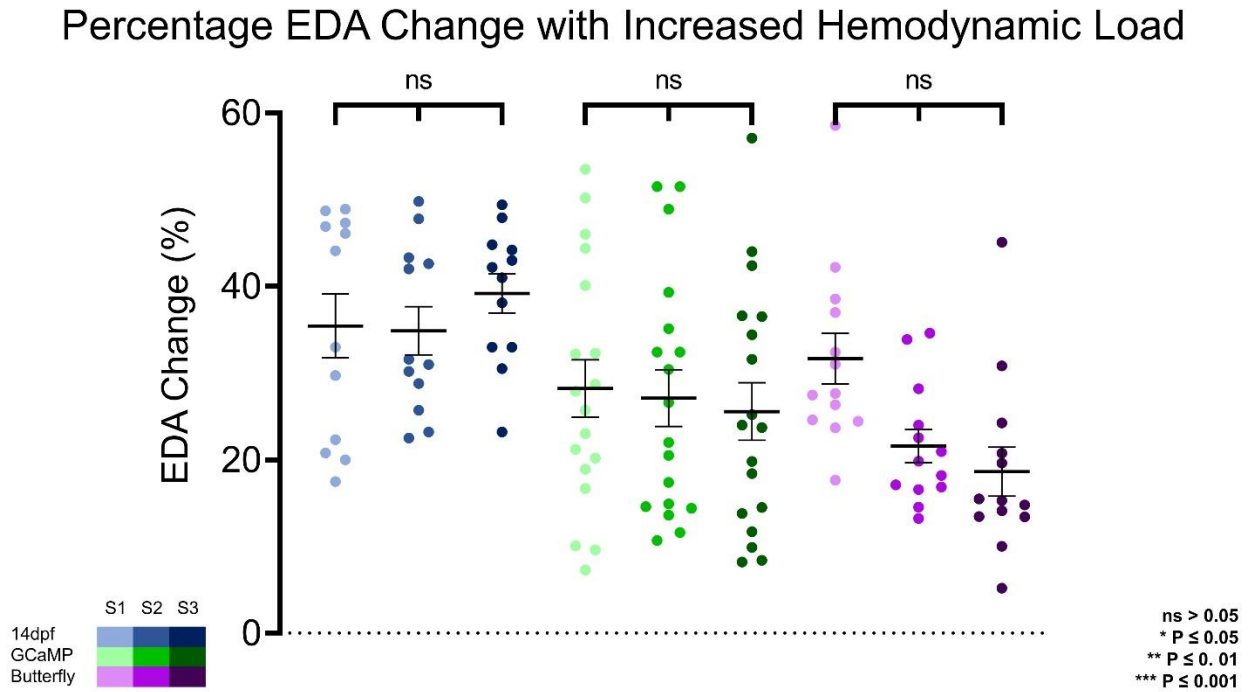

Percentage EDA Change with Increased Hemodynamic Load

Figure 4.7 | Average percent EDA change in 14 dpf_P3, GCaMP, and butterfly zebrafish. Exposure to blebbistatin resulted in a significant decrease in average EDA percent change in both groups compared to 14 dpf_P3. 14 dpf_P3; blue, 14 dpf_GCaMP; green, 14 dpf_butterfly; purple. In each group there were no significant differences within each group, across each stretch phase. (ns; non significant = p > 0.05, * = p ≤ 0.05. ** p = ≤ 0.01, *** = p ≤ 0.001).

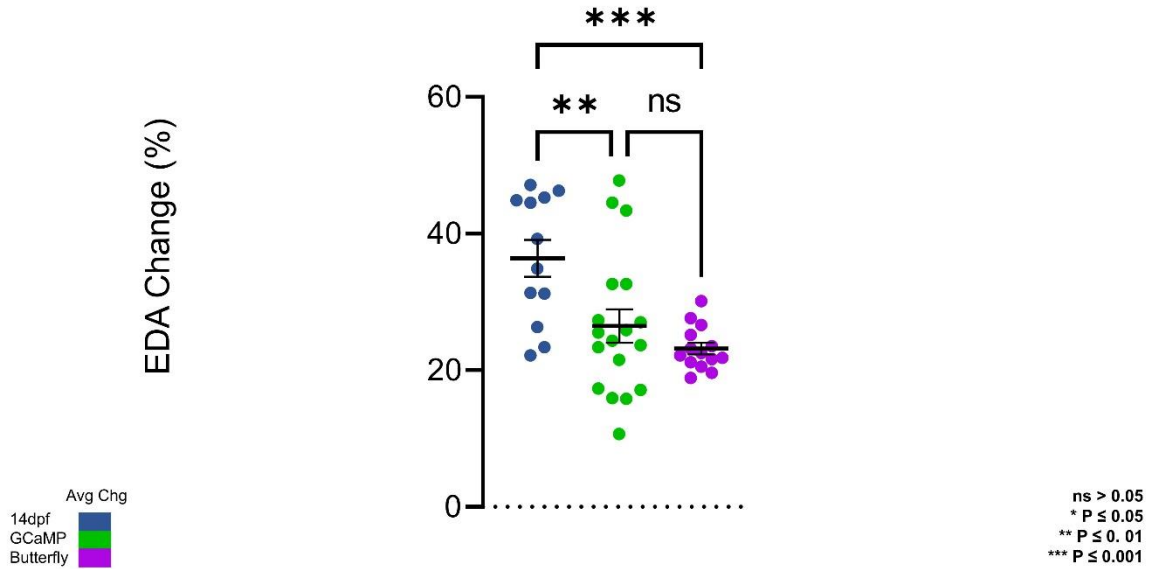Average EDA Change with Increased Hemodynamic Load

Figure 4.8 | Absolute HR change in 14 dpf zebrafish with and without ANS pharmacological interrogation. S1, S2, S3 represents each stretch across each group. 14 dpf_P3; blue, atropine; green, timolol; cerulean, atropine+timolol; violet. In each group there were no significant differences within each group, across each stretch phase (p < 0.05).
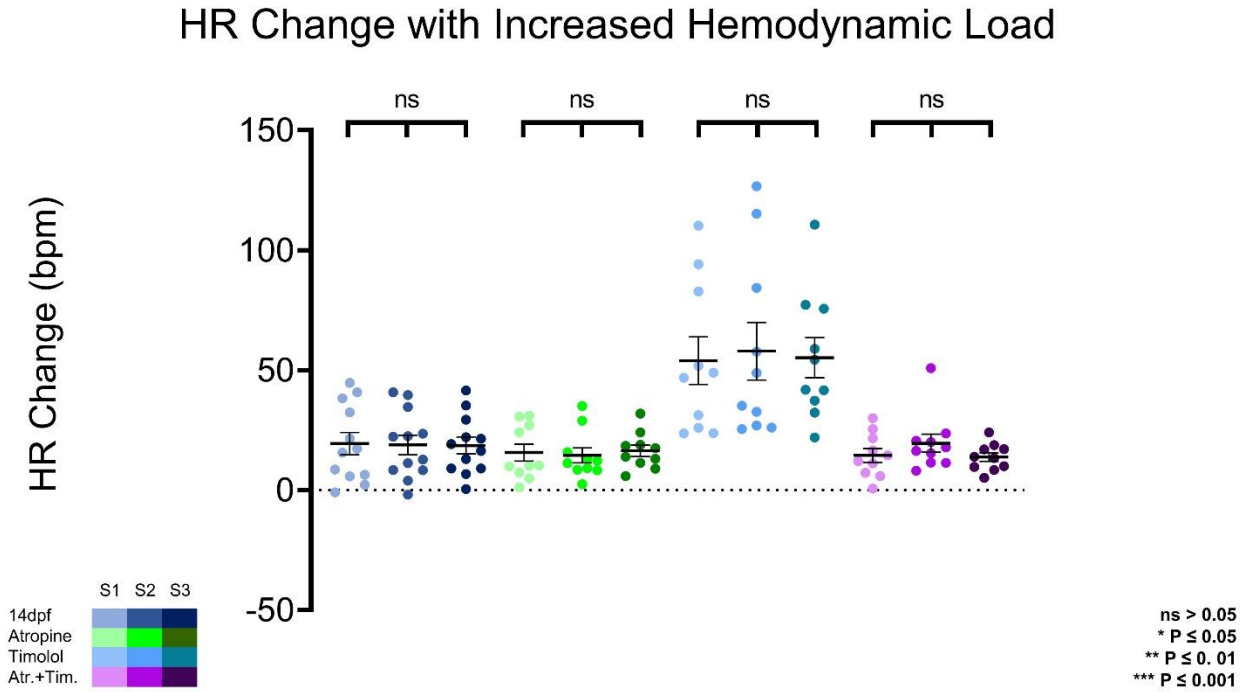
Figure 4.9 | Average absolute HR change in 14 dpf zebrafish with and without ANS interrogation. There was a significant increase in HR in the timolol group compared to 14 dpf_P3. There were no signicant differences between 14 dpf_P3 and atropine or atropine+timolol groups. 14 dpf_P3; blue, atropine; green, timolol; cerulean, atropine+timolol; violet. (ns; non significant = p > 0.05, * = p ≤ 0.05. ** p = ≤ 0.01, *** = p ≤ 0.001).

Figure 4.10 | Absolute HR change in 14 dpf zebrafish with and without SAC$_{NS}$ inhibition. S1, S2, S3 represents each stretch across each group. 14 dpf_P3; blue, 14 dpf_Streptomycin; teal. In each group there were no significant differences within each group, across each stretch phase (p < 0.05).

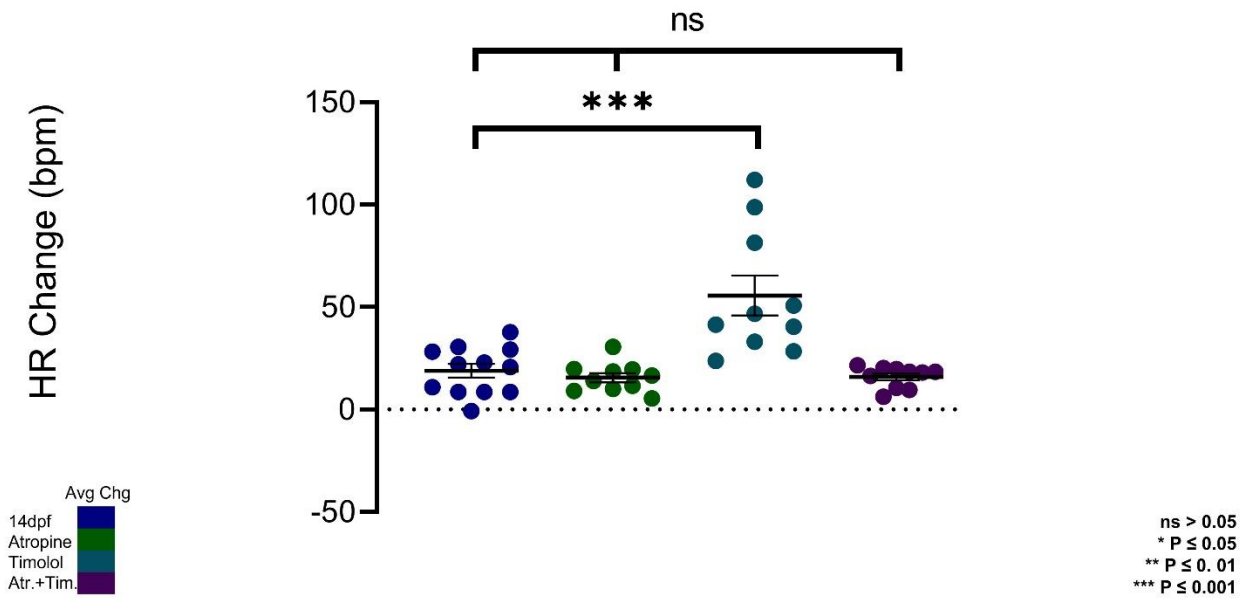HR Change with Increased Hemodynamic Load

Figure 4.11 | Average absolute HR change in 14 dpf zebrafish with and without SAC_NS inhibition. There was a significant decrease in HR in the streptomycin group compared to the 14 dpf_P3 group. 14 dpf_P3; blue, 14 dpf_Streptomycin; teal. (ns; non significant = p > 0.05, * = p ≤ 0.05. ** p = ≤ 0.01, *** = p ≤ 0.001).
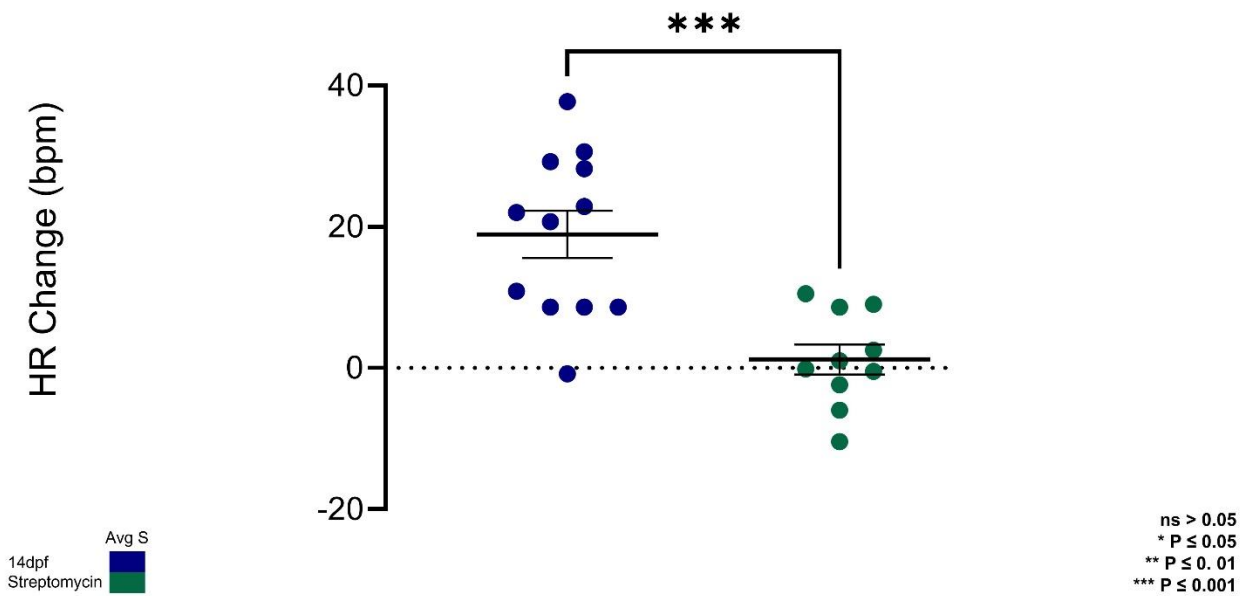
Figure 4.12 | Absolute HR change in 14 dpf_P3, GCaMP, and butterfly zebrafish.
S1, S2, S3 represents each stretch across each group. 14 dpf_P3; blue, 14 dpf_GCaMP;
green, 14 dpf_butterfly; purple. In each group there were no significant differences within
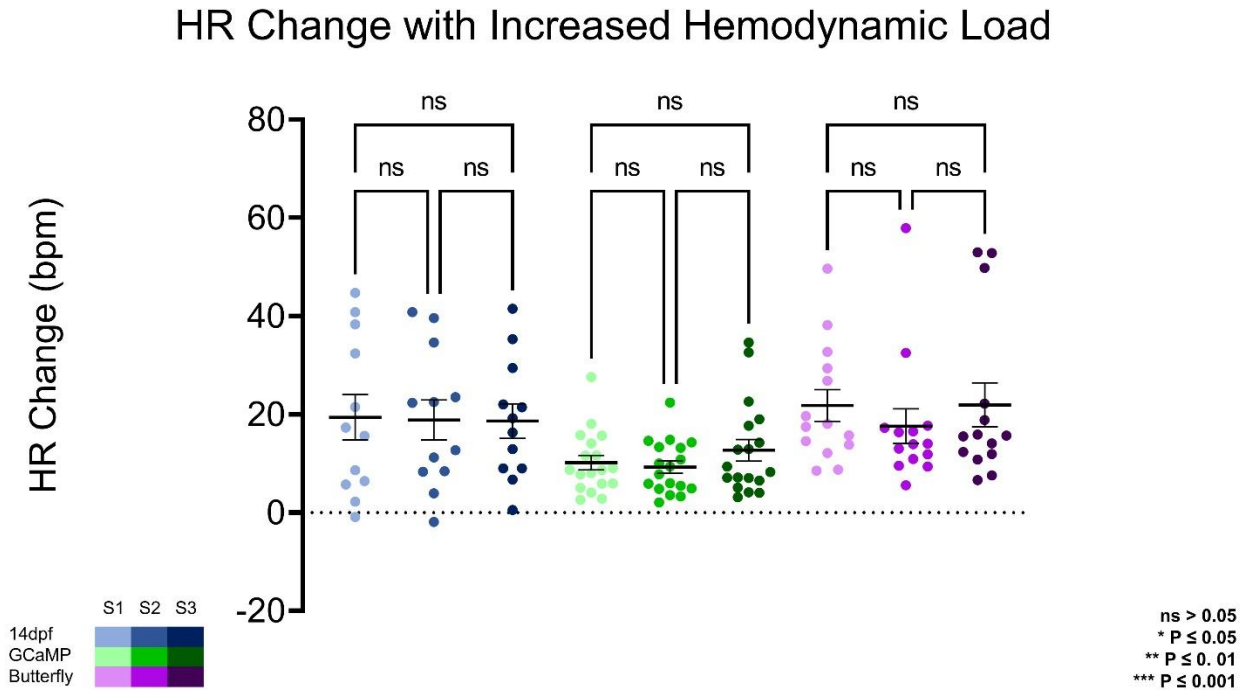each group, across each stretch phase (p < 0.05).

Figure 4.13 | Average absolute HR change in 14 dpf_P3, GCaMP, and butterfly zebrafish. There were no significant differences in HR between 14 dpf_P3 and the GCaMP or butterfly groups. 14 dpf_P3; blue, 14 dpf_GCaMP; green, 14 dpf_butterfly; purple. The effect of blebbistatin did not significantly alter the HR response in either group compared to the 14 dpf control group. (ns; non significant = p > 0.05, * = p ≤ 0.05. ** p = ≤ 0.01, *** = p ≤ 0.001).
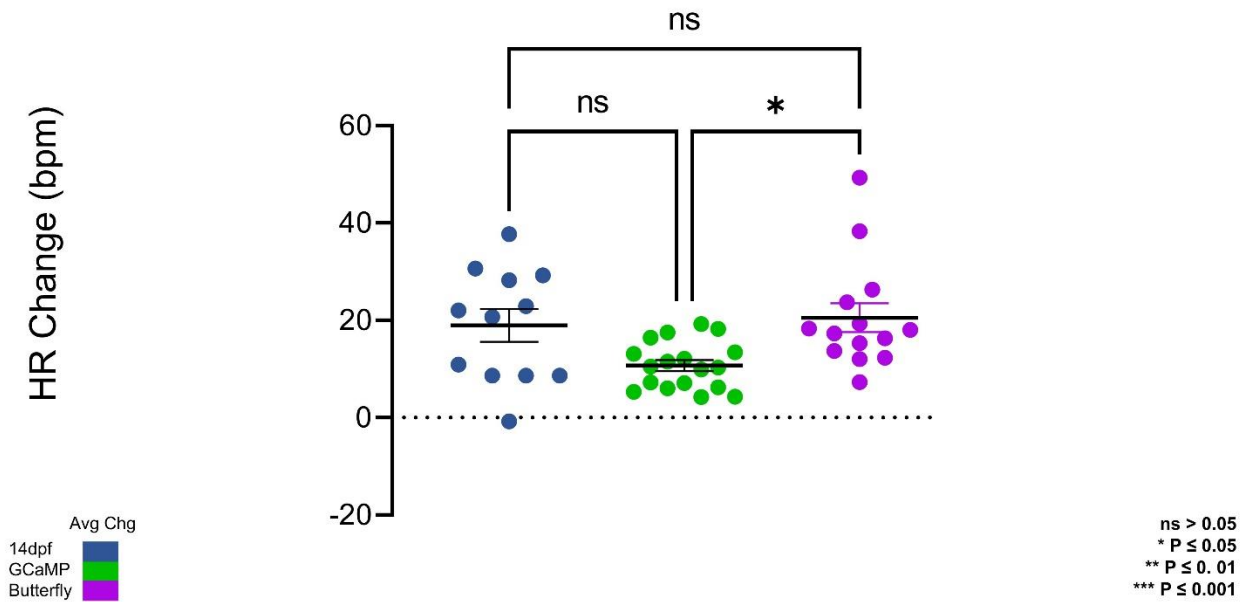

HR Change with Increased Hemodynamic Load

Figure 4.14 | Absolute SA change in 14 dpf zebrafish with and without ANS pharmacological interrogation. S1, S2, S3 represents each stretch across each group. 14 dpf_P3; blue, atropine; green, timolol; cerulean, atropine+timolol; violet. In each group there were no significant differences within each group, across each stretch phase (p < 0.05).

Figure 4.15 | Average absolute SA change in 14 dpf zebrafish with and without ANS pharmacological interrogation. There were no significant differences in SA between the 14 dpf_P3 compared to 14 dpf groups ANS block. 14 dpf_P3; blue, atropine; green, timolol; cerulean, atropine+timolol; violet. (p < 0.05).
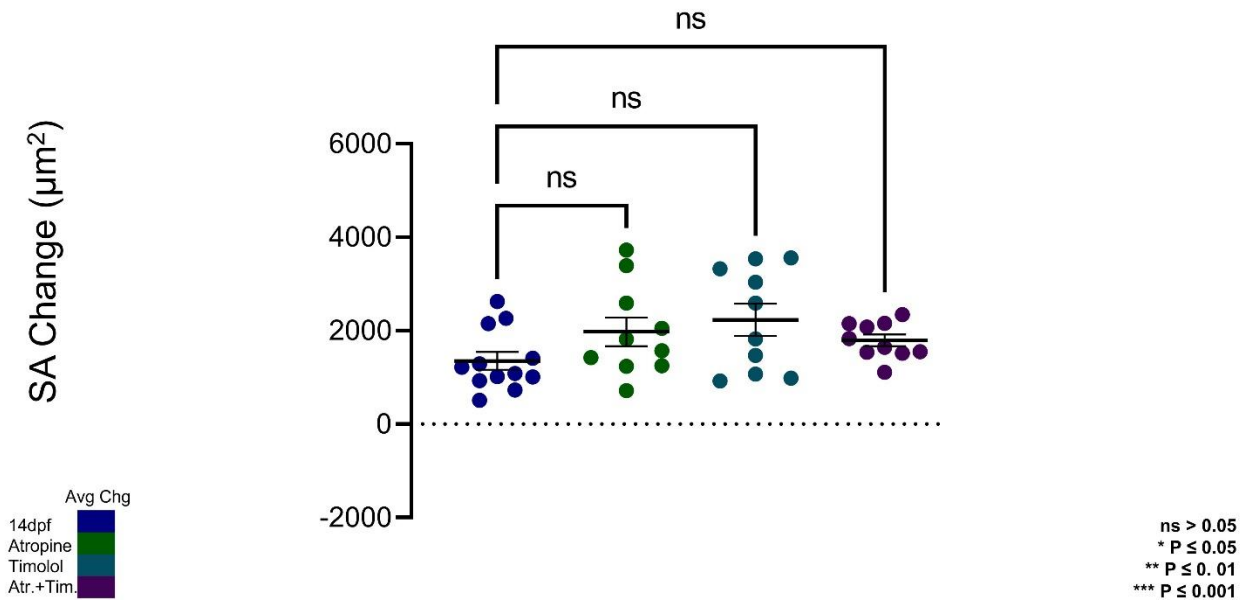
Figure 4.16 | Absolute SA change in 14 dpf zebrafish with and without SAC_{NS} inhibition. S1, S2, S3 represents each stretch across each group. 14 dpf_P3; blue, 14 dpf_Streptomycin; teal. In each group there were no significant differences within each group, across each stretch phase (p < 0.05).

Figure 4.17 | Average absolute SA change in 14 dpf zebrafish with and without SAC_NS inhibition. There was a significant increase in SA in the streptomycin group compared to 14 dpf_P3. 14 dpf_P3; blue, 14 dpf_Streptomycin; teal. (ns; non significant = p > 0.05, * = p ≤ 0.05. ** p = ≤ 0.01, *** = p ≤ 0.001).

Average SA Change with Increased Hemodynamic Load

Figure 4.18 | Absolute CO$_A$ change in 14 dpf zebrafish with and without ANS pharmacological interrogation. S1, S2, S3 represents each stretch across each group. 14 dpf_P3; blue, atropine; green, timolol; cerulean, atropine+timolol; violet. In each group there were no significant differences within each group, across each stretch phase (p < 0.05).
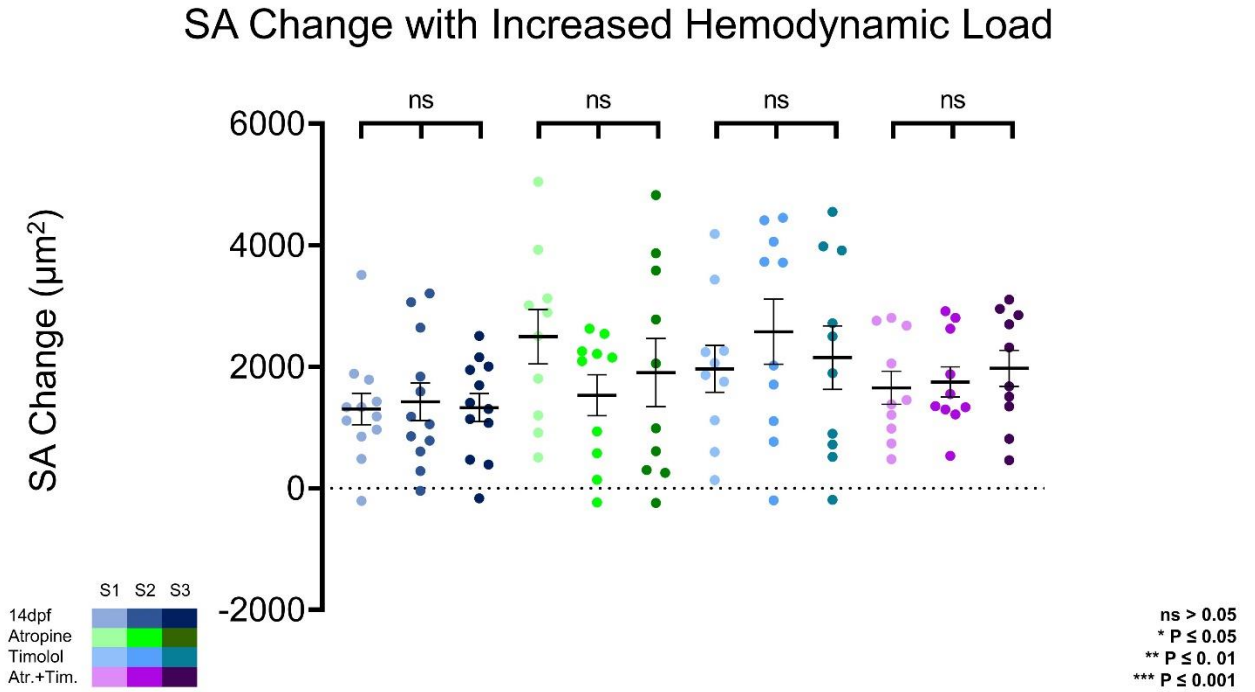

CO$_A$ Change with Increased Hemodynamic Load
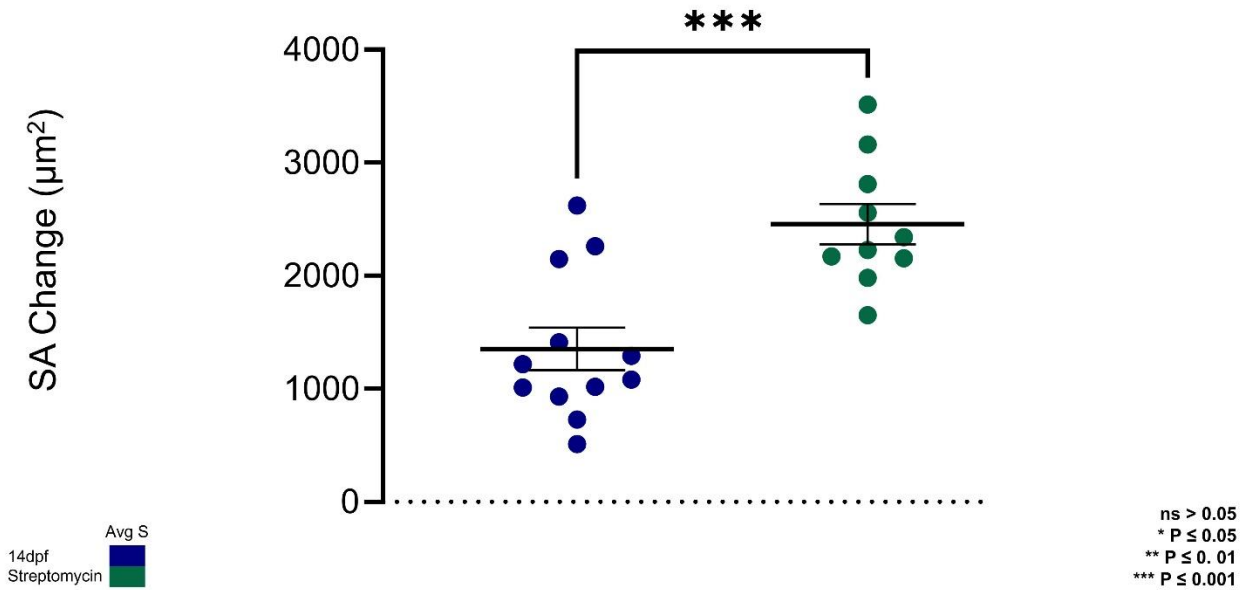
Figure 4.19 | Average absolute CO$_A$ change in 14 dpf zebrafish with and without ANS pharmacological interrogation. There was a significant increase in the timolol group compared to the 14 dpf control group. 14 dpf_P3; blue, atropine; green, timolol; cerulean, atropine+timolol; violet. (ns; non significant = p > 0.05, * = p $\leq$ 0.05. ** p = $\leq$ 0.01, *** = p $\leq$ 0.001).

Average CO$_A$ Change with Increased Hemodynamic Load
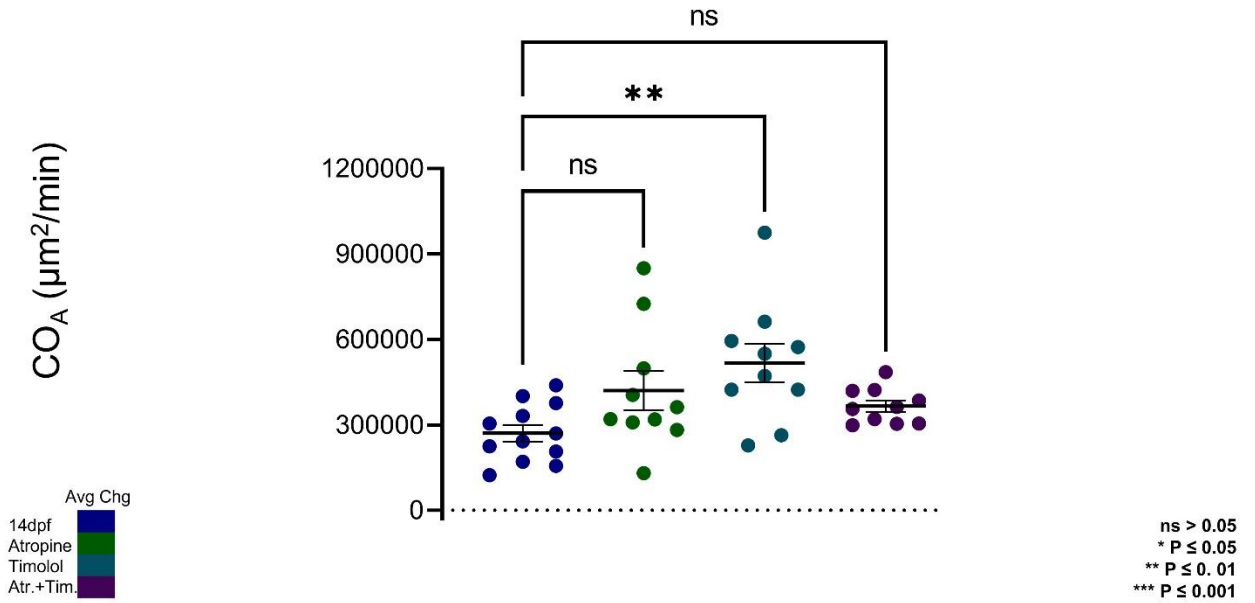
Figure 4.20 | Absolute CO$_A$ change in 14 dpf zebrafish with and with SAC$_{NS}$ inhibition. S1, S2, S3 represents each stretch across each group. 14 dpf_P3; blue, 14 dpf_Streptomycin; teal. In each group there were no significant differences within each group, across each stretch phase (p < 0.05).
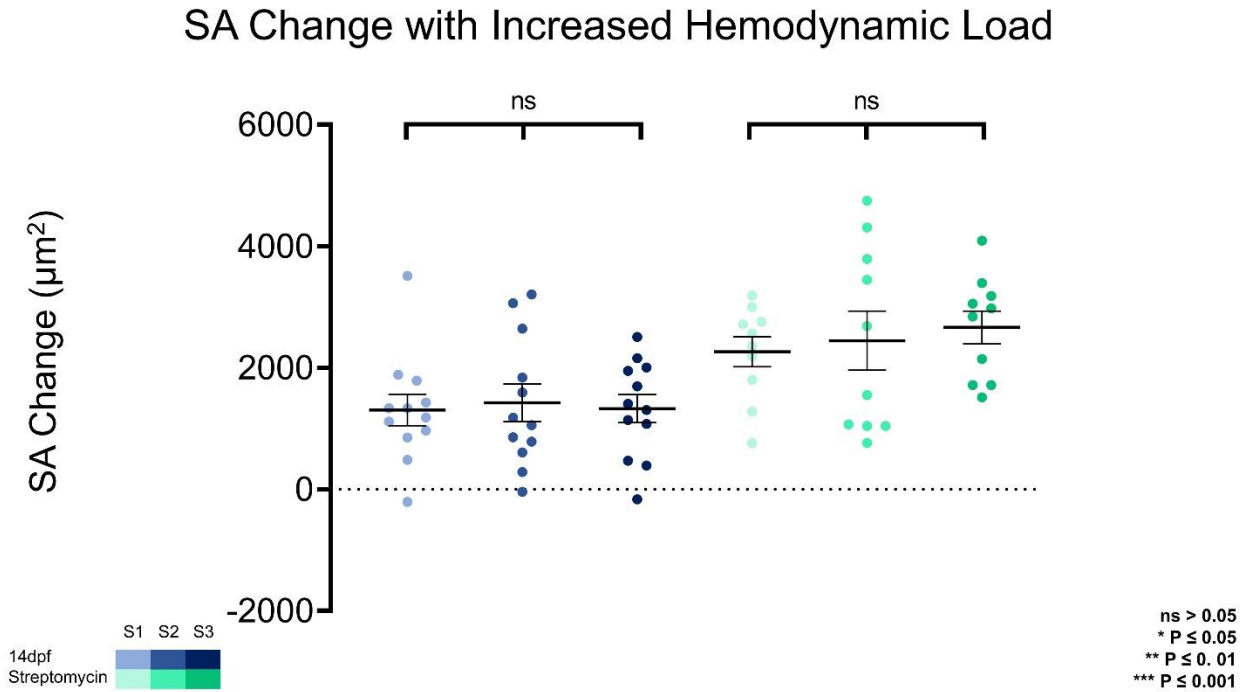

CO$_A$ Change with Increased Hemodynamic Load
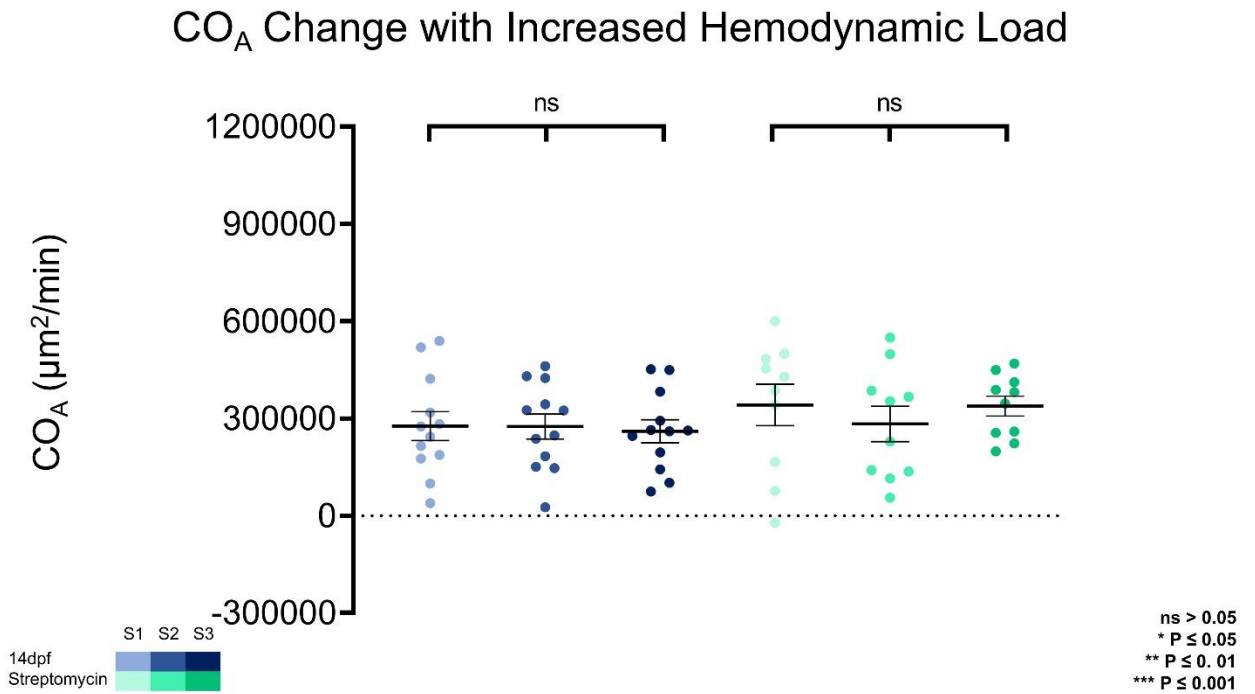
Figure 4.21 | Average absolute CO$_A$ change in 14 dpf zebrafish with and without SACNS inhibition. There was no significant difference between 14 dpf control group and the SAC$_{NS}$ block group. 14 dpf_P3; blue, 14 dpf_Streptomycin; teal. (p < 0.05).

Average CO$_A$ Change with Increased Hemodynamic Load

ns > 0.05
* P ≤ 0.05
** P ≤ 0. 01
*** P ≤ 0.001

Figure 4.22 | Absolute maximum upstroke change in 14 dpf zebrafish during increased hemodynamic load. S1, S2, S3 represents each stretch across each group. 14 dpf_P3; blue, 14 dpf_GCaMP; green, 14 dpf_butterfly; purple. In each group there were no significant differences within each group, across each stretch phase (p < 0.05).

Change in Upstroke with Increased Hemodynamic Load
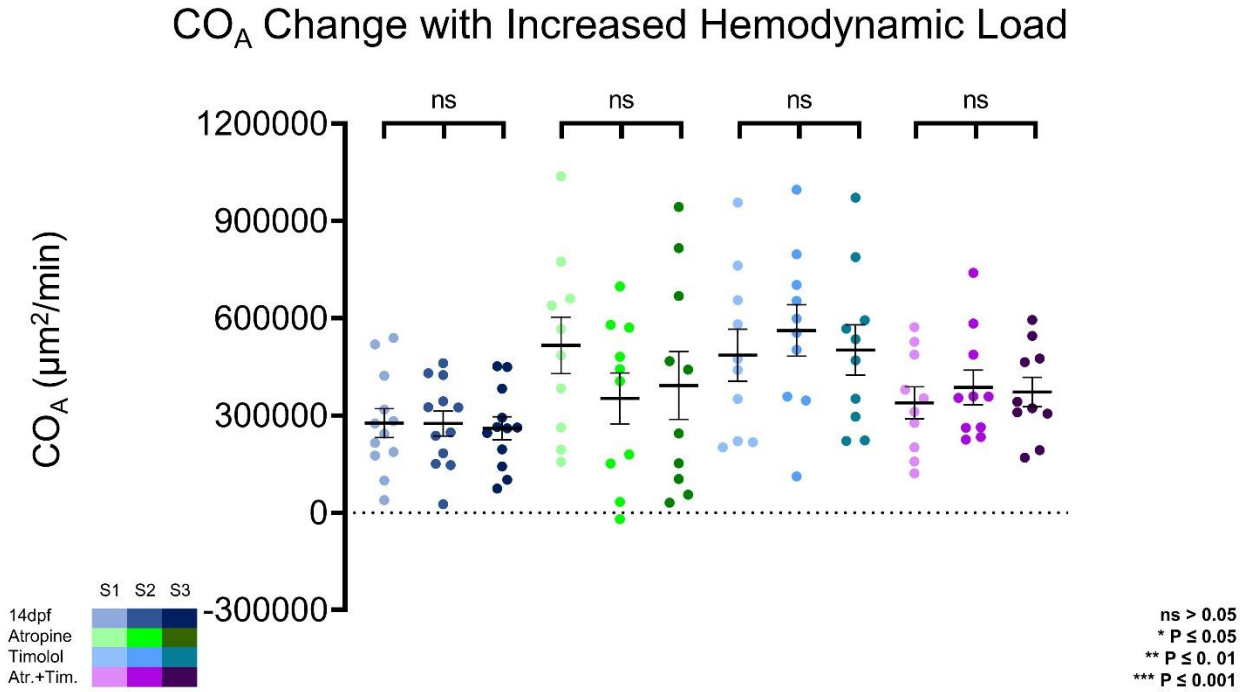
Figure 4.23 | Absolute change in time to peak in 14 dpf zebrafish during increased hemodynamic load. S1, S2, S3 represents each stretch across each group. 14 dpf_P3; blue, 14 dpf_GCaMP; green, 14 dpf_butterfly; purple. In each group there were no significant differences within each group, across each stretch phase (p < 0.05).

Change in Time to Peak with Increased Hemodynamic Load

Figure 4.24 | Absolute change in CaTD$_{80}$ and APD$_{80}$ in 14 dpf zebrafish during increased hemodynamic load. S1, S2, S3 represents each stretch across each group. 14 dpf_P3; blue, 14 dpf_GCaMP; green, 14 dpf_butterfly; purple. In each group there were no significant differences within each group, across each stretch phase (p < 0.05).

Change in CaTD$_{80}$ and APD$_{80}$ with Increased Hemodynamic Load

ns > 0.05
* P ≤ 0.05
** P ≤ 0.01
*** P ≤ 0.001

Figure 4.25 | Absolute change in CaTD$_{50}$ and APD$_{50}$ in 14 dpf zebrafish during increased hemodynamic load. S1, S2, S3 represents each stretch across each group. 14 dpf_P3; blue, 14 dpf_GCaMP; green, 14 dpf_butterfly; purple. In each group there were no significant differences within each group, across each stretch phase (p < 0.05).

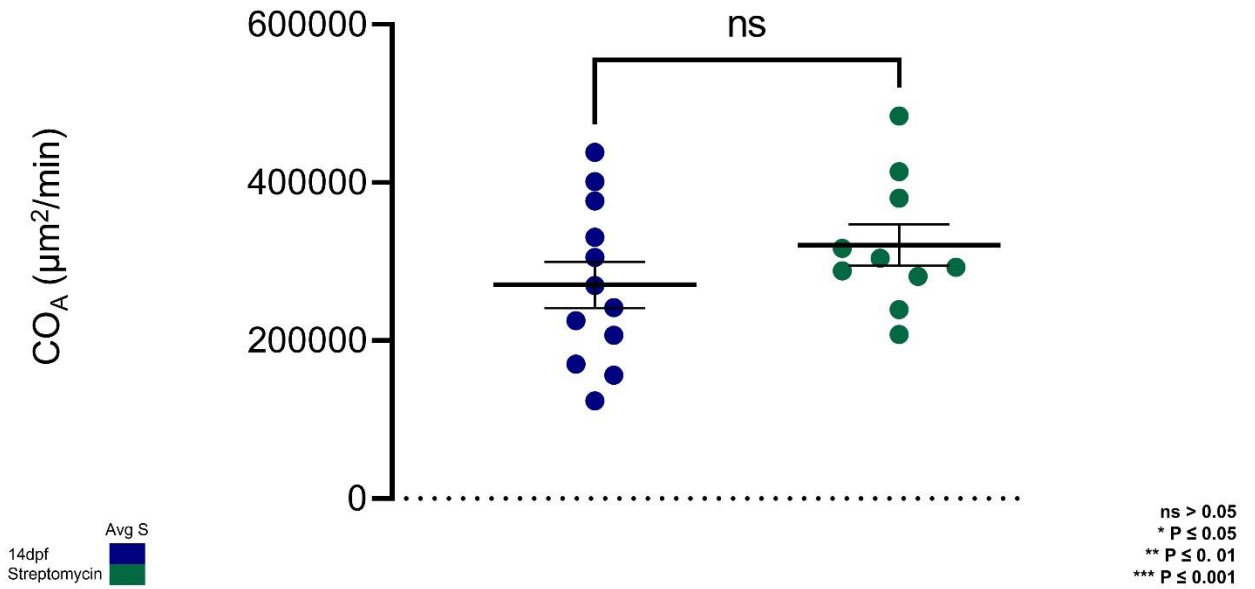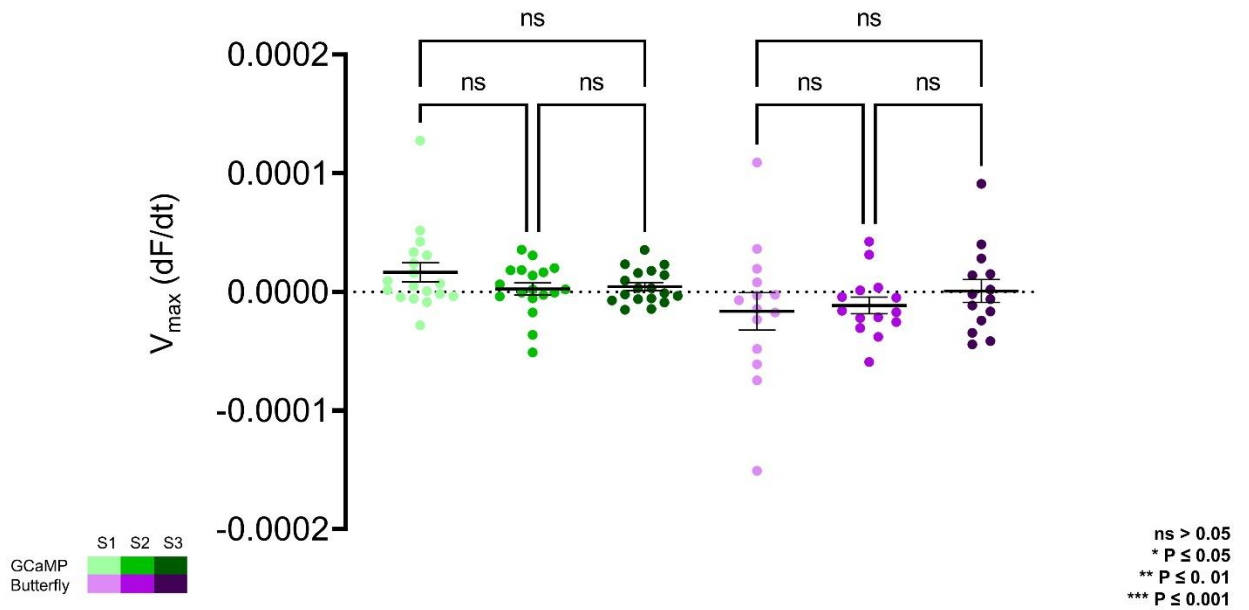Change in CaTD$_{50}$ and APD$_{50}$ with Increased Hemodynamic Load

Figure 4.26 | Absolute APD30/CaTD30 change in 14 dpf zebrafish during hemodynamic load. S1, S2, S3 represents each stretch across each group. 14 dpf_P3; blue, 14 dpf_GCaMP; green, 14 dpf_butterfly; purple. In each group there were no significant differences within each group, across each stretch phase (p < 0.05).

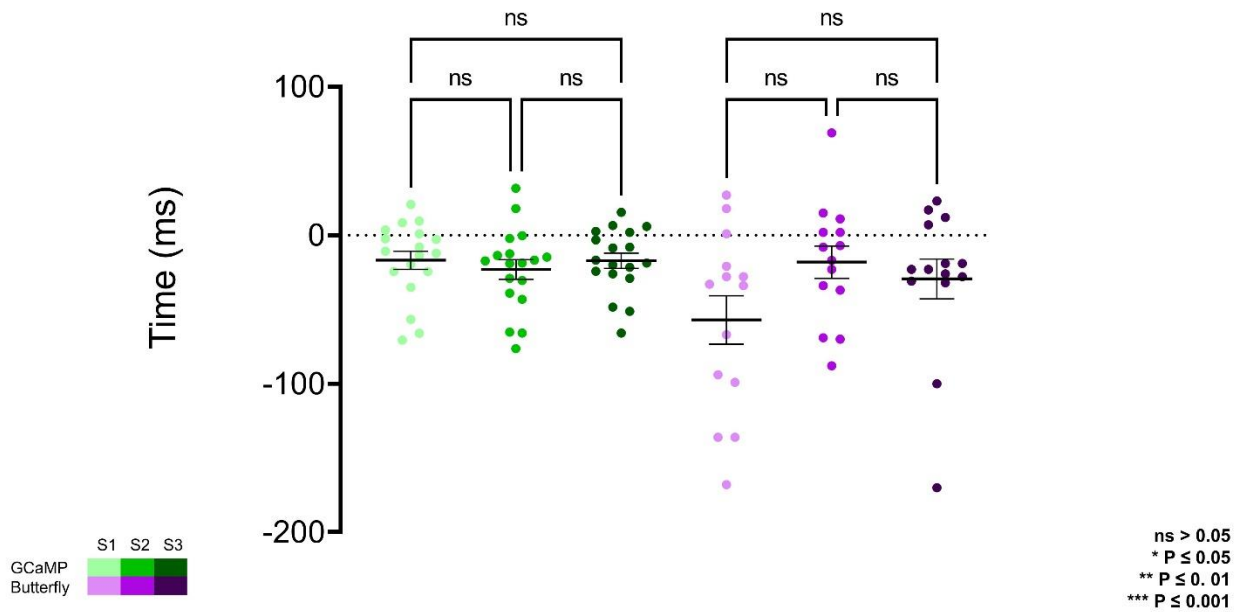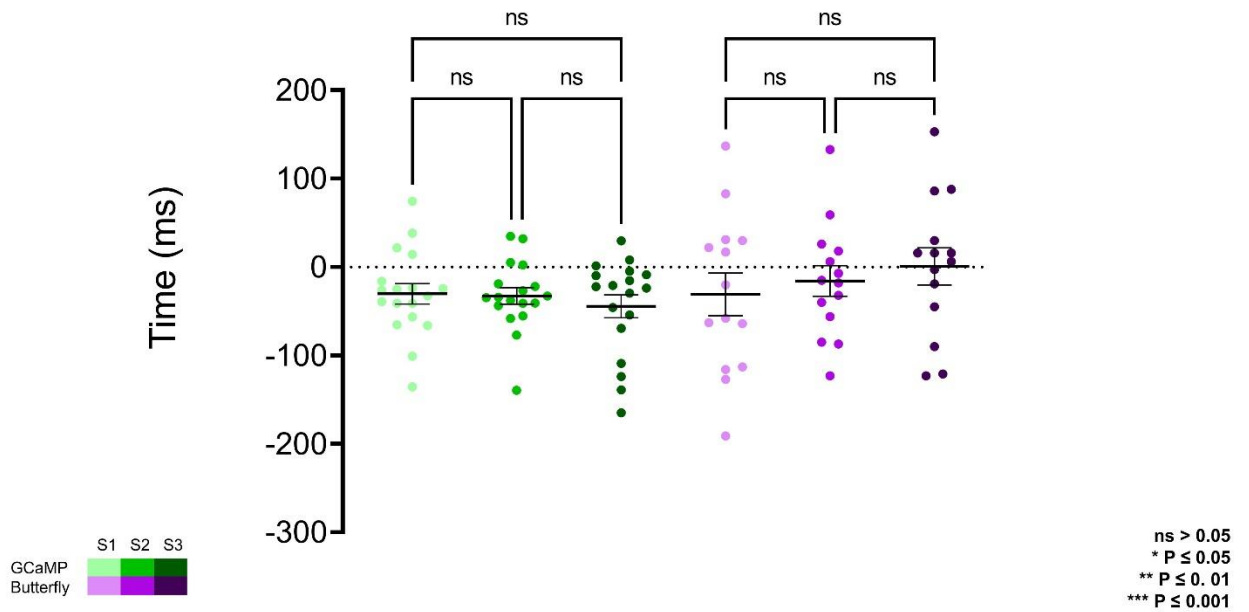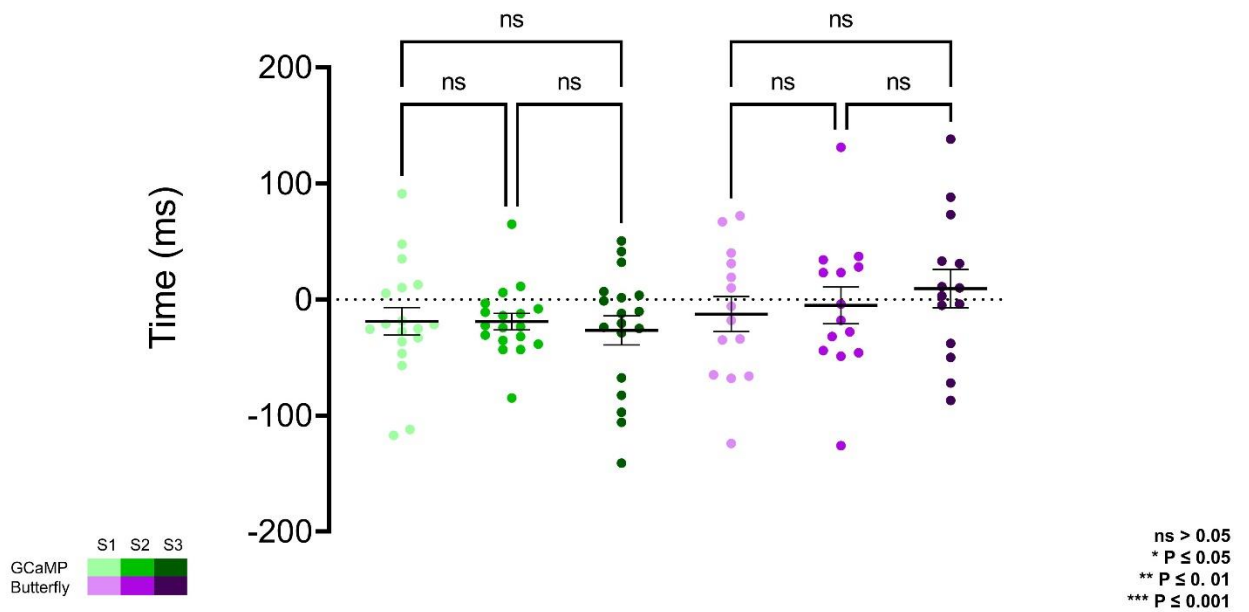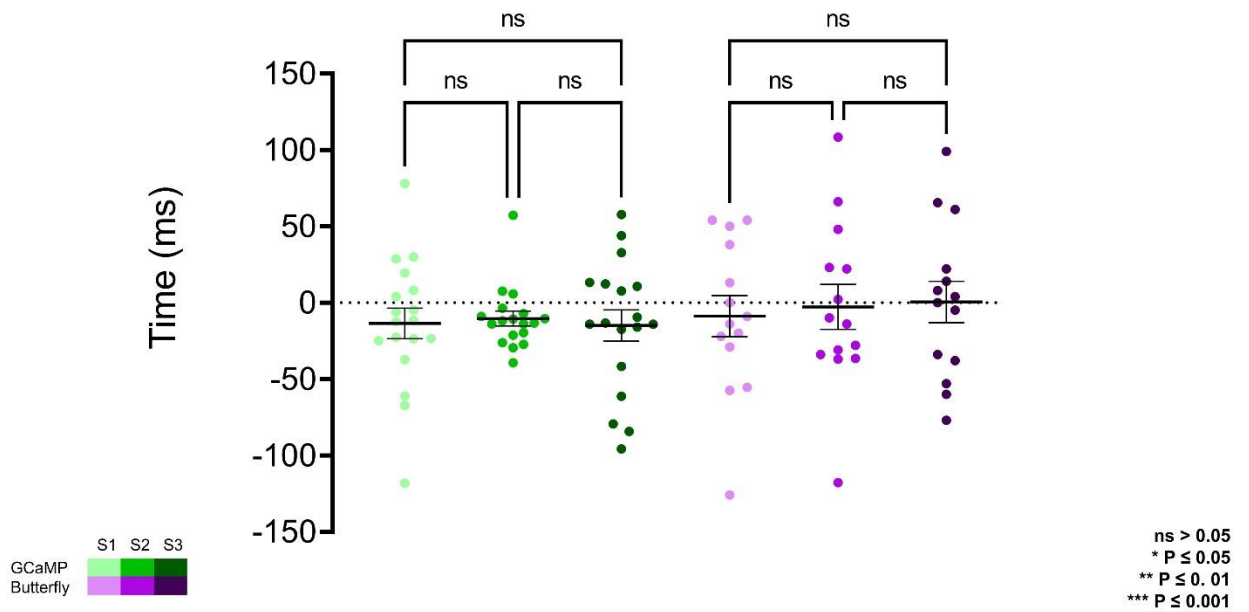Change in CaTD$_{30}$ and APD$_{30}$ with Increased Hemodynamic Load

ns > 0.05
* P ≤ 0.05
** P ≤ 0. 01
*** P ≤ 0.001

CHAPTER 5: OPTOGENETICS FOR THE MEASUREMENT AND MANIPULATION OF ZEBRAFISH CARDIAC ELECTROPHYSIOLOGY

5.1. Introduction

The study of optogenetics has only recently been adopted from the field of neuroscience and applied to the heart to optically control its function [274,516–518]. Optogenetics utilises light-sensitive proteins that are genetically expressed in cells of interest, allowing for non-invasive control and monitoring of biological function in a highly precise, spatiotemporal manner [519]. Cardiac research has utilised the potential of optical mapping allowing a better understanding of the mechanisms relating to cardiac electrical disturbances and foster development of new device technologies and high spatiotemporal understanding of cardiac behaviour in response to optical actuation that will optimistically integrate into clinical therapies.

5.1.1. Optogenetics in cardiac research

Optogenetics involves the measurement and manipulation of cellular activity using genetically encoded light-sensitive proteins [520,521]. Originally developed as a set of tools for neuroscience to activate or silence neuronal circuits and observe neuronal activity [522,523], optogenetic 'reporters' (for measurement of V_m [524–526]) or $[Ca^{2+}]_i$ [527–529]) and 'actuators' (for modulation of V_m [530–532]) have now been utilised in cardiac research for over a decade [519]. Cardiac optogenetics has had a wide-range of applications, including: (i) all-optical studies of cardiac electrophysiology and high-throughput drug screening; (ii) cell-specific measurement or control to investigate cardiac sub-populations (*e.g.*, myocytes, Purkinje cells, fibroblasts, neurons, and immune cells); (iii) manipulation of cardiac ion channels, G protein- coupled receptor signalling, and energetics; (iv)

control of AP morphology or excitation waves; and (v) cardiac pacing, cardioversion/defibrillation, or arrhythmia termination/ablation. Some of the pioneering studies that applied optogenetics to the heart were performed in zebrafish (*Danio rerio*) [519].

5.1.2. The use of zebrafish for optogenetic studies of the heart

The zebrafish has become an important integrative animal model for cardiac research, based on its particular advantages as an experimental tool (Table 5.1) [265,266]. The zebrafish offers a fully sequenced genome, which can be easily altered using standard genetic techniques at relatively low cost (in terms of time, effort, and money) [267,337], and almost every cardiac gene has a human ortholog with analogous function [269]. This high degree of genetic similarity has permitted researchers to recapitulate a variety of human cardiac diseases in the zebrafish [533], which can be studied in a high throughput manner [534]. Functionally, the zebrafish heart has comparable HR, AP morphologies, ion channels [270], and Ca^{2+}-handling proteins [273] to human. Furthermore, it has been shown that intrinsic [32] and extrinsic [277] cardiac regulatory pathways and mechanisms are similar to human, as is with the cardiac electrophysiology of the zebrafish [289].

Considering its use specifically for cardiac optogenetic studies, the zebrafish has a further advantage over other animal models, in that the entire zebrafish heart can be optically accessed *in vivo* in the transparent, externally developing embryo [345] or *in situ* in the relatively small, isolated adult heart [346], in a manner not possible in mammals. While other non-mammalian models may have a similar advantage (*e.g.*, *Drosophila melanogaster* [535] and *Xenopus laevis* [536]), they are limited in other ways. For instance, while *Drosophila* have been highly utilised for studies of cardiac genetics [535], it is an

invertebrate, and differences in the morphology of its heart – which is a tube –limits its applicability for functional studies [537]. The heart of *Xenopus*, on the other hand, is in some ways more anatomically similar to humans than zebrafish – for instance, it has a pulmonary circulation – but there is a limited genetic tool box for their transgenesis [538].

Ultimately, the similarities of zebrafish to human, and its particular experimental advantages, have resulted in it being a popular experimental model for optogenetic investigations, both for neuroscience (the brain and nervous system can also be optically accessed in the whole animal [539–541]) and for cardiovascular research (Table 5.1).

5.1.3. Studies utilising cardiac optogenetic reporters in zebrafish

The electrical activity of the heart has been optically monitored for decades, well before the emergence of modern optogenetics and the use of functional fluorescent proteins. In the 1970s, Salama and Morad published the first reports of the use of voltage sensitive fluorescent dyes to record cardiac APs [542,543]. Since that time, optical mapping of V_m and $[Ca^{2+}]_i$ in the whole heart or isolated tissue and cells has become a 'standard' technique in many research labs [544–546], including studies using zebrafish [547,548]. The use of optogenetic reporters (genetically encoded voltage and Ca^{2+} indicators, GEVIs and GECIs, respectively) have additional advantages as they allow for organ-, organelle-, and cell-specific measurements and for *in vitro* and *in vivo* longitudinal studies. There is now a wide array of GEVIs and GECIs available for use in the heart, with a range of excitation and emission spectra, light sensitivity and signal intensity, temporal dynamics, and other properties that dictate their specific use (Figure 5.1) [549–551].

5.1.3.1. Genetically encoded Ca^{2+} indicators (GECIs)

The first use of an optogenetic reporter in the heart was described in the early 2000s. This involved GCaMP2, which includes a circularly permutated EGFP within an M13/Calmodulin fusion protein that fluoresces when it binds Ca^{2+}, to record Ca^{2+} waves in the isolated mouse heart and in open chest animals [552]. This was followed by a study that used GCaMP2 to demonstrate successful engraftment and electrical coupling of embryonic CM with surrounding myocardium in the infarcted mouse heart [553]. Around the same time, the potential for using zebrafish to image intracellular Ca^{2+} in the intact animal was also being realised. The first published report involved the use of a transgenic zebrafish line with cardiac-specific expression of gGCaMP driven by the cardiac myosin light chain 2 (*cmlc2*) gene promoter (*Tg(cmlc2:gCaMP)^{s878}*). It was used to investigate a transgenic zebrafish model of inherited long QT syndrome in which a loss of I_{Kr} due to a mutation in the *s290* allele of the *kcnh2* gene (*kcnh2^{s290}*) results in mechanical ventricular asystole [554]. Using selective plane illumination microscopy (SPIM) and excitation-contraction uncoupling with a silent heart cardiac troponin (*tnnt2*) morpholino (to eliminate optical mapping motion artefact associated with contraction), Ca^{2+} transients were measured *in vivo* at various regions of the zebrafish atrium and ventricle in 2 dpf embryos. In wild-type *tnnt2* morpholino-injected zebrafish, repetitive fluorescent waves representing an increase in cytosolic Ca^{2+} during systole were visualised, spreading from the atrium through the AV junction and into the ventricle (Figure 5.2A). In contrast, in the *kcnh2^{s290}* homozygous mutants, Ca^{2+} waves were visible in the atrium but not in the ventricle (Figure 5.2A), implying impaired ventricular Ca^{2+} cycling.

The above investigation was followed by a study using the same zebrafish line to map Ca^{2+} waves across the whole heart in intact embryos at various ages to investigate the development of the vertebrate cardiac conduction system (Figure 5.2B) [385]. Four distinct stages of conduction development were identified, which corresponded to specific cellular and anatomical changes in the developing heart and were dependent on epigenetic mechanical factors such as hemodynamic flow and contraction. An *in vivo* optical mapping technique was then used as a phenotypic assay to perform a forward genetic screen, which identified 17 conduction-specific mutations (Fig 5.2B), thought to represent novel genetic regulators of the cardiac conduction system. A similar approach has been applied to other genes whose mutation is known to affect cardiac conduction, such as the Popeye domain containing (*Popdc*) gene family, with morpholino knock down of *popdc2* in 5-6 dpf_P2 embryos causing SAN conduction failure, irregular atrial and ventricular activity, and varying degrees of AV block [555].

More recently, zebrafish have been used to help in the assessment of novel GECIs for cardiac-specific applications, such as those with a ratiometric readout, which is useful for assessing absolute changes in Ca^{2+} and to help correct for the motion artefact that occurs with optical mapping in the beating heart. Four available ratiometric Förster resonance energy transfer (FRET)-based GECIs with varying Ca^{2+}-binding affinity (TN-XXL, Twitch-1, Twitch-2B, and Twitch-4) were transiently expressed in the hearts of zebrafish embryos (driven by the *cmlc2* promoter) and kinetic parameters of atrial and ventricular Ca^{2+} transients were measured at 3 dpf under various conditions. Ultimately, this revealed that Twitch-1 and Twitch-4 are the most promising for use in the heart,

based on their greater sensitivity, faster kinetics, and higher affinity for Ca^{2+} (Figure 5.3) [556].

5.1.3.2. Genetically encoded voltage indicators (GEVIs)

The development of effective GEVIs has been slower than GECIs, owing to difficulties in achieving sufficiently fast kinetics and avoiding electrophysiological interference. Recently, significant progress has been made, which includes their application for cardiac research. The first reported use of GEVIs in the heart was in fact in zebrafish [557], which utilised a FRET-based voltage-sensitive fluorescent protein (VSFP) called Mermaid [558]. The Mermaid construct consists of a green-emitting fluorescent donor (mUKG; *Umi-Kinoko* from *Sarcophyton*) and an orange-emitting fluorescent acceptor (mKOκ; *Kusabira* from *Fungia concinna)* fused to a voltage sensing phosphatase from *Ciona intestinalis* (Ci-VSP) with a transmembrane domain homologous to the S1-S4 segments of voltage-gated potassium (Kv) channels [559]. The Mermaid reporter was expressed specifically in the zebrafish heart under the *cmcl2* promotor (*Tg(cmlc2:Mermaid)*) and used for *in vivo* voltage mapping in 2-3 dpf embryos under normal conditions and after application of the histamine H1 receptor blocker astemizole (known to also block I_{Kr}). Measurements showed that astemizole disrupted the normal sequence of cardiac excitation, causing retrograde propagation from the AV boundary to the atrium (Figure 5.4A) [557].

Since that time, a variety of new GEVIs have been developed with improved sensitivity and kinetics. In a recent study using zebrafish [345], the novel GEVI chimeric VSFP-butterfly CY (cyan-yellow, mCitrine/mCerulean) [560] or the updated GECI GCaMP6f [561] were expressed in the heart of pigment-deficient, optically-transparent

casper mutant zebrafish [383], with the myosin light chain 7 (*myl7*) promotor

(*Tg(myl7:chimeric VSFP-butterfly)*) and *Tg(myl7:Gal4FF; UAS:GCaMP6f)*). The hearts

of 3 dpf and 14 dpf zebrafish were imaged after administration of drugs targeting the

SNS or various cardiac ion channels to assess effects on electrical activation, AP

morphology, and $[Ca^{2+}]_i$ dynamics [345] (Figure 5.4B). It was shown that: (i) β-AR

stimulation (with isoproterenol) or blockade (with propranolol) increased or decreased

diastolic Ca^{2+} levels and Ca^{2+} transient amplitudes, respectively; (ii) I_{Kr} block (with E-

4031) increased APD; (iii) $I_{Ca,L}$ block (with nifedipine) prevented Ca^{2+} transients,

increased ventricular APD, and disrupted AV conduction; and (iv) differences exist in

atrial and ventricular Ca^{2+} recovery dynamics between 3 and 14 dpf zebrafish (but not in

the Ca^{2+} upstroke).

5.1.3.3. Combined voltage-Ca^{2+} imaging

Functional fluorescent dyes can be combined for simultaneous mapping of

voltage and Ca^{2+} in the whole heart [544]. There is similar interest in combining GEVIs and

GECIs for dual voltage-Ca^{2+} imaging, however this is generally prevented by spectral

overlap of the relevant fluorescent proteins. The first successful study using a GEVI-

GECI construct in the heart was performed in the zebrafish, using a genetically encoded

dual-function voltage-Ca^{2+} reporter ('CaViar', created by fusing the GEVI Arch(D95N)

with the GECI GCaMP5) under control of the heart-specific *cmlc2* promoter

(*Tg(cmlc2:Arch(D95N)-GCaMP5G)*) [386]. Hearts of 1.5-4.5 dpf embryos were imaged

during application of the $I_{Ca,L}$ blocker nifedipine or Na^+ channel blocker quinidine, which

showed that early in development the zebrafish cardiac AP is initiated by Ca^{2+}, but by 4

dpf the ventricular AP becomes driven by Na^+, while the atrial AP remains Ca^{2+} dependent (Figure 5.4C).

5.1.4. Studies utilising cardiac optogenetic actuators in zebrafish

Optogenetic actuators are light-activated proteins that generate a transmembrane ion flux. The discovery and cloning of the ChR2 from the green alga *Chlamydomonas reinhardtii* in 2003 [531] has led to the development of an extensive toolkit that includes depolarising (excitatory) and hyperpolarising (inhibitory) opsins, which are activated across a wide spectrum of wavelengths, and may be used for manipulation of cardiac membrane potential (Figure 5.1) [519,562,563]. As for the cardiac application of GEVIs and GECIs, one of the first reports of the use of optogenetic actuators in the heart was in zebrafish [274]. This involved the use of both ChR2 (*Tg(E1b:Gal4^{s1101t}; UAS:ChR2(H134R)-eYFP^{s1990t})*) and the Cl⁻-specific ion channel halorhodopsin from *Natronomonas pharaonis* [564] (*Tg(E1b:Gal4-VP16^{s1101t}; UAS:NpHR-mCherry^{s1989t})*), to locate and control cardiac pacemaker cells in intact 1-5 dpf zebrafish embryos. In NpHR-expressing zebrafish, maps were generated at each dpf by sequentially illuminating small, overlapping regions of the heart, and measuring the HR response, or the incidence of cardiac arrest or arrhythmia (Figure 5.5A). It was found that: (i) at 1 dpf, the heart stopped beating when a region at the venous pole was illuminated, indicating the location of the pacemaker; (ii) at 2 dpf, the pacemaker region was more confined to the sinoatrial ring (SAR), with illumination of large adjacent areas having no effect, and AV block (of varying degree, depending on light intensity) occurred with illumination of the AV canal; and (iii) at 3 dpf, the pacemaker region was more defined, being confined to the dorsal

right quadrant of the SAR. It was further found that in 4 dpf embryos, pulsed photo-stimulation of the SAR at a frequency of 2.7-4.7 Hz with ChR2 was able to control HR.

Since the time of that pioneering study, another prominent family of Cl⁻-specific light-activated ion channels has been developed, the *Guillardia theta* anion channelrhodopsin 1 and 2 (GtACR1 and GtACR2) [565], which have been shown to silence neuronal AP generation (including in zebrafish) [566–569]. We have performed the first cardiac application of GtACR1 involved zebrafish (using hearts isolated from 3 months post fertilisation (mpf) adults with cardiac-specific GtACR1 expression, *Tg(cmlc2:GtACR1-eGFP)*), which in combination with experiments in genetically transfected single rabbit ventricular myocytes demonstrated that GtACR1 activation causes depolarisation of ventricular myocytes when applied during the resting (diastolic) phase of the AP (and if suprathreshold, results in excitation), but causes repolarisation when applied during the (systolic) plateau (resulting in shortening of the AP). This biphasic response relates to the reversal potential of Cl⁻ in ventricular myocytes, which is somewhere between -40 mV and -33 mV [570], so that the flow of negative ions switches from outward (causing depolarisation) to inward (causing repolarisation) as cells are excited. As a result, pulsed illumination can be used to pace the heart, while sustained illumination can arrest the heart in a depolarised state (Figure 5.5B) [571]. This indicates that while GtACR1 does not address the need for optogenetic silencing through a physiological means (*i.e.*, hyperpolarisation), it is a potentially attractive tool for exciting CM by transient light-induced depolarisation. This study is described below.

5.2. Methods

5.2.1. Ethics statement

All experimental procedures in zebrafish were approved by the Dalhousie University Committee for Laboratory Animals and followed the guidelines of the Canadian Council on Animal Care. Details of experimental protocols are reported following the Minimum Information about a Cardiac Electrophysiology Experiment (MICEE) reporting standard [382].

5.2.2. Generation of cmlc2:GtACR1-eGFP transgenic zebrafish

A cmlc2:GtACR1-eGFP plasmid was generated using standard cloning and microbiology techniques combined with the multisite Gateway system for Tol2 transposon transgenesis by a Research Associate in our lab, Sara Rafferty [267]. The 5′ entry plasmid p5E-cmlc2, 3′ entry plasmid p3E-polyA, destination plasmid pDestTol2pA2, and donor plasmid pME-TA were obtained from Dr. Jason Berman (Dalhousie University, Halifax, Canada). To generate the middle entry plasmid, the sequence of the L13_CMV_GtACR1-eGFP plasmid was confirmed (using primers CMV_Forward: 5′-CGCAAATGGGCGGTAGGCGTG-3′ and EGFP-C-REV: 5′-GTTCAGGGGGAGGTGTG-3′) and then GtACR1-eGFP was amplified out of the plasmid using polymerase chain reaction (PCR) with primers GtACR1_for: 5′-GCCACCATGAGCAGCATTAC-3′ and EGFP-stop_rev: 5′-TTTACTTGTACAGCTCGTCCAT-3′. The GtACR1-eGFP PCR product, purified using a Gel Extraction Kit (QIAEX II, Qiagen; Hilden, Germany) and with the addition of a polyA (pA) tail was ligated into pME-TA to generate the middle entry plasmid pME-

GtACR1-eGFP-pA, which was then subjected to restriction digest and sequencing (using primers M13F(-21): 5′-TGTAAAACGACGGCCAGT-3′, GtACR1, and EGFP_stop_rev). An expression plasmid was then generated by ligating p5E-cmlc2, pME-GtACR1-eGFP-pA, and p3E-polyA into pDestTol2pA2. Restriction digest and sequencing (using primers T7: 5′-TAATACGACTCACTATAGGG-3′ and EGFP-stop_rev) confirmed the sequence of isolated expression plasmid DNA. The cmlc2-GtACR1-eGFP-pA-pDestTol2pA2 DNA was purified with a PCR Purification Kit (QIAquick, Qiagen) before microinjection of 22.7 ng/μL DNA and 16 ng/μL Tol2 transposase mRNA into one-cell stage Casper zebrafish embryos. Injected fish were screened for successful gene transduction by eGFP expression using a fluorescent microscope (MZ16F, Leica; Wetzlar, Germany).

5.2.3. Zebrafish heart preparation

Hearts were isolated from 3 mpf zebrafish expressing GtACR1-eGFP as previously described [32,277,346]. Fish were anesthetised in Tris-buffered (pH 7.4, BP152, Fisher Scientific; Hampton, United States) tricaine (1.5 mM MS-222) in a controlled room temperature of 21° Celsius tank water until opercular movements ceased and the animals lacked response to fin pinch with forceps. A midline incision was made through the ventral body wall and tissues of the ventral aorta, ventricle, atrium, and venous sinus were removed, pinned into a 15 mL dish lined with Sylgard (DC 170, Dow Corning; Midland, United States) containing Tyrode's solution (in mM: 142 NaCl, 4.7 KCl, 1 MgCl2, 1.8 CaCl2, 10 Glucose, 10 HEPES) of an osmolality of 300 ± 5 mOsm checked with an osmometer (Model 5004 μOsmette, Precision Systems; Natick, United States) and with pH titrated to 7.4 with NaOH. In addition, 10 μM ($\pm$)-Blebbistatin (B592490,

Toronto Research Chemicals; Toronto, Canada), a myosin inhibitor used for excitation-contraction uncoupling was added to the bath to eliminate contraction for stability of intracellular microelectrode recordings.

5.2.4. Intracellular microelectrode measurement in zebrafish ventricular myocyte

Intracellular microelectrode recordings were performed as previously described [572]. Microelectrodes made from borosilicate glass tubing (0.5 mm inner diameter, 1.0 mm outer diameter, with internal filament; type BF/100/50/10, Sutter Instruments; Novato, United States) were pulled on a Brown/Flaming micropipette puller (Model P97, Sutter Instruments) to tip diameters resulting in a 40-60 MΩ resistance when filled with 3 M KCl. Electrodes were coupled to the headstage of an amplifier (Model 1600 Neuroprobe Amplifier, A/M Systems; Everett, United States) operated in current clamp mode with an electrode holder (ESW-M10N, Warner Instruments; Hamden, United States). Electrodes were advanced with a mechanical manipulator (MX/4, Narishige; Tokyo, Japan) into the ventricular epicardium. Before cell penetration, the tip potential of the electrode was nulled using the bridge controls of the intracellular amplifier with the electrode tip in the bath. At the end of a recording, the microelectrode was withdrawn from the cell, the null potential was checked, and the previous data adjusted if necessary. Transmembrane potential was taken as the difference between the potential measured in the bath with a silver/silver- Cl$^-$ lead and the intracellular potential. Successful impalement was signaled by a sudden step of the electrode potential to a negative value. Criteria for accepting a cell were AP with a stable resting V_m < -60 mV and an AP peak >0 mV that were maintained throughout the recording. Transmembrane potential was recorded at 10 kHz

using a software-controlled data acquisition system (LabChart and PowerLab, ADInstruments; Sydney, Australia).

5.2.5. Activation of GtACR1 in zebrafish isolated hearts

Experiments were performed in zebrafish isolated hearts and intact zebrafish larvae at a controlled room temperature of 21° Celsius using an upright microscope (BX51WI, Olympus; Shinjuku, Japan). Light for activation of GtACR1 was delivered by a white LED (CFT-90-W, Luminus Devices; Sunnyvale, USA) through a 531/22 nm filter (FF02-531/22, Semrock; Rochester, USA) focused on the ventricle with a 10X (for isolated hearts) or 20X (for zebrafish larvae) water-immersion objective (UMPLFLN 10XW or XLUMPLFLN 20XW, Olympus). The microscope field stop was set at the smallest aperture to produce a 0.16 mm^2 spot with an intensity of 1-5 mW/mm^2. Light application was either sustained for 15 s or pulsed for 10 ms at a rate 2×sinus HR in regions displaying high or no eGFP expression, checked with 466/40 nm excitation (FF01-466/40, Semrock), 495 nm dichroic (FF495-Di03, Semrock), and 525/50 nm (ET525/50m, Chroma Technology; Bellows Falls, United States) filters. optical pacing was compared to electrical pacing at the same HR applied extracellularly by a pair of silver wire electrodes on either side of the heart coupled to a constant current stimulus isolation unit (PSIU6D, Grass Technologies; West Warwick, USA) driven by 10 ms rectangular pulses from a waveform generator (S44, Grass). Measurements of HR, resting V_m, upstroke velocity (dV/dt_{max}), AP amplitude, APD_{50}, and APD_{90} were averaged over three consecutive heart beats before and during light stimulation. Light intensity was measured at the end of the experiment using a USB power meter (PM16-120, Thorlabs; Newton, United States).

5.2.6. Data analysis

Values are reported as mean±SEM. Data was analyzed with custom routines in Matlab. Statistical analysis was performed in Prism (GraphPad). Group means were compared by two-tailed paired Student's t-test. Significance was indicated by $p<0.05$.

5.3. Results

Zebrafish served as a model system to study effects of GtACR1 activation in native myocardium [267,270]. GtACR1-eGFP was expressed specifically in cardiac myocytes in the hearts of zebrafish using Tol2 transposon transgenesis by microinjection of a cmlc2:GtACR1-eGFP plasmid at the one-cell stage. Fish with successful gene insertion, indicated by cardiac eGFP expression, were raised to 3 months. Hearts were isolated and intracellular microelectrode recordings of ventricular myocyte membrane potential were performed.

5.3.1. Effects of prolonged GtACR1 activation in intact zebrafish hearts

GtACR1-eGFP expression in the ventricle was largely epicardial and heterogeneous at the cellular level (Figure S5.1), with regions of high eGFP expression next to eGFP-free areas at the whole-heart level (Figures 5.5, 5.6). Light for activation of GtACR1 was focused on regions of high or no eGFP expression (spot size of 0.16 mm^2). When sustained light (5 mW/mm^2) was applied to regions of high eGFP expression, there was an immediate depolarisation of resting V_m and a decrease in the maximum rate of V_m change (dV/dt_{max}) during the AP upstroke, as well as in AP amplitude, APD_{50}, and APD_{90}

(Figure 5.5, n= 34 cells, N=7 zebrafish hearts). Additionally, in regions of high eGFP-expression in some hearts (N= 3/7), sustained light locally inhibited AP generation by depolarisation of membrane potential (Figure 5.6). Ventricular contractions could also be inhibited *in vivo* by exposing the entire ventricle (spot size of 0.05 mm^2) of intact eGFP-positive zebrafish larvae (21 dpf, N=3) to sustained light (1.7 mW/mm^2; Supplementary Movie 1).

5.3.2. Optical pacing of zebrafish hearts

When pulsed light (10 ms, 2×sinus HR) of supra-threshold intensity (1.2±0.2 mW/mm^2; determined in each heart by increasing light intensity until AP stimulation occurred) was applied to regions of high eGFP expression, AP were elicited, resulting in optical pacing of the heart (Figure 5.5). Comparison of AP, stimulated by optical pacing and electrical pacing at the same rate, showed no difference in AP characteristics (Figure S5.2). As with sustained light, pulsed light also had an effect *in vivo* in intact eGFP-positive zebrafish larvae, eliciting ventricular contractions resulting from optical pacing. In contrast to GtACR1-expressing regions, neither sustained nor pulsed light application to eGFP-negative myocardial tissue in the same animals, or to ventricular myocardium from wild-type zebrafish (N=3), induced any changes in V_m.

5.4.Discussion

Tools to modulate cardiac electrophysiology in a spatio-temporally defined, cell-specific manner hold a key to improving our understanding of electrophysiological signaling in health and disease. ChR2 can be used for optical pacing, and for inhibition of AP generation – albeit by non-physiological sustained depolarisation of the resting V_m.

Prolonged membrane depolarisation will lead to ion concentration imbalances, which could be particularly problematic in diseased tissue [573]. ACR have been used to inhibit AP generation in neuronal cell populations and neonatal rat ventricular CM [566–569,574].

Green-light activation of GtACR1 triggers depolarising photocurrents in resting CM. GtACR1 currents are based on Cl^- conductance, with only minor current contributions by cations, such as Na^+, K^+, or H^+. Accordingly, CM inhibition by sustained illumination is based on polarising cells toward the reversal potential for Cl^-. In line with an estimated reversal potential between -40 and -33 mV in CM [570,575], GtACR1-mediated myocyte inhibition relies on membrane depolarisation, thus preventing myocyte repolarisation. While keeping CM at a depolarised potential can block re-excitation and conduction, sustained depolarisation will result in Ca^{2+} and Na^+ overload *via* activation of additional ion fluxes through L- and T-type Ca^{2+} or background Na^+ channels. This would be detrimental in cases where cells are already overloaded with Ca^{2+} or Na^+, such as when using GtACR1 for inhibition of CM activity to terminate arrhythmias in pathologically remodeled myocardium.

In contrast to CM, the reversal potential for Cl^- is closer to the resting V_m in the somatodendritic compartment of neurons, in which ACR have a hyper- or re-polarising effect. Thus, ACR activation mimics neuronal inhibition by postsynaptic $GABA_A$ receptors [576]. It would be wrong, though, to assume that ACR necessarily hyperpolarise all resting cells. There are neuronal compartments with elevated intracellular Cl^- concentrations, including presynaptic terminals and axons, where ACR activation can lead to depolarising photocurrents. In fact, several studies have reported ACR-triggered presynaptic vesicle release and antidromic spikes [568,577]. To overcome these excitatory

effects, soma-targeted ACR have been constructed by addition of the soma-targeting motifs of the K$^+$ channel K$_v$2.1 and telencephalin [347,578]. While optical inhibition with soma-targeted ACR can be effective in neurons, ACR-based CM inhibition is based on non-physiological sustained depolarisation, as shown here both for isolated cells and myocytes within intact myocardium. A light-gated K$^+$ conductance could serve as a potent alternative for optical inhibition of excitatory cells [579], as the resting potential of excitable cells is close to the K$^+$ reversal potential, thereby limiting secondary ion fluxes.

GtACR1 has been reported to show biphasic channel closure, with the fast component accelerating at depolarised potentials, whereas the slow component is similar at both positive and negative membrane voltages [580]. To prevent prolongation of optical triggered AP, one could use an ACR with faster closing kinetics, such as the GtACR1-C237A mutant [581], PsACR1 [582,583] or ZipACR [584]. In ventricular cells of intact zebrafish hearts, optically evoked AP display comparable amplitude and kinetics to same-frequency electrically stimulated AP.

While ACR do not allow hyperpolarisation of CM, they may be used to mimic Cl$^-$ currents in cardiac cells. Both inward and outward Cl$^-$ currents are present during the cardiac AP cycle and at least six families of Cl$^-$ channels are functionally expressed in CM. Cl$^-$ channels have been found to play a role in cardiac arrhythmogenesis, myocardial hypertrophy and heart failure, as well as in cardioprotection against ischemia reperfusion [585]. ACR may be used to investigate the underlying roles of Cl$^-$ channels in these disease settings, with light not only allowing for precise spatiotemporal control of ACR activity, but also enabling titration of current amplitudes by variation of light intensity and/or duration. Cell-type specific gene targeting may further enable

investigating effects of Cl^- conductance on cells other than CM, and might be useful for studying heterocellular interactions between CM and non-myocytes [586]. Recent studies expressing optogenetic probes specifically in either cardiac macrophages of healthy mouse hearts, or in non-myocytes of ventricular scar-border zone tissue, showed functional electronic coupling of the targeted cell types to adjacent CM [587,588]. The relevance of such coupling, however, both in normal homeostasis and in the context of cardiac tissue remodeling, remains to be determined. Optogenetic perturbation of electronically coupled non-myocytes might be a useful approach here, for example to modulate cardiac electrophysiological properties such as conduction velocity without interfering with CM function (as pioneered by [588].

5.5. Conclusion

Optogenetics is a powerful and highly successful [589] set of techniques that has been instrumental in recent developments in neuroscience research [590,591], and more recently also for cardiac research [519]. Zebrafish provide specific advantages as an experimental model for optogenetic cardiac investigations [265,266], and have been instrumental in its early development, suggesting a bright future for this little fish. With the increasing sophistication of optogenetic methods, the zebrafish represents an experimental model with great potential for cardiac optogenetic studies. Hopefully more cardiac researchers will soon begin to see the light.

5.6. Tables

Table 5.1 | Previous applications of cardiac optogenetics using zebrafish.

	Publication	Age of Study	Optogenetic Line	Application / Finding
Optogenetic Reporters	Arnaout *et al*., 2007	2 dpf	*Tg(cmlc2:gCaMP)*[s878]	Investigated mutant model of inherited long QT syndrome, in which loss of rapid delayed-rectifier potassium current (I_{Kr}) due to *kcnh2* mutation results in mechanical ventricular asystole. Showed lack of calcium (Ca^{2+}) waves in the ventricle, suggesting impaired Ca^{2+} cycling.
	Chi *et al*., 2008	1-21 dpf	*Tg(cmlc2:gCaMP)*[s878]	Investigated development of the vertebrate cardiac conduction system and performed a forward genetic screen. Identified four stages of conduction development, which depended on epigenetic mechanical factors, and identified 17 conduction-specific mutations that may represent novel genetic regulators of the cardiac conduction system.
	Tsutsui *et al*., 2010	2-3 dpf	*Tg(cmlc2:Mermaid)*	Investigated the effect of the histamine H1 receptor blocker astemizole on cardiac excitation. Showed that astemizole caused retrograde propagation from the atrioventricular boundary to the atrium.
	Kirchmaier *et al*. 2012	5-6	*Tg(cmlc2:gCaMP)*[s878]	Investigated effect of Popeye domain containing gene 2 knock-down. Caused sinoatrial node conduction failure, irregular atrial and ventricular activity, and varying degrees of atrioventricular block.
	Hou *et al*., 2014s	1.5-4 dpf	*Tg(cmlc2:Arch(D95N)-GCaMP5G)* ['*CaViar*']	Investigated the effects of L-type Ca^{2+} ($I_{Ca,L}$) or fast sodium current block. Showed that <4 dpf, cardiac excitation is initiated by Ca^{2+}, but by 4 dpf ventricular excitation it is initiated by sodium, while atrial excitation remains Ca^{2+} dependent.
	van Opbergen *et al*., 2018a	3, 14 dpf	*Tg(myl7:chimeric VSFP-butterfly CY)* *Tg(myl7:Gal4FF; UAS:GCaMP6f)*	Investigated effects of pharmacological modulation of the sympathetic nervous system or ion channels on cardiac electrophysiology and Ca^{2+} cycling. Showed that: (i) sympathetic stimulation or block increased or decreased diastolic Ca^{2+} and Ca^{2+} transient amplitudes; (ii) I_{Kr} block increased action potential duration; (iii) $I_{Ca,L}$ block prevented Ca^{2+} transients, increased ventricular action potential duration, and disrupted atrioventricular conduction; and (iv) differences exist in

			atrial and ventricular Ca^{2+} cycling during development.
Salgado-Almario *et al.*, 2020	3 dpf	*Tg(cmlc2:Twitch-1)*	Tested various novel genetically encoded ratiometric calcium indicators to determine which are the most promising for use in the heart.
		Tg(cmlc2:Twitch-2B)	
		Tg(cmlc2:Twitch-4)	
		Tg(cmlc2:TN-XXL)	

5.7. Figures

Figure 5.1 | The optogenetic toolbox for measurement and manipulation of cardiac activity. There is a large array of optogenetic actuators and reporters with a broad range of activation spectra available for use in the heart. These comprise light-activated depolarising (excitatory) and hyperpolarising (inhibitory) opsins that pass cations, anions, and protons and genetically encoded voltage (GEVI) and calcium (GECI) indicators that can be used to measure membrane potential and intracellular calcium. Opsin schematic from Ferenczi et al. (2019), middle panel from Entcheva and Kay (2021), and GEVI and GECI schematics from van Opbergen et al. (2018a).
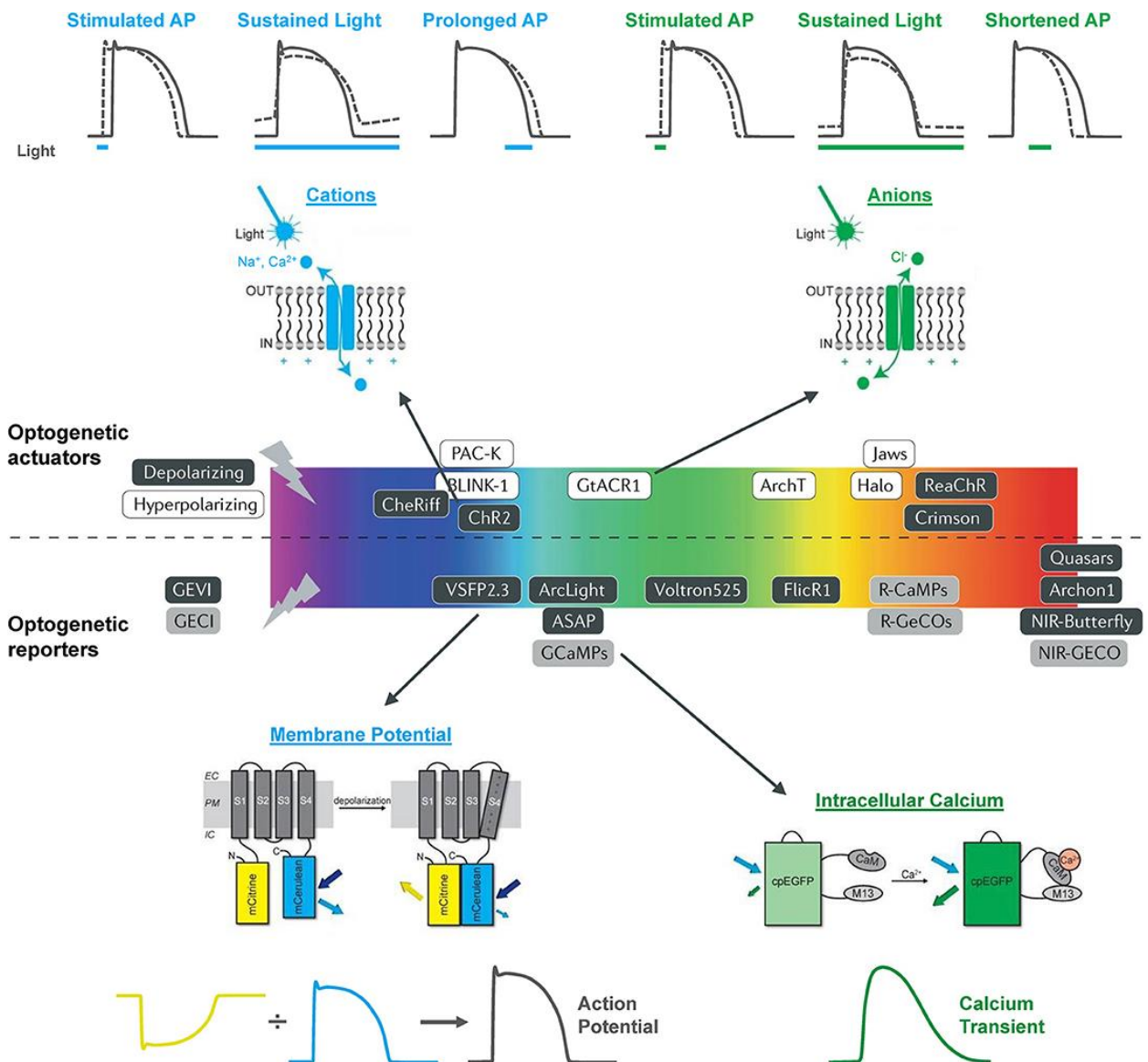
Figure 5.2 | *In vivo* imaging of intracellular calcium using genetically encoded calcium indicators (GECIs) in intact zebrafish embryos. (A) Hearts in 48 h post-fertilisation (hpf) wild-type embryos with cardiac-specific expression of gGCaMP exhibit atrial and ventricular calcium release (left), while hearts in kcnh2s290 mutants exhibit atrial but no ventricular release (right). Each selected region in the images has a corresponding fluorescence signal plotted below. The dotted lines mark an arbitrary point in time to facilitate comparison across the different signals. From Arnaout et al. (2007). (B) In hearts from 48 hpf wild-type embryos, calcium activation travels from the sinus venosus across the atrium (Atr) and ventricle (Ven), with a delay at the atrioventricular (AV) junction (left), while ventricular conduction is absent in silent ventricle (siv) mutants and disorganised in dococs215, 226 (dcc) mutants (right). Isochronal lines represent 60 ms. From Chi et al. (2008).
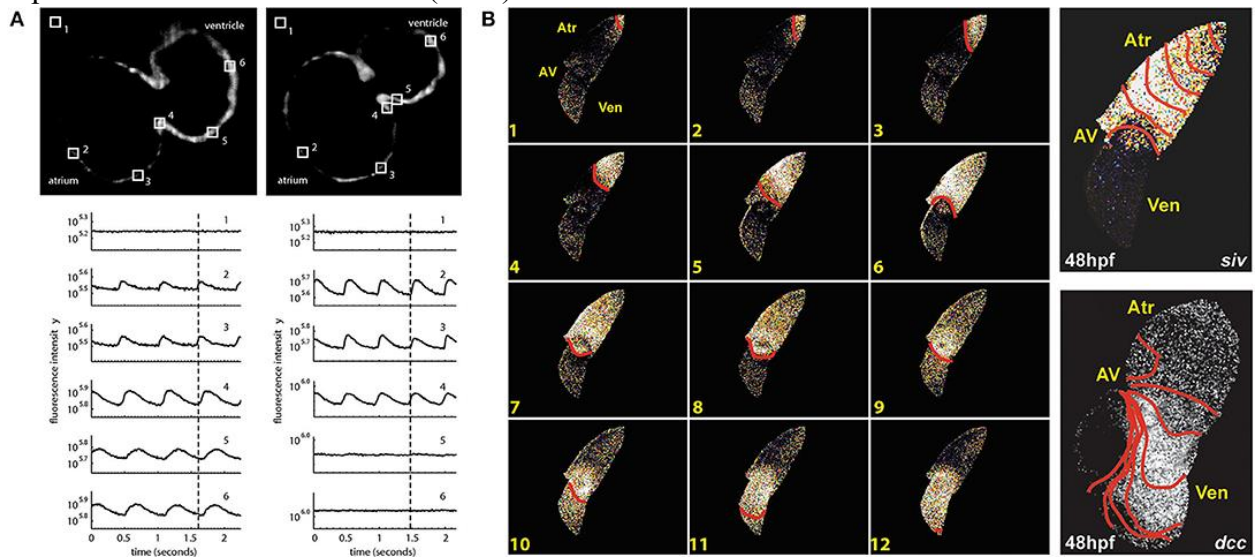
Figure 5.3 | *In vivo* ratiometric intracellular calcium measurements with a genetically encoded calcium indicator (GECI) in intact zebrafish embryos. Ratiometric intracellular calcium signals were acquired with Twitch-1, Twitch-4, or a Förster resonance energy transfer (FRET) construct insensitive to calcium (ECFP-16aa-EYFP) from the atrium (red region-of-interest) and ventricle (white region-of-interest) of 3 days post-fertilisation embryos. The change in fluorescence in the donor and FRET channels normalised to the first diastolic period (F/FDiast; upper graphs in atrium and ventricle) and their ratio (R/RDiast; lower graphs in atrium and ventricle) are shown. From Salgado-Almario et al. (2020).
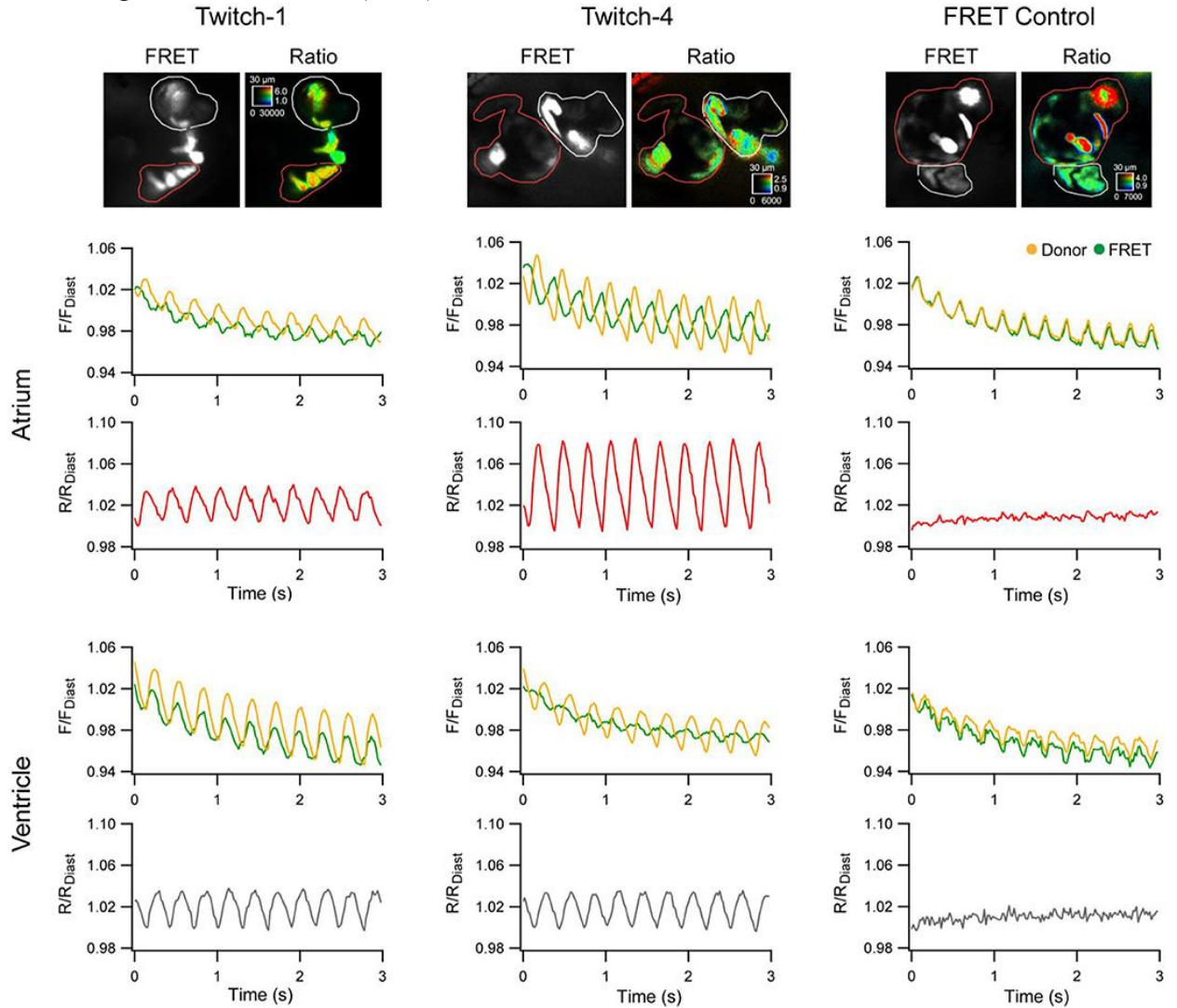
Figure 5.4 | *In vivo* imaging of membrane potential using genetically encoded voltage indicators (GEVIs), combined with genetically encoded calcium indicators (GECIs) in intact zebrafish embryos. (A) Signals (left) from a donor (mUKG, green) and acceptor (mKOκ, red) Förster resonance energy transfer (FRET) pair of fluorescent proteins and their ratio (mKOκ/mUKG, black) acquired from the ventricle of a 3 days post-fertilisation (dpf) zebrafish embryo with cardiac-specific expression of the GEVI Mermaid. Pseudo-colored ratio images (right) representing a single cardiac cycle in wild-type, Mermaid-expressing zebrafish (upper) showing propagation of excitation from the sinus venosus in the atrium (a) to the ventricle (v), and in astemizole-treated (5 µM, 15 min) zebrafish (lower) showing retrograde propagation from the ventricle to the atrium (highlighted with arrows). Scale bar, 100 µm. From Tsutsui et al. (2010). (B) Signals (upper left) from a donor (mCerulean, blue) and acceptor (mCitrine, yellow) Förster resonance energy transfer (FRET) pair of fluorescent proteins and their ratio (mCitrine/mCerulean, black) acquired from the regions of interest (boxes in fluorescent images) indicated on the atrium (A) and ventricle (V) of a 3 dpf zebrafish embryo with cardiac-specific expression of GEVI VSFP-butterfly CY. Signals (upper right) acquired from the atrium (blue) and ventricle (red) of a 3 dpf zebrafish embryo with cardiac-specific expression of the GECI GCaMP6f. Line plots of chimeric VSFP-butterfly CY (lower left) and GCaMP6f (lower right) background-corrected fluorescence intensities averaged across the width of the myocardial wall superimposed on heat maps of trajectory vs. time illustrating electrical impulse and Ca^{2+} propagation throughout the heart. cpEGFP, circularly permutated enhanced green fluorescent protein. From van Opbergen et al. (2018a). (C) Single optical sections of a 4 dpf zebrafish heart with cardiac-specific expression of the GEVI-GECI construct CaViar showing GEVI Arch(D95N) (top) and GECI GCaMP5G (middle) fluorescence as excitation propagates from the atrium (A) to ventricle (V). Voltage (Vm, red) and calcium (Ca^{2+}, blue) signals acquired from the atrium and ventricle of 50 (upper left) and 102 (lower right) hours post-fertilisation (hpf) zebrafish embryos exposed to nifedipine (L-type Ca^{2+} channel blocker) and quinidine (fast sodium channel blocker). At 52 hpf, nifedipine reversibly suppressed voltage and Ca^{2+} dynamics in both chambers, while quinidine had no effect. At 102 hpf, nifedipine largely suppressed calcium transients in both chambers but only suppressed atrial voltage, while quinidine largely suppressed voltage and calcium transients in the ventricle but did not affect either transient in the atrium. Scale bar, 50 µm. From Hou et al. (2014).
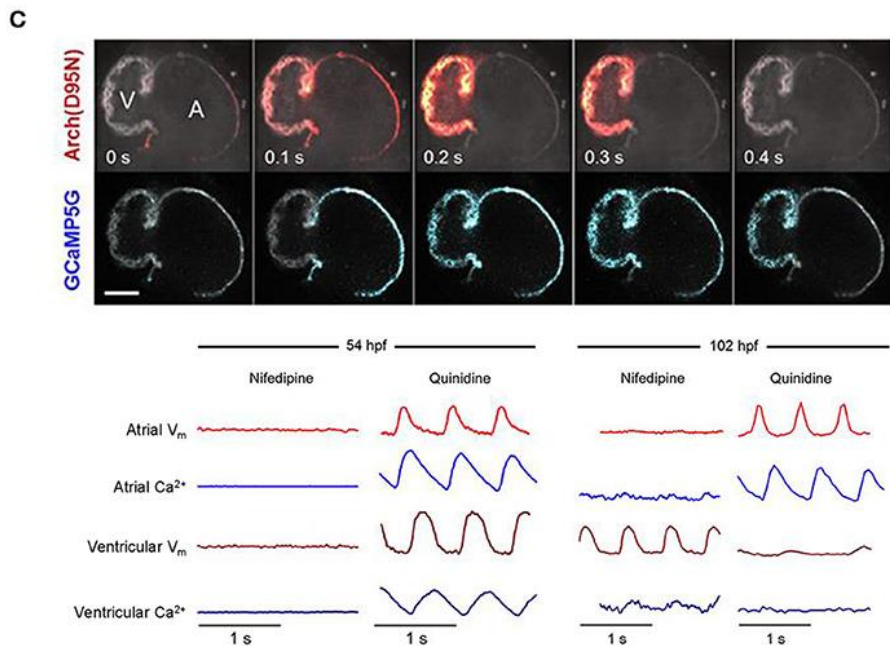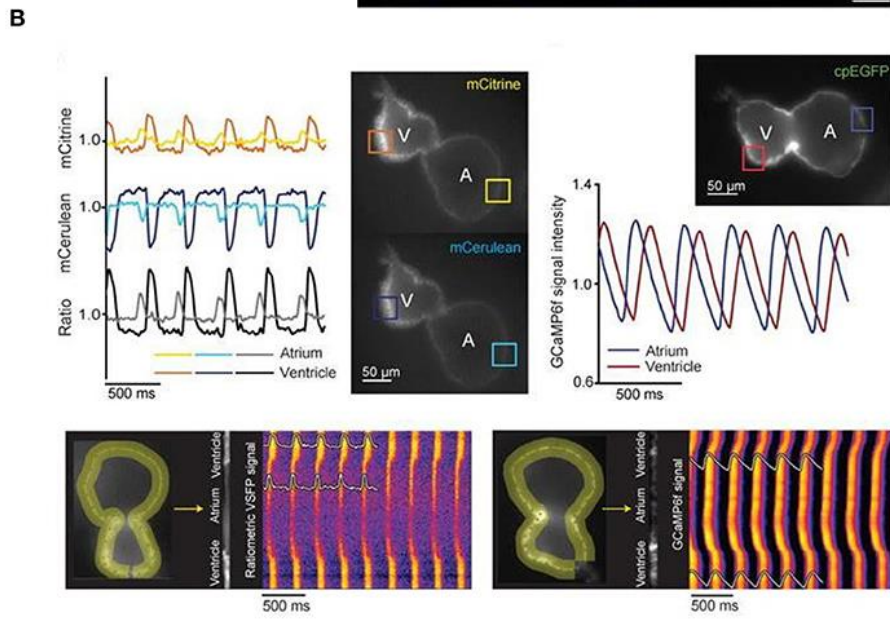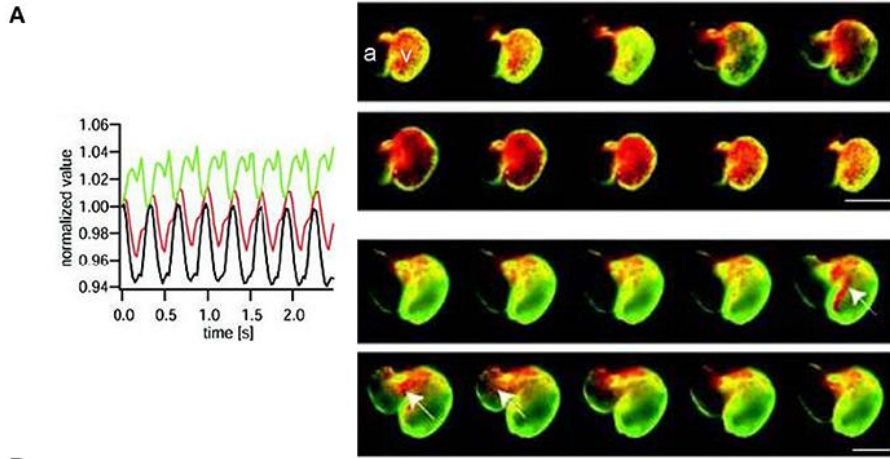
Figure 5.5 | GtACR1 activation depolarises ventricular myocyte membrane potential in isolated zebrafish hearts. Regions of high or no eGFP expression on the ventricle of 3-months post fertilisation (mpf) zebrafish isolated hearts were illuminated by a 0.16 mm2 spot of 531/22 nm light sustained for 15 s or pulsed for 10 ms at a rate 2–3 × sinus heart rate. (A,D–E) In the case of sustained light, in regions displaying eGFP expression (red circle in C) there was an immediate increase in resting membrane potential (ER) and a decrease in the maximum rate of membrane depolarisation (dE/dtmax), AP amplitude (APAmp), and APD at 50% and 90% repolarisation (APD50 and APD90). (B) In the case of pulsed light, the heart could be stimulated when light intensity was increased to supra-threshold values. (A,B) In both cases, there was no effect seen in regions displaying no eGFP expression (blue circle in C). *indicates $p < 0.0001$ by two-tailed paired Student's t-test. (Borrowed from Kopton et al., 2018).
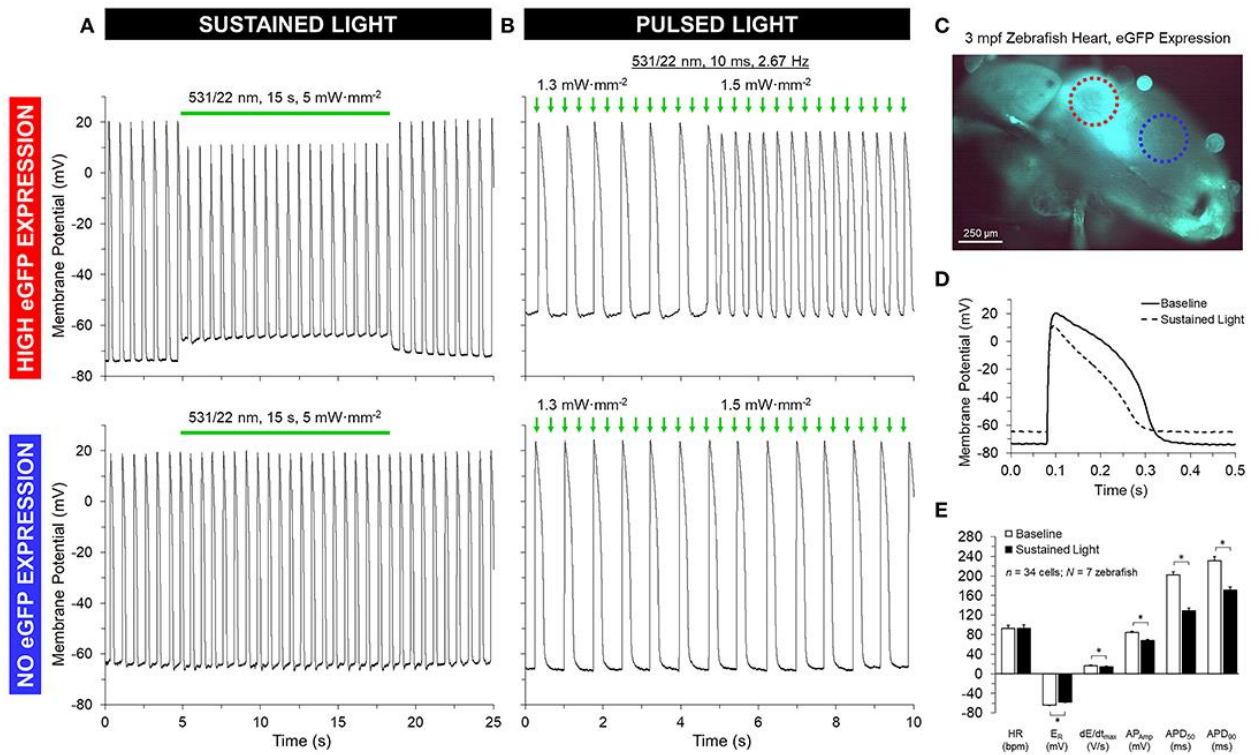
Figure 5.6 | GtACR1 activation can inhibit ventricular myocyte action potentials in isolated zebrafish hearts. In a subset of 3-months post fertilisation (mpf) isolated zebrafish hearts (n = 3/7), a 0.16 mm2 spot of 531/22 nm light applied to some eGFP expressing regions locally inhibited AP by depolarisation of membrane potential, while there was no effect in regions with no eGFP expression (confirmed by live confocal microscopy) (From Kopton et al., 2018).
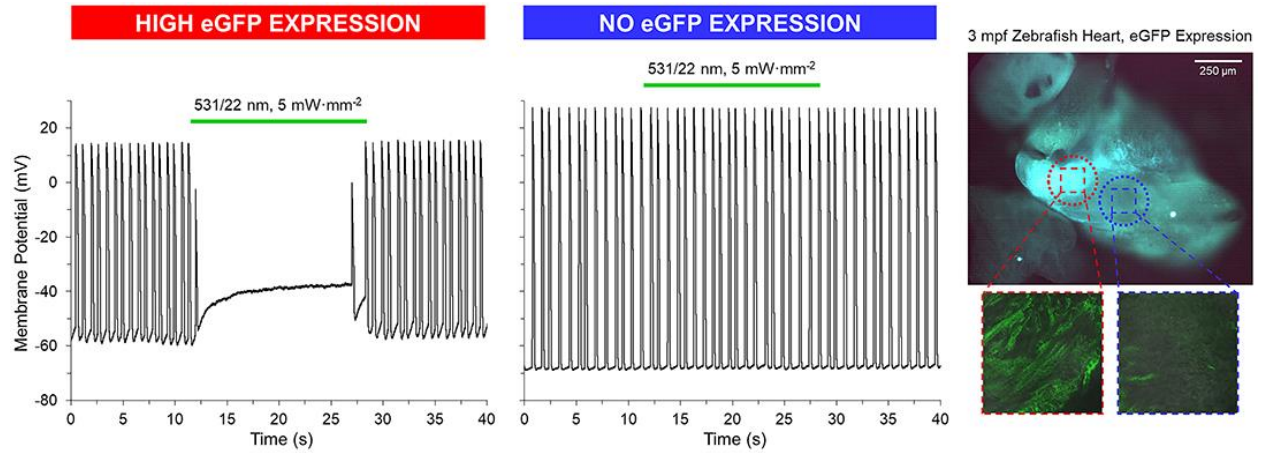
CHAPTER 6: CONCLUSIONS AND FUTURE DIRECTIONS

An overarching strength of the projects that have been discussed in this dissertation is the continued evidence for the effectiveness of zebrafish as a dynamic and appropriate tool for studies of cardiac physiology. Application of the experimental methods used in these projects would not be possible in larger mammalian models or humans, particularly in an intact *in vivo* setting. For this reason, some may initially question the relevance or transferability of such methods toward clinical treatment options. However, many scientists that use the zebrafish model to investigate physiology, and pathophysiology, will quickly inform listeners that their field of study is physiology, and not specifically fish physiology. Otherwise, the need for genetic manipulation, state-of-the-art optical imaging, along with an abundance of other innovative technologies, would not be necessary. It is due to these technologies paired with tested-and-true, as well as novel methods, that allows progression of understanding mechanisms in health, and perhaps more importantly, in disease.

6.1. A novel method to manipulate hemodynamic load *in vivo*

The introduction of this document began by discussing the importance of a unified approach toward a common goal, to take a stand in support of the advancement of science through international collaboration and sharing of knowledge. The method that was utilised in Chapters 2, 3, and 4, is a glaring example of this notion. At an international biomechanical engineering conference where scientists came together to share ideas, methods, and results, led to a chance encounter that resulted in a collaboration between our lab, and Dr. David Bark's lab at Colorado State University. It

was here that this method originated, and the lessons learned throughout this 12-week research visit were paramount in the successful initiation of this project.

Upon returning from Dr. Bark's lab, we implemented this method and began to tailor it to address our specific questions, while further optimising various parameters related to control of hemodynamic load (time, flow rate, rest) in 2 dpf zebrafish (Chapter 2; Methods). After successful proof-of-principle - in terms of manipulating EDA, we established a systematic approach to collect measurements of cardiac function (HR, SA, CO_A). When exposed to repeated episodes of sustained hemodynamic load, there was no response in HR (Bainbridge reflex), but instead a over compensatory increase in the SA, (Frank-Starling Law).

Indeed, with the onset of increased hemodynamic load, an increase in HR response would be expected in the adult heart, however; in the case of a 2 dpf zebrafish embryo, these results were not entirely surprising as the development of the heart is still in its infancy and not yet fully functional, or dependent for survival at this stage. This did provide motivation to determine when the expected effect takes place while also attempting to uncover the intricate details relating to the mechanism(s) responsible (Chapter 3). Parameters of cardiac function were investigated in older aged zebrafish (2 – 14 dpf) sample groups and the HR response became visible by 6 dpf, and much more robust by 14 dpf. From this study, it is apparent that the FSL is not age dependent as this response was present in each age group. In fact, the percentage change in SA was most prominent in 2 dpf compared to 14 dpf, which may be a protective compensatory mechanism.

The next study included investigation of pharmacological interrogation to determine contribution from the ANS and intrinsic input (Chapter 4), comparing parameters of cardiac function in 14 dpf groups exposed to various blockers to a 14 dpf control group. To summarise the results found, the response to increased hemodynamic load is not a neuronal-specific response on a beat-by-beat basis but does appear to be HR dependent. The absolute HR response was greater in the block of SNS stimulation (Timolol) compared to control or PNS block (Atropine) or control. Whether this is dependent on the potential, as the RHR was significantly reduced in the Timolol group, whereas the other groups are closer to their physiological HR ceiling, and thus require a much greater stimulus to reach this effect. In the streptomycin group, which blocks SAC_{NS} contribution, the Bainbridge reflex was eliminated and instead, a substantial increase in the FSL contributed to the ability of the heart to remain functional. As EDA began to increase beyond 50 to 60 percent from the baseline value, HR began to cease and cardiac function became compromised, increase in SA via the FSL acted to counter this effect.

6.2. Future directions

We demonstrated the use of a novel *in vivo* method in 48 hpf zebrafish embryos and later expanded this into later stages of development up to 14 dpf, and integration with pharmacological interrogation. This method was also combined with fluorescent imaging using a GEVI or GECI to measure effects on cellular properties such as V_m and $[Ca^{2+}]_i$ cycling and gain insight into subcellular mechanisms driving changes in whole heart function [368]. Using the zebrafish will also allow for genetic manipulations, to more specifically understand the molecular mechanisms involved [267,337]. Moreover, the

zebrafish is an excellent model for cardiac disease [265,285], so that potential contributions of MEC and MMC – and their disruption – to cardiac structural malformations and functional problem in development may be studied, to better understand congenital heart defects and early cardiac dysfunction. Finally, as imaging technology continues to advance, the above may be enhanced by the use of four-dimensional imaging techniques [592,593], for a more comprehensive, whole heart understanding of physiological and pathophysiological cardiac adaptation. Additionally, furthering our understanding in MEC, and more specifically SAC ion-specific preferential determination will help to provide targeted treatment approach that considers potential electrophysiological benefits in the context of the need to maintain volume regulatory capacity (in ischaemia, and even more so, reperfusion) and the ability to tune cell contractility to the mechanical environment.

6.3. Shedding light on cardiac function and arrhythmogenesis

An opportunity to collaborate with a cardiac research team at the Institute for Experimental Cardiovascular Medicine in Freiburg, Germany was presented, working on a project focused on cardiac optogenetics. The results of this project were exciting, collecting intracellular microelectrode recordings while manipulating HR, and providing insight into the field of cardiac optogenetics. GtACR1 represents a potent tool for light-induced depolarization of defined cardiac cell populations, which can be used both to activate and to silence AP generation in CM. However, we must consider that the sustained membrane depolarization for cardiac silencing will give rise to secondary ion fluxes that may affect transmembrane ion distribution. This could increase

174

arrhythmogenicity in myocardium and be particularly counter-productive when using optogenetic approaches in ischemic myocardium where CM are already overloaded with Na^+ and/or Ca^{2+}. Current research investigating a K^+ gated optogenetic tool is currently underway and may provide a more optimal channel to explore silencing of cardiac APs.

6.4. Future directions for the use of cardiac optogenetics in zebrafish

Unlike the prevalent use of optogenetics in zebrafish to study the nervous system [539–541], there have been relatively few cardiac optogenetic studies performed in zebrafish (summarised in Table 1.1), yet those studies have been fundamental in progressing the application of optogenetic technologies to the heart. With the continual improvement of optogenetic techniques [519], the use of zebrafish for integrative (patho-)physiological cardiac structure-function studies holds great promise. Future research will be driven by technological advances such as high-speed, cell-accurate, three-dimensional mapping [593–595], more effective methods for cell-specific spatial and temporal gene expression [596,597], and novel optogenetic actuators and reporters with enhanced expression, fluorescence, and kinetics, combined with improved light delivery [519]. As the field continues to develop, the zebrafish may be invaluable for cardiac optogenetic studies directly related to its strengths as an experimental model (Table 5.1; *i.e.*, development, genetic screening, drug discovery, cardiotoxicity testing, disease modelling, all-optical studies of electrophysiology and cell signalling, and anti-arrhythmic strategy development). It may also be a powerful tool for fundamental investigations of the hetero-cellular heart (*e.g.*, structure-function interactions of myocytes, fibroblasts, intracardiac neurons, and immune and endothelial cells) and in helping to overcome hindrances related to the clinical translation of optogenetic techniques (*e.g.*, genetic transfection, immune

responses, phototoxicity) [598]. This will be enhanced by the large number of currently available transgenic lines, genetic material, and tools (easily found through online resources and central repositories), facilitated by the open zebrafish community willing to share them [267,268].

While a majority of cardiac optogenetic studies in the zebrafish have been performed in the early stages of development, technological advances in fluorescence imaging approaches and methods for spatially-resolved light stimulation have the promise to enable studies to be performed in the adult isolated whole heart and *in vivo*. This will be aided by the continuing development of transgenic lines that lack pigment and are thus largely transparent throughout their lifespan (*i.e.*, 'casper' [383] and 'crystal' [424]), and can be used as a background on which to express optogenetic reporters and actuators along with mutations of interest.

REFERENCES

1. Burggren, W. W. *et al.* Comparative cardiovascular physiology: future trends, opportunities and challenges. *Acta Physiol.* **210**, 257–276 (2014).
2. Bartos, D. C., Grandi, E. & Ripplinger, C. M. Ion Channels in the Heart. *Compr. Physiol.* **5**, 1423 (2015).
3. Zhang, J., Chatham, J. C. & Young, M. E. Circadian Regulation of Cardiac Physiology: Rhythms that Keep the Heart Beating. *Annu. Rev. Physiol.* **82**, 79 (2020).
4. Quinn, T. A. & Kohl, P. Cardiac mechano-electric coupling: Acute effects of mechanical stimulation on heart rate and rhythm. *Physiol. Rev.* **101**, 37–92 (2021).
5. Quinn, T. A. Cardiac mechano-electric coupling: a role in regulating normal function of the heart? *Cardiovasc. Res.* **108**, 1–3 (2015).
6. Quinn, T. A. & Kohl, P. Rabbit models of cardiac mechano-electric and mechano-mechanical coupling. *Prog. Biophys. Mol. Biol.* **121**, 110–122 (2016).
7. Grant, A. O. Cardiac Ion Channels. *Circ. Arrhythmia Electrophysiol.* **2**, 185–194 (2009).
8. Eisner, D. A. & Cerbai, E. Beating to time: calcium clocks, voltage clocks, and cardiac pacemaker activity. (2009) doi:10.1152/ajpheart.00056.2009.
9. Difrancesco, D. The role of the funny current in pacemaker activity. *Circ. Res.* **106**, 434–446 (2010).
10. Joung, B., Ogawa, M., Lin, S. F. & Chen, P. S. The Calcium and Voltage Clocks in Sinoatrial Node Automaticity. *Korean Circ. J.* **39**, 217 (2009).
11. Mesirca, P., Torrente, A. G. & Mangoni, M. E. Functional role of voltage gated Ca2+ channels in heart automaticity. *Front. Physiol.* **6**, 19 (2015).
12. Wei, X., Yohannan, S. & Richards, J. R. Physiology, Cardiac Repolarization Dispersion and Reserve. *StatPearls* (2022).
13. Bers, D. M. Cardiac excitation–contraction coupling. *Nat. 2002 4156868* **415**, 198–205 (2002).
14. Bers, D. M. Excitation-Contraction Coupling and Cardiac Contractile Force. **237**, (2001).
15. Thoresen, T., Lenz, M. & Gardel, M. L. Thick Filament Length and Isoform Composition Determine Self-Organized Contractile Units in Actomyosin Bundles. *Biophys. J.* **104**, 655–665 (2013).
16. Ojima, K. Myosin: Formation and maintenance of thick filaments. *Anim. Sci. J.* **90**, 801–807 (2019).
17. Clarke, M. Muscle sliding filaments. *Nat. Rev. Mol. Cell Biol.* **9**, s7–s7 (2010).
18. Maciej Serda *et al.* Normal myocardial metabolism: Fueling cardiac contraction. *Adv. Stud. Med.* **4**, S457–S463 (2004).
19. Frank, K. F., Bölck, B., Erdmann, E. & Schwinger, R. H. G. Sarcoplasmic reticulum Ca2+-ATPase modulates cardiac contraction and relaxation. *Cardiovasc. Res.* **57**, 20–27 (2003).
20. Neves, J. S. *et al.* Acute myocardial response to stretch: What we (don't) know. *Front. Physiol.* **6**, 408 (2016).
21. Calaghan, S. C. & White, E. The role of calcium in the response of cardiac muscle to stretch. **71**, 59–90 (1999).
22. de Tombe, P. P. *et al.* Myofilament length dependent activation. *J. Mol. Cell.*

Cardiol. **48**, 851–858 (2010).

23. Lakin, R., Wright, S. & Polidovitch, N. Hook, line and sinker: adult zebrafish offer a valid model to study mammalian cardiac contractile mechanics. *J. Physiol.* **592**, 4609 (2014).

24. Fukuda, N., Terui, T., Ohtsuki, I., Ishiwata, S. & Kurihara, S. Titin and Troponin: Central Players in the Frank-Starling Mechanism of the Heart. *Curr. Cardiol. Rev.* **5**, 119 (2009).

25. Quinn, T. A., Kohl, P. & Ravens, U. Cardiac mechano-electric coupling research: Fifty years of progress and scientific innovation. *Prog. Biophys. Mol. Biol.* **115**, 71–75 (2014).

26. Kohl, P. & Ravens, U. Cardiac mechano-electric feedback: past, present, and prospect. *Prog. Biophys. Mol. Biol.* **82**, 3–9 (2003).

27. Ravens, U. Mechano-electric feedback and arrhythmias. *Prog. Biophys. Mol. Biol.* **82**, 255–266 (2003).

28. Quinn, T. A., Bayliss, R. A. & Kohl, P. Mechano-Electric Feedback in the Heart: Effects on Heart Rate and Rhythm. *Hear. Rate Rhythm* 133–151 (2011) doi:10.1007/978-3-642-17575-6_7.

29. Bainbridge, F. A. The influence of venous filling upon the rate of the heart. *J. Physiol.* **50**, 65–84 (1915).

30. Bernardi, L. *et al.* Evidence for an intrinsic mechanism regulating heart rate variability in the transplanted and the intact heart during submaximal dynamic exercise? *Cardiovasc. Res.* **24**, 969–981 (1990).

31. Bernardi, L. *et al.* Respiratory sinus arrhythmia in the denervated human heart. *https://doi.org/10.1152/jappl.1989.67.4.1447* **67**, 1447–1455 (1989).

32. MacDonald, E. A., Stoyek, M. R., Rose, R. A. & Quinn, T. A. Intrinsic regulation of sinoatrial node function and the zebrafish as a model of stretch effects on pacemaking. *Prog. Biophys. Mol. Biol.* **130**, 198–211 (2017).

33. Cooper, P. J., Lei, M., Cheng, L. X. & Kohl, P. Selected contribution: axial stretch increases spontaneous pacemaker activity in rabbit isolated sinoatrial node cells. *J. Appl. Physiol.* **89**, 2099–2104 (2000).

34. Paton, J. F. R., Kasparov, S., Wilson, S. J. & Bolter, C. P. Do cardiac neurons play a role in the intrinsic control of heart rate in the rat? *Exp. Physiol.* **87**, 675–682 (2002).

35. Chiba, S. Pharmacologic Analysis of Stretch-Induced Sinus Acceleration of the Isolated Dog Atrium. *Jpn. Heart J.* **18**, 398–405 (1977).

36. Blinks, J. R. Positive Chronotropic Effect of Increasing Right Atrial Pressure in the Isolated Mammalian Heart. *https://doi.org/10.1152/ajplegacy.1956.186.2.299* **186**, 299–303 (1956).

37. Mc Brooks, C. *et al.* Effects of localized stretch of the sinoatrial node region of the dog heart'.

38. Pathak, C. L. Autoregulation of Chronotropic Response of the Heart Through Pacemaker Stretch. *Cardiology* **58**, 45–64 (1973).

39. Donald, D. E. & Shepherd, J. T. Reflexes from the heart and lungs: physiological curiosities or important regulatory mechanisms. *Cardiovasc. Res.* **12**, 449–469 (1978).

40. Barrabés, J. A. *et al.* Regional expansion during myocardial ischemia predicts

ventricular fibrillation and coronary reocclusion. *Am. J. Physiol. - Hear. Circ. Physiol.* **274**, (1998).

41. Barrabés, J. A. *et al.* Ventricular fibrillation during acute coronary occlusion is related to the dilation of the ischemic region. *Basic Res. Cardiol.* **97**, 445–451 (2002).

42. Barrabés, J. A. *et al.* Effects of the Selective Stretch-Activated Channel Blocker GsMtx4 on Stretch-Induced Changes in Refractoriness in Isolated Rat Hearts and on Ventricular Premature Beats and Arrhythmias after Coronary Occlusion in Swine. *PLoS One* **10**, (2015).

43. Baumeister, P. A. *et al.* Mechanically-Induced Ventricular Arrhythmias during Acute Regional Ischemia. *J. Mol. Cell. Cardiol.* **124**, 87–88 (2018).

44. Coronel, R., Wilms-Schopman, F. J. G. & Degroot, J. R. Origin of ischemia-induced phase 1b ventricular arrhythmias in pig hearts. *J. Am. Coll. Cardiol.* **39**, 166–176 (2002).

45. Sideris, D. A. High blood pressure and ventricular arrhythmias. *Eur. Heart J.* **14**, 1548–1553 (1993).

46. Siogas, K. *et al.* Segmental wall motion abnormalities alter vulnerability to ventricular ectopic beats associated with acute increases in aortic pressure in patients with underlying coronary artery disease. *Heart* **79**, 268 (1998).

47. Sutherland, G. R. Sudden cardiac death: the pro-arrhythmic interaction of an acute loading with an underlying substrate. *Eur. Heart J.* **38**, 2986–2994 (2017).

48. Taggart, P. & Sutton, P. M. I. Cardiac mechano-electric feedback in man: clinical relevance. *Prog. Biophys. Mol. Biol.* **71**, 139–154 (1999).

49. Deck, K. A. Dehnungseffekte am spontanschlagenden, isolierten Sinusknoten. *Pflüger's Arch. für die gesamte Physiol. des Menschen und der Tiere 1964 2802* **280**, 120–130 (1964).

50. Craelius, W., Chen, V. & El-Sherif, N. Stretch activated ion channels in ventricular myocytes. **8**, 407–414 (1988).

51. Guharay, F. & Sachs, F. Stretch-activated single ion channel currents in tissue-cultured embryonic chick skeletal muscle. *J. Physiol.* **352**, 685–701 (1984).

52. Cooper, P. J. & Kohl, P. Species- and Preparation-Dependence of Stretch Effects on Sino-Atrial Node Pacemaking. *Ann. N. Y. Acad. Sci.* **1047**, 324–335 (2005).

53. Stockbridge, L. L. & French, A. S. Stretch-activated cation channels in human fibroblasts. *Biophys. J.* **54**, 187–190 (1988).

54. Camelliti, P., Green, C. R., LeGrice, I. & Kohl, P. Fibroblast Network in Rabbit Sinoatrial Node. *Circ. Res.* **94**, 828–835 (2004).

55. Kohl, P., Kamkin, A., Kiseleva, I. & Noble, D. Mechanosensitive fibroblasts in the sino-atrial node region of rat heart: interaction with cardiomyocytes and possible role. *Exp. Physiol.* **79**, 943–956 (1994).

56. Kohl, P. & Noble, D. Mechanosensitive connective tissue: potential influence on heart rhythm. *Cardiovasc. Res.* **32**, 62–68 (1996).

57. Canale, E., Campbell, G. R., Uehara, Y., Fujiwara, T. & Smolich, J. J. Sheep cardiac Purkinje fibers: configurational changes during the cardiac cycle. *Cell Tissue Res.* **232**, 97–110 (1983).

58. Kaufmann, R. & Theophile, U. [Autonomously promoted extension effect in Purkinje fibers, papillary muscles and trabeculae carneae of rhesus monkeys].

Pflugers Arch. Gesamte Physiol. Menschen Tiere **297**, 174–189 (1967).

59. Sanders, R., Myerburg, R. J., Gelband, H. & Bassett, A. L. Dissimilar length-- tension relations of canine ventricular muscle and false tendon: electrophysiologic alterations accompanying deformation. *J. Mol. Cell. Cardiol.* **11**, (1979).

60. Dominguez, G. & Fozzard, H. A. Effect of stretch on conduction velocity and cable properties of cardiac Purkinje fibers. *https://doi.org/10.1152/ajpcell.1979.237.3.C119* **6**, (1979).

61. Rosen, M. R., Legato, M. J. & Weiss, R. M. Developmental changes in impulse conduction in the canine heart. *https://doi.org/10.1152/ajpheart.1981.240.4.H546* **9**, (1981).

62. Bolter, C. P. Intrinsic cardiac rate regulation in the anaesthetized rabbit. *Acta Physiol. Scand.* **151**, 421–428 (1994).

63. Bolter, C. P. & Wilson, S. J. Influence of right atrial pressure on the cardiac pacemaker response to vagal stimulation. *Am. J. Physiol. - Regul. Integr. Comp. Physiol.* **276**, (1999).

64. Barrett, C. J., Bolter, C. P. & Wilson, S. J. The intrinsic rate response of the isolated right atrium of the rat, Rattus norvegicus. *Comp. Biochem. Physiol. Part A Mol. Integr. Physiol.* **120**, 391–397 (1998).

65. Bolter, C. P. Effect of changes in transmural pressure on contraction frequency of the isolated right atrium of the rabbit. *Acta Physiol. Scand.* **156**, 45–50 (1996).

66. Wilson, S. J. & Bolter, C. P. Interaction of the autonomic nervous system with intrinsic cardiac rate regulation in the guinea-pig, Cavia porcellus. *Comp. Biochem. Physiol. Part A Mol. Integr. Physiol.* **130**, 723–730 (2001).

67. Han, S., Wilson, S. J. & Bolter, C. P. Tertiapin-Q removes a mechanosensitive component of muscarinic control of the sinoatrial pacemaker in the rat. *Clin. Exp. Pharmacol. Physiol.* **37**, 900–904 (2010).

68. Brooks McC., C. & Lance, G. Interaction of myogenic and neurogenic mechanisms that control heart rate. *Proc. Natl. Acad. Sci. U. S. A.* **74**, 1761–1762 (1977).

69. Reed, A., Kohl, P. & Peyronnet, R. Molecular candidates for cardiac stretch- activated ion channels. *Glob. Cardiol. Sci. Pract.* **2014**, 19 (2014).

70. Takahashi, K., Kakimoto, Y., Toda, K. & Naruse, K. Mechanobiology in cardiac physiology and diseases. *J. Cell. Mol. Med.* **17**, 225–232 (2013).

71. Bett, G. C. L. & Sachs, F. Cardiac Mechanosensitivity and Stretch-Activated Ion Channels. *Trends Cardiovasc. Med.* **7**, 4–8 (1997).

72. Matsuda, N., Hagiwara, N., Shoda, M., Kasanuki, H. & Hosoda, S. Enhancement of the L-Type Ca2+ Current by Mechanical Stimulation in Single Rabbit Cardiac Myocytes. *Circ. Res.* **78**, 650–659 (1996).

73. Kim, D. A mechanosensitive K+ channel in heart cells. Activation by arachidonic acid. *J. Gen. Physiol.* **100**, 1021–1040 (1992).

74. Gomis, A. *et al.* Hypoosmotic- and pressure-induced membrane stretch activate TRPC5 channels. *J. Physiol.* **586**, 5633–5649 (2008).

75. Bett, G. C. L. & Sachs, F. Whole-Cell Mechanosensitive Currents in Rat Ventricular Myocytes Activated by Direct Stimulation. *J. Membr. Biol. 2000 1733* **173**, 255–263 (2000).

76. Peyronnet, R., Nerbonne, J., research, P. K.-C. & 2016, undefined. Cardiac

mechano-gated ion channels and arrhythmias. *Am Hear. Assoc* **118**, 311–329 (2016).

77. Kohl, P., Bollensdorff, C. & Garny, A. Effects of mechanosensitive ion channels on ventricular electrophysiology: experimental and theoretical models. *Exp. Physiol.* **91**, 307–321 (2006).

78. Wang, W. *et al.* An increased TREK-1-like potassium current in ventricular myocytes during rat cardiac hypertrophy. *J. Cardiovasc. Pharmacol.* **61**, 302–310 (2013).

79. Xian Tao Li *et al.* The stretch-activated potassium channel TREK-1 in rat cardiac ventricular muscle. *Cardiovasc. Res.* **69**, 86–97 (2006).

80. Tan, J. H. C., Liu, W. & Saint, D. A. Trek-like potassium channels in rat cardiac ventricular myocytes are activated by intracellular ATP. *J. Membr. Biol.* **185**, 201–207 (2002).

81. Asnes, C. F., Marquez, J. P., Elson, E. L. & Wakatsuki, T. Reconstitution of the Frank-Starling mechanism in engineered heart tissues. *Biophys. J.* **91**, 1800–1810 (2006).

82. Allen, D. G. & Kentish, J. C. The cellular basis of the length-tension relation in cardiac muscle. *J. Mol. Cell. Cardiol.* **17**, 821–840 (1985).

83. Shiels, H. A. & White, E. The Frank–Starling mechanism in vertebrate cardiac myocytes. *J. Exp. Biol.* **211**, 2005–2013 (2008).

84. Gordon, A. M., Regnier, M. & Homsher, E. Skeletal and cardiac muscle contractile activation: Tropomyosin 'rocks and rolls'. *News Physiol. Sci.* **16**, 49–55 (2001).

85. Fitzsimons, D. P. & Moss, R. L. Strong Binding of Myosin Modulates Length-Dependent Ca2+ Activation of Rat Ventricular Myocytes. *Circ. Res.* **83**, 602–607 (1998).

86. Konhilas, J. P., Irving, T. C. & De Tombe, P. P. Frank-Starling law of the heart and the cellular mechanisms of length-dependent activation. *Pflugers Arch.* **445**, 305–310 (2002).

87. Gordon, A. M. *et al.* Cross-bridges affect both TnC structure and calcium affinity in muscle fibers. *Adv. Exp. Med. Biol.* **332**, 183–194 (1993).

88. Fukuda, N. & Granzier, H. L. Titin/connectin-based modulation of the Frank-Starling mechanism of the heart. *J. Muscle Res. Cell Motil.* **26**, 319–323 (2005).

89. Trebak, M. & Putney, J. W. ORAI Calcium Channels. *Physiology (Bethesda).* **32**, 332–342 (2017).

90. Lariccia, V., Piccirillo, S., Preziuso, A., Amoroso, S. & Magi, S. Cracking the code of sodium/calcium exchanger (NCX) gating: Old and new complexities surfacing from the deep web of secondary regulations. *Cell Calcium* **87**, (2020).

91. Ferreira-Gomes, M. S. *et al.* Selectivity of plasma membrane calcium ATPase (PMCA)-mediated extrusion of toxic divalent cations in vitro and in cultured cells. *Arch. Toxicol.* **92**, 273–288 (2018).

92. Gilbert, G. *et al.* T-type voltage gated calcium channels are involved in endothelium-dependent relaxation of mice pulmonary artery. *Biochem. Pharmacol.* **138**, 61–72 (2017).

93. Krebs, J., Agellon, L. B. & Michalak, M. Ca(2+) homeostasis and endoplasmic reticulum (ER) stress: An integrated view of calcium signaling. *Biochem. Biophys.*

Res. Commun. **460**, 114–121 (2015).

94. Marchi, S. *et al.* Mitochondrial and endoplasmic reticulum calcium homeostasis and cell death. *Cell Calcium* **69**, 62–72 (2018).

95. Schachter, M. Vascular smooth muscle cell migration, atherosclerosis, and calcium channel blockers. *Int. J. Cardiol.* **62 Suppl 2**, (1997).

96. Wang, Y. *et al.* Cross-Talk between Mechanosensitive Ion Channels and Calcium Regulatory Proteins in Cardiovascular Health and Disease. *Int. J. Mol. Sci. 2021, Vol. 22, Page 8782* **22**, 8782 (2021).

97. Chubinskiy-Nadezhdin, V. I. *et al.* Local calcium signalling is mediated by mechanosensitive ion channels in mesenchymal stem cells. *Biochem. Biophys. Res. Commun.* **482**, 563–568 (2017).

98. Ilkan, Z. *et al.* Evidence for shear-mediated Ca2+ entry through mechanosensitive cation channels in human platelets and a megakaryocytic cell line. *J. Biol. Chem.* **292**, 9204–9217 (2017).

99. Coste, B. *et al.* Piezo1 and Piezo2 are essential components of distinct mechanically activated cation channels. *Science (80-.).* **330**, 55–60 (2010).

100. Li, J. *et al.* Piezo1 integration of vascular architecture with physiological force. *Nat. 2014 5157526* **515**, 279–282 (2014).

101. Ranade, S. S. *et al.* Piezo1, a mechanically activated ion channel, is required for vascular development in mice. *Proc. Natl. Acad. Sci. U. S. A.* **111**, 10347–10352 (2014).

102. Beech, D. J. & Kalli, A. C. Force Sensing by Piezo Channels in Cardiovascular Health and Disease. *Arterioscler. Thromb. Vasc. Biol.* **39**, 2228–2239 (2019).

103. Zhang, T., Chi, S., Jiang, F., Zhao, Q. & Xiao, B. A protein interaction mechanism for suppressing the mechanosensitive Piezo channels. *Nat. Commun.* **8**, (2017).

104. Beech, D. J. & Kalli, A. C. Force Sensing by Piezo Channels in Cardiovascular Health and Disease. *Arterioscler. Thromb. Vasc. Biol.* **39**, 2228 (2019).

105. Franchini, K. G. & Cowley, A. W. Autonomic Control of Cardiac Function. *Prim. Auton. Nerv. Syst. Second Ed.* 134–138 (2004) doi:10.1016/B978-012589762-4/50035-9.

106. Drew, R. C. & Sinoway, L. I. Autonomic Control of the Heart. *Prim. Auton. Nerv. Syst.* 177–180 (2012) doi:10.1016/B978-0-12-386525-0.00036-6.

107. Van Stee, E. W. Autonomic innervation of the heart. *Environ. Health Perspect.* **VOL. 26**, 151–158 (1978).

108. Levy, M. N. & Zieske, H. Autonomic control of cardiac pacemaker activity and atrioventricular transmission. *https://doi.org/10.1152/jappl.1969.27.4.465* **27**, 465–470 (1969).

109. Coote, J. H. & Chauhan, R. A. The sympathetic innervation of the heart: Important new insights. *Auton. Neurosci.* **199**, 17–23 (2016).

110. Pather, N., Partab, P., Singh, B. & Satyapal, K. S. The sympathetic contributions to the cardiac plexus. *Surg. Radiol. Anat.* **25**, 210–215 (2003).

111. Balajewicz-Nowak, M. *et al.* The dynamics of autonomic nervous system activity and hemodynamic changes in pregnant women. *Neuroendocr. Lett* **37**, 70–77 (2016).

112. Fedele, L. & Brand, T. The Intrinsic Cardiac Nervous System and Its Role in Cardiac Pacemaking and Conduction. *J. Cardiovasc. Dev. Dis. 2020, Vol. 7, Page*

54 **7**, 54 (2020).

113. Lopez, M. U., Mitchell, J. R., Sheldon, R. S. & Tyberg, J. V. Effector mechanisms in the baroreceptor control of blood pressure. *Adv. Physiol. Educ.* **46**, 282–285 (2022).

114. Sagawa, K. The end-systolic pressure-volume relation of the ventricle: definition, modifications and clinical use. *Circulation* **63**, 1223–1227 (1981).

115. Sarnoff, S. J. & Berglund, E. Ventricular Function. *Circulation* **9**, 706–718 (1954).

116. Abboud, F. M., Heistad, D. D., Mark, A. L. & Schmid, P. G. Reflex control of the peripheral circulation. *Prog. Cardiovasc. Dis.* **18**, 371–403 (1976).

117. Kirchheim, H. R. Systemic arterial baroreceptor reflexes. *https://doi.org/10.1152/physrev.1976.56.1.100* **56**, 100–176 (1976).

118. Katz, B. Depolarization of sensory terminals and the initiation of impulses in the muscle spindle. *J. Physiol.* **111**, 261 (1950).

119. Bezold, A. von. Uber die physiologischen Wirkungen des essigsauren Veratrines. *Unterschungen aus dem Physiol.* (1867).

120. Jarisch, A. & Richter, H. Die afferenten Bahnen des Veratrineffektes in den Herznerven. *Naunyn-Schmiedebergs Arch. für Exp. Pathol. und Pharmakologie 1939 1932* **193**, 355–371 (1939).

121. Wehrwein, E. A. & Joyner, M. J. Regulation of blood pressure by the arterial baroreflex and autonomic nervous system. *Handb. Clin. Neurol.* **117**, 89–102 (2013).

122. Moertl, M. G. *et al.* Changes in haemodynamic and autonomous nervous system parameters measured non-invasively throughout normal pregnancy. *Eur. J. Obstet. Gynecol. Reprod. Biol.* **144**, (2009).

123. Chapleau, M. W., Lu, J., Hajduczok, G. & Abboud, F. M. Mechanism of baroreceptor adaptation in dogs: attenuation of adaptation by the K+ channel blocker 4-aminopyridine. *J. Physiol.* **462**, 291–306 (1993).

124. Coleridge, H. M., Coleridge, J. C., Poore, E. R., Roberts, A. M. & Schultz, H. D. Aortic wall properties and baroreceptor behaviour at normal arterial pressure and in acute hypertensive resetting in dogs. *J. Physiol.* **350**, 309–326 (1984).

125. Andresen, M. C. Short- and long-term determinants of baroreceptor function in aged normotensive and spontaneously hypertensive rats. *Circ. Res.* **54**, 750–759 (1984).

126. Mircoli, L. *et al.* Preservation of the baroreceptor heart rate reflex by chemical sympathectomy in experimental heart failure. *Circulation* **106**, 866–872 (2002).

127. Brändie, M., Wang, W. & Zucker, I. H. Hemodynamic correlates of baroreflex impairment of heart rate in experimental canine heart failure. *Basic Res. Cardiol. 1996 912* **91**, 147–154 (1996).

128. La Rovere, M. T., Porta, A. & Schwartz, P. J. Autonomic Control of the Heart and Its Clinical Impact. A Personal Perspective. *Front. Physiol.* **11**, 582 (2020).

129. Chapleau, M. W., Hajduczok, A. & Abboud, F. M. Pulsatile activation of baroreceptors causes central facilitation of baroreflex. *Am. J. Physiol. - Hear. Circ. Physiol.* **256**, (1989).

130. Min, S. *et al.* Arterial Baroreceptors Sense Blood Pressure through Decorated Aortic Claws. *Cell Rep.* **29**, 2192-2201.e3 (2019).

131. Sigg, D., Iaizzo, P., Xiao, Y. & He, B. *Cardiac electrophysiology methods and*

models. (2010).

132. Kang, C. *et al.* Technical advances in studying cardiac electrophysiology – Role of rabbit models. *Prog. Biophys. Mol. Biol.* **121**, 97–109 (2016).

133. Burridge, P. W., Keller, G., Gold, J. D. & Wu, J. C. Production of de novo cardiomyocytes: human pluripotent stem cell differentiation and direct reprogramming. *Cell Stem Cell* **10**, 16–28 (2012).

134. Matsa, E., Burridge, P. W. & Wu, J. C. Human stem cells for modeling heart disease and for drug discovery. *Sci. Transl. Med.* **6**, (2014).

135. Mordwinkin, N. M., Lee, A. S. & Wu, J. C. Patient-specific stem cells and cardiovascular drug discovery. *JAMA* **310**, 2039–2040 (2013).

136. Kapur, N. & Banach, K. Inositol-1,4,5-trisphosphate-mediated spontaneous activity in mouse embryonic stem cell-derived cardiomyocytes. *J. Physiol.* **581**, 1113–1127 (2007).

137. Méry, A. *et al.* Initiation of embryonic cardiac pacemaker activity by inositol 1,4,5-trisphosphate-dependent calcium signaling. *Mol. Biol. Cell* **16**, 2414–2423 (2005).

138. Fu, J.-D. *et al.* Crucial role of the sarcoplasmic reticulum in the developmental regulation of Ca2+ transients and contraction in cardiomyocytes derived from embryonic stem cells. *FASEB J.* **20**, 181–183 (2006).

139. Satin, J. *et al.* Calcium Handling in Human Embryonic Stem Cell-Derived Cardiomyocytes. *Stem Cells* **26**, 1961–1972 (2008).

140. Santana, W.-Z. F. & Laflamme, L. F. Local Control of Excitation-Contraction Coupling in Human Embryonic Stem Cell-Derived Cardiomyocytes. *PLoS One* **4**, 5407 (2009).

141. Liu, J., Dong Fu, J., Wah Siu, C., Li, R. A. & Dong, J. F. Functional Sarcoplasmic Reticulum for Calcium Handling of Human Embryonic Stem Cell-Derived Cardiomyocytes: Insights for Driven Maturation. *Stem Cells* **25**, 3038–3044 (2007).

142. Zhang, J. *et al.* Functional cardiomyocytes derived from human induced pluripotent stem cells. *Circ. Res.* **104**, (2009).

143. Yang, L. *et al.* Human cardiovascular progenitor cells develop from a KDR+ embryonic-stem-cell-derived population. *Nature* **453**, 524–528 (2008).

144. Sharma, A. *et al.* Use of human induced pluripotent stem cell–derived cardiomyocytes to assess drug cardiotoxicity. *Nat. Protoc. 2018 1312* **13**, 3018–3041 (2018).

145. Karakikes, I., Ameen, M., Termglinchan, V. & Wu, J. C. Human Induced Pluripotent Stem Cell–Derived Cardiomyocytes. *Circ. Res.* **117**, 80–88 (2015).

146. Ojala, M. *et al.* Mutation-specific phenotypes in hiPSC-derived cardiomyocytes carrying either myosin-binding protein C or α -tropomyosin mutation for hypertrophic cardiomyopathy. *Stem Cells Int.* **2016**, (2016).

147. Medvedev, S. P., Shevchenko, A. I. & Zakian, S. M. Induced Pluripotent Stem Cells: Problems and Advantages when Applying them in Regenerative Medicine. *Acta Naturae* **2**, 18 (2010).

148. Ellermann, C., Wolfes, J., Eckardt, L. & Frommeyer, G. Role of the rabbit whole-heart model for electrophysiologic safety pharmacology of non-cardiovascular drugs. *Europace* **23**, 828–836 (2021).

149. Lou, Q., Li, W. & Efimov, I. R. Multiparametric optical mapping of the langendorff-perfused rabbit heart. *J. Vis. Exp.* (2011) doi:10.3791/3160.

150. Kaese, S. *et al.* The ECG in cardiovascular-relevant animal models of electrophysiology. *Herzschrittmachertherapie und Elektrophysiologie* **24**, 84–91 (2013).

151. Jung, B. *et al.* A quantitative comparison of regional myocardial motion in mice, rabbits and humans using in-vivo phase contrast CMR. *J. Cardiovasc. Magn. Reson.* **14**, 1–15 (2012).

152. Bers, D. M. Cardiac Na/Ca exchange function in rabbit, mouse and man: what's the difference? *J. Mol. Cell. Cardiol.* **34**, 369–373 (2002).

153. Nattel, S., Duker, G. & Carlsson, L. Model systems for the discovery and development of antiarrhythmic drugs. *Prog. Biophys. Mol. Biol.* **98**, 328–339 (2008).

154. Nerbonne, J. M. Molecular basis of functional voltage-gated K+ channel diversity in the mammalian myocardium. *J. Physiol.* **525**, 285–298 (2000).

155. Panfilov, A. V. Is heart size a factor in ventricular fibrillation? Or how close are rabbit and human hearts? *Hear. Rhythm* **3**, 862–864 (2006).

156. Burton, R. A. B. *et al.* Microscopic magnetic resonance imaging reveals high prevalence of third coronary artery in human and rabbit heart. *EP Eur.* **14**, v73–v81 (2012).

157. Harken, A. H. *et al.* Early ischemia after complete coronary ligation in the rabbit, dog, pig, and monkey. *https://doi.org/10.1152/ajpheart.1981.241.2.H202* **10**, 202–210 (1981).

158. Valentin, J. P., Hoffmann, P., De Clerck, F., Hammond, T. G. & Hondeghem, L. Review of the predictive value of the Langendorff heart model (Screenit system) in assessing the proarrhythmic potential of drugs. *J. Pharmacol. Toxicol. Methods* **49**, 171–181 (2004).

159. Salata, J. J. *et al.* IK of rabbit ventricle is composed of two currents: evidence for IKs. *https://doi.org/10.1152/ajpheart.1996.271.6.H2477* **271**, (1996).

160. Clauss, S. *et al.* Animal models of arrhythmia: classic electrophysiology to genetically modified large animals. *Nat. Rev. Cardiol. 2019 168* **16**, 457–475 (2019).

161. Baczkó, I., Jost, N., Virág, L., Bősze, Z. & Varró, A. Rabbit models as tools for preclinical cardiac electrophysiological safety testing: Importance of repolarization reserve. *Prog. Biophys. Mol. Biol.* **121**, 157–168 (2016).

162. Odening, K. E. *et al.* Animals in cardiovascular research: important role of rabbit models in cardiac electrophysiology. *Br J Pharmacol* **41**, 2046–2061 (2020).

163. Nattel, S. The Molecular and Ionic Specificity of Antiarrhythmic Drug Actions. *J. Cardiovasc. Electrophysiol.* **10**, 272–282 (1999).

164. Bers, D. M. & Despa, S. Cardiac Myocytes Ca2+ and Na+ Regulation in Normal and Failing Hearts. *J. Pharmacol. Sci.* **100**, 315–322 (2006).

165. Bassani, J. W., Bassani, R. A. & Bers, D. M. Relaxation in rabbit and rat cardiac cells: species-dependent differences in cellular mechanisms. *J. Physiol.* **476**, 279–293 (1994).

166. Puglisi, J. L., Bassani, R. A., Bassani, J. W. M., Amin, J. N. & Bers, D. M. Temperature and relative contributions of Ca transport systems in cardiac myocyte

relaxation. *https://doi.org/10.1152/ajpheart.1996.270.5.H1772* **270**, (1996).

167. Piacentino, V. *et al.* Cellular Basis of Abnormal Calcium Transients of Failing Human Ventricular Myocytes. *Circ. Res.* **92**, 651–658 (2003).

168. Su, Z. *et al.* Comparison of sarcoplasmic reticulum Ca2+-ATPase function in human, dog, rabbit, and mouse ventricular myocytes. *J. Mol. Cell. Cardiol.* **35**, 761–767 (2003).

169. Janssen, P. M. L., Lehnart, S. E., Prestle, J. ürgen & Hasenfuss, G. Preservation of Contractile Characteristics of Human Myocardium in Multi-day Cell Culture. *J. Mol. Cell. Cardiol.* **31**, 1419–1427 (1999).

170. Maier, L. S., Bers, D. M. & Pieske, B. Differences in Ca2+-Handling and Sarcoplasmic Reticulum Ca2+-Content in Isolated Rat and Rabbit Myocardium. *J. Mol. Cell. Cardiol.* **32**, 2249–2258 (2000).

171. Pieske, B., Maier, L. S., Bers, D. M. & Hasenfuss, G. Ca2+ Handling and Sarcoplasmic Reticulum Ca2+ Content in Isolated Failing and Nonfailing Human Myocardium. *Circ. Res.* **85**, 38–46 (1999).

172. Katsnelson, L. *et al.* Sinoatrial Node Structure, Mechanics, Electrophysiology and the Chronotropic Response to Stretch in Rabbit and Mouse. *Front. Physiol.* **11**, 809 (2020).

173. Bleeker, W. K., Mackaay, A. J. C., Masson-Pevet, M., Bouman, L. N. & Becker, A. E. Functional and morphological organization of the rabbit sinus node. *Circ. Res.* **46**, 11–22 (1980).

174. Opthof, T., De Jonge, B., Jongsma, H. J. & Bouman, L. N. Functional morphology of the mammalian sinuatrial node. *Eur. Heart J.* **8**, 1249–1259 (1987).

175. Verheijck, E. E. *et al.* Distribution of Atrial and Nodal Cells Within the Rabbit Sinoatrial Node. *Circulation* **97**, 1623–1631 (1998).

176. Monfredi, O. *et al.* Electrophysiological heterogeneity of pacemaker cells in the rabbit intercaval region, including the SA node: Insights from recording multiple ion currents in each cell. *Am. J. Physiol. - Hear. Circ. Physiol.* **314**, H403–H414 (2018).

177. De Carvalho, A. P., De Mello, W. C. & Hoffman, B. F. Electrophysiological evidence for specialized fiber types in rabbit atrium. *https://doi.org/10.1152/ajplegacy.1959.196.3.483* **196**, 483–488 (1959).

178. Allessie, M. A., Bonke, F. I. M. & Schopman, F. J. G. Circus movement in rabbit atrial muscle as a mechanism of tachycardia. III. The 'leading circle' concept: a new model of circus movement in cardiac tissue without the involvement of an anatomical obstacle. *Circ. Res.* **41**, 9–18 (1977).

179. Smeets, J. L. R. M., Allessie, M. A., Lammers, W. J. E. P., Bonke, F. I. & Hollen, J. The wavelength of the cardiac impulse and reentrant arrhythmias in isolated rabbit atrium. The role of heart rate, autonomic transmitters, temperature, and potassium. *Circ. Res.* **58**, 96–108 (1986).

180. Li, G. R., Feng, J., Wang, Z., Fermini, B. & Nattel, S. Comparative mechanisms of 4-aminopyridine-resistant Ito in human and rabbit atrial myocytes. *https://doi.org/10.1152/ajpheart.1995.269.2.H463* **269**, (1995).

181. Fermini, B., Wang, Z., Duan, D. & Nattel, S. Differences in rate dependence of transient outward current in rabbit and human atrium. *https://doi.org/10.1152/ajpheart.1992.263.6.H1747* **263**, (1992).

182. Bordas, R. *et al.* Rabbit-specific ventricular model of cardiac electrophysiological function including specialized conduction system. *Prog. Biophys. Mol. Biol.* **107**, 90–100 (2011).

183. Pogwizd, S. M., Qi, M., Yuan, W., Samarel, A. M. & Bers, D. M. Upregulation of Na(+)/Ca(2+) exchanger expression and function in an arrhythmogenic rabbit model of heart failure. *Circ. Res.* **85**, 1009–1019 (1999).

184. Mahaffey, K. W., Raya, T. E., Pennock, G. D., Morkin, E. & Goldman, S. Left ventricular performance and remodeling in rabbits after myocardial infarction. Effects of a thyroid hormone analogue. *Circulation* **91**, 794–801 (1995).

185. Shah, A. S. *et al.* Intracoronary Adenovirus-Mediated Delivery and Overexpression of the β2-Adrenergic Receptor in the Heart. *Circulation* **101**, 408–414 (2000).

186. Jover, B., McGrath, B. P. & Ludbrook, J. Haemodynamic and metabolic responses to near-maximal treadmill exercise. *Clin. Exp. Pharmacol. Physiol.* **14**, 811–823 (1987).

187. Gaustad, S. E., Rolim, N. & Wisløff, U. A valid and reproducible protocol for testing maximal oxygen uptake in rabbits. *Eur. J. Cardiovasc. Prev. Rehabil.* **17**, 83–88 (2010).

188. Flamm, S. D. *et al.* Redistribution of regional and organ blood volume and effect on cardiac function in relation to upright exercise intensity in healthy human subjects. *Circulation* **81**, 1550–1559 (1990).

189. Stratton, J. R., Levy, W. C., Cerqueira, M. D., Schwartz, R. S. & Abrass, I. B. Cardiovascular responses to exercise. Effects of aging and exercise training in healthy men. *Circulation* **89**, 1648–1655 (1994).

190. Milani-Nejad, N. & Janssen, P. M. L. Small and large animal models in cardiac contraction research: Advantages and disadvantages. *Pharmacol. Ther.* **141**, 235–249 (2014).

191. Wang, Z. *et al.* Potential Molecular Basis of Different Physiological Properties of the Transient Outward K+ Current in Rabbit and Human Atrial Myocytes. *Circ. Res.* **84**, 551–561 (1999).

192. Zicha, S. *et al.* Molecular basis of species-specific expression of repolarizing K + currents in the heart. *Am. J. Physiol. - Hear. Circ. Physiol.* **285**, 1641–1649 (2003).

193. Cazorla, O. *et al.* Differential Expression of Cardiac Titin Isoforms and Modulation of Cellular Stiffness. *Circ. Res.* **86**, 59–67 (2000).

194. Neagoe, C., Opitz, C. A., Makarenko, I. & Linke, W. A. Gigantic variety: expression patterns of titin isoforms in striated muscles and consequences for myofibrillar passive stiffness. *J. Muscle Res. Cell Motil. 2003 242* **24**, 175–189 (2003).

195. Makarenko, I. *et al.* Passive Stiffness Changes Caused by Upregulation of Compliant Titin Isoforms in Human Dilated Cardiomyopathy Hearts. *Circ. Res.* **95**, 708–716 (2004).

196. Nagueh, S. F. *et al.* Altered Titin Expression, Myocardial Stiffness, and Left Ventricular Function in Patients With Dilated Cardiomyopathy. *Circulation* **110**, 155–162 (2004).

197. Egido, J. *et al.* Animal models of cardiovascular diseases. *J. Biomed. Biotechnol.* **2011**, (2011).

198. Takamatsu, T. Arrhythmogenic substrates in myocardial infarct. *Pathol. Int.* **58**, 533–543 (2008).

199. Ytrehus, K. *et al.* Rat and rabbit heart infarction: effects of anesthesia, perfusate, risk zone, and method of infarct sizing. *Am. J. Physiol.* **267**, (1994).

200. Volk, T., Nguyen, T. H. D., Schultz, J. H., Faulhaber, J. & Ehmke, H. Regional alterations of repolarizing K+ currents among the left ventricular free wall of rats with ascending aortic stenosis. *J. Physiol.* **530**, 443 (2001).

201. Gómez, A. M. *et al.* Modulation of electrical heterogeneity by compensated hypertrophy in rat left ventricle. *Am. J. Physiol.* **272**, (1997).

202. Mészáros, J., Ryder, K. O. & Hart, G. Transient outward current in catecholamine-induced cardiac hypertrophy in the rat. *Am. J. Physiol.* **271**, (1996).

203. Boixel, C. *et al.* Fibrosis of the left atria during progression of heart failure is associated with increased matrix metalloproteinases in the rat. *J. Am. Coll. Cardiol.* **42**, 336–344 (2003).

204. Yamashita, T. *et al.* Thrombomodulin and tissue factor pathway inhibitor in endocardium of rapidly paced rat atria. *Circulation* **108**, 2450–2452 (2003).

205. Yamashita, T. *et al.* Short-term effects of rapid pacing on mRNA level of voltage-dependent K(+) channels in rat atrium: electrical remodeling in paroxysmal atrial tachycardia. *Circulation* **101**, 2007–2014 (2000).

206. Shattock, M. J. & Bers, D. M. Rat vs. rabbit ventricle: Ca flux and intracellular Na assessed by ion-selective microelectrodes. *Am. J. Physiol.* **256**, (1989).

207. Wettwer, E. *et al.* Transient outward current in human and rat ventricular myocytes. *Cardiovasc. Res.* **27**, 1662–1669 (1993).

208. Kögler, H. *et al.* Mechanical load-dependent regulation of gene expression in monocrotaline-induced right ventricular hypertrophy in the rat. *Circ. Res.* **93**, 230–237 (2003).

209. Hessel, M. H. M., Steendijk, P., Den Adel, B., Schutte, C. I. & Van Der Laarse, A. Characterization of right ventricular function after monocrotaline-induced pulmonary hypertension in the intact rat. *Am. J. Physiol. - Hear. Circ. Physiol.* **291**, (2006).

210. Seyfarth, T. *et al.* The Cardiac β -Adrenoceptor-G-protein(s)-adenylyl Cyclase System in Monocrotaline-treated Rats. *J. Mol. Cell. Cardiol.* **32**, 2315–2326 (2000).

211. Redout, E. M. *et al.* Right-ventricular failure is associated with increased mitochondrial complex II activity and production of reactive oxygen species. *Cardiovasc. Res.* **75**, 770–781 (2007).

212. Nerbonne, J. M. & Kass, R. S. Molecular physiology of cardiac repolarization. *Physiol. Rev.* **85**, 1205–1253 (2005).

213. Janse, M. J., Opthof, T. & Kleber, A. G. Animal models of cardiac arrhythmias. *Cardiovasc. Res.* **39**, 165–177 (1998).

214. Knollmann, B. C., Schober, T., Petersen, A. O., Sirenko, S. G. & Franz, M. R. Action potential characterization in intact mouse heart: Steady-state cycle length dependence and electrical restitution. *Am. J. Physiol. - Hear. Circ. Physiol.* **292**, 614–621 (2007).

215. Knollmann, B. C., Katchman, A. N. & Franz, M. R. Monophasic Action Potential Recordings from Intact Mouse Heart: Validation, Regional Heterogeneity, and

Relation to Refractoriness. *J. Cardiovasc. Electrophysiol.* **12**, 1286–1294 (2001).

216. Pleger, S. T. *et al.* Stable Myocardial-Specific AAV6-S100A1 Gene Therapy Results in Chronic Functional Heart Failure Rescue. *Circulation* **115**, 2506–2515 (2007).

217. Elnakish, M. T., Hassanain, H. H. & Janssen, P. M. L. Vascular remodeling-associated hypertension leads to left ventricular hypertrophy and contractile dysfunction in profilin-1 transgenic mice. *J. Cardiovasc. Pharmacol.* **60**, 544–552 (2012).

218. Rafael-Fortney, J. A. *et al.* Early Treatment With Lisinopril and Spironolactone Preserves Cardiac and Skeletal Muscle in Duchenne Muscular Dystrophy Mice. *Circulation* **124**, 582–588 (2011).

219. Moon, H. *et al.* Noninvasive assessment of myocardial inflammation by cardiovascular magnetic resonance in a rat model of experimental autoimmune myocarditis. *Circulation* **125**, 2603–2612 (2012).

220. Fischer, R. *et al.* Angiotensin II-induced sudden arrhythmic death and electrical remodeling. *Am. J. Physiol. - Hear. Circ. Physiol.* **293**, 1242–1253 (2007).

221. Georgakopoulos, D. & Kass, D. A. Minimal force-frequency modulation of inotropy and relaxation of in situ murine heart. *J. Physiol.* **534**, 535–545 (2001).

222. Joho, S. *et al.* Left ventricular pressure-volume relationship in conscious mice. *Am. J. Physiol. - Hear. Circ. Physiol.* **292**, 369–377 (2007).

223. Lieber, S. C. *et al.* Cardiac dysfunction in aging conscious rats: Altered cardiac cytoskeletal proteins as a potential mechanism. *Am. J. Physiol. - Hear. Circ. Physiol.* **295**, 860–866 (2008).

224. Ostergaard, G., Hansen, H. N. & Ottesen, J. L. *Physiological, Hematological, and Clinical Chemistry Parameters, Including Conversion Factors. Handbook of Laboratory Animal Science, Volume I* (CRC Press, 2010). doi:10.1201/B10416.

225. Liu, J., Dobrzynski, H., Yanni, J., Boyett, M. R. & Lei, M. Organisation of the mouse sinoatrial node: structure and expression of HCN channels. *Cardiovasc. Res.* **73**, 729–738 (2007).

226. Hao, X. *et al.* TGF-β1-mediated fibrosis and ion channel remodeling are key mechanisms in producing the sinus node dysfunction associated with SCN5A deficiency and aging. *Circ. Arrhythm. Electrophysiol.* **4**, 397–406 (2011).

227. Glukhov, A. V. *et al.* Calsequestrin 2 deletion causes sinoatrial node dysfunction and atrial arrhythmias associated with altered sarcoplasmic reticulum calcium cycling and degenerative fibrosis within the mouse atrial pacemaker complex1. *Eur. Heart J.* **36**, 686-697a (2015).

228. Zadelaar, S. *et al.* Mouse Models for Atherosclerosis and Pharmaceutical Modifiers. *Arterioscler. Thromb. Vasc. Biol.* **27**, 1706–1721 (2007).

229. Bullard, T. A. *et al.* Identification of Nogo as a novel indicator of heart failure. *Physiol. Genomics* **32**, 182–189 (2008).

230. Unsld, B. *et al.* Age-dependent changes in contractile function and passive elastic properties of myocardium from mice lacking muscle LIM protein (MLP). *Eur. J. Heart Fail.* **14**, 430–437 (2012).

231. de Lange, W. J., Grimes, A. C., Hegge, L. F. & Ralphe, C. J. Ablation of cardiac myosin-binding protein-C accelerates contractile kinetics in engineered cardiac tissue. *J. Gen. Physiol.* **141**, 73–84 (2013).

232. Sarkar, S. *et al.* Myocardial cell death and regeneration during progression of cardiac hypertrophy to heart failure. *J. Biol. Chem.* **279**, 52630–52642 (2004).

233. Elliott, J. F. *et al.* Autoimmune cardiomyopathy and heart block develop spontaneously in HLA-DQ8 transgenic IAbeta knockout NOD mice. *Proc. Natl. Acad. Sci. U. S. A.* **100**, 13447–13452 (2003).

234. Fayssoil, A. *et al.* Cardiac characterization of mdx mice using high-resolution doppler echocardiography. *J. Ultrasound Med.* **32**, 757–761 (2013).

235. Delfín, D. A. *et al.* Improvement of cardiac contractile function by peptide-based inhibition of NF-κB in the utrophin/dystrophin-deficient murine model of muscular dystrophy. *J. Transl. Med.* **9**, (2011).

236. Larcher, T. *et al.* Characterization of dystrophin deficient rats: a new model for Duchenne muscular dystrophy. *PLoS One* **9**, (2014).

237. Janssen, P. M. L., Hiranandani, N., Mays, T. A. & Rafael-Fortney, J. A. Utrophin deficiency worsens cardiac contractile dysfunction present in dystrophin-deficient mdx mice. *Am. J. Physiol. Heart Circ. Physiol.* **289**, (2005).

238. Berry, S. E., Andruszkiewicz, P., Chun, J. L. & Hong, J. Nestin expression in end-stage disease in dystrophin-deficient heart: implications for regeneration from endogenous cardiac stem cells. *Stem Cells Transl. Med.* **2**, 848–861 (2013).

239. Nitahara-Kasahara, Y. *et al.* Dystrophic mdx mice develop severe cardiac and respiratory dysfunction following genetic ablation of the anti-inflammatory cytokine IL-10. *Hum. Mol. Genet.* **23**, 3990–4000 (2014).

240. Ozcan, C., Battaglia, E., Young, R. & Suzuki, G. LKB1 knockout mouse develops spontaneous atrial fibrillation and provides mechanistic insights into human disease process. *J. Am. Heart Assoc.* **4**, (2015).

241. Wakimoto, H. *et al.* Induction of atrial tachycardia and fibrillation in the mouse heart. *Cardiovasc. Res.* **50**, 463–473 (2001).

242. Kovoor, P. *et al.* Evaluation of the role of I(KACh) in atrial fibrillation using a mouse knockout model. *J. Am. Coll. Cardiol.* **37**, 2136–2143 (2001).

243. Li, L., Chu, G., Kranias, E. G. & Bers, D. M. Cardiac myocyte calcium transport in phospholamban knockout mouse: Relaxation and endogenous CaMKII effects. *Am. J. Physiol. - Hear. Circ. Physiol.* **274**, (1998).

244. Edwards, A. G. & Louch, W. E. Species-dependent mechanisms of cardiac arrhythmia: A cellular focus. *Clin. Med. Insights Cardiol.* **11**, (2017).

245. Ni, L. *et al.* Atrial-Specific Gene Delivery Using an Adeno-Associated Viral Vector. *Circ. Res.* **124**, 256–262 (2019).

246. Podliesna, S., Bezzina, C. R. & Lodder, E. M. Complex Genetics of Cardiovascular Traits in Mice: F2-Mapping of QTLs and Their Underlying Genes. *Methods Mol. Biol.* **1488**, 431–454 (2017).

247. Nicod, J. *et al.* Genome-wide association of multiple complex traits in outbred mice by ultra-low-coverage sequencing. *Nat. Genet. 2016 488* **48**, 912–918 (2016).

248. Adriaens, M. E. *et al.* Systems Genetics Approaches in Rat Identify Novel Genes and Gene Networks Associated With Cardiac Conduction. *J. Am. Heart Assoc.* **7**, (2018).

249. Odening, K. E. *et al.* ESC working group on cardiac cellular electrophysiology position paper: relevance, opportunities, and limitations of experimental models for cardiac electrophysiology research. *EP Eur.* **23**, 1795–1814 (2021).

250. Nerbonne, J. M. Studying Cardiac Arrhythmias in the Mouse—A Reasonable Model for Probing Mechanisms? *Trends Cardiovasc. Med.* **14**, 83–93 (2004).

251. Glukhov, A. V., Flagg, T. P., Fedorov, V. V., Efimov, I. R. & Nichols, C. G. Differential KATP channel pharmacology in intact mouse heart. *J. Mol. Cell. Cardiol.* **48**, 152–160 (2010).

252. Glukhov, A. V. *et al.* Transmural Dispersion of Repolarization in Failing and Nonfailing Human Ventricle. *Circ. Res.* **106**, 981–991 (2010).

253. Fedorov, V. V. *et al.* Effects of KATP channel openers diazoxide and pinacidil in coronary-perfused atria and ventricles from failing and non-failing human hearts. *J. Mol. Cell. Cardiol.* **51**, 215–225 (2011).

254. Hamilton, N. & Ianuzzo, C. D. Contractile and calcium regulating capacities of myocardia of different sized mammals scale with resting heart rate. *Mol. Cell. Biochem. 1991 1062* **106**, 133–141 (1991).

255. Alpert, N. R. *et al.* Molecular mechanics of mouse cardiac myosin isoforms. *Am. J. Physiol. - Hear. Circ. Physiol.* **283**, 1446–1454 (2002).

256. Wang, J. *et al.* Modification of Myosin Gene Expression by Imidapril in Failing Heart due to Myocardial Infarction. *J. Mol. Cell. Cardiol.* **34**, 847–857 (2002).

257. Krenz, M. *et al.* Analysis of myosin heavy chain functionality in the heart. *J. Biol. Chem.* **278**, 17466–17474 (2003).

258. Lemon, D. D., Papst, P. J., Joly, K., Plato, C. F. & McKinsey, T. A. A high-performance liquid chromatography assay for quantification of cardiac myosin heavy chain isoform protein expression. *Anal. Biochem.* **408**, 132–135 (2011).

259. Milani-Nejad, N., Xu, Y., Davis, J. P., Campbell, K. S. & Janssen, P. M. L. Effect of muscle length on cross-bridge kinetics in intact cardiac trabeculae at body temperature. *J. Gen. Physiol.* **141**, 133–139 (2013).

260. Rundell, V. L. M., Manaves, V., Martin, A. F. & De Tombe, P. P. Impact of β-myosin heavy chain isoform expression on cross-bridge cycling kinetics. *Am. J. Physiol. - Hear. Circ. Physiol.* **288**, 896–903 (2005).

261. Locher, M. R. *et al.* Determination of rate constants for turnover of myosin isoforms in rat myocardium: Implications for in vivo contractile kinetics. *Am. J. Physiol. - Hear. Circ. Physiol.* **297**, 247–256 (2009).

262. Miyata, S., Minobe, W., Bristow, M. R. & Leinwand, L. A. Myosin Heavy Chain Isoform Expression in the Failing and Nonfailing Human Heart. *Circ. Res.* **86**, 386–390 (2000).

263. Reiser, P. J., Portman, M. A., Ning, X. H. & Moravec, C. S. Human cardiac myosin heavy chain isoforms in fetal and failing adult atria and ventricles. *Am. J. Physiol. - Hear. Circ. Physiol.* **280**, (2001).

264. Echeazarra, L., Hortigón-Vinagre, M. P., Casis, O. & Gallego, M. Adult and Developing Zebrafish as Suitable Models for Cardiac Electrophysiology and Pathology in Research and Industry. *Front. Physiol.* **11**, 1692 (2021).

265. Gut, P., Reischauer, S., Stainier, D. Y. R. & Arnaout, R. Little fish, big data: Zebrafish as a model for cardiovascular and metabolic disease. *Physiol. Rev.* **97**, 889–938 (2017).

266. Stoyek, M. R. & Quinn, T. A. One fish, two fish, red fish, blue fish*: Zebrafish as a model for cardiac research. *Progress in Biophysics and Molecular Biology* vol. 138 1–2 (2018).

267. Rafferty, S. A. & Quinn, T. A. A beginner's guide to understanding and implementing the genetic modification of zebrafish. *Progress in Biophysics and Molecular Biology* vol. 138 3–19 (2018).
268. Stoyek, M. R., Rafferty, S. A. & Quinn, T. A. *Genetically modified zebrafish as experimental model*. (CRC Press, 2021).
269. Howe, K. *et al.* The zebrafish reference genome sequence and its relationship to the human genome. **496**, 498–503 (2013).
270. Ravens, U. Ionic basis of cardiac electrophysiology in zebrafish compared to human hearts. *Prog. Biophys. Mol. Biol.* **138**, 38–44 (2018).
271. Vornanen, M. & Hassinen, M. Zebrafish heart as a model for human cardiac electrophysiology. *https://doi.org/10.1080/19336950.2015.1121335* **10**, 101–110 (2016).
272. Rayani, K. *et al.* Zebrafish as a model of mammalian cardiac function: Optically mapping the interplay of temperature and rate on voltage and calcium dynamics. **138**, 69–90 (2018).
273. van Opbergen, C. J. M., van der Voorn, S. M., Vos, M. A., de Boer, T. P. & van Veen, T. A. B. Cardiac Ca2+ signalling in zebrafish: Translation of findings to man. *Prog. Biophys. Mol. Biol.* **138**, 45–58 (2018).
274. Arrenberg, A. B., Stainier, D. Y. R., Baier, H. & Huisken, J. Optogenetic control of cardiac function. *Science (80-.).* **330**, 971–974 (2010).
275. Tessadori, F. *et al.* Identification and functional characterization of cardiac pacemaker cells in zebrafish. *PLoS One* **7**, (2012).
276. Stoyek, M. R., Croll, R. P. & Smith, F. M. Intrinsic and extrinsic innervation of the heart in zebrafish (Danio rerio). *J. Comp. Neurol.* **523**, 1683–1700 (2015).
277. Stoyek, M. R., Quinn, T. A., Croll, R. P. & Smith, F. M. Zebrafish heart as a model to study the integrative autonomic control of pacemaker function. *Am. J. Physiol. Heart Circ. Physiol.* **311**, H676–H688 (2016).
278. Nahia, K. A. *et al.* Genomic and physiological analyses of the zebrafish atrioventricular canal reveal molecular building blocks of the secondary pacemaker region. **78**, 6669–6687 (2021).
279. Burkhard, S., van Eif, V., Garric, L., Christoffels, V. M. & Bakkers, J. On the Evolution of the Cardiac Pacemaker. *J. Cardiovasc. Dev. Dis.* **4**, (2017).
280. Martin, K. E. & Waxman, J. S. Atrial and Sinoatrial Node Development in the Zebrafish Heart. *J. Cardiovasc. Dev. Dis.* **8**, 1–17 (2021).
281. Minhas, R. *et al.* Transcriptome profile of the sinoatrial ring reveals conserved and novel genetic programs of the zebrafish pacemaker. *BMC Genomics* **22**, (2021).
282. Baker, K., Warren, K. S., Yellen, G. & Fishman, M. C. Defective 'pacemaker' current (Ih) in a zebrafish mutant with a slow heart rate. *Proc. Natl. Acad. Sci. U. S. A.* **94**, 4554–4559 (1997).
283. Warren, K. S., Baker, K. & Fishman, M. C. The slow mo mutation reduces pacemaker current and heart rate in adult zebrafish. *Am. J. Physiol. Heart Circ. Physiol.* **281**, (2001).
284. Marchant, J. L. & Farrell, A. P. Membrane and calcium clock mechanisms contribute variably as a function of temperature to setting cardiac pacemaker rate in zebrafish Danio rerio. *J. Fish Biol.* **95**, 1265–1274 (2019).
285. González-Rosa, J. M. Zebrafish Models of Cardiac Disease: From Fortuitous

Mutants to Precision Medicine. *Circ. Res.* **130**, 1803–1826 (2022).

286. Chablais, F., Veit, J., Rainer, G. & Jawiska, A. The zebrafish heart regenerates after cryoinjury-induced myocardial infarction. *BMC Dev. Biol.* **11**, (2011).

287. Giardoglou, P. & Beis, D. On Zebrafish Disease Models and Matters of the Heart. *Biomedicines* **7**, (2019).

288. Bakkers, J. Zebrafish as a model to study cardiac development and human cardiac disease. *Cardiovasc. Res.* **91**, 279–288 (2011).

289. Nemtsas, P., Wettwer, E., Christ, T., Weidinger, G. & Ravens, U. Adult zebrafish heart as a model for human heart? An electrophysiological study. *J. Mol. Cell. Cardiol.* **48**, 161–171 (2010).

290. Hu, N., Yost, H. J. & Clark, E. B. Cardiac morphology and blood pressure in the adult zebrafish. *Anat. Rec.* **264**, 1–12 (2001).

291. Genge, C. E. *et al.* The Zebrafish Heart as a Model of Mammalian Cardiac Function. *Rev. Physiol. Biochem. Pharmacol.* **171**, 99–136 (2016).

292. Brette, F. *et al.* Characterization of isolated ventricular myocytes from adult zebrafish (Danio rerio). *Biochem. Biophys. Res. Commun.* **374**, 143–146 (2008).

293. Bovo, E., Dvornikov, A. V., Mazurek, S. R., de Tombe, P. P. & Zima, A. V. Mechanisms of Ca2+ handling in zebrafish ventricular myocytes. *Pflügers Arch. - Eur. J. Physiol. 2013 46512* **465**, 1775–1784 (2013).

294. Haustein, M. *et al.* Excitation-Contraction Coupling in Zebrafish Ventricular Myocardium Is Regulated by Trans-Sarcolemmal Ca2+ Influx and Sarcoplasmic Reticulum Ca2+ Release. *PLoS One* **10**, e0125654 (2015).

295. Llach, A. *et al.* Detection, Properties, and Frequency of Local Calcium Release from the Sarcoplasmic Reticulum in Teleost Cardiomyocytes. *PLoS One* **6**, e23708 (2011).

296. Zhang, P.-C., Llach, A., Sheng, X. Y., Hove-Madsen, L. & Tibbits, G. F. Calcium handling in zebrafish ventricular myocytes. *https://doi.org/10.1152/ajpregu.00377.2010* **300**, 56–66 (2011).

297. Sidi, S., Busch-Nentwich, E., Friedrich, R., Schoenberger, U. & Nicolson, T. gemini encodes a zebrafish L-type calcium channel that localizes at sensory hair cell ribbon synapses. *J. Neurosci.* **24**, 4213–4223 (2004).

298. Cribbs, L. L. *et al.* Cloning and characterization of alpha1H from human heart, a member of the T-type Ca2+ channel gene family. *Circ. Res.* **83**, 103–109 (1998).

299. Ono, K. & Iijima, T. Cardiac T-type Ca(2+) channels in the heart. *J. Mol. Cell. Cardiol.* **48**, 65–70 (2010).

300. Alday, A. *et al.* Ionic channels underlying the ventricular action potential in zebrafish embryo. **84**, 26–31 (2014).

301. Auman, H. J. & Yelon, D. Vertebrate Organogenesis: Getting the Heart into Shape. *Curr. Biol.* **14**, R152–R153 (2004).

302. Srivastava, D. Making or breaking the heart: from lineage determination to morphogenesis. *Cell* **126**, 1037–1048 (2006).

303. Christoffels, V. M. *et al.* Chamber formation and morphogenesis in the developing mammalian heart. *Dev. Biol.* **223**, 266–278 (2000).

304. Bakkers, J., Verhoeven, M. C. & Abdelilah-Seyfried, S. Shaping the zebrafish heart: from left-right axis specification to epithelial tissue morphogenesis. *Dev. Biol.* **330**, 213–220 (2009).

305. Jacot, J. G., Martin, J. C. & Hunt, D. L. Mechanobiology of cardiomyocyte development. *J. Biomech.* **43**, 93–98 (2010).

306. Santhanakrishnan, A. & Miller, L. A. Fluid Dynamics of Heart Development. *Cell Biochem. Biophys.* **61**, 1–22 (2011).

307. Chiou, K. K. *et al.* Mechanical signaling coordinates the embryonic heartbeat. *Proc. Natl. Acad. Sci. U. S. A.* **113**, 8939–8944 (2016).

308. Lehoux, S., Castier, Y. & Tedgui, A. Molecular mechanisms of the vascular responses to haemodynamic forces. *J. Intern. Med.* **259**, 381–392 (2006).

309. Granados-Riveron, J. T. & Brook, J. D. Formation, contraction, and mechanotransduction of myofribrils in cardiac development: Clues from genetics. *Biochem. Res. Int.* (2012) doi:10.1155/2012/504906.

310. Staudt, D. & Stainier, D. Uncovering the molecular and cellular mechanisms of heart development using the zebrafish. *Annual Review of Genetics* vol. 46 397–418 (2012).

311. Taber, L. A. Morphomechanics: transforming tubes into organs. *Curr. Opin. Genet. Dev.* **27**, 7–13 (2014).

312. Kimmel, C. B., Ballard, W. W., Kimmel, S. R., Ullmann, B. & Schilling, T. F. Stages of embryonic development of the zebrafish. *Dev. Dyn.* **203**, 253–310 (1995).

313. Lindsey, S. E., Butcher, J. T. & Yalcin, H. C. Mechanical regulation of cardiac development. *Front. Physiol.* **5**, (2014).

314. Brown, D. R., Samsa, L. A., Qian, L. & Liu, J. Advances in the Study of Heart Development and Disease Using Zebrafish. *J. Cardiovasc. Dev. Dis. 2016, Vol. 3, Page 13* **3**, 13 (2016).

315. Wittig, J. G. & Münsterberg, A. The Early Stages of Heart Development: Insights from Chicken Embryos. **3**, 12 (2016).

316. Reckova, M. *et al.* Hemodynamics Is a Key Epigenetic Factor in Development of the Cardiac Conduction System. *Circ. Res.* **93**, 77–85 (2003).

317. Sedmera, D. *et al.* Developmental transitions in electrical activation patterns in chick embryonic heart. *Anat. Rec. A. Discov. Mol. Cell. Evol. Biol.* **280**, 1001–1009 (2004).

318. Midgett, M. & Rugonyi, S. Congenital heart malformations induced by hemodynamic altering surgical interventions. *Front. Physiol.* **5 JUL**, 287 (2014).

319. Bartman, T. & Hove, J. Mechanics and function in heart morphogenesis. *Dev. Dyn.* **233**, 373–381 (2005).

320. Samsa, L. A. *et al.* Cardiac contraction activates endocardial Notch signaling to modulate chamber maturation in zebrafish. *Development* **142**, 4080–4091 (2015).

321. Grego-Bessa, J. *et al.* Notch Signaling Is Essential for Ventricular Chamber Development. *Dev. Cell* **12**, 415–429 (2007).

322. Lee, J. *et al.* Spatial and temporal variations in hemodynamic forces initiate cardiac trabeculation. *JCI insight* **3**, (2018).

323. Lin, Y. F., Swinburne, I. & Yelon, D. Multiple influences of blood flow on cardiomyocyte hypertrophy in the embryonic zebrafish heart. *Dev. Biol.* **362**, 242–253 (2012).

324. Soufan, A. T. *et al.* Regionalized Sequence of Myocardial Cell Growth and Proliferation Characterizes Early Chamber Formation. *Circ. Res.* **99**, 545–552

(2006).

325. Auman, H. J. *et al.* Functional Modulation of Cardiac Form through Regionally Confined Cell Shape Changes. *PLOS Biol.* **5**, e53 (2007).

326. Yu, J. G. & Russell, B. Cardiomyocyte remodeling and sarcomere addition after uniaxial static strain in vitro. *J. Histochem. Cytochem.* **53**, 839–844 (2005).

327. Russell, B., Curtis, M. W., Koshman, Y. E. & Samarel, A. M. Mechanical stress-induced sarcomere assembly for cardiac muscle growth in length and width. *J. Mol. Cell. Cardiol.* **48**, 817–823 (2010).

328. Fishman, M. C. & Chien, K. R. Fashioning the vertebrate heart: earliest embryonic decisions. *Development* **124**, 2099–2117 (1997).

329. Schoenebeck, J. J. & Yelon, D. Illuminating cardiac development: Advances in imaging add new dimensions to the utility of zebrafish genetics. *Semin. Cell Dev. Biol.* **18**, 27–35 (2007).

330. Pierpont, M. E. *et al.* Genetic Basis for Congenital Heart Defects: Current Knowledge. *Circulation* **115**, 3015–3038 (2007).

331. Chico, T. J. A., Ingham, P. W. & Crossman, D. C. Modeling Cardiovascular Disease in the Zebrafish. *Trends Cardiovasc. Med.* **18**, 150–155 (2008).

332. Bournele, D. & Beis, D. Zebrafish models of cardiovascular disease. *Heart Fail. Rev.* **21**, 803–813 (2016).

333. Choi, W. Y. *et al.* In vivo monitoring of cardiomyocyte proliferation to identify chemical modifiers of heart regeneration. *Development* **140**, 660–666 (2013).

334. Sakaue-Sawano, A. *et al.* Visualizing spatiotemporal dynamics of multicellular cell-cycle progression. *Cell* **132**, 487–498 (2008).

335. Han, Y. *et al.* Vitamin D Stimulates Cardiomyocyte Proliferation and Controls Organ Size and Regeneration in Zebrafish. *Dev. Cell* **48**, 853-863.e5 (2019).

336. Armour, J. A. Potential clinical relevance of the 'little brain' on the mammalian heart. *Exp. Physiol.* **93**, 165–176 (2008).

337. Stoyek, M. R., Hortells, L. & Quinn, T. A. From Mice to Mainframes: Experimental Models for Investigation of the Intracardiac Nervous System. *J. Cardiovasc. Dev. Dis. 2021, Vol. 8, Page 149* **8**, 149 (2021).

338. Ardell, J. L. & Armour, J. A. Neurocardiology: Structure-Based Function. *Compr. Physiol.* **6**, 1635–1653 (2016).

339. Armour, J. A. Cardiac neuronal hierarchy in health and disease. *Am. J. Physiol. - Regul. Integr. Comp. Physiol.* **287**, (2004).

340. Irisawa, H. Comparative physiology of the cardiac pacemaker mechanism. *Physiol. Rev.* **58**, 461–498 (1978).

341. Li, N. *et al.* Molecular Mapping of Sinoatrial Node HCN Channel Expression in the Human Heart. **8**, 1219–1227 (2015).

342. Mangoni, M. E. & Nargeot, J. Genesis and regulation of the heart automaticity. **88**, 919–982 (2008).

343. Pauza, D. H. *et al.* Neuroanatomy of the murine cardiac conduction system: A combined stereomicroscopic and fluorescence immunohistochemical study. *Auton. Neurosci.* **176**, 32–47 (2013).

344. Pauza, D. H. *et al.* Innervation of sinoatrial nodal cardiomyocytes in mouse. A combined approach using immunofluorescent and electron microscopy. **75**, 188–197 (2014).

345. van Opbergen, C. J. M. *et al.* Optogenetic sensors in the zebrafish heart: A novel in vivo electrophysiological tool to study cardiac arrhythmogenesis. *Theranostics* **8**, 4750–4764 (2018).

346. Stoyek, M. R., Rog-Zielinska, E. A. & Quinn, T. A. Age-associated changes in electrical function of the zebrafish heart. *Prog. Biophys. Mol. Biol.* **138**, 91–104 (2018).

347. Messier, J. E., Chen, H., Cai, Z. L. & Xue, M. Targeting light-gated chloride channels to neuronal somatodendritic domain reduces their excitatory effect in the axon. *Elife* **7**, (2018).

348. Quinn, T. A. & Kohl, P. The Bainbridge effect: stretching our understanding of cardiac pacemaking for more than a century. *J. Physiol.* (2022) doi:10.1113/JP283610.

349. Quinn, T. A. & Kohl, P. Mechano-sensitivity of cardiac pacemaker function: Pathophysiological relevance, experimental implications, and conceptual integration with other mechanisms of rhythmicity. *Prog. Biophys. Mol. Biol.* **110**, 257–268 (2012).

350. Katz, A. M. Ernest Henry Starling, his predecessors, and the 'Law of the Heart'. *Circulation* **106**, 2986–2992 (2002).

351. Boselli, F., Freund, J. B. & Vermot, J. Blood flow mechanics in cardiovascular development. *Cell. Mol. Life Sci.* **72**, 2545–2559 (2015).

352. Culver, J. C. & Dickinson, M. E. The Effects of Hemodynamic Force on Embryonic Development. *Microcirculation* **17**, 164–178 (2010).

353. Happe, C. L. & Engler, A. J. Mechanical Forces Reshape Differentiation Cues That Guide Cardiomyogenesis. *Circ. Res.* **118**, 296–310 (2016).

354. Duchemin, A. L., Vignes, H., Vermot, J. & Chow, R. Mechanotransduction in cardiovascular morphogenesis and tissue engineering. *Curr. Opin. Genet. Dev.* **57**, 106–116 (2019).

355. Bressan, M. C., Louie, J. D. & Mikawa, T. Hemodynamic forces regulate developmental patterning of atrial conduction. *PLoS One* **9**, (2014).

356. Mikawa, T. & Hurtado, R. Development of the cardiac conduction system. *Semin. Cell Dev. Biol.* **18**, 90–100 (2007).

357. Opthof, T. Embryological development of pacemaker hierarchy and membrane currents related to the function of the adult sinus node: implications for autonomic modulation of biopacemakers. *Med. Biol. Eng. Comput.* **45**, 119–132 (2007).

358. Jansen, H. J. & Quinn, T. A. Cellular Sinoatrial Node and Atrioventricular Node Activity in the Heart. *Encycl. Cardiovasc. Res. Med.* 1–17 (2017) doi:10.1016/B978-0-12-801238-3.99759-9.

359. Quinn, T. A., Magder, S., Quinn, T. A. & Magder, S. Physiology of Heart Rate. *Springer* 87–106 (2021) doi:10.1007/978-3-030-73387-2_7.

360. Rajala, G. M., Kalbfleisch, J. H. & Kaplan, S. Evidence that blood pressure controls heart rate in the chick embryo prior to neural control. *Development* **36**, 685–695 (1976).

361. Rajala, G. M., Pinter, M. J. & Kaplan, S. Response of the quiescent heart tube to mechanical stretch in the intact chick embryo. *Dev. Biol.* **61**, 330–337 (1977).

362. Kowalski, W. J., Pekkan, K., Tinney, J. P. & Keller, B. B. Investigating developmental cardiovascular biomechanics and the origins of congenital heart

defects. *Front. Physiol.* **5**, 408 (2014).

363. Hu, N., Sedmera, D., Yost, H. J. & Clark, E. B. Structure and Function of the Developing Zebrafish Heart. (2000) doi:10.1002/1097-0185.

364. Parichy, D. M., Elizondo, M. R., Mills, M. G., Gordon, T. N. & Engeszer, R. E. Normal table of postembryonic zebrafish development: staging by externally visible anatomy of the living fish. *Dev. Dyn.* **238**, 2975–3015 (2009).

365. Li, R., Baek, K. I., Chang, C. C., Zhou, B. & Hsiai, T. K. Mechanosensitive Pathways Involved in Cardiovascular Development and Homeostasis in Zebrafish. *J. Vasc. Res.* **56**, 273–283 (2019).

366. Sidhwani, P. & Yelon, D. Fluid forces shape the embryonic heart: Insights from zebrafish. *Curr. Top. Dev. Biol.* **132**, 395–416 (2019).

367. Stainier, D. Y. R. *et al.* Mutations affecting the formation and function of the cardiovascular system in the zebrafish embryo. *Development* **123**, 285–292 (1996).

368. Baillie, J. S., Stoyek, M. R. & Quinn, T. A. Seeing the Light: The Use of Zebrafish for Optogenetic Studies of the Heart. *Front. Physiol.* **12**, 2001 (2021).

369. Stoyek, M. R. *et al.* Drivers of Sinoatrial Node Automaticity in Zebrafish: Comparison With Mechanisms of Mammalian Pacemaker Function. *Front. Physiol.* **0**, 175 (2022).

370. Werdich, A. A. *et al.* The zebrafish as a novel animal model to study the molecular mechanisms of mechano-electrical feedback in the heart. *Prog. Biophys. Mol. Biol.* **110**, 154–165 (2012).

371. Boselli, F., Steed, E., Freund, J. B. & Vermot, J. Anisotropic shear stress patterns predict the orientation of convergent tissue movements in the embryonic heart. *Development* **144**, 4322–4327 (2017).

372. Fukui, H. *et al.* Bioelectric signaling and the control of cardiac cell identity in response to mechanical forces. *Science* **374**, 351–354 (2021).

373. Bornhorst, D. *et al.* Biomechanical signaling within the developing zebrafish heart attunes endocardial growth to myocardial chamber dimensions. *Nat. Commun.* **10**, (2019).

374. Yang, J., Hartjes, K. A., Nelson, T. J. & Xu, X. Cessation of contraction induces cardiomyocyte remodeling during zebrafish cardiogenesis. *Am. J. Physiol. Heart Circ. Physiol.* **306**, (2014).

375. Foo, Y. Y. *et al.* Effects of extended pharmacological disruption of zebrafish embryonic heart biomechanical environment on cardiac function, morphology, and gene expression. *Dev. Dyn.* **250**, 1759–1777 (2021).

376. Duchemin, A.-L., Vignes, H. & Vermot, J. Mechanically activated piezo channels modulate outflow tract valve development through the Yap1 and Klf2-Notch signaling axis. *Elife* **8**, (2019).

377. Watanabe, M. *et al.* Probing the Electrophysiology of the Developing Heart. *J. Cardiovasc. Dev. Dis.* **3**, (2016).

378. Gendernalik, A., Zebhi, B., Ahuja, N., Garrity, D. & Bark, D. In Vivo Pressurization of the Zebrafish Embryonic Heart as a Tool to Characterize Tissue Properties During Development. *Ann. Biomed. Eng.* **49**, 834–845 (2021).

379. Tobita, K., Schrode, E. A., Tinney, J. P., Garrison, J. B. & Keller, B. B. Regional passive ventricular stress-strain relations during development of altered loads in chick embryo. *Am. J. Physiol. Heart Circ. Physiol.* **282**, (2002).

380. Bark, D. L., Johnson, B., Garrity, D. & Dasi, L. P. Valveless pumping mechanics of the embryonic heart during cardiac looping: Pressure and flow through micro-PIV. *J. Biomech.* **50**, 50–55 (2017).

381. Glickman, N. S. & Yelon, D. Cardiac development in zebrafish: coordination of form and function. *Semin. Cell Dev. Biol.* **13**, 507–513 (2002).

382. Quinn, T. A. *et al.* Minimum Information about a Cardiac Electrophysiology Experiment (MICEE): Standardised reporting for model reproducibility, interoperability, and data sharing. *Prog. Biophys. Mol. Biol.* **107**, 4–10 (2011).

383. White, R. M. *et al.* Transparent Adult Zebrafish as a Tool for In Vivo Transplantation Analysis. *Cell Stem Cell* **2**, 183–189 (2008).

384. Verhasselt, S. *et al.* Discovery of (S)-3'-hydroxyblebbistatin and (S)-3'-aminoblebbistatin: polar myosin II inhibitors with superior research tool properties. *Org. Biomol. Chem.* **15**, 2104–2118 (2017).

385. Chi, N. C. *et al.* Genetic and Physiologic Dissection of the Vertebrate Cardiac Conduction System. *PLOS Biol.* **6**, e109 (2008).

386. Hou, J. H., Kralj, J. M., Douglass, A. D., Engert, F. & Cohen, A. E. Simultaneous mapping of membrane voltage and calcium in zebrafish heart in vivo reveals chamber-specific developmental transitions in ionic currents. *Front. Physiol.* **5**, 344 (2014).

387. Roth, G. A. *et al.* Global Burden of Cardiovascular Diseases and Risk Factors, 1990–2019: Update From the GBD 2019 Study. *J. Am. Coll. Cardiol.* **76**, 2982–3021 (2020).

388. Liu, J. & Stainier, D. Y. R. Zebrafish in the Study of Early Cardiac Development. *Circ. Res.* **110**, 870–874 (2012).

389. Lin, E. *et al.* Optical mapping of the electrical activity of isolated adult zebrafish hearts: Acute effects of temperature. *Am. J. Physiol. - Regul. Integr. Comp. Physiol.* **306**, 823–836 (2014).

390. Srivastava, D. & Olson, E. N. A genetic blueprint for cardiac development. *Nat. 2000 4076801* **407**, 221–226 (2000).

391. Goenezen, S., Rennie, M. Y. & Rugonyi, S. Biomechanics of Early Cardiac Development. *Biomech. Model. Mechanobiol.* **11**, 1187 (2012).

392. Schleich, J. M., Abdulla, T., Summers, R. & Houyel, L. An overview of cardiac morphogenesis. *Arch. Cardiovasc. Dis.* **106**, 612–623 (2013).

393. Brade, T., Pane, L. S., Moretti, A., Chien, K. R. & Laugwitz, K. L. Embryonic Heart Progenitors and Cardiogenesis. *Cold Spring Harb. Perspect. Med.* **3**, (2013).

394. Männer, J. & Yelbuz, T. M. Functional Morphology of the Cardiac Jelly in the Tubular Heart of Vertebrate Embryos. *J. Cardiovasc. Dev. Dis. 2019, Vol. 6, Page 12* **6**, 12 (2019).

395. Samsa, L. A., Yang, B. & Liu, J. Embryonic cardiac chamber maturation: Trabeculation, conduction, and cardiomyocyte proliferation. *Am. J. Med. Genet. Part C Semin. Med. Genet.* **163**, 157–168 (2013).

396. Mammoto, T. & Ingber, D. E. Mechanical control of tissue and organ development. *Development* **137**, 1407–1420 (2010).

397. Yalcin, H. C., Amindari, A., Butcher, J. T., Althani, A. & Yacoub, M. Heart function and hemodynamic analysis for zebrafish embryos. *Dev. Dyn.* **246**, 868–880 (2017).

398. Wyczalkowski, M. A., Chen, Z., Filas, B. A., Varner, V. D. & Taber, L. A. Computational models for mechanics of morphogenesis. *Birth Defects Res. Part C Embryo Today Rev.* **96**, 132–152 (2012).

399. Moorman, A. F. M. & Christoffels, V. M. Cardiac chamber formation: Development, genes, and evolution. *Physiol. Rev.* **83**, 1223–1267 (2003).

400. Virani, S. S. *et al.* Heart Disease and Stroke Statistics—2020 Update: A Report From the American Heart Association. *Circulation* **141**, E139–E596 (2020).

401. Kopf, P. G. & Walker, M. K. Overview of Developmental Heart Defects by Dioxins, PCBs, and Pesticides. *http://dx.doi.org/10.1080/10590500903310195* **27**, 276–285 (2009).

402. Zhu, H., Kartiko, S. & Finnell, R. H. Importance of gene–environment interactions in the etiology of selected birth defects. *Clin. Genet.* **75**, 409–423 (2009).

403. Dewan, P. & Gupta, P. Burden of congenital rubella syndrome (CRS) in India: A systematic review. *Indian Pediatr.* **49**, 377–399 (2012).

404. Watts, D. H. *et al.* Birth defects among a cohort of infants born to HIV-infected women on antiretroviral medication. *J. Perinat. Med.* **39**, 163–170 (2011).

405. Madsen, N. L., Schwartz, S. M., Lewin, M. B. & Mueller, B. A. Prepregnancy Body Mass Index and Congenital Heart Defects among Offspring: A Population-based Study. *Congenit. Heart Dis.* **8**, 131–141 (2013).

406. Wren, C., Birrell, G. & Hawthorne, G. Cardiovascular malformations in infants of diabetic mothers. *Heart* **89**, 1217–1220 (2003).

407. Smedts, H. P. M. *et al.* A derangement of the maternal lipid profile is associated with an elevated risk of congenital heart disease in the offspring. *Nutr. Metab. Cardiovasc. Dis.* **22**, 477–485 (2012).

408. Fishman, M. C. & Olson, E. N. Parsing the heart: Genetic modules for organ assembly. *Cell* **91**, 153–156 (1997).

409. Evans, S. M., Yelon, D., Conlon, F. L. & Kirby, M. L. Myocardial Lineage Development. *Circ. Res.* **107**, 1428–1444 (2010).

410. Vincent, S. D. & Buckingham, M. E. How to Make a Heart: The Origin and Regulation of Cardiac Progenitor Cells. *Curr. Top. Dev. Biol.* **90**, 1–41 (2010).

411. Singh, N. *et al.* Histone deacetylase 3 regulates smooth muscle differentiation in neural crest cells and development of the cardiac outflow tract. *Circ. Res.* **109**, 1240–1249 (2011).

412. Von Gise, A. & Pu, W. T. Endocardial and Epicardial Epithelial to Mesenchymal Transitions in Heart Development and Disease. *Circ. Res.* **110**, 1628–1645 (2012).

413. Munshi, N. V. Gene Regulatory Networks in Cardiac Conduction System Development. *Circ. Res.* **110**, 1525–1537 (2012).

414. Kim, K. H., Rosen, A., Bruneau, B. G., Hui, C. C. & Backx, P. H. Iroquois homeodomain transcription factors in heart development and function. *Circ. Res.* **110**, 1513–1524 (2012).

415. Boettger, T. & Braun, T. A New Level of Complexity. *Circ. Res.* **110**, 1000–1013 (2012).

416. Jarrell, D. K., Lennon, M. L. & Jacot, J. G. Epigenetics and Mechanobiology in Heart Development and Congenital Heart Disease. *Dis. 2019, Vol. 7, Page 52* **7**, 52 (2019).

417. Paolini, A. & Abdelilah-Seyfried, S. The mechanobiology of zebrafish cardiac

valve leaflet formation. *Curr. Opin. Cell Biol.* **55**, 52–58 (2018).

418. Jorba, I. *et al.* In Vitro Methods to Model Cardiac Mechanobiology in Health and Disease. *Tissue Eng. - Part C Methods* **27**, 139–151 (2021).

419. Leone, M., Magadum, A. & Engel, F. B. Cardiomyocyte proliferation in cardiac development and regeneration: A guide to methodologies and interpretations. *Am. J. Physiol. - Hear. Circ. Physiol.* **309**, H1237–H1250 (2015).

420. Voorhees, A. P. & Han, H. C. Biomechanics of Cardiac Function. *Compr. Physiol.* **5**, 1623 (2015).

421. Hove, J. R. *et al.* Intracardiac fluid forces are an essential epigenetic factor for embryonic cardiogenesis. *Nat. 2003 4216919* **421**, 172–177 (2003).

422. Craig, M. P., Gilday, S. D., Dabiri, D. & Hove, J. R. An Optimized Method for Delivering Flow Tracer Particles to Intravital Fluid Environments in the Developing Zebrafish. *https://home.liebertpub.com/zeb* **9**, 108–119 (2012).

423. Benslimane, F. M. *et al.* Cardiac function and blood flow hemodynamics assessment of zebrafish (Danio rerio) using high-speed video microscopy. *Micron* **136**, 102876 (2020).

424. Antinucci, P. & Hindges, R. A crystal-clear zebrafish for in vivo imaging. *Sci. Reports 2016 61* **6**, 1–10 (2016).

425. D'Agati, G. *et al.* A defect in the mitochondrial protein mpv17 underlies the transparent casper zebrafish. *Dev. Biol.* **430**, 11 (2017).

426. Fukuta, H. & Little, W. C. The cardiac cycle and the physiologic basis of left ventricular contraction, ejection, relaxation, and filling. *Heart Fail. Clin.* **4**, 1–11 (2008).

427. Mason, D. T. Regulation of cardiac performance in clinical heart disease. Interactions between contractile state mechanical abnormalities and ventricular compensatory mechanisms. *Am. J. Cardiol.* **32**, 437–448 (1973).

428. Vincent, J. L. Understanding cardiac output. *Crit. Care* **12**, (2008).

429. Hulshof, H. G. *et al.* Acute impact of changes to hemodynamic load on the left ventricular strain-volume relationship in young and older men. *Am. J. Physiol. - Regul. Integr. Comp. Physiol.* **318**, R743–R750 (2020).

430. Burns, A. T., La Gerche, A., D'hooge, J., Macisaac, A. I. & Prior, D. L. Left ventricular strain and strain rate: characterization of the effect of load in human subjects. *Eur. J. Echocardiogr.* **11**, 283–289 (2010).

431. Donal, E. *et al.* Influence of afterload on left ventricular radial and longitudinal systolic functions: a two-dimensional strain imaging study. *Eur. J. Echocardiogr.* **10**, 914–921 (2009).

432. Dong, S. J. *et al.* Independent effects of preload, afterload, and contractility on left ventricular torsion. *Am. J. Physiol. - Hear. Circ. Physiol.* **277**, (1999).

433. Lord, R. *et al.* Reduced left ventricular filling following blood volume extraction does not result in compensatory augmentation of cardiac mechanics. *Exp. Physiol.* **103**, 495–501 (2018).

434. Oki, T. *et al.* Effect of an acute increase in afterload on left ventricular regional wall motion velocity in healthy subjects. *J. Am. Soc. Echocardiogr.* **12**, 476–483 (1999).

435. Williams, A. M., Shave, R. E., Stembridge, M. & Eves, N. D. Females have greater left ventricular twist mechanics than males during acute reductions to

preload. *Am. J. Physiol. - Hear. Circ. Physiol.* **311**, H76–H84 (2016).

436. Sharma, S., Merghani, A. & Mont, L. Exercise and the heart: The good, the bad, and the ugly. *European Heart Journal* vol. 36 1445–1453 (2015).

437. Duncker, D. J. & Bache, R. J. Regulation of coronary blood flow during exercise. *Physiol. Rev.* **88**, 1009–1086 (2008).

438. Liu, J. *et al.* A dual role for ErbB2 signaling in cardiac trabeculation. *Development* **137**, 3867–3875 (2010).

439. Kugler, E. *et al.* The effect of absent blood flow on the zebrafish cerebral and trunk vasculature. *Vasc. Biol.* **3**, 1 (2021).

440. Stainier, D. Y. R. & Fishman, M. C. The zebrafish as a model system to study cardiovascular development. *Trends Cardiovasc. Med.* **4**, 207–212 (1994).

441. Youm, J. B. *et al.* Role of Stretch-activated Channels in the Heart: Action Potential and Ca2+ Transients. *Mechanosensitivity in Cells and Tissues* (2005).

442. Kamkin, A., Kiseleva, I. & Isenberg, G. Stretch-activated currents in ventricular myocytes: amplitude and arrhythmogenic effects increase with hypertrophy. *Cardiovasc. Res.* **48**, 409–420 (2000).

443. Zhang, Y. H. *et al.* Stretch-activated and background non-selective cation channels in rat atrial myocytes. *J. Physiol.* **523 Pt 3**, 607–619 (2000).

444. Fuchs, F. & Smith, S. H. Calcium, cross-bridges, and the Frank-Starling relationship. *News Physiol. Sci.* **16**, 5–10 (2001).

445. Anwar, A. M., Geleijnse, M. L., Soliman, O. I. I., Nemes, A. & Ten Cate, F. J. Left atrial Frank–Starling law assessed by real-time, three-dimensional echocardiographic left atrial volume changes. *Heart* **93**, 1393 (2007).

446. Nystoriak, M. A. & Bhatnagar, A. Cardiovascular Effects and Benefits of Exercise. *Frontiers in Cardiovascular Medicine* vol. 5 135 (2018).

447. Crandall, C. G. & Wilson, T. E. Human Cardiovascular Responses to Passive Heat Stress. *Compr. Physiol.* **5**, 17 (2015).

448. Peshkovsky, C., Totong, R. & Yelon, D. Dependence of cardiac trabeculation on neuregulin signaling and blood flow in zebrafish. *Dev. Dyn.* **240**, 446–456 (2011).

449. Madamanchi, A. β-Adrenergic receptor signaling in cardiac function and heart failure. *McGill J. Med. MJM* **10**, 99 (2007).

450. Zhang, R., Zhao, J., Mandveno, A. & Potter, J. D. Cardiac Troponin I Phosphorylation Increases the Rate of Cardiac Muscle Relaxation. *Circ. Res.* **76**, 1028–1035 (1995).

451. Ginsburg, K. S. & Bers, D. M. Modulation of excitation–contraction coupling by isoproterenol in cardiomyocytes with controlled SR Ca2+ load and Ca2+ current trigger. *J. Physiol.* **556**, 463–480 (2004).

452. Kent, K. M., Epstein, S. E., Cooper, T. & Jacobowitz, D. M. Cholinergic innervation of the canine and human ventricular conducting system. Anatomic and electrophysiologic correlations. *Circulation* **50**, 948–955 (1974).

453. Roy, A., Guatimosim, S., Prado, V. F., Gros, R. & Prado, M. A. M. Cholinergic Activity as a New Target in Diseases of the Heart. *Mol. Med.* **20**, 527 (2014).

454. Brodde, O. E., Bruck, H., Leineweber, K. & Seyfarth, T. Presence, distribution and physiological function of adrenergic and muscarinic receptor subtypes in the human heart. *Basic Res. Cardiol.* **96**, 528–538 (2001).

455. Agonstoni, E., Chinnock, J. E., De Daly, M. B. & Murray, J. G. Functional and

histological studies of the vagus nerve and its branches to the heart, lungs and abdominal viscera in the cat. *J. Physiol.* **135**, 182–205 (1957).

456. Sunahara, R. K., Dessauer, C. W. & Gilman, A. G. Complexity and diversity of mammalian adenylyl cyclases. *Annu. Rev. Pharmacol. Toxicol.* **36**, 461–480 (1996).

457. Ishikawa, Y. & Homcy, C. J. The adenylyl cyclases as integrators of transmembrane signal transduction. *Circ. Res.* **80**, 297–304 (1997).

458. DiFrancesco, D., Ducouret, P. & Robinson, R. B. Muscarinic modulation of cardiac rate at low acetylcholine concentrations. *Science* **243**, 669–671 (1989).

459. DiFrancesco, D. & Tromba, C. Acetylcholine inhibits activation of the cardiac hyperpolarizing-activated current, if. *Pflugers Arch.* **410**, 139–142 (1987).

460. Sigurdson, W., Ruknudin, A. & Sachs, F. Calcium imaging of mechanically induced fluxes in tissue-cultured chick heart: role of stretch-activated ion channels. *Am. J. Physiol.* **262**, (1992).

461. Baumgarten, C. M. Origin of Mechanotransduction: Stretch-Activated Ion Channels. (2013).

462. Sadoshima, J. & Izumo, S. The cellular and molecular response of cardiac myocytes to mechanical stress. *Annu. Rev. Physiol.* **59**, 551–571 (1997).

463. Kudoh, S. *et al.* Stretch-modulation of second messengers: Effects on cardiomyocyte ion transport. *Prog. Biophys. Mol. Biol.* **82**, 57–66 (2003).

464. Briggs, J. P. The zebrafish: a new model organism for integrative physiology. *https://doi.org/10.1152/ajpregu.00589.2001* **282**, (2002).

465. Dvornikov, A. V., Dewan, S., Alekhina, O. V., Pickett, F. B. & De Tombe, P. P. Novel approaches to determine contractile function of the isolated adult zebrafish ventricular cardiac myocyte. *J. Physiol.* **592**, 1949–1956 (2014).

466. Rider, S. A. *et al.* Techniques for the in vivo assessment of cardio-renal function in zebrafish (Danio rerio) larvae. *J. Physiol.* **590**, 1803–1809 (2012).

467. Nakai, J., Ohkura, M. & Imoto, K. A high signal-to-noise Ca 2+ probe composed of a single green fluorescent protein. *Nat. Biotechnol. 2001 192* **19**, 137–141 (2001).

468. Kovács, M., Tóth, J., Hetényi, C., Málnási-Csizmadia, A. & Seller, J. R. Mechanism of blebbistatin inhibition of myosin II. *J. Biol. Chem.* **279**, 35557–35563 (2004).

469. Nilsson, S. Comparative anatomy of the autonomic nervous system. *Auton. Neurosci.* **165**, 3–9 (2011).

470. Zhan, H., Zhang, J., Jiao, A. & Wang, Q. Stretch-activated current in human atrial myocytes and Na+ current and mechano-gated channels' current in myofibroblasts alter myocyte mechanical behavior: A computational study. *Biomed. Eng. Online* **18**, 1–15 (2019).

471. Salmon, A. H. J., Mays, J. L., Dalton, G. R., Jones, J. V & Levi, A. J. Effect of streptomycin on wall-stress-induced arrhythmias in the working rat heart. *Cardiovasc. Res.* **34**, 493–503 (1997).

472. Eckardt, L., Kirchhof, P., Breithardt, G. & Haverkamp, W. Load-induced changes in repolarization: evidence from experimental and clinical data. *Basic Res. Cardiol. 2001 964* **96**, 369–380 (2001).

473. Trapero, I. *et al.* Effect of Streptomycin on Stretch-Induced Change in Myocardial

Activation During Ventricular Fibrillation. *Rev. Española Cardiol. (English Ed.* **61**, 201–205 (2008).

474.   Ninio, D. M. & Saint, D. A. The role of stretch-activated channels in atrial fibrillation and the impact of intracellular acidosis. *Progress in Biophysics and Molecular Biology* vol. 97 401–416 (2008).

475.   Kim, D. Y., White, E. & Saint, D. A. Increased mechanically-induced ectopy in the hypertrophied heart. *Prog. Biophys. Mol. Biol.* **110**, 331–339 (2012).

476.   Franz, M. R., Cima, R., Wang, D., Profitt, D. & Kurz, R. Electrophysiological effects of myocardial stretch and mechanical determinants of stretch-activated arrhythmias. *Circulation* **86**, 968–978 (1992).

477.   Franz, M. R., Burkhoff, D., Yue, D. T. & Sagawa, K. Mechanically induced action potential changes and arrhythmia in isolated and in situ canine hearts. *Cardiovasc. Res.* **23**, 213–223 (1989).

478.   Stacy, G. P., Jobe, R. L., Taylor, L. K. & Hansen, D. E. Stretch-induced depolarizations as a trigger of arrhythmias in isolated canine left ventricles. *Am. J. Physiol.* **263**, (1992).

479.   Boland, J. & Troquet, J. Intracellular action potential changes induced in both ventricles of the rat by an acute right ventricular pressure overload. *Cardiovasc. Res.* **14**, 735–740 (1980).

480.   Tung, L. & Zou, S. Influence of stretch on excitation threshold of single frog ventricular cells. *Exp. Physiol.* **80**, 221–235 (1995).

481.   White, E. *et al.* The effects of increasing cell length on auxotonic contractions; membrane potential and intracellular calcium transients in single guinea-pig ventricular myocytes. *Exp. Physiol.* **78**, 65–78 (1993).

482.   Kamkin, A., Kiseleva, I. & Isenberg, G. Ion selectivity of stretch-activated cation currents in mouse ventricular myocytes. *Pflugers Arch.* **446**, 220–231 (2003).

483.   Zeng, T., Bett, G. C. L. & Sachs, F. Stretch-activated whole cell currents in adult rat cardiac myocytes. *Am. J. Physiol. Heart Circ. Physiol.* **278**, (2000).

484.   Gamble, J., Taylor, P. B. & Kenno, K. A. Myocardial stretch alters twitch characteristics and Ca2+ loading of sarcoplasmic reticulum in rat ventricular muscle. *Cardiovasc. Res.* **26**, 865–870 (1992).

485.   Iribe, G. & Kohl, P. Axial stretch enhances sarcoplasmic reticulum Ca2+ leak and cellular Ca2+ reuptake in guinea pig ventricular myocytes: Experiments and models. *Prog. Biophys. Mol. Biol.* **97**, 298–311 (2008).

486.   Iribe, G. *et al.* Axial stretch of rat single ventricular cardiomyocytes causes an acute and transient increase in Ca2+ spark rate. *Circ. Res.* **104**, 787–795 (2009).

487.   Prosser, B. L., Ward, C. W. & Lederer, W. J. X-ROS signaling: Rapid mechano-chemo transduction in heart. *Science (80-.).* **333**, 1440–1445 (2011).

488.   Prosser, B. L., Ward, C. W. & Jonathan Lederer, W. X-ROS signalling is enhanced and graded by cyclic cardiomyocyte stretch. *Cardiovasc. Res.* **98**, 307–314 (2013).

489.   Belmonte, S. & Morad, M. 'Pressure–flow'-triggered intracellular Ca2+ transients in rat cardiac myocytes: possible mechanisms and role of mitochondria. *J. Physiol.* **586**, 1379–1397 (2008).

490.   Yaniv, Y. *et al.* Crosstalk between Mitochondrial and Sarcoplasmic Reticulum Ca2+ Cycling Modulates Cardiac Pacemaker Cell Automaticity. *PLoS One* **7**, e37582 (2012).

491. Guhathakurta, P., Prochniewicz, E. & Thomas, D. D. Actin-Myosin Interaction: Structure, Function and Drug Discovery. *Int. J. Mol. Sci. 2018, Vol. 19, Page 2628* **19**, 2628 (2018).

492. Iorga, B. *et al.* Micromechanical function of myofibrils isolated from skeletal and cardiac muscles of the zebrafish. *J. Gen. Physiol.* **137**, 255–270 (2011).

493. Mateja, R. D. & De Tombe, P. P. Myofilament Length-Dependent Activation Develops within 5 ms in Guinea-Pig Myocardium. *Biophys. J.* **103**, L13–L15 (2012).

494. Fedorov, V. V. *et al.* Application of blebbistatin as an excitation–contraction uncoupler for electrophysiologic study of rat and rabbit hearts. *Hear. Rhythm* **4**, 619–626 (2007).

495. Swift, L. M., Kay, M. W., Ripplinger, C. M. & Posnack, N. G. Stop the beat to see the rhythm: Excitation-contraction uncoupling in cardiac research. *Am. J. Physiol. - Hear. Circ. Physiol.* **231**, H1005–H1013 (2021).

496. Armour, J. A., Murphy, D. A., Yuan, B.-X., Macdonald, S. & Hopkins, D. A. Gross and Microscopic Anatomy of the Human Intrinsic Cardiac Nervous System. doi:10.1002/(SICI)1097-0185(199702)247:2.

497. Leger, J., Croll, R. P. & Smith, F. M. Regional Distribution and Extrinsic Innervation of Intrinsic Cardiac Neurons in the Guinea Pig. *J. Comp. Neurol* **407**, 303–317 (1999).

498. Pauza, D. H., Skripka, V., Pauziene, N. & Stropus, R. Morphology, Distribution, and Variability of the Epicardiac Neural Ganglionated Subplexuses in the Human Heart. (2000) doi:10.1002/1097-0185.

499. Steele, P. A. & Choate, J. K. Innervation of the pacemaker in guinea-pig sinoatrial node. *J. Auton. Nerv. Syst.* **47**, 177–187 (1994).

500. Steele, P. A., Gibbins, I. L. & Morris, J. L. Projections of intrinsic cardiac neurons to different targets in the guinea-pig heart. *J. Auton. Nerv. Syst.* **56**, 191–200 (1996).

501. Kember, G., Armour, J. A. & Zamir, M. Neural control of heart rate: The role of neuronal networking. *J. Theor. Biol.* **277**, 41–47 (2011).

502. Smith, F. M., McGuirt, A. S., Leger, J., Armour, J. A. & Ardell, J. L. Effects of chronic cardiac decentralization on functional properties of canine intracardiac neurons in vitro. *Am. J. Physiol. - Regul. Integr. Comp. Physiol.* **281**, (2001).

503. Ardell, J. L., Butler, C. K., Smith, F. M., Hopkins, D. A. & Armour, J. A. Activity of in vivo atrial and ventricular neurons in chronically decentralized canine hearts. *https://doi.org/10.1152/ajpheart.1991.260.3.H713* **260**, (1991).

504. Irisawa, H. Comparative Physiology of the Cardiac Pacemaker Mechanism. *REVIEWS* **58**, (1978).

505. Goldberg, J. M., Geesbreght, J. M., Randall, W. C. & Brynjolfsson, G. Sympathetically induced pacemaker shifts following sinus node excision. *Am. J. Physiol.* **224**, (1973).

506. Saito, T. & Tenma, K. Effects of left and right vagal stimulation on excitation and conduction of the carp heart (Cyprinus carpio). *J. Comp. Physiol. 1976 1111* **111**, 39–53 (1976).

507. Shibata, N. *et al.* Pacemaker Shift in the Rabbit Sinoatrial Node in Response to Vagal Nerve Stimulation. *Exp. Physiol.* **86**, 177–184 (2001).

508. Fang, X. Z. *et al.* Structure, kinetic properties and biological function of mechanosensitive Piezo channels. *Cell Biosci. 2021 111* **11**, 1–20 (2021).

509. Barrionuevo, W. R. & Burggren, W. W. O2 consumption and heart rate in developing zebrafish (Danio rerio): influence of temperature and ambient O2. *Am. J. Physiol.* **276**, (1999).

510. Jacob, E., Drexel, M., Schwerte, T. & Pelster, B. Influence of hypoxia and of hypoxemia on the development of cardiac activity in zebrafish larvae. *Am. J. Physiol. Regul. Integr. Comp. Physiol.* **283**, (2002).

511. Schwerte, T., Prem, C., Mairösl, A. & Pelster, B. Development of the sympatho-vagal balance in the cardiovascular system in zebrafish (Danio rerio) characterized by power spectrum and classical signal analysis. *J. Exp. Biol.* **209**, 1093–1100 (2006).

512. Steele, S. L. *et al.* Loss of M2 muscarinic receptor function inhibits development of hypoxic bradycardia and alters cardiac beta-adrenergic sensitivity in larval zebrafish (Danio rerio). *Am. J. Physiol. Regul. Integr. Comp. Physiol.* **297**, (2009).

513. Smith, D. G., Nilsson, S., Wahlqvist, I. & Eriksson, B. M. Nervous control of the blood pressure in the Atlantic cod, Gadus morhua. *J. Exp. Biol.* **117**, 335–347 (1985).

514. Smith, F. M. & Jones, D. R. Localization of receptors causing hypoxic bradycardia in trout (Salmo gairdneri) . *Can. J. Zool.* **56**, 1260–1265 (1978).

515. Jonz, M. G., Zachar, P. C., Da Fonte, D. F. & Mierzwa, A. S. Peripheral chemoreceptors in fish: A brief history and a look ahead. *Comp. Biochem. Physiol. A. Mol. Integr. Physiol.* **186**, 27–38 (2015).

516. Bruegmann, T. *et al.* Optogenetic control of heart muscle in vitro and in vivo. *Nat. Methods* **7**, 897–900 (2010).

517. Hofmann, B. *et al.* Light induced stimulation and delay of cardiac activity. *Lab Chip* **10**, 2588–2596 (2010).

518. Jia, Z. *et al.* Stimulating cardiac muscle by light: cardiac optogenetics by cell delivery. *Circ. Arrhythm. Electrophysiol.* **4**, 753–760 (2011).

519. Entcheva, E. & Kay, M. W. Cardiac optogenetics: a decade of enlightenment. *Nat. Rev. Cardiol.* **18**, 349 (2021).

520. Deisseroth, K. *et al.* Next-generation optical technologies for illuminating genetically targeted brain circuits. in *Journal of Neuroscience* vol. 26 10380–10386 (Society for Neuroscience, 2006).

521. Miesenböck, G. The Optogenetic Catechism. *Science (80-.).* **326**, 395–399 (2009).

522. Li, X. *et al.* Fast noninvasive activation and inhibition of neural and network activity by vertebrate rhodopsin and green algae channelrhodopsin. *Proc. Natl. Acad. Sci.* **102**, 17816–17821 (2005).

523. Nagel, G. *et al.* Light Activation of Channelrhodopsin-2 in Excitable Cells of Caenorhabditis elegans Triggers Rapid Behavioral Responses. *Curr. Biol.* **15**, 2279–2284 (2005).

524. Siegel, M. S. & Isacoff, E. Y. A Genetically Encoded Optical Probe of Membrane Voltage. *Neuron* **19**, 735–741 (1997).

525. Sakai, R., Repunte-Canonigo, V., Raj, C. D. & Knöpfel, T. Design and characterization of a DNA-encoded, voltage-sensitive fluorescent protein. *Eur. J. Neurosci.* **13**, 2314–2318 (2001).

526. Ataka, K. & Pieribone, V. A. A Genetically Targetable Fluorescent Probe of Channel Gating with Rapid Kinetics. *Biophys. J.* **82**, 509–516 (2002).

527. Miyawaki, A., Griesbeck, O., Heim, R. & Tsien, R. Y. Dynamic and quantitative Ca2+ measurements using improved cameleons. *Proc. Natl. Acad. Sci.* **96**, 2135–2140 (1999).

528. Miyawaki, A. *et al.* Fluorescent indicators for Ca2+ based on green fluorescent proteins and calmodulin. *Nature* **388**, 882–887 (1997).

529. Baird, G. S., Zacharias, D. A. & Tsien, R. Y. Circular permutation and receptor insertion within green fluorescent proteins. *Proc. Natl. Acad. Sci.* **96**, 11241–11246 (1999).

530. Nagel, G. *et al.* Channelrhodopsin-1: A Light-Gated Proton Channel in Green Algae. *Science (80-.).* **296**, 2395–2398 (2002).

531. Nagel, G. *et al.* Channelrhodopsin-2, a directly light-gated cation-selective membrane channel. *Proc. Natl. Acad. Sci.* **100**, 13940–13945 (2003).

532. Boyden, E. S., Zhang, F., Bamberg, E., Nagel, G. & Deisseroth, K. Millisecond-timescale, genetically targeted optical control of neural activity. *Nat. Neurosci. 2005 89* **8**, 1263–1268 (2005).

533. Bowley, G. *et al.* Zebrafish as a tractable model of human cardiovascular disease. *Br. J. Pharmacol.* **179**, 1–18 (2021).

534. Kithcart, A. P. & MacRae, C. A. Zebrafish assay development for cardiovascular disease mechanism and drug discovery. *Prog. Biophys. Mol. Biol.* **138**, 126–131 (2018).

535. Wolf, M. J. *et al.* Drosophila as a model for the identification of genes causing adult human heart disease. *Proc. Natl. Acad. Sci.* **103**, 1394–1399 (2006).

536. Warkman, A. S. & Krieg, P. A. Xenopus as a model system for vertebrate heart development. *Semin. Cell Dev. Biol.* **18**, 46–53 (2007).

537. Rotstein, B. & Paululat, A. On the Morphology of the Drosophila Heart. *J. Cardiovasc. Dev. Dis. 2016, Vol. 3, Page 15* **3**, 15 (2016).

538. Ishibashi, S., Kroll, K. L. & Amaya, E. A Method for Generating Transgenic Frog Embryos. *Methods Mol. Biol.* **461**, 447–466 (2008).

539. Bene, F. Del & Wyart, C. Optogenetics: A new enlightenment age for zebrafish neurobiology. *Dev. Neurobiol.* **72**, 404–414 (2012).

540. Simmich, J., Staykov, E. & Scott, E. Zebrafish as an appealing model for optogenetic studies. *Prog. Brain Res.* **196**, 145–162 (2012).

541. Portugues, R., Severi, K. E., Wyart, C. & Ahrens, M. B. Optogenetics in a transparent animal: Circuit function in the larval zebrafish. *Current Opinion in Neurobiology* vol. 23 119–126 (2013).

542. Salama, G. & Morad, M. Merocyanine 540 as an optical probe of transmembrane electrical activity in the heart. *Science (80-.).* **191**, 485–487 (1976).

543. Morad, M. & Salama, G. Optical probes of membrane potential in heart muscle. *J. Physiol.* **292**, 267–295 (1979).

544. Herron, T. J., Lee, P. & Jalife, J. Optical Imaging of Voltage and Calcium in Cardiac Cells & Tissues. *Circ. Res.* **110**, 609–623 (2012).

545. Jaimes, R. *et al.* Arrhythmias, Electrophysiology, and Optical Mapping: A technical review of optical mapping of intracellular calcium within myocardial tissue. *Am. J. Physiol. - Hear. Circ. Physiol.* **310**, H1388 (2016).

546. Berenfeld, O. & Efimov, I. Optical Mapping. *Card. Electrophysiol. Clin.* **11**, 495–510 (2019).

547. Sabeh, M. K., Kekhia, H. & MacRae, C. A. Optical Mapping in the Developing Zebrafish Heart. *Pediatr. Cardiol. 2012 336* **33**, 916–922 (2012).

548. Lin, E. *et al. Physiological phenotyping of the adult zebrafish heart*. vol. 49 100701 (2020).

549. Koopman, C. D., Zimmermann, W. H., Knöpfel, T. & de Boer, T. P. Cardiac optogenetics: using light to monitor cardiac physiology. *Basic Research in Cardiology* vol. 112 1–13 (2017).

550. Kaestner, L. *et al.* Genetically Encoded Ca2+ Indicators in Cardiac Myocytes. *Circ. Res.* **114**, 1623–1639 (2014).

551. Kaestner, L. *et al.* Genetically Encoded Voltage Indicators in Circulation Research. *Int. J. Mol. Sci. 2015, Vol. 16, Pages 21626-21642* **16**, 21626–21642 (2015).

552. Tallini, Y. N. *et al.* Imaging cellular signals in the heart in vivo: Cardiac expression of the high-signal Ca2+ indicator GCaMP2. *Proc. Natl. Acad. Sci.* **103**, 4753–4758 (2006).

553. Roell, W. *et al.* Engraftment of connexin 43-expressing cells prevents post-infarct arrhythmia. *Nat. 2007 4507171* **450**, 819–824 (2007).

554. Arnaout, R. *et al.* Zebrafish model for human long QT syndrome. *Proc. Natl. Acad. Sci.* **104**, 11316–11321 (2007).

555. Kirchmaier, B. C. *et al.* The Popeye domain containing 2 (popdc2) gene in zebrafish is required for heart and skeletal muscle development. *Dev. Biol.* **363**, 438–450 (2012).

556. Salgado-Almario, J., Vicente, M., Vincent, P., Domingo, B. & Llopis, J. Mapping Calcium Dynamics in the Heart of Zebrafish Embryos with Ratiometric Genetically Encoded Calcium Indicators. *Int. J. Mol. Sci. 2020, Vol. 21, Page 6610* **21**, 6610 (2020).

557. Tsutsui, H., Higashijima, S., Miyawaki, A. & Okamura, Y. Visualizing voltage dynamics in zebrafish heart. *J. Physiol.* **588**, 2017–2021 (2010).

558. Tsutsui, H., Karasawa, S., Okamura, Y. & Miyawaki, A. Improving membrane voltage measurements using FRET with new fluorescent proteins. *Nat. Methods 2008 58* **5**, 683–685 (2008).

559. Murata, Y., Iwasaki, H., Sasaki, M., Inaba, K. & Okamura, Y. Phosphoinositide phosphatase activity coupled to an intrinsic voltage sensor. *Nat. 2005 4357046* **435**, 1239–1243 (2005).

560. Mishina, Y., Mutoh, H., Song, C. & Knöpfel, T. Exploration of genetically encoded voltage indicators based on a chimeric voltage sensing domain. *Front. Mol. Neurosci.* **0**, 78 (2014).

561. Chen, T.-W. *et al.* Ultrasensitive fluorescent proteins for imaging neuronal activity. *Nat. 2013 4997458* **499**, 295–300 (2013).

562. Schneider-Warme, F. The power of optogenetics. *Herzschrittmachertherapie + Elektrophysiologie 2018 291* **29**, 24–29 (2018).

563. Ferenczi, E. A., Tan, X. & Huang, C. L. H. Principles of Optogenetic Methods and Their Application to Cardiac Experimental Systems. *Frontiers in Physiology* vol. 10 1096 (2019).

564. Zhang, F. *et al.* Multimodal fast optical interrogation of neural circuitry. *Nat. 2007 4467136* **446**, 633–639 (2007).

565. Govorunova, E. G., Sineshchekov, O. A., Janz, R., Liu, X. & Spudich, J. L. Natural light-gated anion channels: A family of microbial rhodopsins for advanced optogenetics. *Science (80-.).* **349**, 647–650 (2015).

566. Mohamed, G. A. *et al.* Optical inhibition of larval zebrafish behaviour with anion channelrhodopsins. **15**, 1–12 (2017).

567. Mauss, A. S., Busch, C. & Borst, A. Optogenetic Neuronal Silencing in Drosophila during Visual Processing. *Sci. Reports 2017 71* **7**, 1–12 (2017).

568. Malyshev, A. Y. *et al.* Chloride conducting light activated channel GtACR2 can produce both cessation of firing and generation of action potentials in cortical neurons in response to light. *Neurosci. Lett.* **640**, 76–80 (2017).

569. Forli, A. *et al.* Two-Photon Bidirectional Control and Imaging of Neuronal Excitability with High Spatial Resolution In Vivo. *Cell Rep.* **22**, 3087–3098 (2018).

570. Clemo, H. F., Stambler, B. S. & Baumgarten, C. M. Swelling-Activated Chloride Current Is Persistently Activated in Ventricular Myocytes From Dogs With Tachycardia-Induced Congestive Heart Failure. *Circ. Res.* **84**, 157–165 (1999).

571. Kopton, R. A. *et al.* Cardiac Electrophysiological Effects of Light-Activated Chloride Channels. *Front. Physiol.* **9**, (2018).

572. Smith, F. M., Vermeulen, M. & Cardinal, R. Long-term spinal cord stimulation modifies canine intrinsic cardiac neuronal properties and ganglionic transmission during high-frequency repetitive activation. *Physiol. Rep.* **4**, e12855 (2016).

573. Schneider-Warme, F. & Ravens, U. Using light to fight atrial fibrillation. *Cardiovasc. Res.* **114**, 635–637 (2018).

574. Govorunova, E. G., Cunha, S. R., Sineshchekov, O. A. & Spudich, J. L. Anion channelrhodopsins for inhibitory cardiac optogenetics. **6**, 1–7 (2016).

575. Baumgarten, C. M., Browe, D. M. & Ren, Z. Swelling- and Stretch-activated Chloride Channels in the Heart: Regulation and Function. *Mechanosensitivity in Cells and Tissues* (2005).

576. Wiegert, J. S., Mahn, M., Prigge, M., Printz, Y. & Yizhar, O. Silencing Neurons: Tools, Applications, and Experimental Constraints. *Neuron* **95**, 504–529 (2017).

577. Mahn, M., Prigge, M., Ron, S., Levy, R. & Yizhar, O. Biophysical constraints of optogenetic inhibition at presynaptic terminals. *Nat. Neurosci. 2016 194* **19**, 554–556 (2016).

578. Mahn, M. *et al.* High-efficiency optogenetic silencing with soma-targeted anion-conducting channelrhodopsins. *Nat. Commun. 2018 91* **9**, 1–15 (2018).

579. Bernal Sierra, Y. A. *et al.* Potassium channel-based optogenetic silencing. *Nat. Commun. 2018 91* **9**, 1–13 (2018).

580. Sineshchekov, O. A., Govorunova, E. G., Li, H. & Spudich, J. L. Gating mechanisms of a natural anion channelrhodopsin. *Proc. Natl. Acad. Sci. U. S. A.* **112**, 14236–14241 (2015).

581. Kim, Y. S. *et al.* Crystal structure of the natural anion-conducting channelrhodopsin GtACR1. *Nat. 2018 5617723* **561**, 343–348 (2018).

582. Govorunova, E. G., Sineshchekov, O. A. & Spudich, J. L. Proteomonas sulcata ACR1: A Fast Anion Channelrhodopsin. *Photochem. Photobiol.* **92**, 257–263

(2016).

583. Wietek, J., Broser, M., Krause, B. S. & Hegemann, P. Identification of a Natural Green Light Absorbing Chloride Conducting Channelrhodopsin from Proteomonas sulcata. *J. Biol. Chem.* **291**, 4121–4127 (2016).

584. Govorunova, E. G. *et al.* The Expanding Family of Natural Anion Channelrhodopsins Reveals Large Variations in Kinetics, Conductance, and Spectral Sensitivity. *Sci. Rep.* **7**, (2017).

585. Duan, D. D. Phenomics of cardiac chloride channels. *Compr. Physiol.* **3**, 667–692 (2013).

586. Johnston, C. M. *et al.* Optogenetic targeting of cardiac myocytes and non-myocytes: Tools, challenges and utility. *Prog. Biophys. Mol. Biol.* **130**, 140–149 (2017).

587. Quinn, T. A. *et al.* Electrotonic coupling of excitable and nonexcitable cells in the heart revealed by optogenetics. *Proc. Natl. Acad. Sci. U. S. A.* **113**, 14852–14857 (2016).

588. Hulsmans, M. *et al.* Macrophages Facilitate Electrical Conduction in the Heart. *Cell* **169**, 510-522.e20 (2017).

589. Deisseroth, K. Optogenetics. *Nat. Methods 2011 81* **8**, 26–29 (2010).

590. Kim, C. K., Adhikari, A. & Deisseroth, K. Integration of optogenetics with complementary methodologies in systems neuroscience. *Nat. Rev. Neurosci. 2017 184* **18**, 222–235 (2017).

591. Deisseroth, K. Optogenetics: 10 years of microbial opsins in neuroscience. *Nat. Neurosci. 2015 189* **18**, 1213–1225 (2015).

592. Vedula, V. *et al.* A method to quantify mechanobiologic forces during zebrafish cardiac development using 4-D light sheet imaging and computational modeling. *PLoS Comput. Biol.* **13**, (2017).

593. Sacconi, L. *et al.* KHz-Rate Volumetric Voltage Imaging of the Whole Zebrafish Heart. *SSRN Electron. J.* **2**, 100046 (2021).

594. Mickoleit, M. *et al.* High-resolution reconstruction of the beating zebrafish heart. *Nat. Methods* **11**, 919–922 (2014).

595. Weber, M. *et al.* Cell-accurate optical mapping across the entire developing heart. *Elife* **6**, (2017).

596. Reade, A. *et al.* TAEL: A zebrafish-optimized optogenetic gene expression system with fine spatial and temporal control. *Dev.* **144**, 345–355 (2017).

597. LaBelle, J. *et al.* TAEL 2.0: An Improved Optogenetic Expression System for Zebrafish. *Zebrafish* 20–28 (2021) doi:10.1089/zeb.2020.1951.

598. Richter, C. & Bruegmann, T. No light without the dark: Perspectives and hindrances for translation of cardiac optogenetics. *Prog. Biophys. Mol. Biol.* **154**, 39–50 (2020).

Supplemental Figure 3.1 | Absolute HR change in 2 dpf zebrafish embryo. B1 B2 B3 represents each baseline phase measurement. S1 S2 S3 represents each stretch phase measurement. There were no significant differences in HR response between baseline and stretch phase. There were also no significant differences between baseline phases. (ns = no significant difference; $p > 0.05$, * = $p \leq 0.05$, ** = $p \leq 0.01$, *** = $p \leq 0.001$).
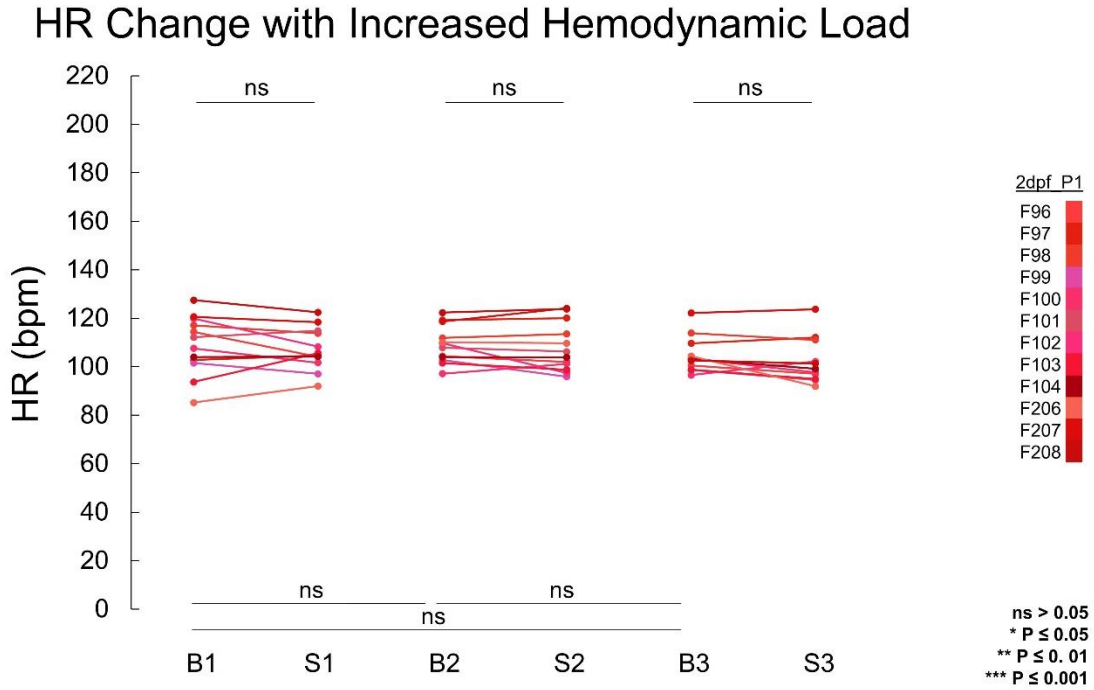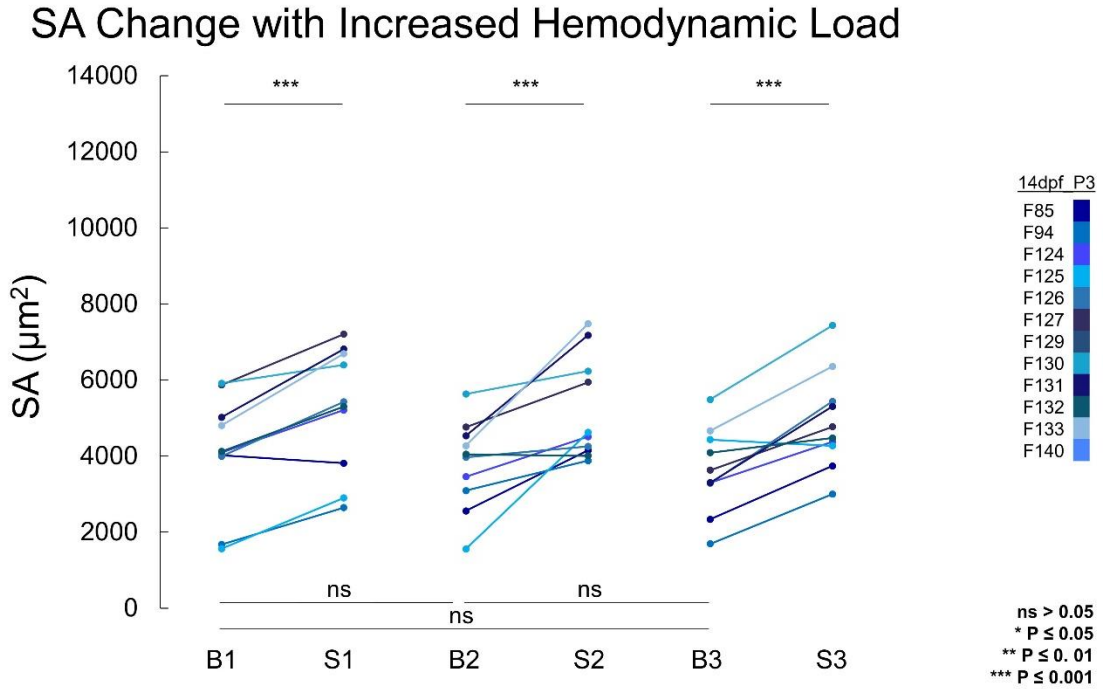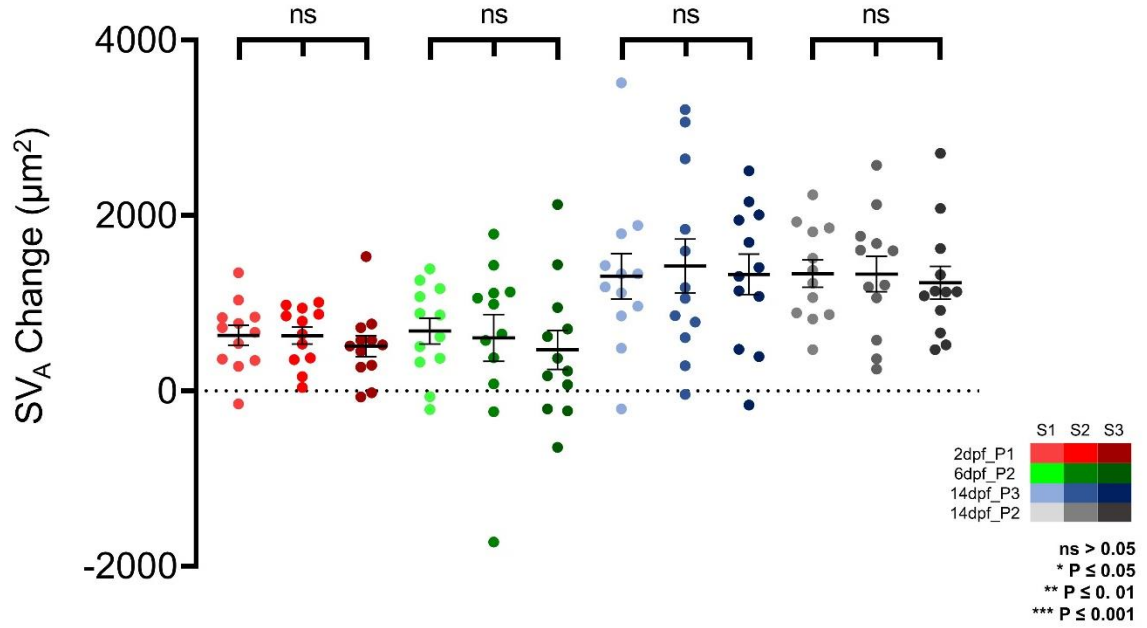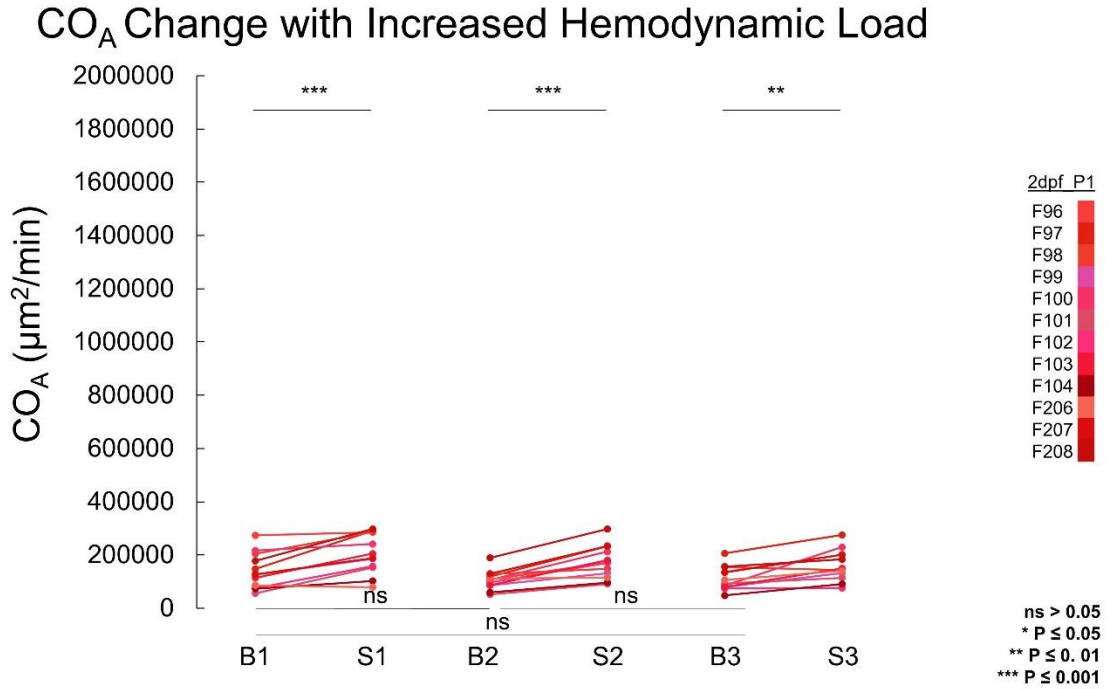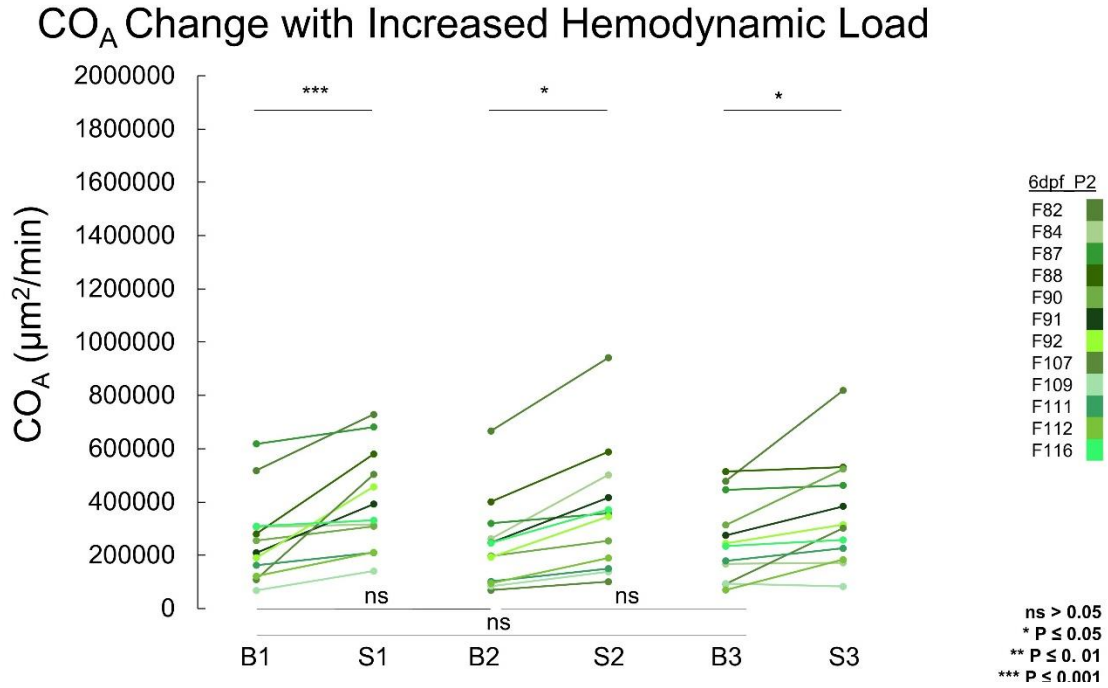
Supplemental Figure 3.2 | Absolute HR change in 6 dpf zebrafish embryo. B1 B2 B3 represents each baseline phase measurement. S1 S2 S3 represents each stretch phase measurement. There were no significant differences in HR response between B1 and S1, or B2 and S2, however, there was a significant difference between B3 and S3. There were no significant differences between baseline phases. (ns = no significant difference; p > 0.05, * = p ≤ 0.05, ** = p ≤ 0.01, *** = p ≤ 0.001).
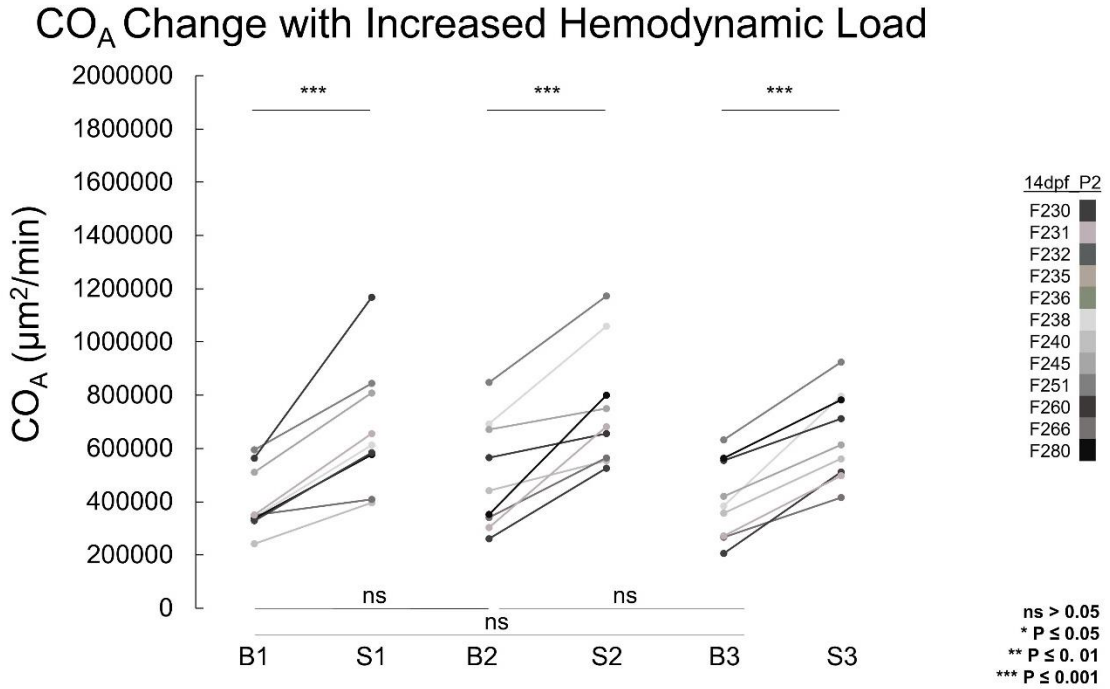

HR Change with Increased Hemodynamic Load
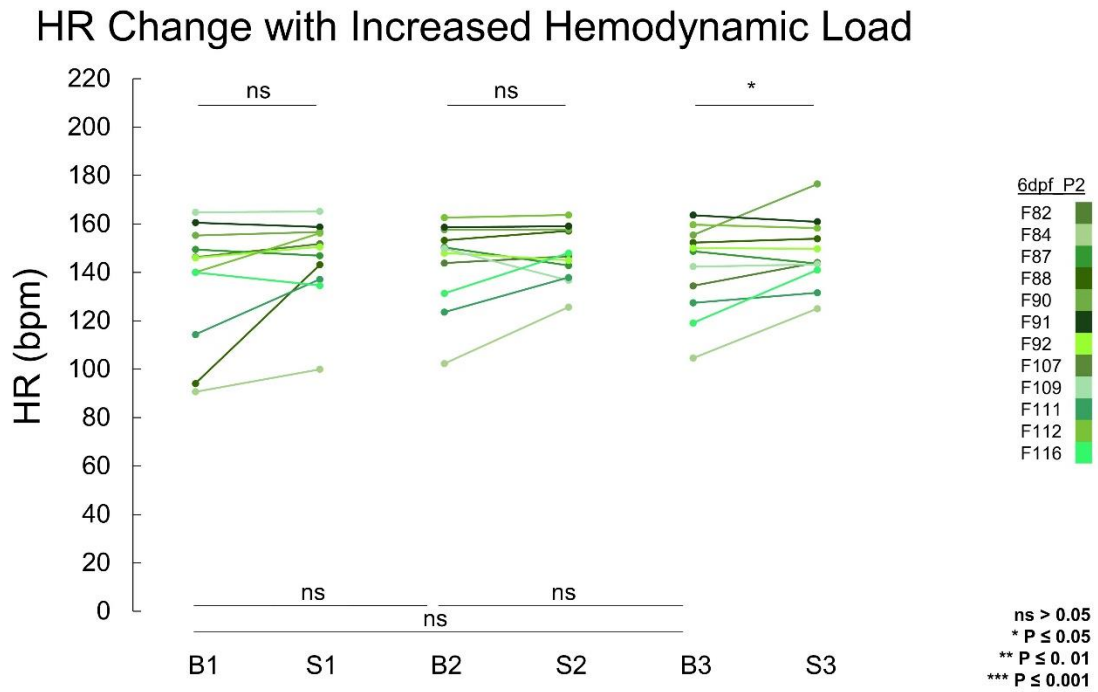
Supplemental Figure 3.3 | Absolute HR change in 14 dpf zebrafish embryo. Absolute HR change in 14 dpf zebrafish larvae exposed to P2. B1 B2 B3 represents each baseline phase measurement. S1 S2 S3 represents each stretch phase measurement. There were significant differen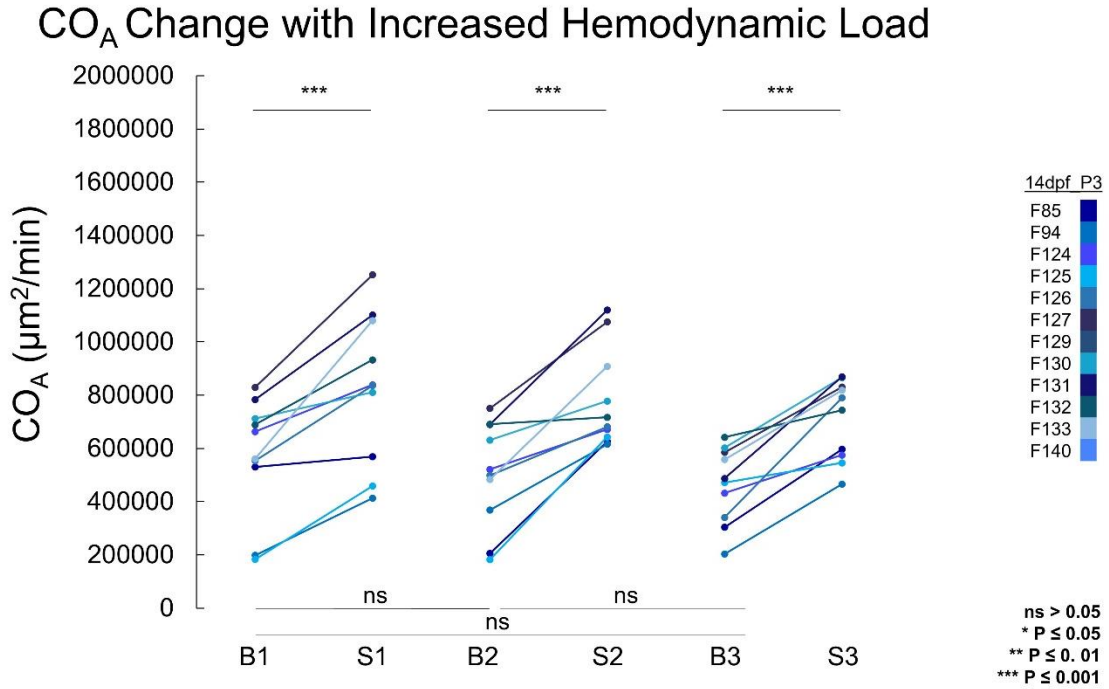ces in HR response between each baseline and stretch phases. There were no significant differences between baseline phases. (ns = no significant difference; p > 0.05, * = p ≤ 0.05, ** = p ≤ 0.01, *** = p ≤ 0.001).

HR Change with Increased Hemodynamic Load
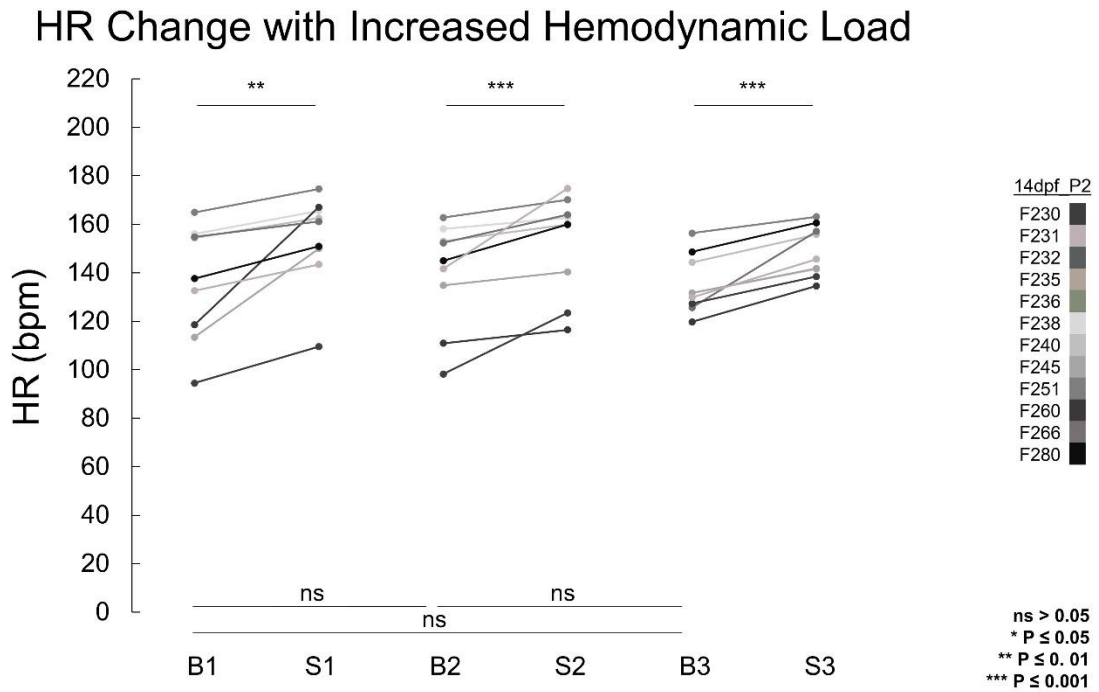
Supplemental Figure 3.4 | Absolute HR change in 14 dpf zebrafish embryo. Absolute HR change in 14 dpf zebrafish larvae exposed to P3. B1 B2 B3 represents each baseline phase measurement. S1 S2 S3 represents each stretch phase measurement. There were significant differences in HR response between each baseline and stretch phases. There were no significant differences between baseline phases. (ns = no significant difference; p > 0.05, * = p ≤ 0.05, ** = p ≤ 0.01, *** = p ≤ 0.001).


HR Change with Increased Hemodynamic Load
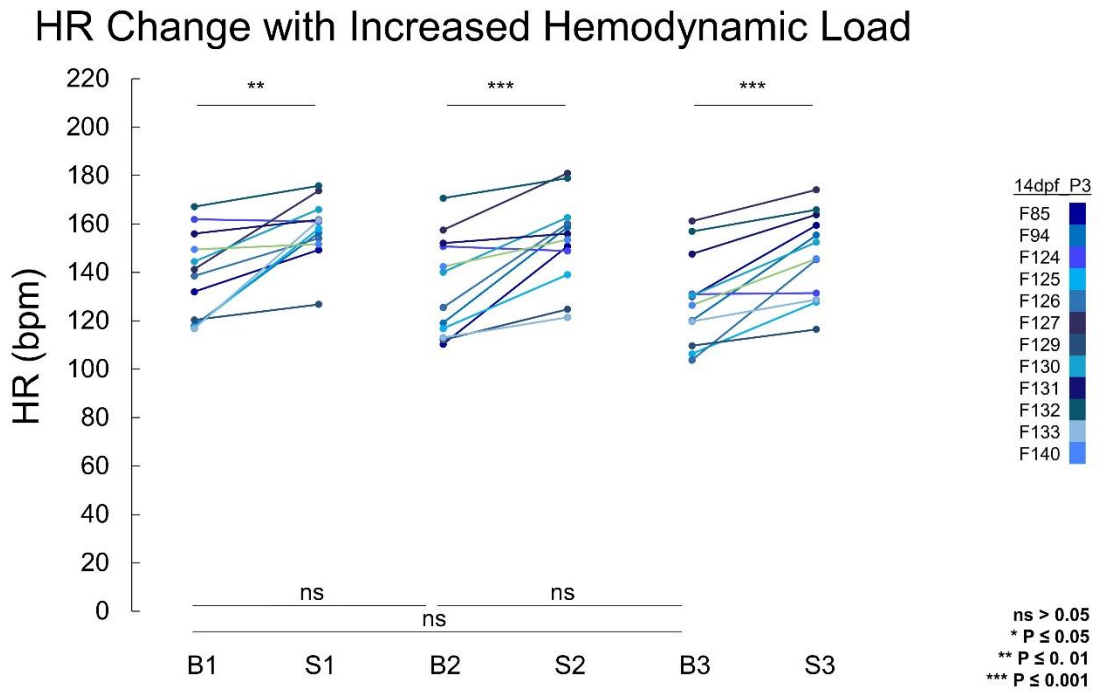
Supplemental Figure 3.5 | Absolute change in HR response between each stretch in each age group. The absolute change in HR during each stretch phase. S1, S2, S3 represents each stretch across each group. 2 dpf; red, 6 dpf; green, 14 dpf_P3; blue, 14 dpf_P2; grey. In each group there were no significant differences within each group, across each stretch phase (p < 0.05).

Absolute HR Change with Increased Hemodynamic Load
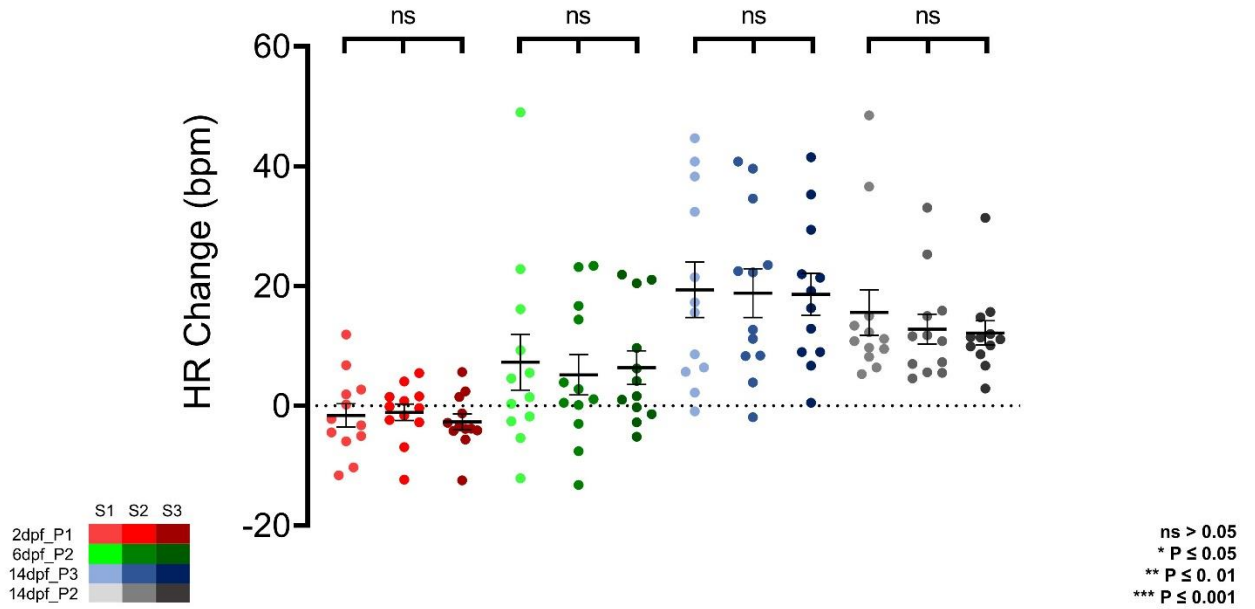
Supplemental Figure 3.6 | Absolute SA change in 2 dpf zebrafish embryo. Absolute SA change in 2 dpf zebrafish larvae exposed to P1. B1 B2 B3 represents each baseline phase measurement. S1 S2 S3 represents each stretch phase measurement. There were significant differences in SA response between baseline and stretch phase. There were also no significant differences between baseline phases. (ns = no significant difference; p > 0.05, * = p ≤ 0.05, ** = p ≤ 0.01, *** = p ≤ 0.001).
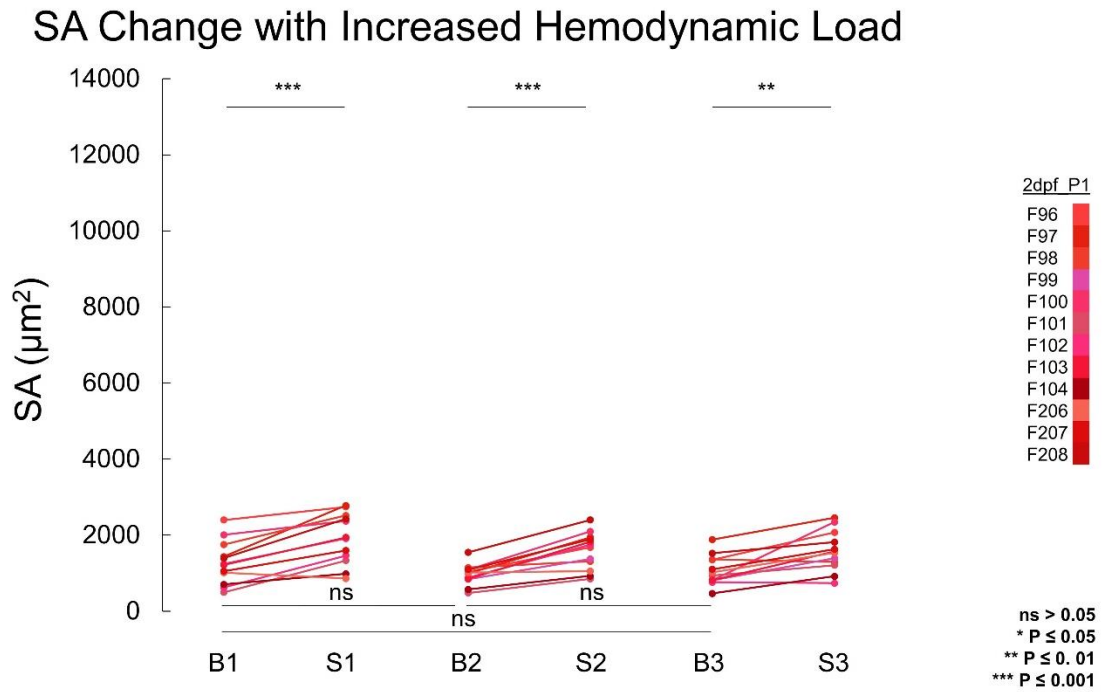
Supplemental Figure 3.7 | Absolute SA change in 6 dpf zebrafish embryo. Absolute SA change in 6 dpf zebrafish larvae exposed to P2. B1 B2 B3 represents each baseline phase measurement. S1 S2 S3 represents each stretch phase measurement. There were significant differences in SA response between B1 and S1, B2 and S2, however, there was no significant difference between B3 and S3. There were no significant differences between baseline phases. (ns = no significant difference; p > 0.05, * = p ≤ 0.05, ** = p ≤ 0.01, *** = p ≤ 0.001).

SA Change with Increased Hemodynamic Load
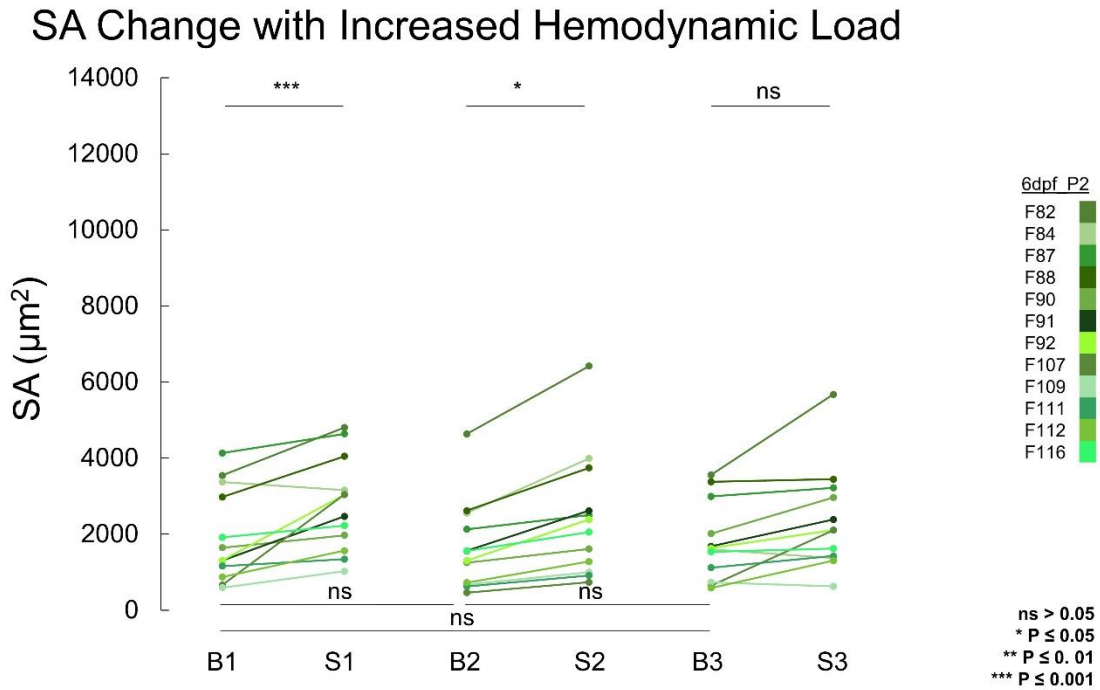
Supplemental Figure 3.8 | Absolute SA change in 14 dpf zebrafish embryo. Absolute SA change in 14 dpf zebrafish larvae exposed to P2. B1 B2 B3 represents each baseline phase measurement. S1 S2 S3 represents each stretch phase measurement. There were significant differences in SA response between baseline and stretch phase. There were also no significant differences between baseline phases. (ns = no significant difference; p > 0.05, * = p ≤ 0.05, ** = p ≤ 0.01, *** = p ≤ 0.001).
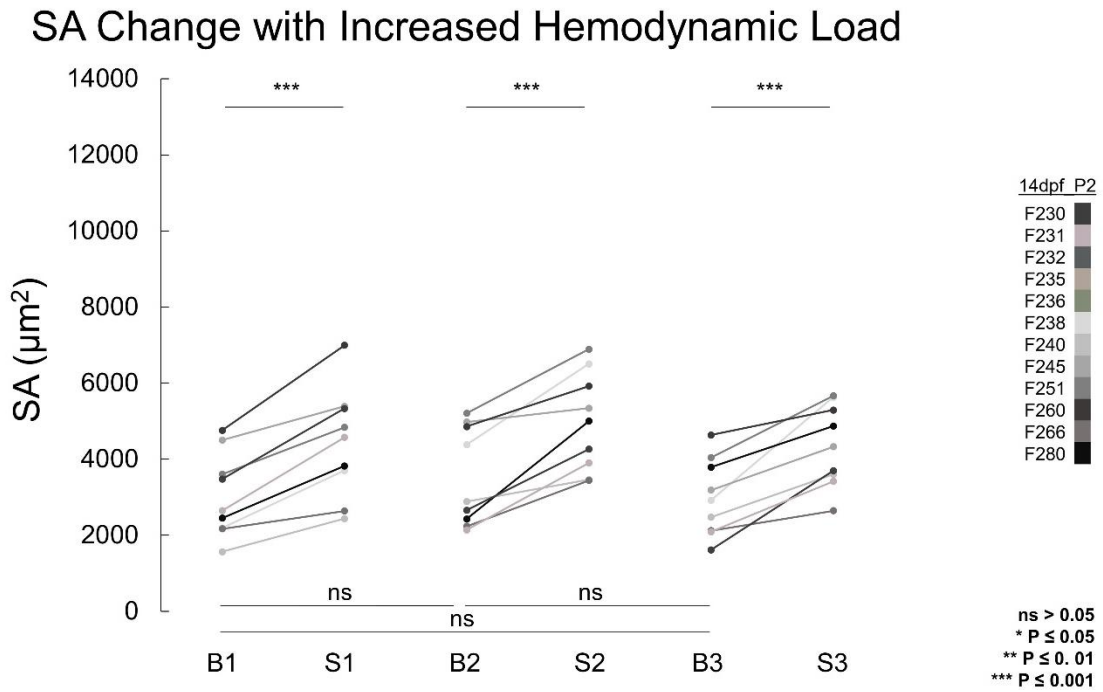
Supplemental Figure 3.9 | Absolute SA change in 14 dpf zebrafish embryo. A Absolute SA change in 14 dpf zebrafish larvae exposed to P3. B1 B2 B3 represents each baseline phase measurement. S1 S2 S3 represents each stretch phase measurement. There were significant differences in SA response between baseline and stretch phase. There were also no significant differences between baseline phases. (ns = no significant difference; p > 0.05, * = p ≤ 0.05, ** = p ≤ 0.01, *** = p ≤ 0.001).

SA Change with Increased Hemodynamic Load

Supplemental Figure 3.10 | Absolute change in SA response between each stretch in each age group. The absolute change in SA during each stretch phase. S1, S2, S3 represents each stretch across each group. 2 dpf; red, 6 dpf; green, 14 dpf_P3; blue, 14 dpf_P2; grey. In each group there were no significant differences within each group, across each stretch phase (p < 0.05).

Supplemental Figure 3.11 | Absolute CO$_A$ change in 2 dpf zebrafish embryo.
Absolute CO$_A$ change in 2 dpf zebrafish larvae exposed to P1. B1 B2 B3 represents each baseline phase measurement. S1 S2 S3 represents each stretch phase measurement. There were significant differences in CO$_A$ response between each baseline and stretch phase. There were also no significant differences between baseline phases. (ns = no significant difference; p > 0.05, * = p ≤ 0.05, ** = p ≤ 0.01, *** = p ≤ 0.001).

CO$_A$ Change with Increased Hemodynamic Load

Supplemental Figure 3.12 | Absolute CO_A change in 6 dpf zebrafish embryo.
Absolute CO_A change in 6 dpf zebrafish larvae exposed to P2. B1 B2 B3 represents each baseline phase measurement. S1 S2 S3 represents each stretch phase measurement. There were significant differences in CO_A response between each baseline and stretch phase. There were also no significant differences between baseline phases. (ns = no significant difference; $p > 0.05$, $* = p \leq 0.05$, $** = p \leq 0.01$, $*** = p \leq 0.001$).

Supplemental Figure 3.13 | Absolute CO$_A$ change in 14 dpf zebrafish embryo.
Absolute CO$_A$ change in 14 dpf zebrafish larvae exposed to P2. B1 B2 B3 represents each baseline phase measurement. S1 S2 S3 represents each stretch phase measurement. There were significant differences in CO$_A$ response between each baseline and stretch phase. There were also no significant differences between baseline phases. (ns = no significant difference; $p > 0.05$, * = $p \leq 0.05$, ** = $p \leq 0.01$, *** = $p \leq 0.001$).

Supplemental Figure 3.14 | Absolute CO$_A$ change in 14 dpf zebrafish embryo.
Absolute CO$_A$ change in 14 dpf zebrafish larvae exposed to P3. B1 B2 B3 represents
each baseline phase measurement. S1 S2 S3 represents each stretch phase measurement.
There were significant differences in CO$_A$ response between each baseline and stretch
phase. There were also no significant differences between baseline phases. (ns = no
significant difference; p > 0.05, * = p ≤ 0.05, ** = p ≤ 0.01, *** = p ≤ 0.001).

Supplemental Figure 3.15 | Absolute change in CO_A response between each stretch in each age group. The absolute change in CO_A during each stretch phase. S1, S2, S3 represents each stretch across each group. 2 dpf; red, 6 dpf; green, 14 dpf_P3; blue, 14 dpf_P2; grey. In each group there were no significant differences within each group, across each stretch phase (p < 0.05).

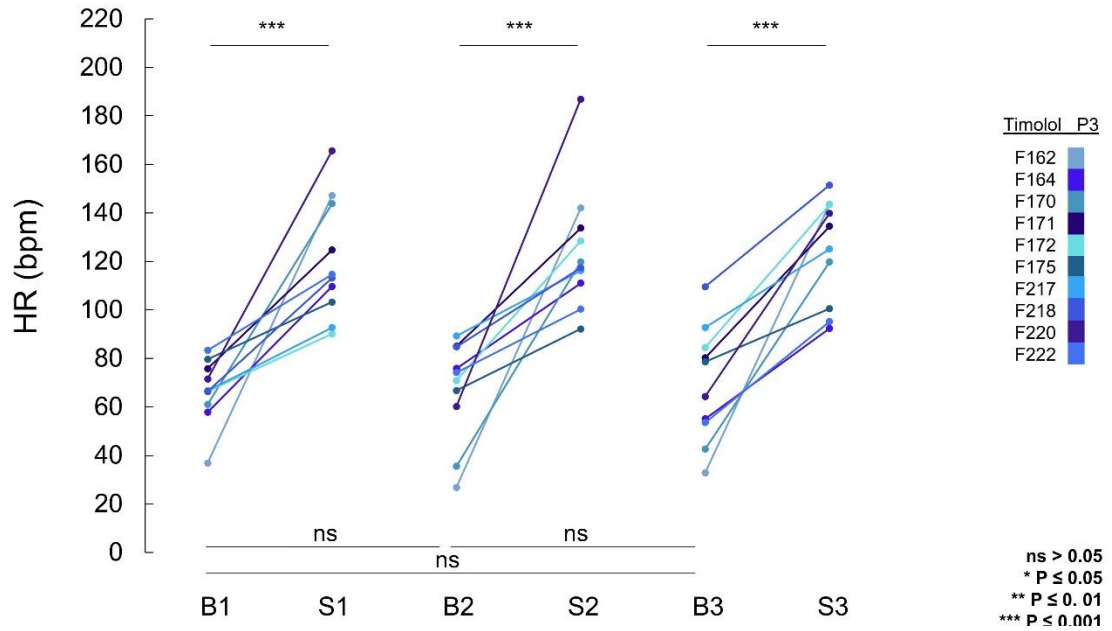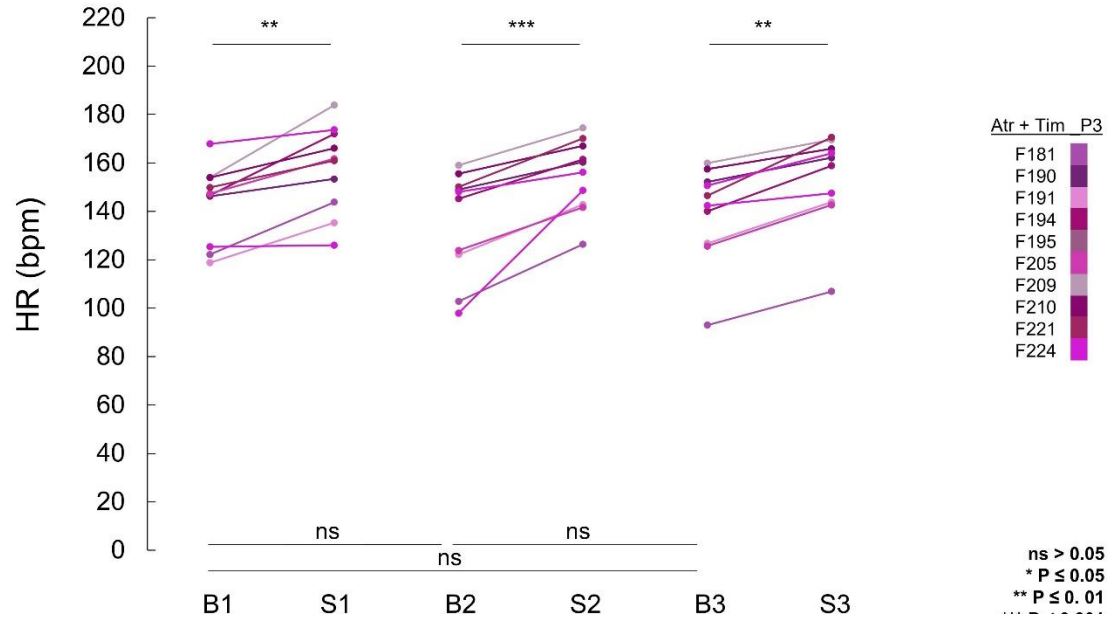Absolute CO_A Change with Increased Hemodynamic Load
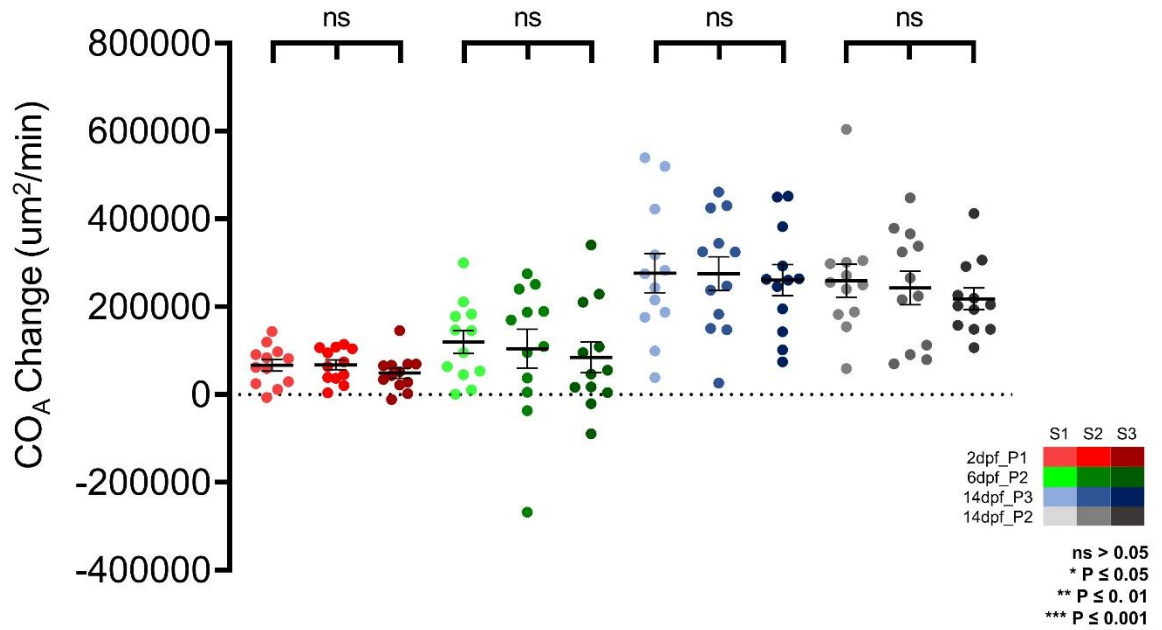
Supplemental Figure 4.1 | Absolute EDA Change in 14 dpf zebrafish embryo with M_2R block. B1 B2 B3 represents each baseline phase measurement. S1 S2 S3 represents each stretch phase measurement. In each stretch phase there was a significant difference between baseline and stretch phases. There were no significant differences between baseline phases. (*** = $p < 0.001$, ns = no significant difference ($p < 0.05$).
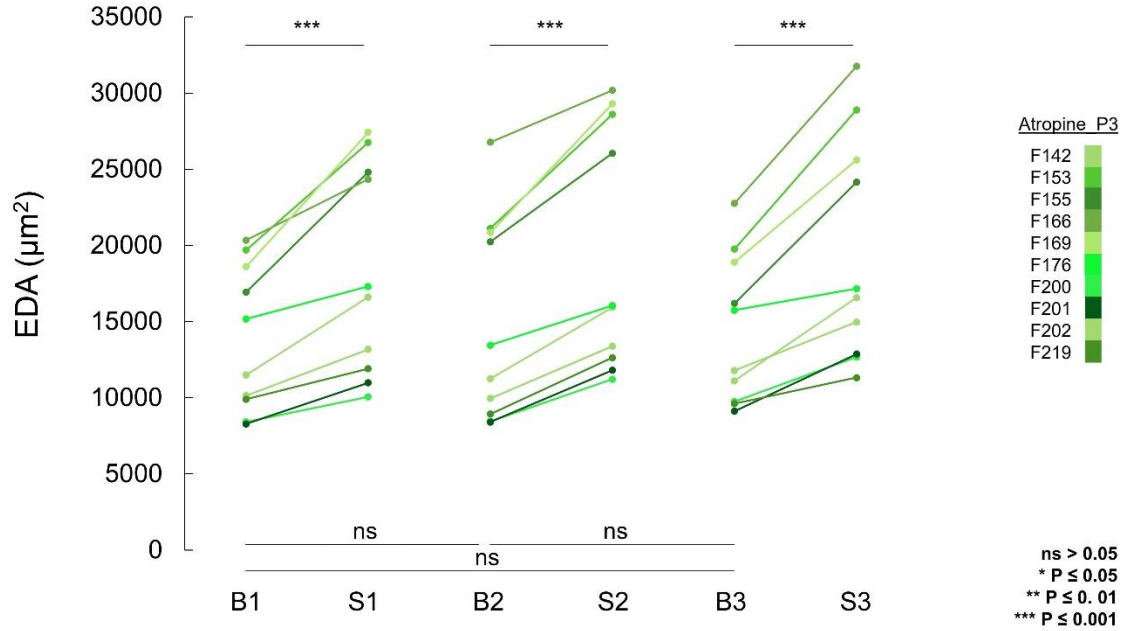
Supplemental Figure 4.2 | Absolute EDA Change in 14 dpf zebrafish embryo with β-AR block. B1 B2 B3 represents each baseline phase measurement. S1 S2 S3 represents each stretch phase measurement. In each stretch phase there was a significant difference between baseline and stretch phases. There were no significant differences between baseline phases. (*** = p < 0.001, ns = no significant difference, p < 0.05).
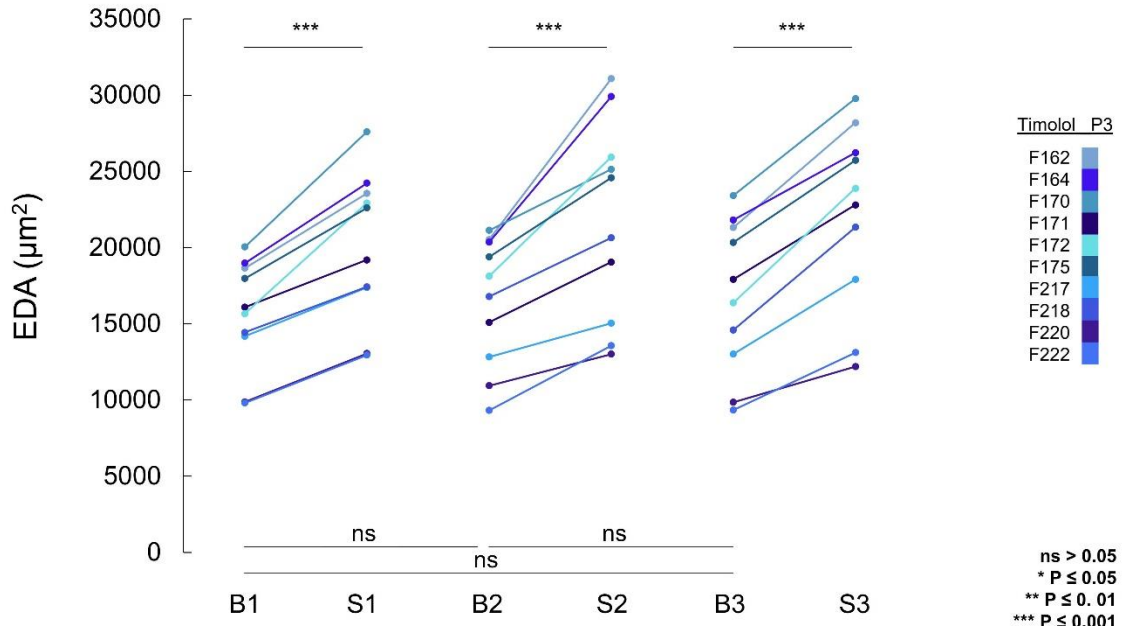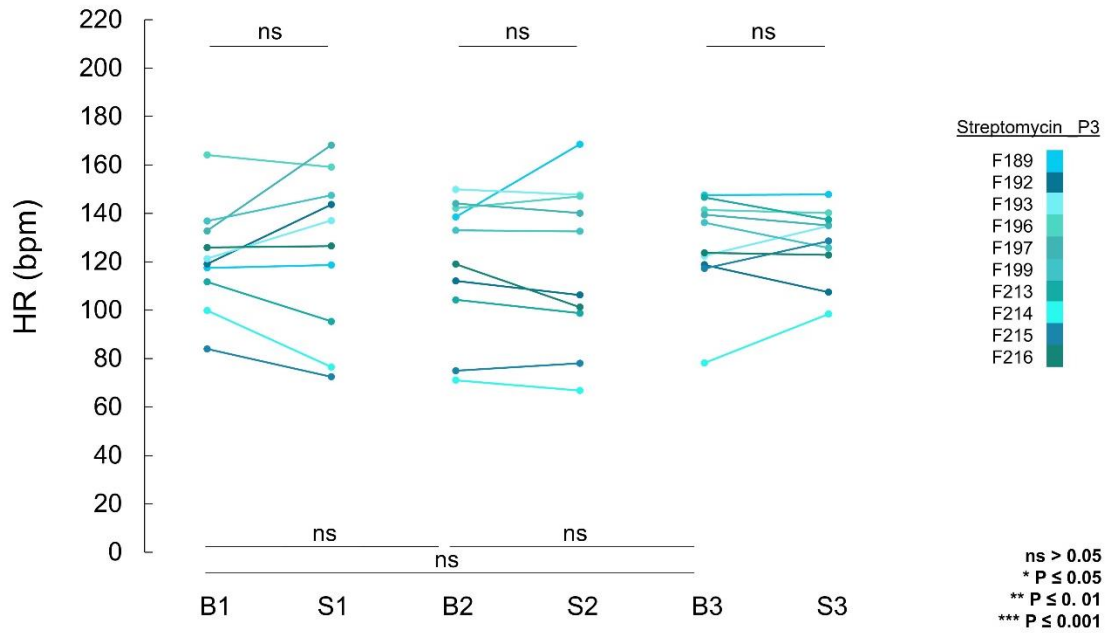
Supplemental Figure 4.3 | Absolute EDA Change in 14 dpf zebrafish embryo with M₂R and β-AR block. B1 B2 B3 represents each baseline phase measurement. S1 S2 S3 represents each stretch phase measurement. In each stretch phase there was a significant difference between baseline and stretch phases. There were no significant differences between baseline phases. (*** = p < 0.001, ns = no significant difference, p < 0.05).
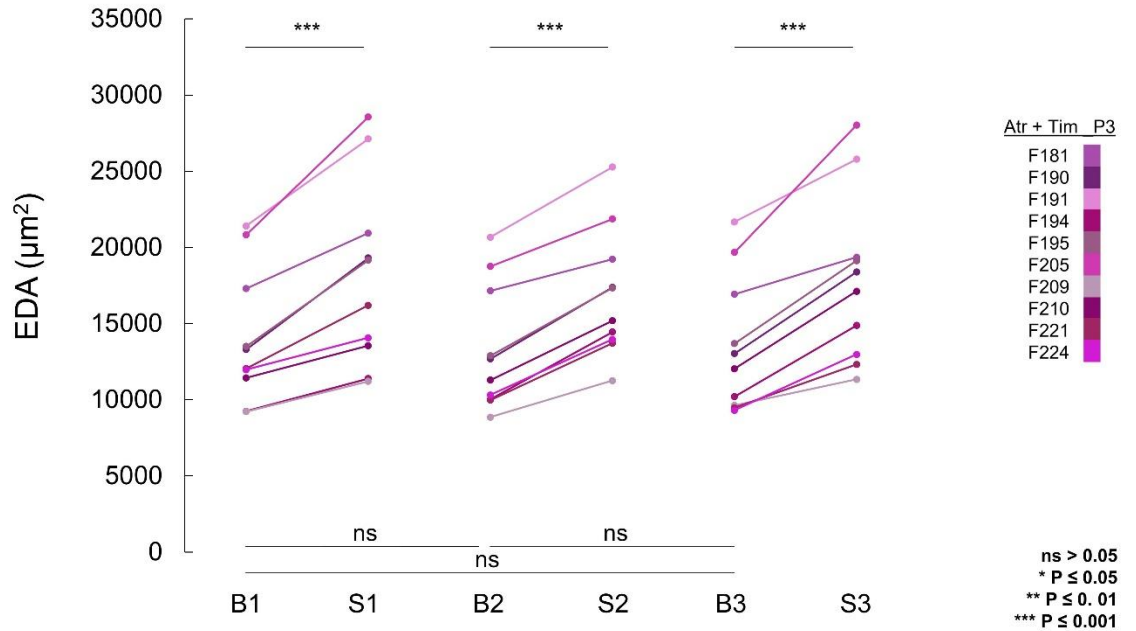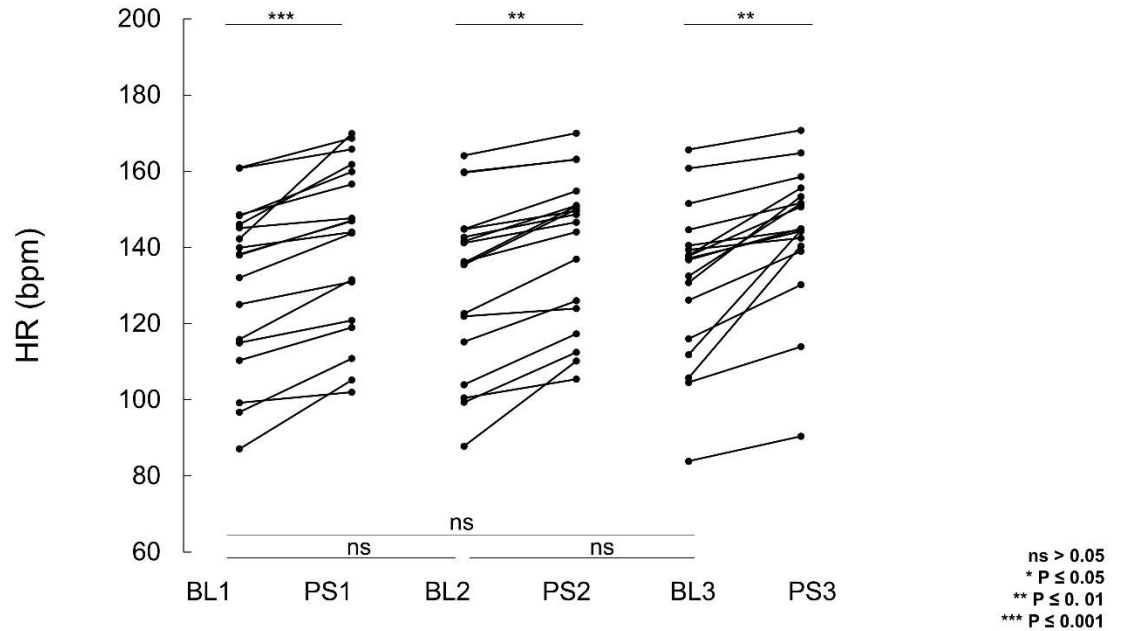
Supplemental Figure 4.4 | Absolute EDA Change in 14 dpf zebrafish embryo with SAC$_{NS}$ block. B1 B2 B3 represents each baseline phase measurement. S1 S2 S3 represents each stretch phase measurement. In each stretch phase there was a significant difference between baseline and stretch phases. There were no significant differences between baseline phases. (*** = p < 0.001, ns = no significant difference, p < 0.05).

Supplemental Figure 4.5 | Absolute EDA Change in 14 dpf zebrafish in GCaMP
B1 B2 B3 represents each baseline phase measurement. S1 S2 S3 represents each stretch
phase measurement. In each stretch phase there was a significant difference between
baseline and stretch phases. There were significant differences between each baseline
phases, likely resulting from the compromised SA due to the effects of blebbistatin. (***
= p < 0.001, ns = no significant difference, p < 0.05).

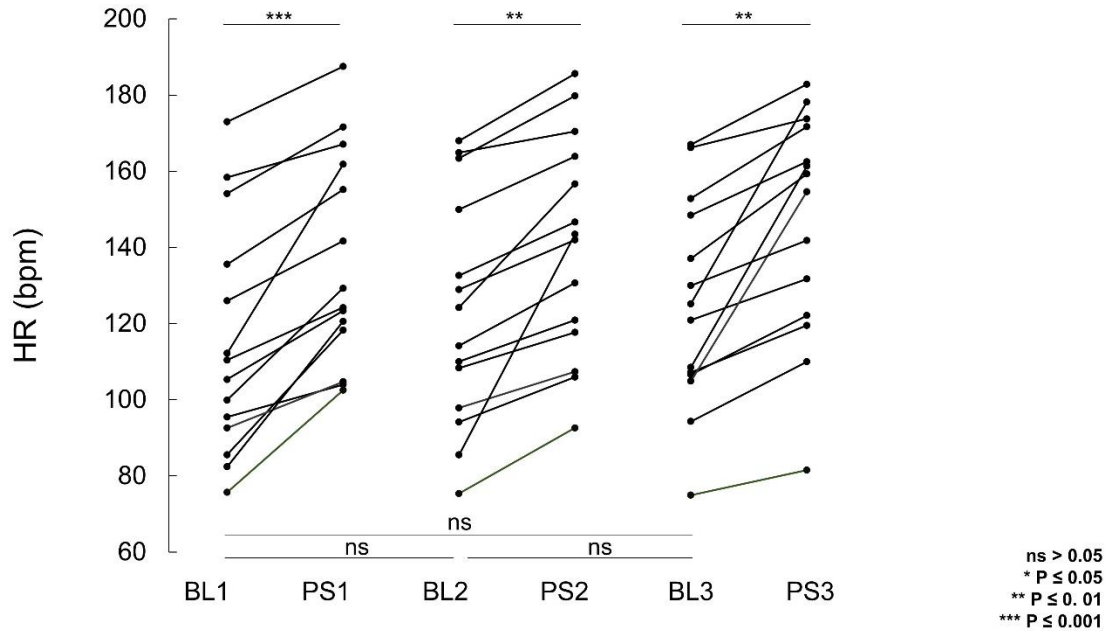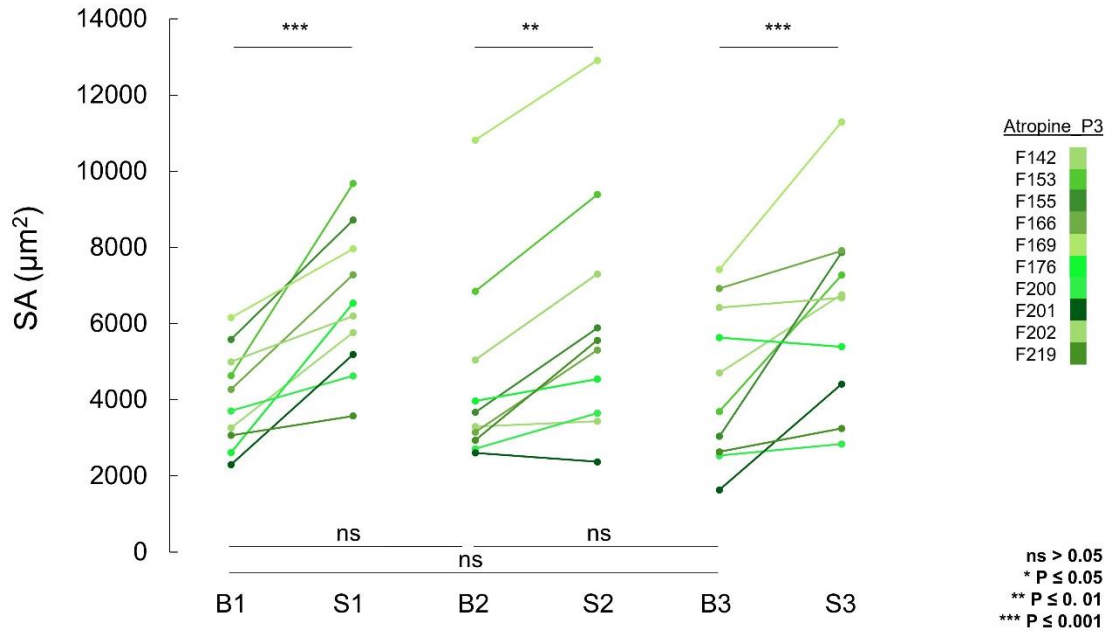
EDA Change + Hemodynamic Loading + Blebbistatin (GCaMP)
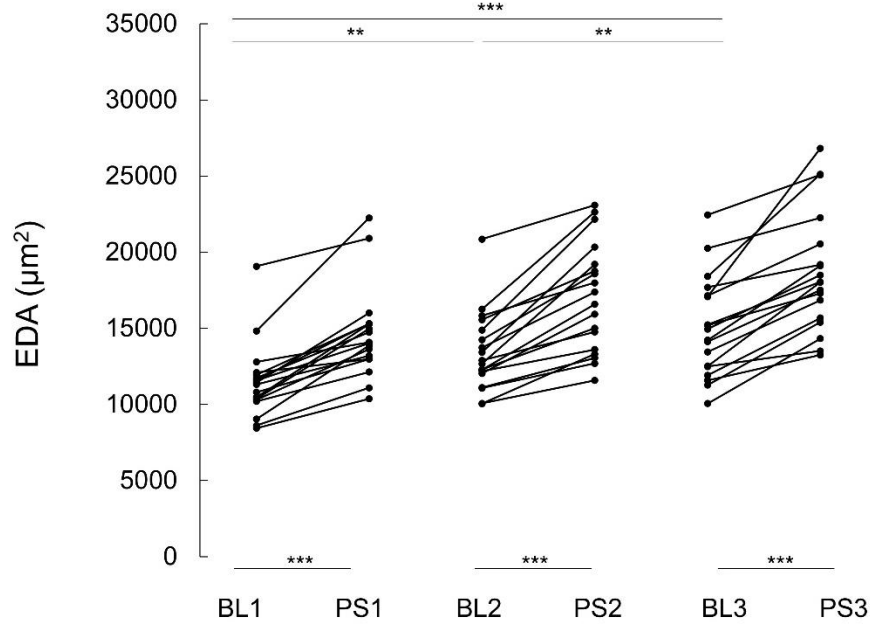
Supplemental Figure 4.6 | Absolute EDA Change in 14 dpf butterfly zebrafish. B1 B2 B3 represents each baseline phase measurement. S1 S2 S3 represents each stretch phase measurement. In each stretch phase there was a significant difference between baseline and stretch phases. There were significant differences between each baseline phases, likely resulting from the compromised SA due to the effects of blebbistatin. (*** = p < 0.001, ns = no significant difference, p < 0.05).

EDA Change + Hemodynamic Loading + Blebbistatin (Butterfly)
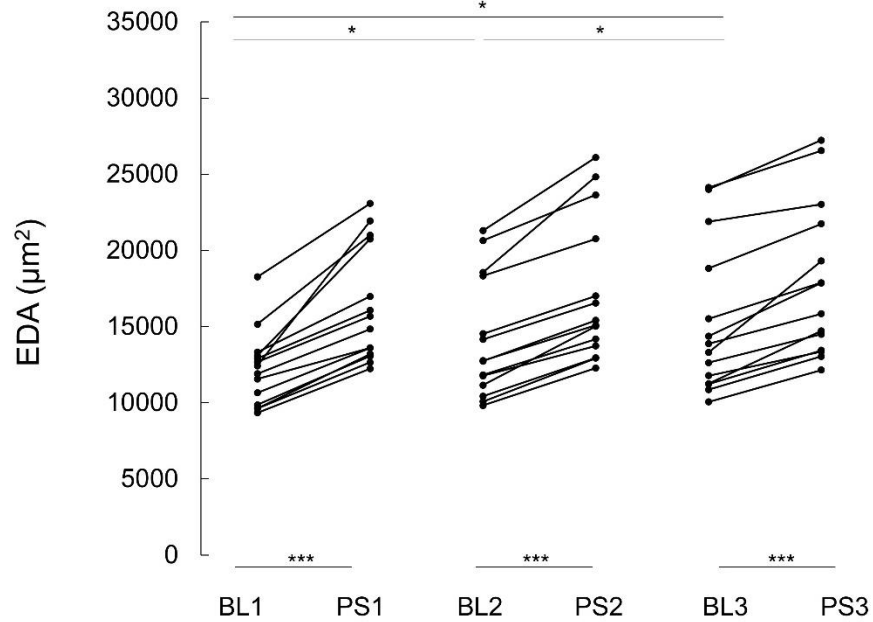
Supplemental Figure 4.7 | Absolute HR change in 14 dpf zebrafish embryo with M_2R block. B1 B2 B3 represents each baseline phase measurement. S1 S2 S3 represents each stretch phase measurement. In each stretch phase there was a significant difference between baseline and stretch phases. There were no significant differences between baseline phases. (*** = p < 0.001, ns = no significant difference (p < 0.05).

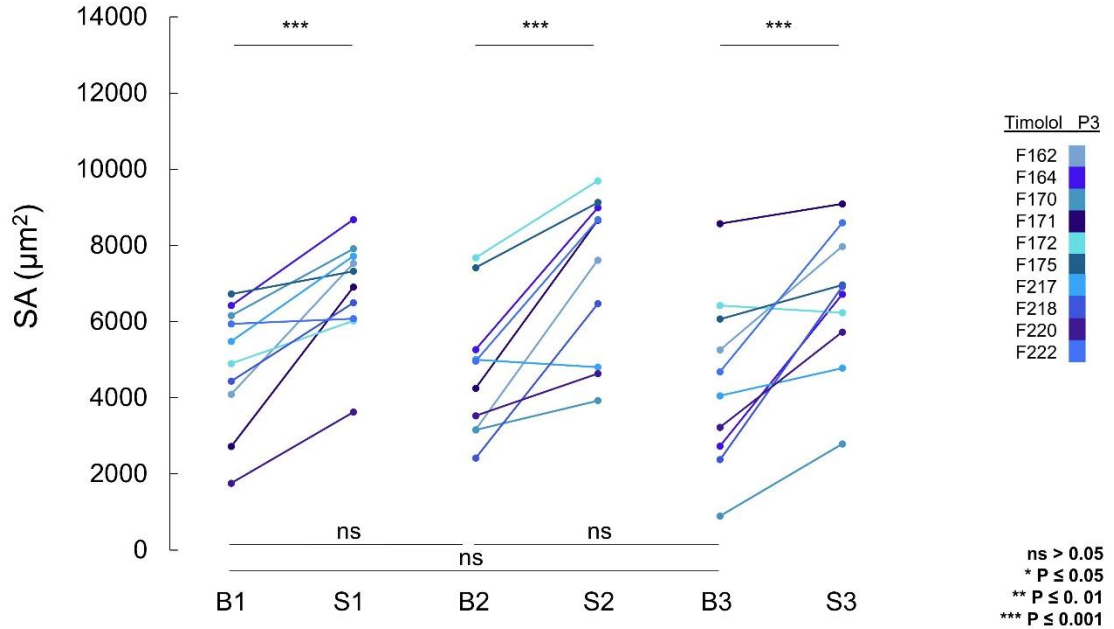## HR Change with M_2R Block + Hemodynamic Loading
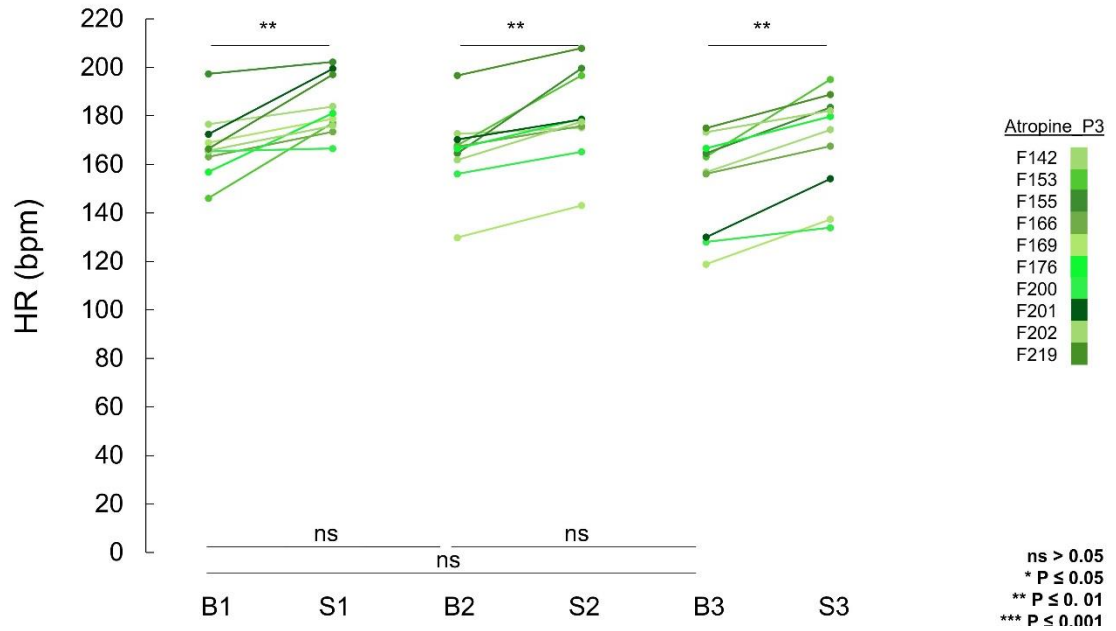
Supplemental Figure 4.8 | Absolute HR change in 14 dpf zebrafish embryo with β-AR block. B1 B2 B3 represents each baseline phase measurement. S1 S2 S3 represents each stretch phase measurement. In each stretch phase there was a significant difference between baseline and stretch phases. There were no significant differences between baseline phases. (*** = p < 0.001, ns = no significant difference, p < 0.05).

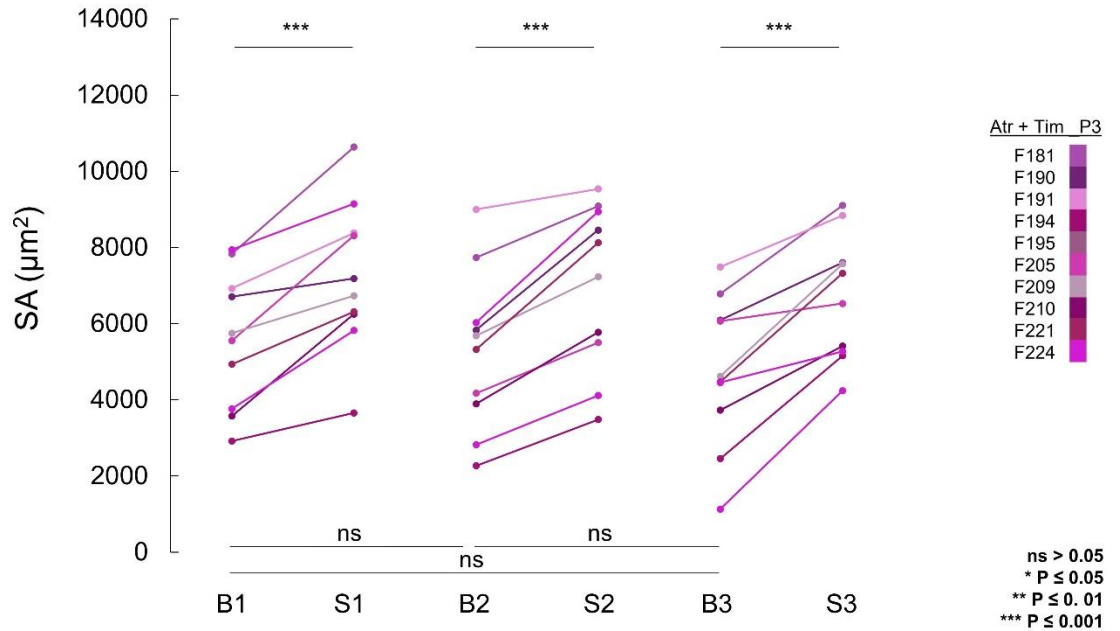HR Change with β-AR Block + Hemodynamic Loading

Supplemental Figure 4.9 | Absolute HR change in 14 dpf zebrafish embryo with M_2R and β-AR block. B1 B2 B3 represents each baseline phase measurement. S1 S2 S3 represents each stretch phase measurement. In each stretch phase there was a significant difference between baseline and stretch phases. There were no significant differences between baseline phases. (*** = p < 0.001, ns = no significant difference, p < 0.05).

HR Change with M_2R and β-AR Block + Hemodynamic Loading

Supplemental Figure 4.10| Absolute HR change in 14 dpf zebrafish embryo with SAC_{NS} block. B1 B2 B3 represents each baseline phase measurement. S1 S2 S3 represents each stretch phase measurement. In each stretch phase there was no significant difference between baseline and stretch phases. There were also no significant differences between baseline phases. (*** = p < 0.001, ns = no significant difference, p < 0.05).

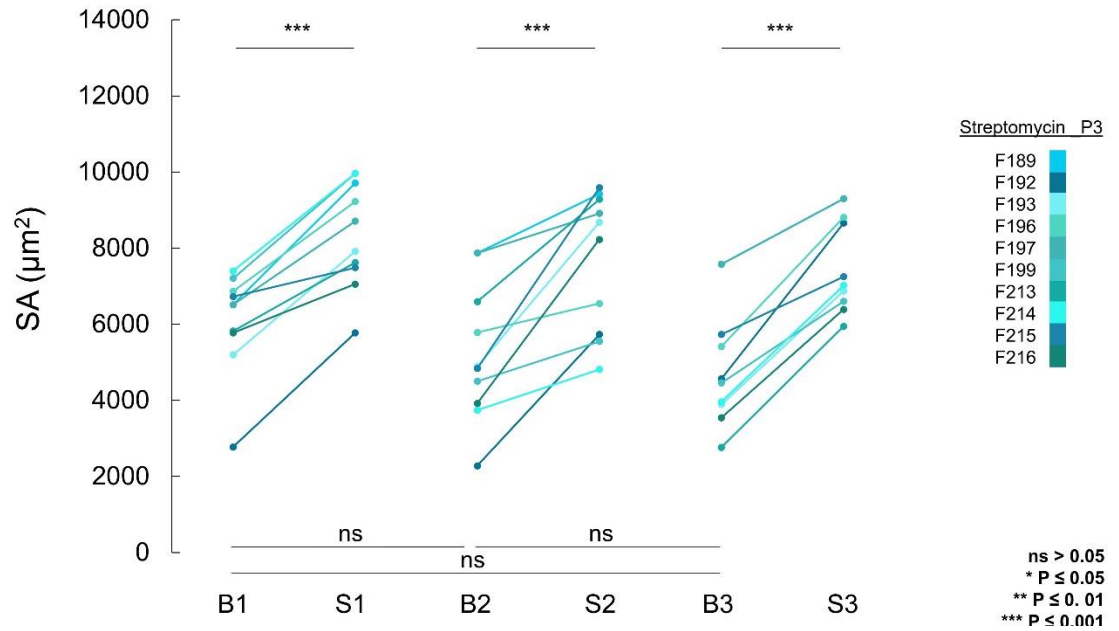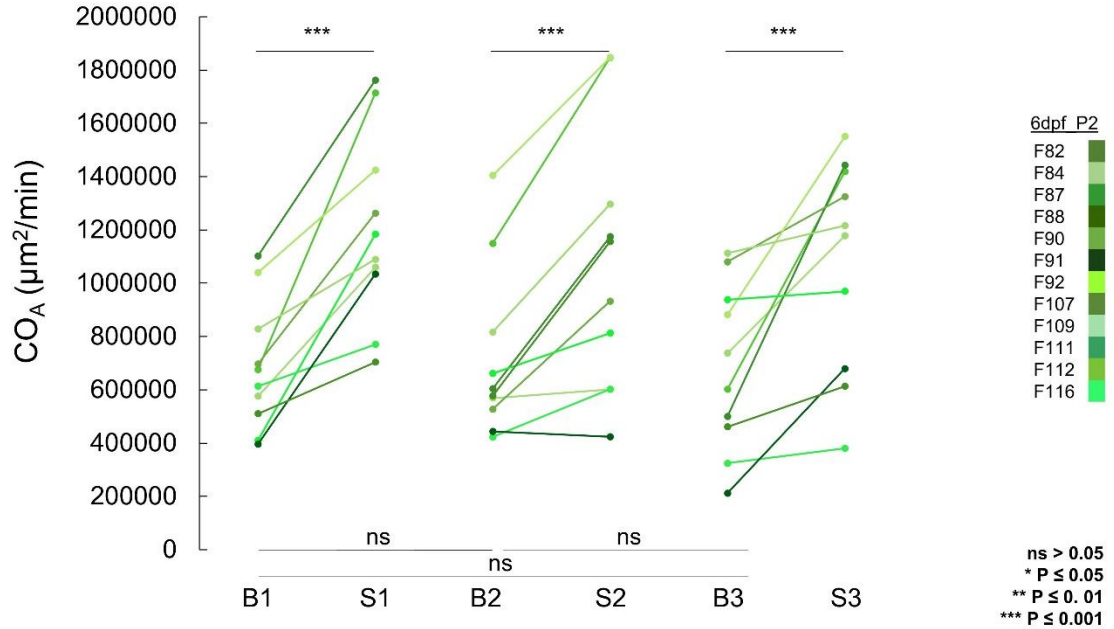HR Change with SAC_{NS} Block + Hemodynamic Loading

Supplemental Figure 4.11 | Absolute HR change in 14 dpf GCaMP zebrafish embryo. B1 B2 B3 represents each baseline phase measurement. S1 S2 S3 represents each stretch phase measurement. In each stretch phase there was a significant difference between baseline and stretch phases. There were no significant differences between each baseline phases (*** = p < 0.001, ns = no significant difference, p < 0.05).

HR Change during Increased Hemodynamic Load, GCaMP

Supplemental Figure 4.12 | Absolute EDA Change in 14 dpf butterfly zebrafish embryo. B1 B2 B3 represents each baseline phase measurement. S1 S2 S3 represents each stretch phase measurement. In each stretch phase there was a significant difference between baseline and stretch phases. There were no significant differences between each baseline phases (*** = p < 0.001, ns = no significant difference, p < 0.05).

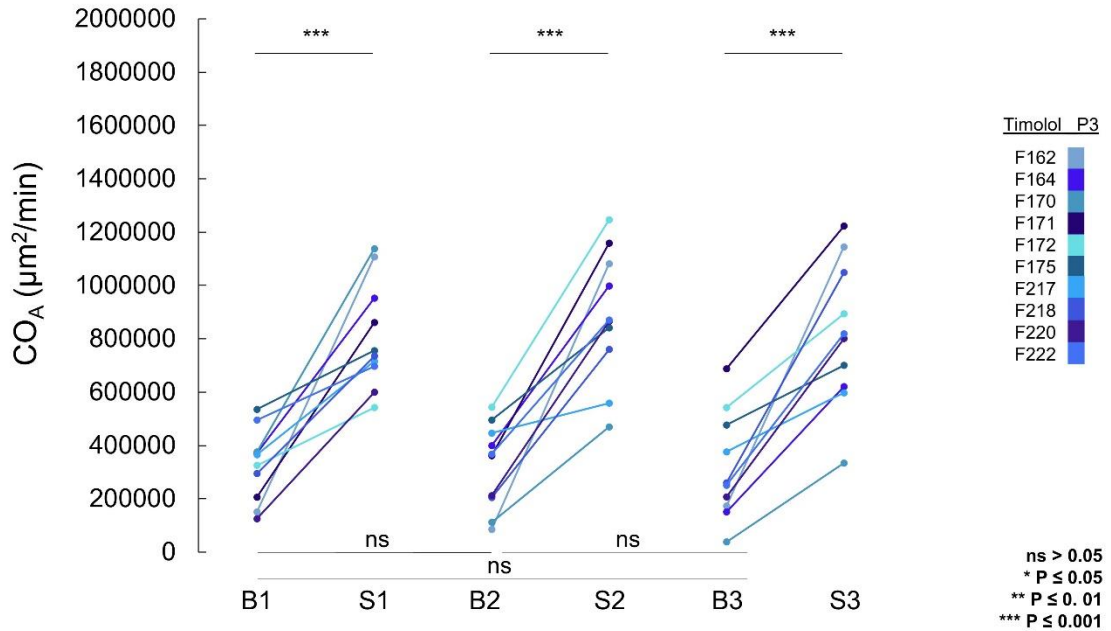HR Change + Hemodynamic Loading + Blebbistatin (BF)

Supplemental Figure 4.13 | Absolute SA change in 14 dpf zebrafish embryo with M_2R block. B1 B2 B3 represents each baseline phase measurement. S1 S2 S3 represents each stretch phase measurement. In each stretch phase there was a significant difference between baseline and stretch phases. There were no significant differences between baseline phases. (*** = p < 0.001, ns = no significant difference (p < 0.05).

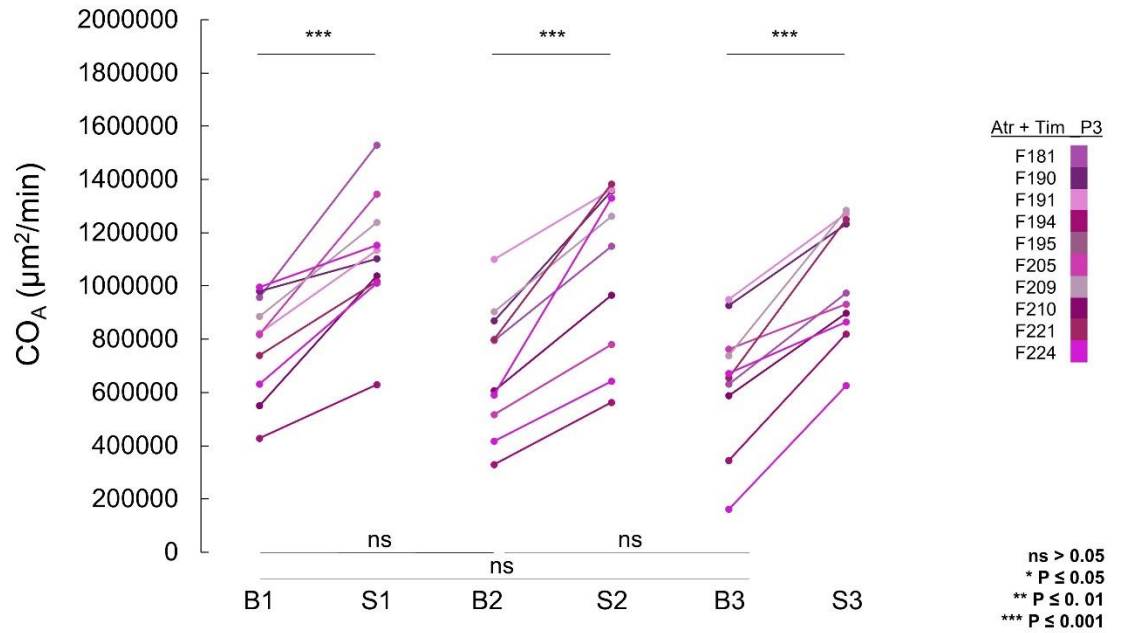SA Change with M_2R Block + Hemodynamic Loading

Supplemental Figure 4.14 | Absolute SA change in 14 dpf zebrafish embryo with β-AR block. B1 B2 B3 represents each baseline phase measurement. S1 S2 S3 represents each stretch phase measurement. In each stretch phase there was a significant difference between baseline and stretch phases. There were no significant differences between baseline phases. (*** = p < 0.001, ns = no significant difference, p < 0.05).
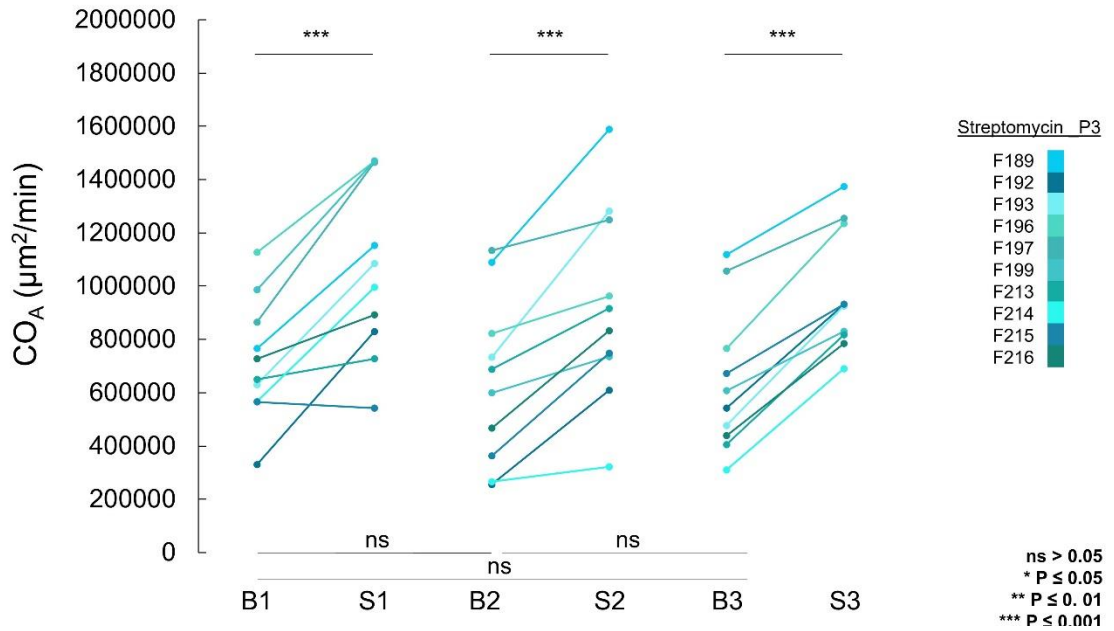

SA Change with β-AR Block + Hemodynamic Loading

Supplemental Figure 4.15 │ Absolute SA change in 14 dpf zebrafish embryo with M_2R and β-AR block. B1 B2 B3 represents each baseline phase measurement. S1 S2 S3 represents each stretch phase measurement. In each stretch phase there was a significant difference between baseline and stretch phases. There were no significant differences between baseline phases. (*** = p < 0.001, ns = no significant difference, p < 0.05).

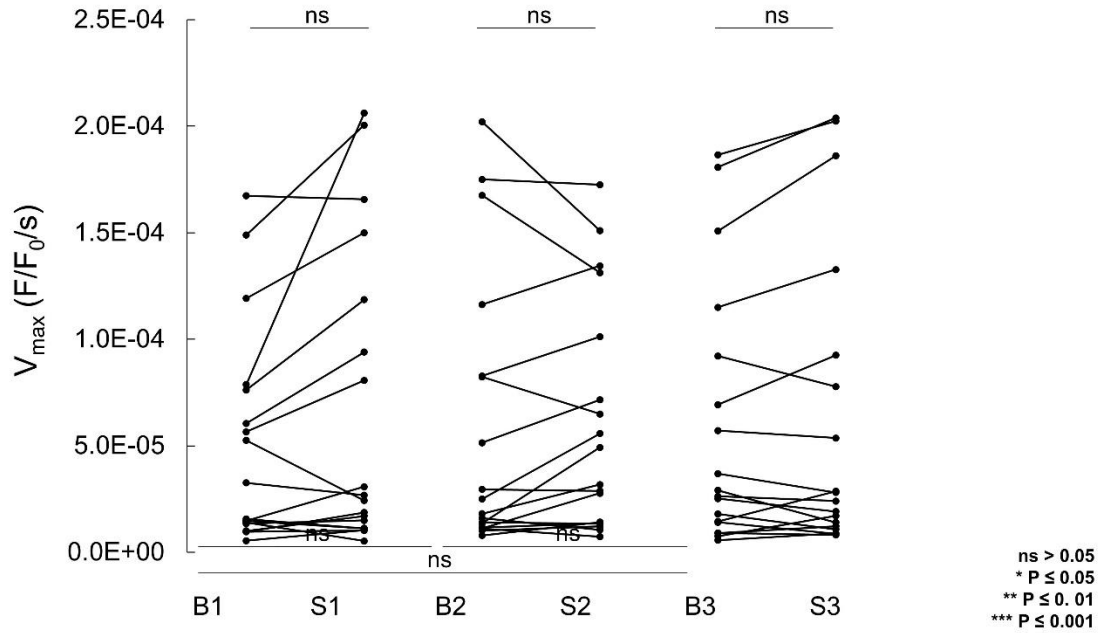
SA Change with M_2R and β-AR Block + Hemodynamic Loading

Supplemental Figure 4.16| Absolute SA change in 14 dpf zebrafish embryo with SAC$_{NS}$ block. B1 B2 B3 represents each baseline phase measurement. S1 S2 S3 represents each stretch phase measurement. In each stretch phase there was no significant difference between baseline and stretch phases. There were also no significant differences between baseline phases. (*** = p < 0.001, ns = no significant difference, p < 0.05).

Supplemental Figure 4.17 | Absolute CO_A change in 14 dpf zebrafish embryo with M_2R block. B1 B2 B3 represents each baseline phase measurement. S1 S2 S3 represents each stretch phase measurement. In each stretch phase there was a significant difference between baseline and stretch phases. There were no significant differences between baseline phases. (*** = p < 0.001, ns = no significant difference (p < 0.05).

Supplemental Figure 4.18 | Absolute CO$_A$ change in 14 dpf zebrafish embryo with β-AR block. B1 B2 B3 represents each baseline phase measurement. S1 S2 S3 represents each stretch phase measurement. In each stretch phase there was a significant difference between baseline and stretch phases. There were no significant differences between baseline phases. (*** = p < 0.001, ns = no significant difference, p < 0.05).

Supplemental Figure 4.19 | Absolute CO_A change in 14 dpf zebrafish embryo with M_2R and β-AR block. B1 B2 B3 represents each baseline phase measurement. S1 S2 S3 represents each stretch phase measurement. In each stretch phase there was a significant difference between baseline and stretch phases. There were no significant differences between baseline phases. (*** = $p < 0.001$, ns = no significant difference, $p < 0.05$).

CO_A Change with M_2R and β-AR Block + Hemodynamic Loading

Supplemental Figure 4.20 | Absolute CO_A change in 14 dpf zebrafish embryo with SAC_{NS} block. B1 B2 B3 represents each baseline phase measurement. S1 S2 S3 represents each stretch phase measurement. In each stretch phase there was no significant difference between baseline and stretch phases. There were also no significant differences between baseline phases. (*** = p < 0.001, ns = no significant difference, p < 0.05).
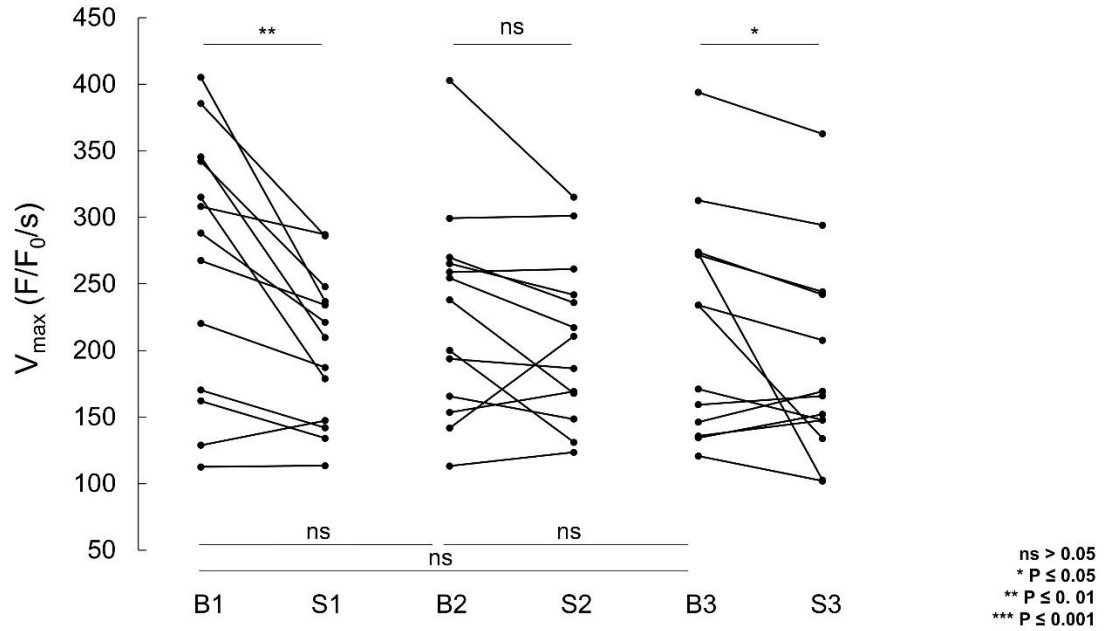
Supplemental Figure 4.21 | Absolute Vmax change in 14 dpf GCaMP zebrafish embryo. B1 B2 B3 represents each baseline phase measurement. S1 S2 S3 represents each stretch phase measurement. In each stretch phase there was no significant difference between baseline and stretch phases. There were also no significant differences between each baseline phases (*** = p < 0.001, ns = no significant difference, p < 0.05).

Supplemental Figure 4.22 | Absolute Vmax change in 14 dpf butterfly zebrafish embryo. B1 B2 B3 represents each baseline phase measurement. S1 S2 S3 represents each stretch phase measurement. In each stretch phase there was no significant difference between baseline and stretch phases. There were also no significant differences between each baseline phases (*** = p < 0.001, ns = no significant difference, p < 0.05).

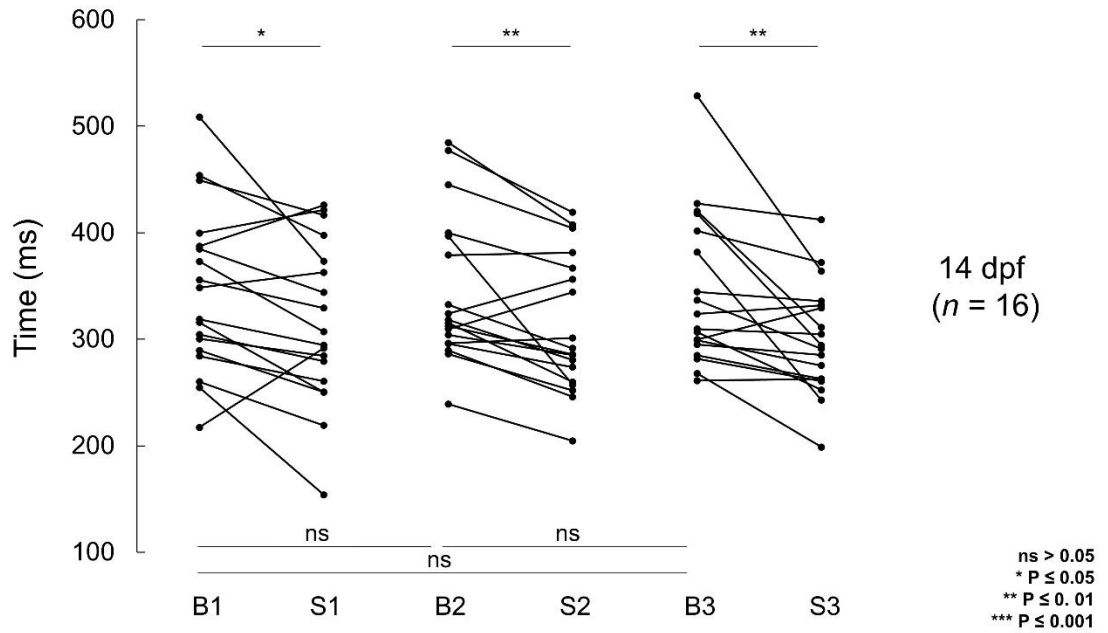Upstroke Velocity + Hemodynamic Loading + Blebbistatin (BF)
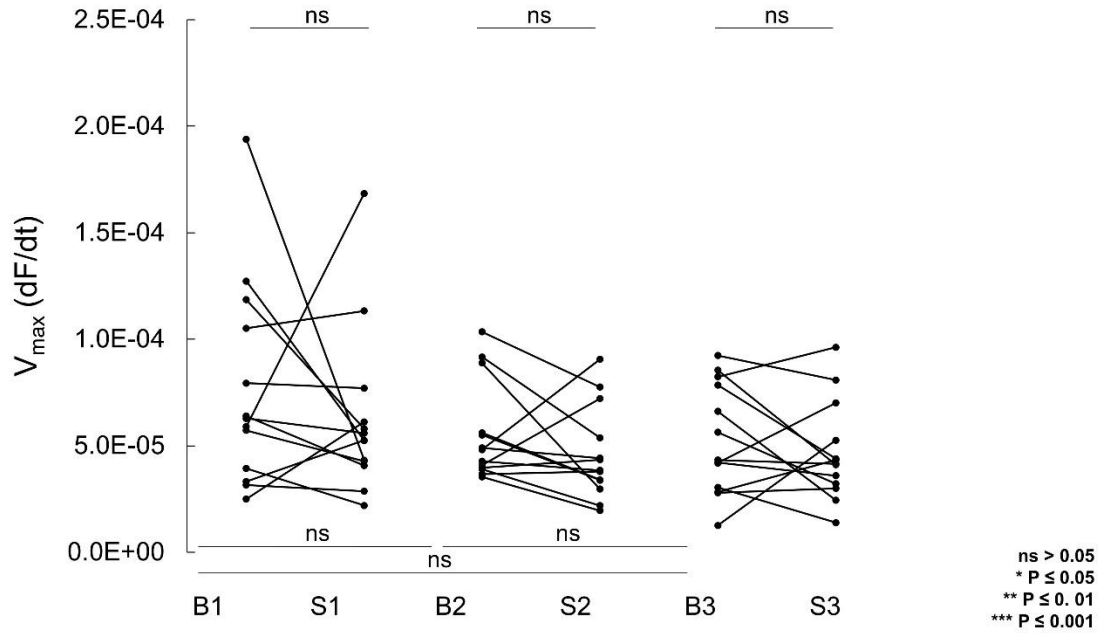
Supplemental Figure 4.23 | Absolute time to peak change in 14 dpf GCaMP zebrafish embryo. B1 B2 B3 represents each baseline phase measurement. S1 S2 S3 represents each stretch phase measurement. In each stretch phase there was no significant difference between baseline and stretch phases. There were also no significant differences between each baseline phases (*** = p < 0.001, ns = no significant difference, p < 0.05).
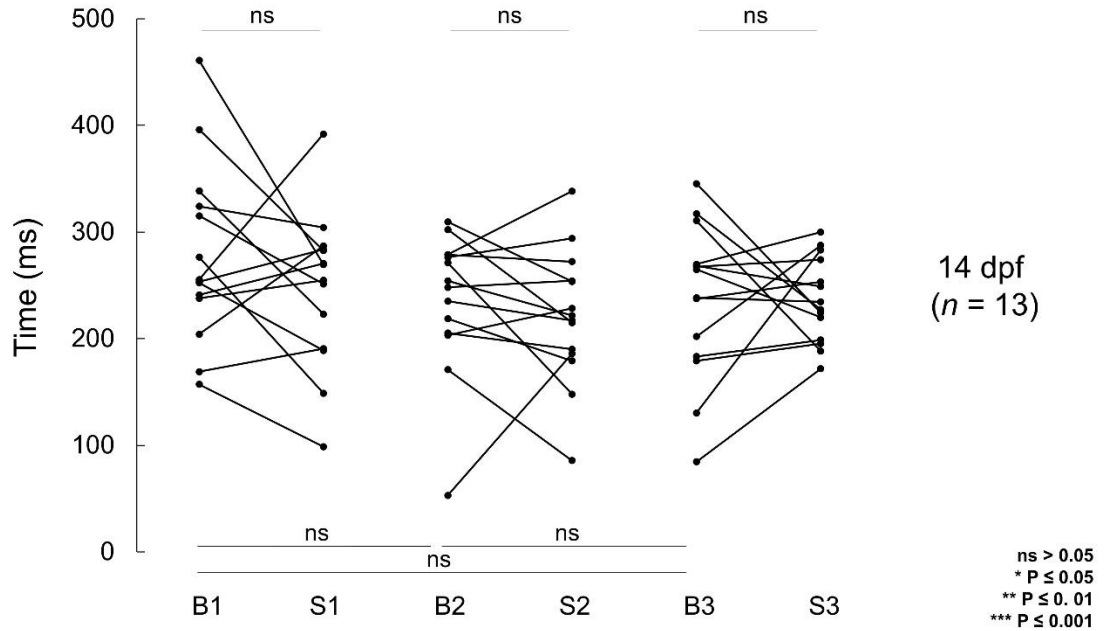
Time to Peak + Hemodynamic Loading + Blebbistatin (GC)
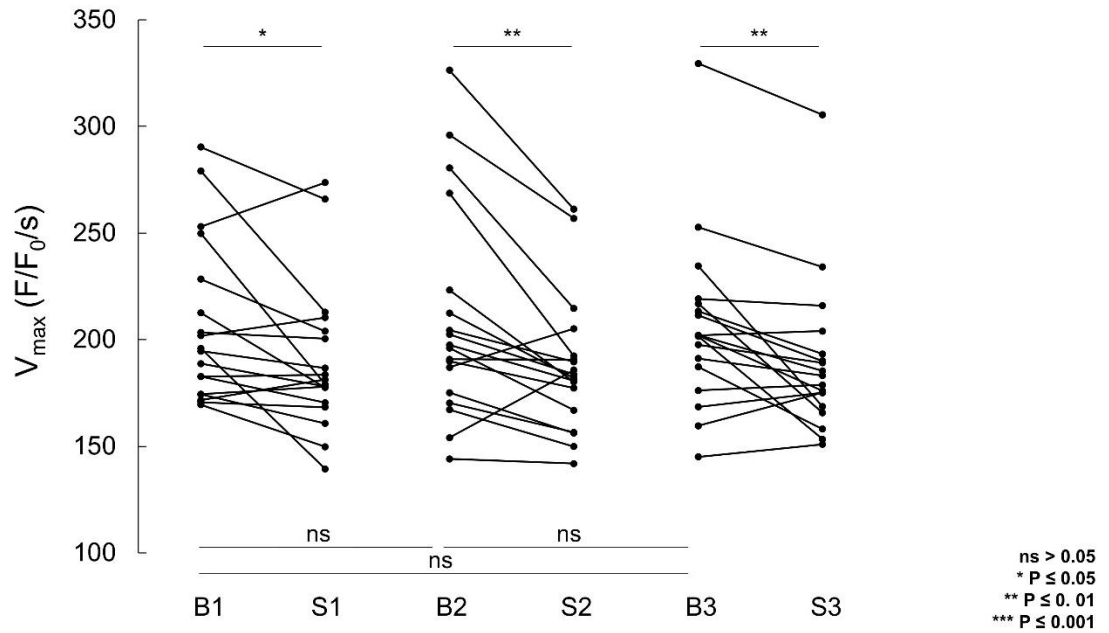
Supplemental Figure 4.24 | Absolute time to peak change in 14 dpf butterfly zebrafish embryo. B1 B2 B3 represents each baseline phase measurement. S1 S2 S3 represents each stretch phase measurement. In each stretch phase there was no significant difference between baseline and stretch phases. There were also no significant differences between each baseline phases (*** = $p < 0.001$, ns = no significant difference, $p < 0.05$).

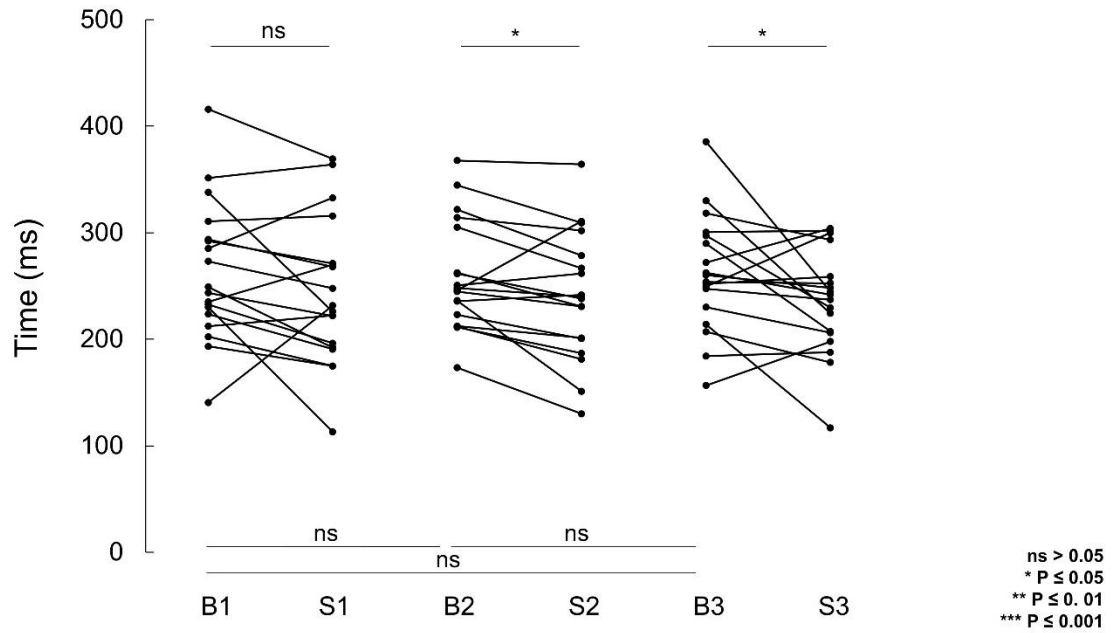## Time to Peak + Hemodynamic Loading + Blebbistatin (BF)

Supplemental Figure 4.25 | Absolute CaTD$_{80}$ change in 14 dpf GCaMP zebrafish embryo. B1 B2 B3 represents each baseline phase measurement. S1 S2 S3 represents each stretch phase measurement. In each stretch phase there was no significant difference between baseline and stretch phases. There were also no significant differences between each baseline phases (*** = p < 0.001, ns = no significant difference, p < 0.05).

Change in CaTD80 with Hemodynamic Loading, GCaMP

14 dpf
(n = 16)

ns > 0.05
* P ≤ 0.05
** P ≤ 0. 01
*** P ≤ 0.001

Supplemental Figure 4.26 | Absolute APD_{80} change in 14 dpf butterfly zebrafish embryo. B1 B2 B3 represents each baseline phase measurement. S1 S2 S3 represents each stretch phase measurement. In each stretch phase there was no significant difference between baseline and stretch phases. There were also no significant differences between each baseline phases (*** = p < 0.001, ns = no significant difference, p < 0.05).


Change in APD80 with Hemodynamic Loading, butterfly

14 dpf
(n = 13)

ns > 0.05
* P ≤ 0.05
** P ≤ 0. 01
*** P ≤ 0.001

Supplemental Figure 4.27 | Absolute CaTD$_{50}$ change in 14 dpf GCaMP zebrafish embryo. B1 B2 B3 represents each baseline phase measurement. S1 S2 S3 represents each stretch phase measurement. In each stretch phase there was no significant difference between baseline and stretch phases. There were also no significant differences between each baseline phases (*** = p < 0.001, ns = no significant difference, p < 0.05).
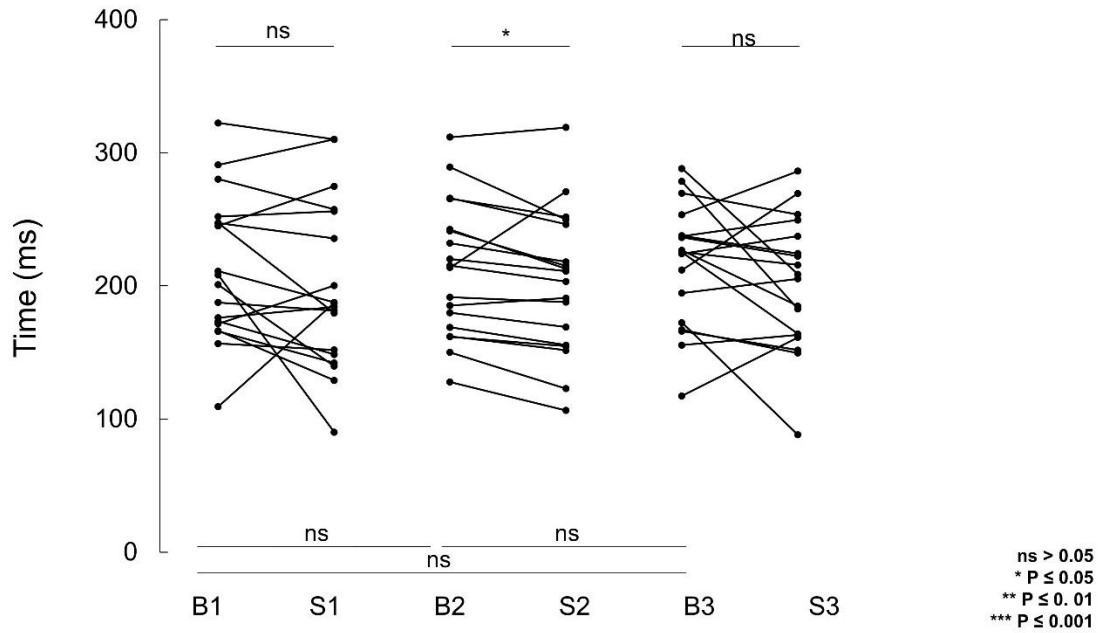

CaTD50 + Hemodynamic Loading + Blebbistatin (GC)

Supplemental Figure 4.28 | Absolute APD_{50} change in 14 dpf butterfly zebrafish embryo. B1 B2 B3 represents each baseline phase measurement. S1 S2 S3 represents each stretch phase measurement. In each stretch phase there was no significant difference between baseline and stretch phases. There were also no significant differences between each baseline phases (*** = p < 0.001, ns = no significant difference, p < 0.05).

## APD50 + Hemodynamic Loading + Blebbistatin, butterfly
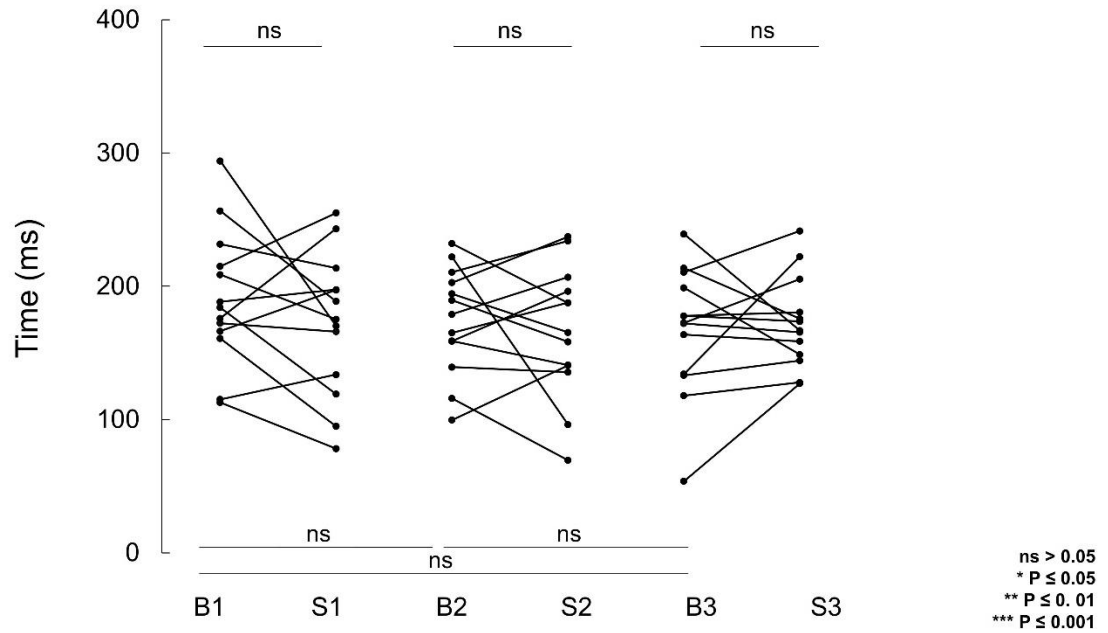
Supplemental Figure 4.29 | Absolute CaTD$_{30}$ change in 14 dpf GCaMP zebrafish embryo. B1 B2 B3 represents each baseline phase measurement. S1 S2 S3 represents each stretch phase measurement. In each stretch phase there was no significant difference between baseline and stretch phases. There were also no significant differences between each baseline phases (*** = $p < 0.001$, ns = no significant difference, $p < 0.05$).

Supplemental Figure 4.30 | Absolute APD$_{30}$ change in 14 dpf butterfly zebrafish embryo. B1 B2 B3 represents each baseline phase measurement. S1 S2 S3 represents each stretch phase measurement. In each stretch phase there was no significant difference between baseline and stretch phases. There were also no significant differences between each baseline phases (*** = p < 0.001, ns = no significant difference, p < 0.05).

APD30 + Hemodynamic Loading + Blebbistatin, butterfly
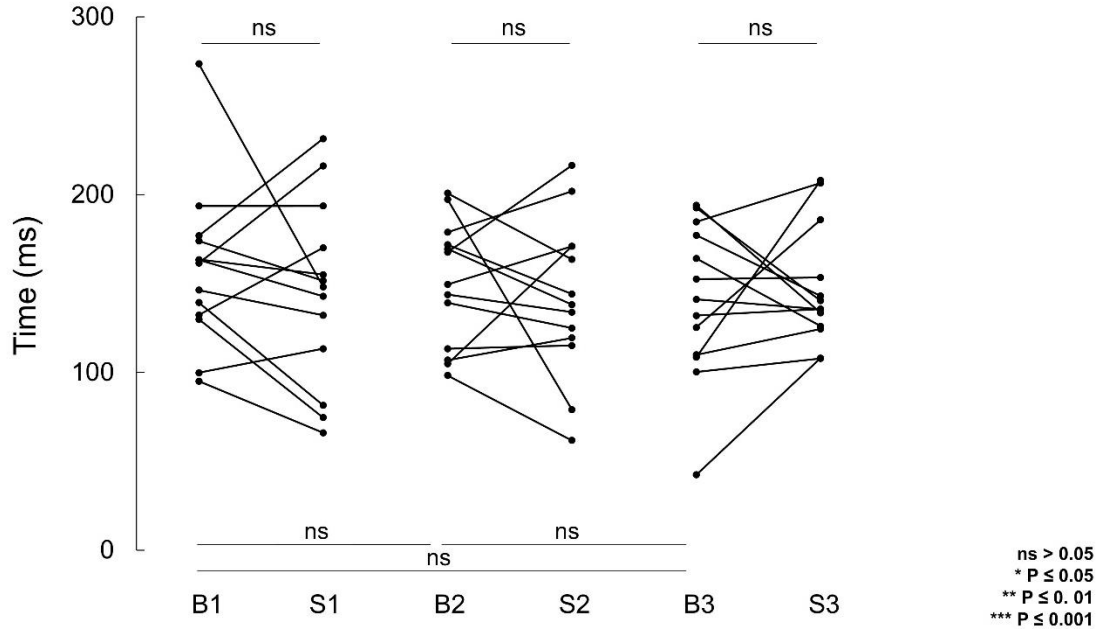
APPENDIX 3: CHAPTER 5 SUPPLEMENTARY FIGURES

Supplemental Figure 5.1 | Confocal microscopy optical slice through the ventricular mid-wall of an immunohistochemically labeled zebrafish isolated heart. Anti-GFP reveals heterogeneous cellular expression of GtACR1-eGFP (indicated by areas of bright green; the duller green represents tissue autofluorescence). The region of high intensity at the apex illustrates epicardial expression (as the optical slice goes through the epicardium in this region), while the bright band in the center of the image represents high expression in trabecular muscle.
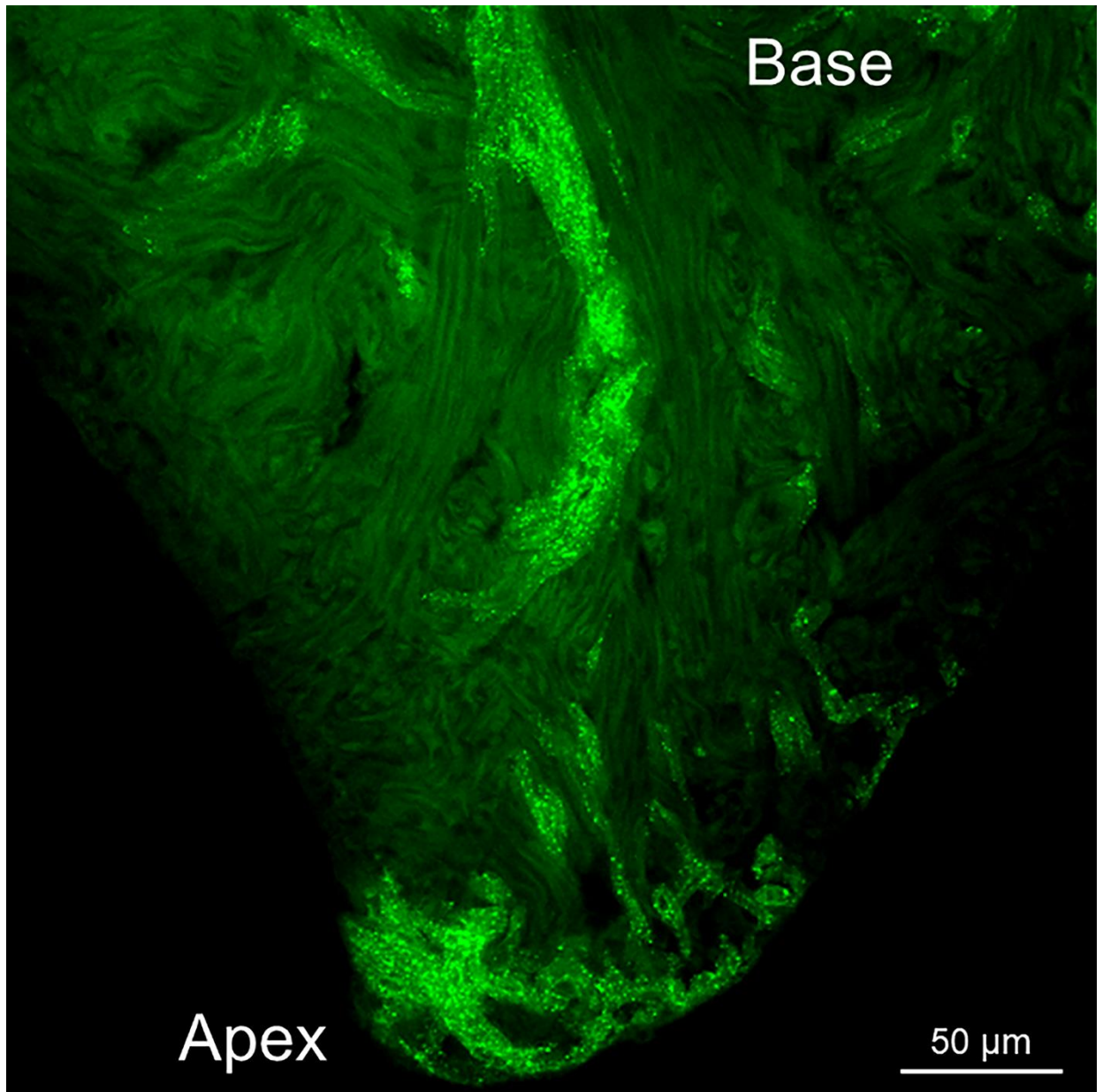
Supplemental Figure 5.2 | Comparison of OP and EP at the same rate shows no difference in the resulting AP morphology of a ventricular cell inside an isolated heart of zebrafish 3 mpf.

3 mpf Zebrafish Heart